Photoproduction of mesons off ^{7}Li :

Properties of hadrons in nuclear matter

Inauguraldissertation

Zur
Erlangung der Würde eines Doktors der Philosophie

vorgelegt der

Philosophisch-Naturwissenschaftlichen Fakultät

der Universität Basel

von

Yasser Maghrbi

aus Kairouan, Tunesien

Basel, 2011.

Genehmigt von der Philosophisch-Naturwissenschaftlichen Fakultät auf Antrag von Prof. Dr. Bernd Krusche und Prof. Dr. Volker Metag.

Basel, den 19. October 2010

Prof. Dr. Martin Spiess, Dekan

Contents

Abstract - structure of this work

The study of hadrons properties has been for long time one of the central interests in strong interactions physics. At low energy (<10 GeV), where the QCD perturbative approach is not valid anymore, hadrons have a very complex behavior. At these energies, the chiral symmetry is broken. However, many models suggest a partial chiral symmetry restoration at high temperature and density. This is indirectly connected to the hotly debated topic of hadrons properties in the nuclear medium. Various theoretical and experimental programs have been pursued through the last decades in view of the investigation of a possible modification of these properties, principally the mass and width of certain mesons and nucleon resonances.

First experimental evidences came from heavy-ion collisions and from pion-induced experiments. An exciting program using meson photproduction and aiming - among other interesting studies - at the same goal has been initiated at different electron accelerators. The present experiment was conducted during 2005 at the MAMI accelerator in Mainz using a lithium target. It profited from 4π solid angle detector setup providing data of excellent statistical quality and small systematic uncertainties. The present work summarizes the results obtained for different reactions related to the topic of hadron properties in nuclear medium.

The main studied reaction was double pion photoproduction in view of the σ -meson properties in medium. The coherent π^0 photoproduction was then investigated in view of the properties of the Δ-resonance in-medium. This reaction served also for the extraction of the ^{7}Li mass form factor and rms radius. Finally, the very interesting topic of meson bound states was investigated through the coherent photoproduction of η-mesons.

Concerning the structure of this work, a general introduction and a brief theoretical overview will be given first. Previous results and the motivation to choose ^{7}Li as a target will then be discussed. The experimental setup will be

presented after that in details (properties, electronics, calibrations, identification techniques..).
In order to extract the detection efficiency and the cross sections, the experimental setup was simulated using the GEANT package. The simulations will be summarized in Chapter V and developed for each reaction in chapter VI. Results will then be presented as the following:

- The double pion channel (separate analysis for the neutral and the mixed charged channels)
  - Reaction identification and signal to background estimation.
  - Simulations.
  - Invariant mass distributions and total cross sections.
  - Comparison and ratio of Neutral/Mixed charged mass distributions.

- The coherent π^0 channel
  - Reaction identification and missing energy spectra.
  - Simulations.
  - Differential and total cross sections.
  - Application: extraction of ^{7}Li form factor and mass rms radius.

- The coherent η channel
  - The quasi-free η channel (Reaction identification, simulations, signal to background estimation, cross sections).
  - Coherent reaction identification and simulation.
  - Missing energy spectra.
  - Coherent η cross section.
  - Comparison to ^{3}He.

Finally, before a conclusion and an outlook are given, the systematic effects will be discussed.

بِسمِ اللّٰهِ الرَّحمٰنِ الرَّحِيمِ
وَ الصَّلآة وَ السَلآم علي اشرَف المرسَلين

إِلي أَخي الحٰج و الدَّولَة العَزيزَة

Acknowledgements

I am extremly grateful to Pr. Bernd Krusche, my thesis director, for his constant support, valuable discussions, precious advices and for his patience with all my questions and problems. I would also like to thank all the A2 and the CB/ELSA collaboration members in Mainz and Bonn, in particular Pr. Volker Metag with whom I had beneficial discussions about the double pion channel. Thanks also to Pr. Colin Wilkin for all his excellent suggestions.

I am very thankful to Igal Jaeglé for the huge progress I made since working with him. I wish him successful future professor and father careers. Many thanks to all the Basel team who helped me during the last years especially D. Werthmueller and I. Keshelashivili. I also would like to thank Francis Pheron (Mèsi onpil et bon chans) and Benedicte Boillat for their support and the fun we had together. A big chnorakaloutioun to T. Rostomayan for the practice help and for sharing training with me. Thanks also to Roman Trojer for the computer support. I also would like to thank all the former and present members of our group with whom I had funny time and delicious barbecues (Fabien, Thierry, Alan, Marcus, Alexander, Manuel, Lilian, Therese) and the neighborhood of the 2.12 office. And of course a warm thank to the two nice ladies of the Secretariat Astrid and Barbara.

On the personal side, I can never thank enough my parents Ali and Rafika and my brother Hamed for their infinite moral and financial support. Asma, Lamia and Riadh, thank you very much. Big kisses to Ouways, Louay and Azza. I love you all!

Finally, I would like to dedicate this work to the Boukhatem and Maghrebi families and to all my friends in Kairouan, France and Switzerland.

Chapter 1

Exploring the matter : Challenges and opportunities

1.1 Early concepts

Nuclear physics made a huge progress during the last century. At its turn the accepted model of the atom was J. J. Thomson's "plum pudding" model in which the atom was naively described as a large positively charged ball with small negatively charged electrons embedded inside it. The discovery of the nucleus by Rutherford followed by the discovery of the nucleons and their spin opened the door to modern nuclear physics.

One of the major unanswered questions of this model was what force overcomes the repulsive electrostatic force of the protons, which tends to push the nucleus apart. In 1935 Hideki Yukawa proposed the first significant theory of the strong force to explain how the nucleus holds together as shown in Fig. 1.1. In the Yukawa interaction, a virtual particle (later found to be a meson) carries a force between the nucleons. This force explained why nuclei did not disintegrate under the influence of proton repulsion. It also gave an explanation of why the attractive strong force had a more limited range than the electromagnetic repulsion between protons.

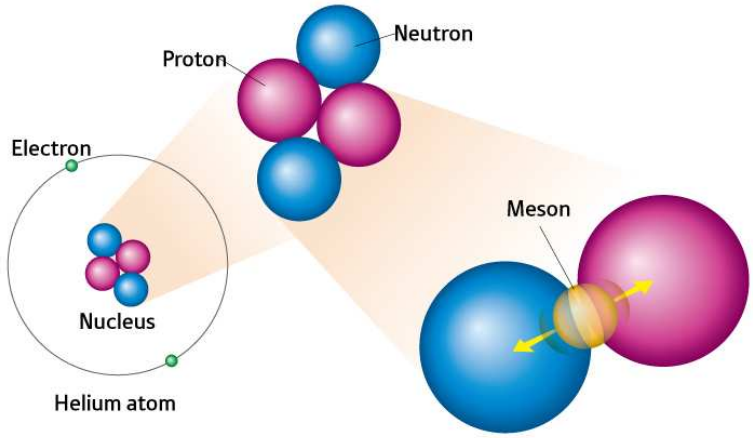

Figure 1.1: *Atom model according to H.Yukawa. The atom consists of electrons and a nucleus, and the nucleus consists of protons and neutrons. Protons and neutrons emit and absorb mesons, giving rise to the nuclear force that binds the nucleus [1].*

The model of the atom has been updated with the work of Yukawa. In the center of the atom, there is a nucleus which is hold together by the strong nuclear force. Unstable nuclei may undergo alpha or beta decay by emitting an energetic helium nucleus or ejecting an electron (or positron) respectively. If the resultant nucleus is left in an excited state, it decays to its ground state via gamma decay by emitting high energy photons.

The study of the strong and weak nuclear forces in the following years led physicists to collide nuclei and electrons at ever higher energies. This research became the science of particle physics, the crown jewel of which is the standard model of particle physics which unifies the strong, weak, and electromagnetic forces.

1.2 Particle classification and standard model

During the 1960s, Gell-Mann and Zweig proposed that hadrons were not elementary particles but were instead composed of combinations of quarks and antiquarks. The quarks which determine the quantum numbers of hadrons are called valence quarks. Any hadron may contain an indefinite number of virtual (or sea) quarks, antiquarks, and gluons which do not influence its quan-

tum numbers. There are two families of hadrons: baryons, with three valence quarks, and mesons, with a valence quark and an antiquark.[1]

This model of elementary particles, described by a quantum field theory, is called the Standard Model. It is the current state of the classification of elementary particles. As shown in Fig. 1.2, it describes the strong, weak, and electromagnetic fundamental forces, using mediating gauge bosons. The species of gauge bosons are the gluons, W^- and W^+ and Z bosons, and the photons. The model contains 24 fundamental particles, which are the constituents of matter. Finally, it predicts the existence of the Higgs boson which is yet to be discovered.[2].

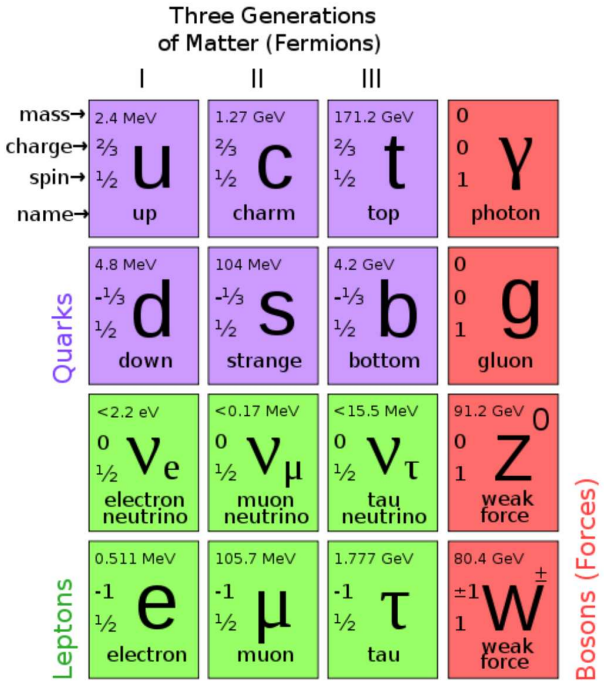

Figure 1.2: *The Standard Model has 17 species of elementary particles (12 fermions (24 if one counts antiparticles separately), 4 vector bosons and 1 scalar boson.*

[1]Quarks are spin-1/2 particles (fermions according to the spin-statistics theorem). They are subject to the Pauli exclusion principle, which states that no two identical fermions can simultaneously occupy the same quantum state. This is in contrast to bosons (particles with integer spin), of which any number can be in the same state. Unlike leptons, quarks possess color charge, which causes them to engage in the strong interaction. The resulting attraction between different quarks causes the formation of hadrons.

[2]The Large Hadron Collider at CERN, which became operational on November 20, 2009 is expected to provide experimental evidence of the existence or non-existence of the Higgs boson. If the Higgs boson is detected and its mass is between 115 and 180 GeV/c2, then the Standard Model can be valid at energy scales up to the Planck scale (10^{16} TeV).

These elementary particles can combine to form composite particles. A lot of them have been discovered since the 1960s. The success of the standard model was overwhelming as it has been found to agree with almost all the experimental tests conducted to date.

The Quantum Chromodynamics (QCD)

Analogically to the Quantum Electrodynamics QED (the science that describes the interaction between light and matter through the exchange of photons), Quantum Chromodynamics or QCD describes the strong interaction between quarks through the exchange of gluons and therefore the structure of hadrons. It is a quantum field theory of a special kind called a non-abelian gauge theory. QCD is an important part of the Standard Model of particle physics. A huge body of experimental evidence for QCD has been gathered over the years.

QCD exhibits two particular properties:

* *Asymptotic freedom*, which means that in very high-energy reactions, quarks and gluons interact weakly[3].

* *Confinement*, which means that the force between quarks does not diminish as they are separated. Because of this, it would take an infinite amount of energy to separate two quarks; they are forever bound into hadrons such as the proton and the neutron. Although analytically unproven, confinement is widely believed to be true because it explains the consistent failure of free quark searches, and it is easy to demonstrate it in lattice QCD [2].

[3]This property of QCD was first proposed in the early 1970s by David Politzer and by Frank Wilczek and David Gross. For this work they were awarded the 2004 Nobel Prize in Physics.

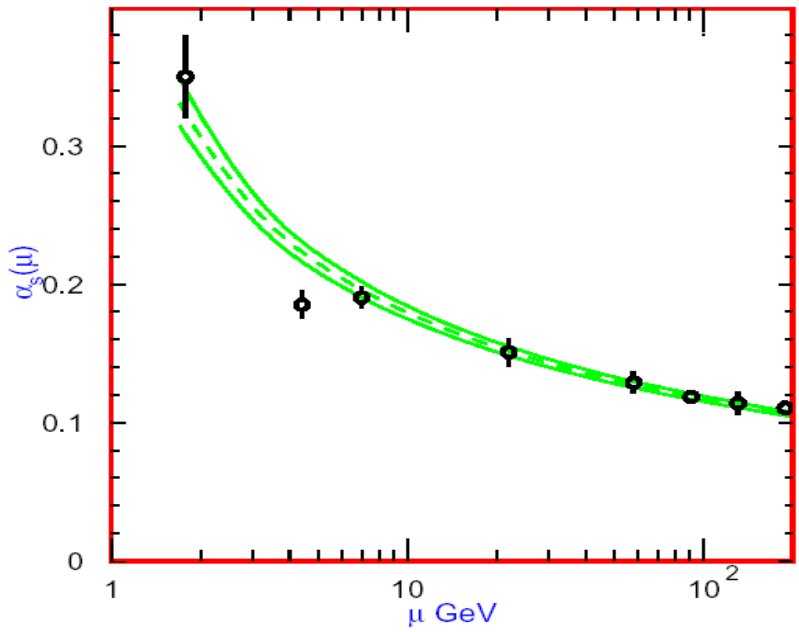

Figure 1.3: *Evolution of the effective constant α_s with the energy scale μ.*

The strong interaction becomes "weak" at small distances which allows the same kind of perturbative treatment for QCD as the one developed by Feynmann and others for the electromagnetic interaction in QED. The perturbative approach to QCD allows the systematic expansion in powers of the strong coupling constant α_s, which is small at large energies, as seen in Fig. 1.3. At a very high energy scale, this approach was very successful.

Classification of hadrons in the Standard Model

Hadrons are categorized into two families, baryons made of three quarks, and mesons made of one quark and one antiquark. Particles could be described with isospin projections and strangeness within the symmetry group SU(3). Concerning mesons, combinations of one u, d or s quark and one u, d, or s antiquark give rise to a nonet ($3 \otimes 3^* = 8 \oplus 1$ of the $SU(3) \otimes SU(3)$). As shown in Fig. 1.4, depending on the quantum numbers of the total angular momentum, one obtains two nonets, one nonet for pseudoscalar mesons with $J^P = 0^-$ and one nonet for vector mesons with $J^P = 1^-$.
In the same way, baryons could be classified within SU(3) through 27 combinations ($3 \otimes 3 \otimes 3 = 10 \oplus 8 \oplus 8 \oplus 1$). One obtains for baryons an octet corresponding to the ground state baryons (spin 1/2 and J=1/2) and a decouplet (spin 3/2 and J=3/2) as seen in Fig. 1.5.

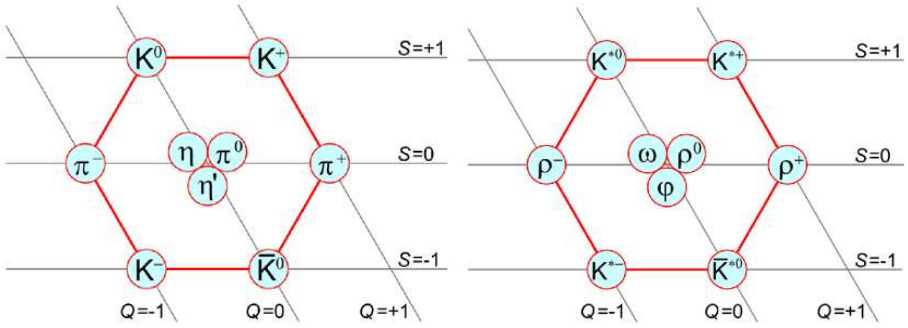

Figure 1.4: *The nonet of pseudoscalar (left) and vector mesons (right)*

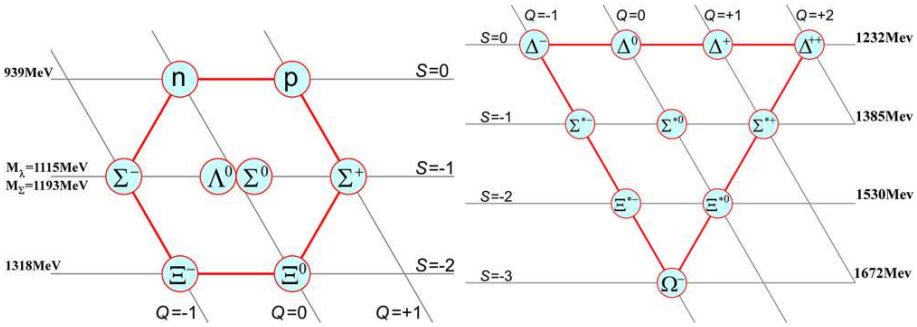

Figure 1.5: *Baryons ground state in the quark model. Left: the baryon octet of* $J = 1/2$*. Right: Baryons decuplet of* $J = 3/2$*.*

Beyond the Standard Model

Despite the success of the standard model, most particle physicists agree that the standard model is an incomplete description of nature, and that a more fundamental theory awaits discovery. Furthermore, the Standard Model is widely considered to be a provisional theory rather than a truly fundamental one. There are most probably hypothetical elementary particles not described by the Standard Model, such as the graviton (the particle that would carry the gravitational force) or the supersymmetric particles[4]. Finally, many physicists are still unsatisfied by the standard model for different reasons. One of

[4]Supersymmetry extends the Standard Model by adding an additional class of symmetries to the Lagrangian. These symmetries exchange fermionic particles with bosonic ones. Such a symmetry predicts the existence of supersymmetric particles, abbreviated as sparticles. Each particle in the Standard Model would have a superpartner whose spin differs by 1/2 from the ordinary particle. Due to the breaking of supersymmetry, the sparticles are much heavier than their ordinary counterparts.

the reasons is that many parameters (masses e.g) cannot be deduced from the model but are put in by hand. The hierarchy problem[5] is also one of these reasons of theoretical considerations. The Grand Unified Theory (GUT) might bring the answer to all these questions through the LHC experiments. Anyway, the Standard Model in its current form still needs modifications to agree with some recent discoveries, such as the non-zero neutrino mass.

1.3 Nucleon resonances and meson photoproduction

At an energy scale on the order of the mass of the nucleon and its excited states, α_s becomes large ($\alpha_s \simeq 1$ at 1 GeV[6], see Fig. 1.3) and the perturbative approach of QCD cannot be applied anymore. For low energies from 100 MeV up to 10 GeV the nucleon can be excited. This is easy to realize in terms of accelerators and expense. However, physics becomes very complex and a lot of things are still unknown.

Since a non-perturbative approach to treat QCD is still nowadays impossible, an alternative to describe the nucleon and its excited states at low energy is the use of the so-called *constituent quark models*. These models consider hadrons as made of internal quarks only, with no further component. The proton for example is made in this framework of no more than two u quarks and one d quark which share the proton total mass. In this way, the individual quark masses (constituent quark masses) are much higher than their masses in the standard model(called current quark masses)[7].

[5] In theoretical physics, a hierarchy problem occurs when the fundamental parameters (couplings or masses) of some Lagrangian are vastly different (usually larger) from the parameters measured by experiment. Hierarchy problems are related to fine-tuning problems and problems of naturalness. In particle physics, the most important hierarchy problem is the question that asks why the weak force is 10^{32} times stronger than gravity. More technically, the question can be why the Higgs boson is so much lighter than the Planck mass. Some partial solutions exist such as the Supersymmetric Solution or the Extra Dimensions (ADD/GOD model).

[6] In particle physics, units are given in eV/c with c=1 in natural units. 1 eV is the energy that a particle with one unit of charge (e.g. an electron) acquires when it passes through a potential of 1 Volt and is equivalent to $1.602 \cdot 10^{-19}$ Joule.

[7] In the constituent quark model, the u and d quark masses would be in the range of 220-300 MeV, much higher than values given in PDG06 (between 1.5 and 7 MeV).

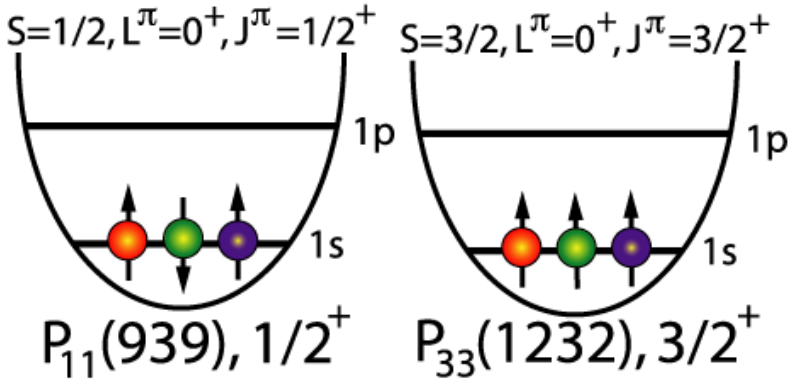

Figure 1.6: *The nucleon in the ground state (left) and the lowest lying resonance in a simplified view of the constituent quark model.*

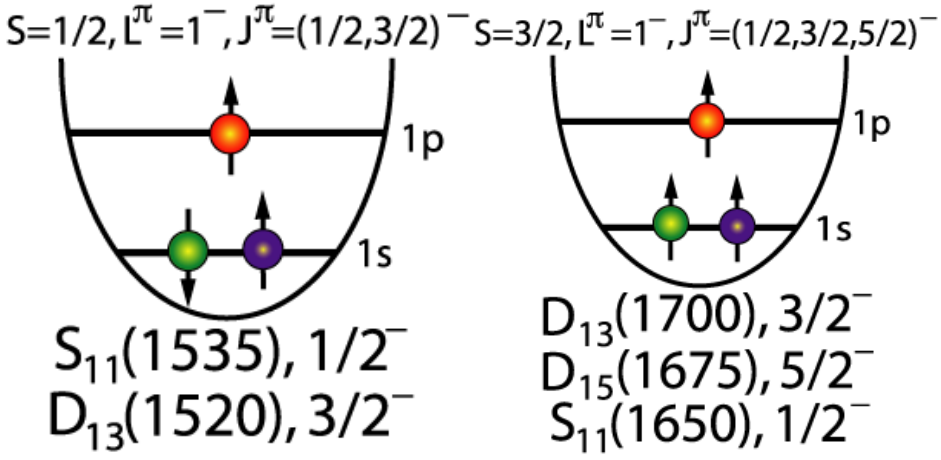

Figure 1.7: *Next nucleon resonances.*

The low lying resonances of the nucleon can be seen in a simple constituent quark model as a combination of spin flips of single quark and an orbital excitation of one of the three valence quark in a harmonic oscillator potential. As seen in Fig. 1.7, the nucleon ground state is realized with three quarks in the $1s$ state : two quarks with spin up and one quark with spin down. The lowest excited state $P_{33}(1232)$ is obtained by aligning the spin of the third quark. The next resonances are obtained by moving one quark to the 1p state (S_{11} and D_{13}). At higher energies, an arbitrary number of resonances can be obtained in the same way.

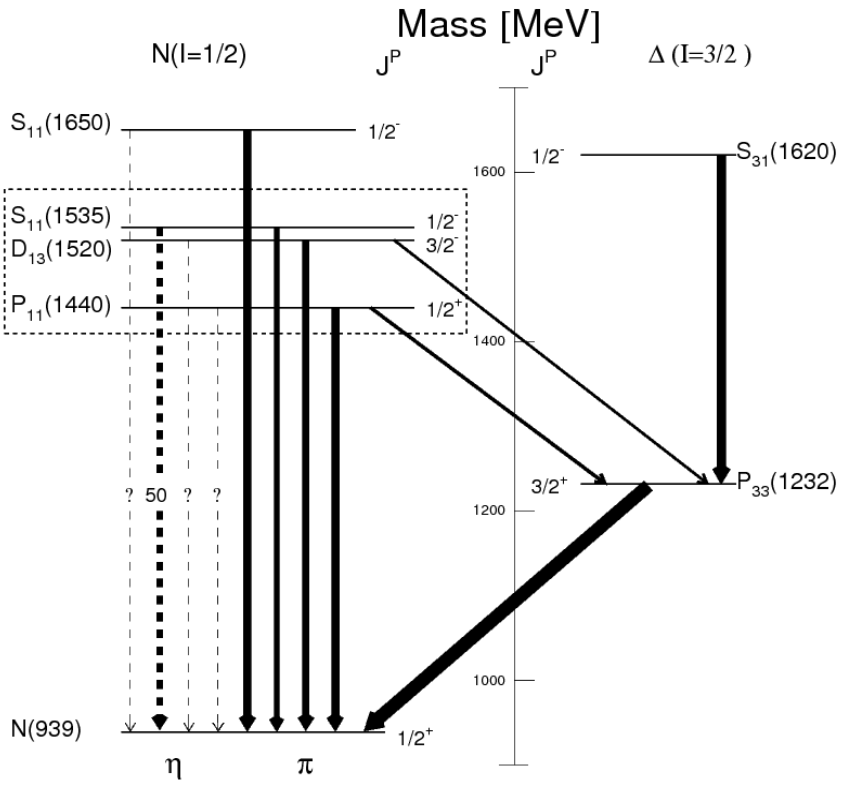

Figure 1.8: *Decay scheme of low lying nucleon resonances. Shown are isospin 1/2 and 3/2 resonances. The solid arrows indicate decays via pion emission, the dashed arrows via η-emission. The line width of the arrows is scaled to the branching ratios of the respective decays, for η-decays the known branching ratios are quoted.*

A level scheme of the low-lying nucleon resonances is shown in Fig. 1.8. Resonances with isospin $I = 3/2$ are called Δ-resonances whereas those with isospin $I = 1/2$ are called N^*-states. These states are defined by their mass and quantum numbers like isospin or parity.
The notation of the resonances is made of a capital letter showing the relative angular momentum between the nucleon and the decay mesons. The usual convention is used (S for l=0; P for $l = 1$; D for $l = 3$). The two indices represent 2×I and 2×J where I is the isospin and J the total momentum of the resonance. Usually the mass of the resonance is given in brackets. The lightest resonance (called Δ resonance) is then named P_{33}(1232). The three other resonances accessible with the available energy of the present work are P_{11}(1440), D_{13}(1520) and S_{11}(1535).

Nucleon resonances decay to the ground state by the emission of a meson such as π and η. Since the strong interaction is mainly responsible for the decay of nucleon resonances (hadronic decay), they have a very short life time (typically $10^{-23}s$) and therefore a large width lying between 100 and 300 MeV. The large width combined with the close masses of the resonances induces an overlapping of the states of the second resonance region. This makes it non trivial to study an individual resonance (except in the particular case if they have exclusive decay channels like the $S_{11}(1535)$ with the Nη decay). Fig. 1.9 shows the positions and widths of the low lying isospin 1/2 resonances.

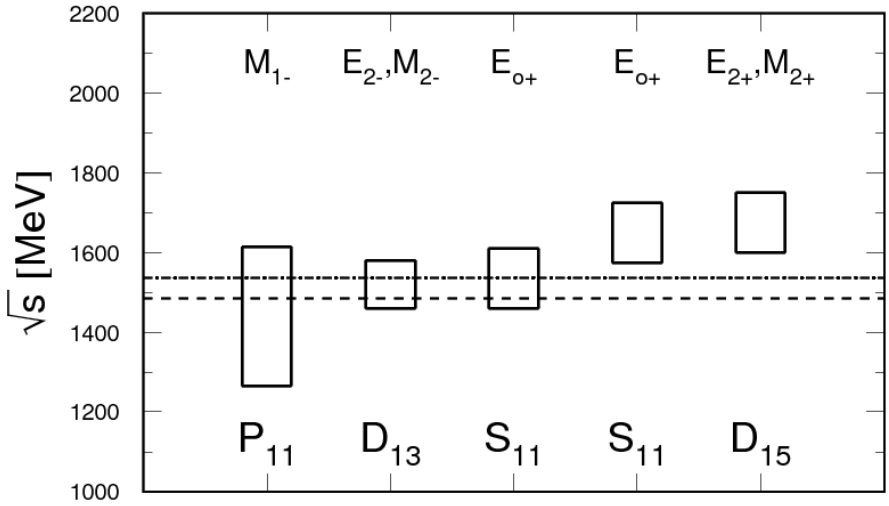

Figure 1.9: *Position and widths of the low lying isospin 1/2 resonances. The dashed line indicates for example the production threshold for the $p(\gamma,\eta)p$ -reaction and the dashed-dotted line the maximum tagged photon energy available at the MAMI[9] accelerator in 2005. The multipoles corresponding to the excitation of the resonances are indicated on top of the figure.*

However, nucleon resonances may also decay via photon emission. The photon decay mode is very interesting since the photon couples only to the spin and flavor degrees of freedom of the quarks and therefore reveals their spin - flavor correlations, which are related to the configuration mixing predicted by QCD. Therefore combining photons and mesons would carry information of both, electromagnetic and strong decays. In this way, production of mesons using photon beams (Meson Photoproduction) is an excellent tool for the investigation of the nucleon resonances and consequently the test of the quark models.

Meson photoproduction

Meson photoproduction has progressively replaced the use of meson-beams in the race for the excitation of the nucleon resonances. Using meson beams of long-lived charged pions or kaons was for a long time the dominant tool for resonance production. The excitation of nucleon resonances using photon probes appeared to be a better alternative to study especially resonances which couple weakly to πN.

However, the non-resonant background terms, which play no role in pion induced reactions, represent on first sight a disadvantage of photon beams. However, a part of this disadvantage can be overcome by using neutral mesons in the final state. The development of high sensitivity, high resolution photon detectors gave a large push to the field of meson photoproduction.

In contrast to the Δ region where the photoproduction of single neutral pions allowed a very good study of the Δ-resonance,in the second resonance region states are strongly overlapping due to the large widths and the closeness of the resonances, in particular P_{11}(1440), D_{13}(1520) and S_{11}(1535) which decay to different final states including Nπ, N$\pi\pi$ and Nη. The study of π^0 , η and $\pi\pi$ photoproduction therefore allows the investigation of the three resonances. Single π^0 -photoproduction is dominated by the D_{13}-resonance, η-photoproduction dominated by the S_{11} and $2\pi^0$ involves both D_{13}- and P_{11}-resonances. Fig. 1.10 of the total photoabsorbtion[10] cross section shows how the resonances of the second resonance region are strongly overlapping [6].

[10]Total photoabsorbtion correspond to the inclusive measurement of all possible reactions. It has the advantage, that no final state interaction effects may influence the results and the disadvantage that many different reaction channels do contribute and not all of them are related to resonance excitation.

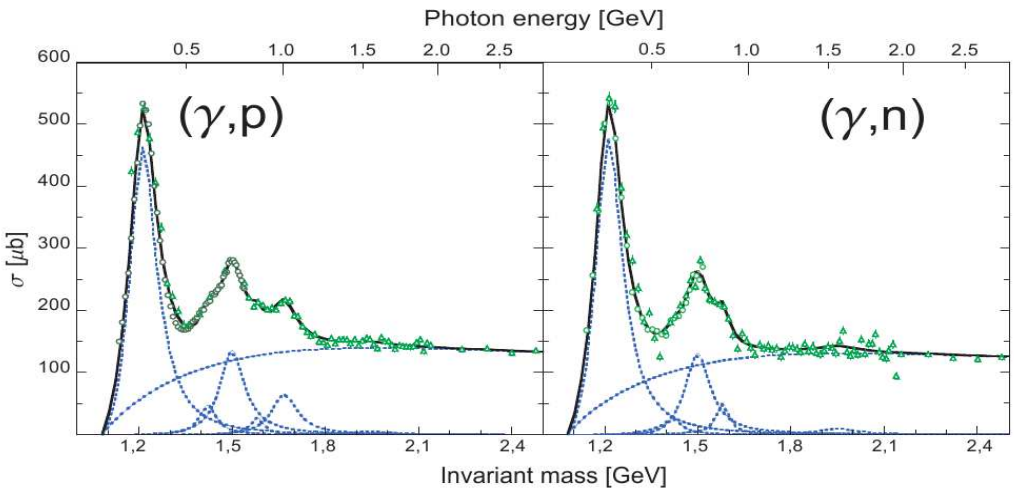

Figure 1.10: *Total photoabsorption cross section on the proton and on the neutron [6]. The non-resonant background and different resonance contributions are shown (dashed lines). From left to right :* $P_{33}(1232)$, $P_{11}(1440)$, $D_{13}(1520)$, $S_{11}(1535)$, $F_{15}(1680)$ *(proton only) and* $F_{37}(1950)$.

Finally, the number of the predicted resonances is much bigger than the number of the observed ones, especially at energies around 2 GeV. This problem commonly known as "the missing resonances" might be due to the effective degrees of freedom in the constituent quark model. It might also be that the experimental conditions do not allow the observation or the excitation of certain resonances. In charged pion induced reactions, the pion could not couple to the missing resonances. In the photon induced reactions, certain resonances are only visible on the excited neutron but not the proton. New photon induced experiments are now focusing on increasing the number of the observables by exploring the degrees of polarization as it is the case at MAMI and ELSA[11] and JLAB[12] [7]. This might indirectly allow the observation of certain missing resonances.

The study and the search for the resonances is one of the most important topics at low energy scale. However, this work will be more centered about understanding the properties of hadrons in the nuclear medium and in particular the mesons. Therefore, the topic of the resonances will not be developed further. More details about the recent progress in the study of the resonances can be found in [3], [4] and [5].

[11] Electron Stretcher and Accelerator, Bonn, Germany.
[12] Thomas Jefferson Lab National Accelerator Facility, Newport News, Virginia, USA.

1.4 In-medium modification of hadrons

General considerations

The topic of in medium properties of hadrons is one of the most interesting in modern nuclear physics. It is much discussed as it concerns the properties of non perturbative QCD at low energy. As stated above, QCD is very well described at high energies, or short scales smaller than 0.1fm, by the perturbative approach with point-like quarks and gluons. At large scales, in particular r>1fm, physics becomes very complex since hadrons should become described as many-body systems composed of valence quarks, sea quarks, and gluons. For vanishing current quark mass, the QCD Lagrangian is invariant under chiral rotations and the right- or lefthandness of quarks is conserved :

$$\psi_{R,L} = \frac{1}{2}(1 \pm \gamma_5)\psi, \psi = (u, d)^T \tag{1.1}$$

This leads to an important symmetry of the strong interaction, the chiral symmetry. Since the current quark masses[13] are almost negligible compared to the mass of hadrons, the explicit breaking of this symmetry is small. However, the spontaneous breaking occurs since the ground state, the QCD vacuum, has only part of the symmetry, which is connected to a non-zero expectation value of scalar $q\bar{q}$ in the vacuum (the chiral condensate).

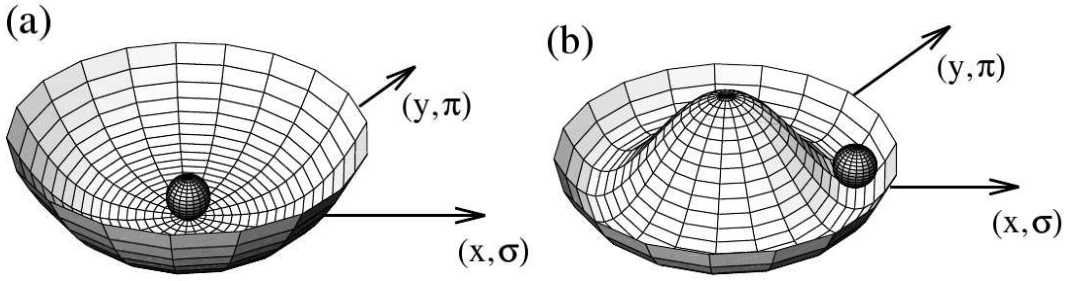

Figure 1.11: *Spontaneous breaking of chiral symmetry. QCD vacuum (a) has only a part of the symmetry, that governs low energy dynamics. Without symmetry breaking hadrons would appear as mass degenerate parity doublets (b).*

[13]Quark mass is only 5-15 MeV for u,d quarks. Most of hadron masses is generated by dynamical effects.

This symmetry breaking is clearly reflected in the hadron spectrum, without it hadrons would appear as mass degenerate parity doublets, which is not true neither for baryons nor for mesons as seen in table 1.1 (masses are in MeV).

Particle, J^{π}**, Mass**	P_{11}, $1/2^{-}$, 939	ρ, 1^{-}, 770	π, 0^{-}, 134.7
Chiral partner, J^{π}**, Mass**	S_{11}, $1/2^{+}$, 1535	a_1, 1^{+}, 1260	σ, 0^{+}, 400-1200
Mass split	≈600	≈500	266-1066

Table 1.1: *Without symmetry breaking hadrons would appear as mass degenerate parity doublets, which is by far not the case as shows the mass split between different chiral partners.*

On the other hand, models suggest a temperature and density dependence of the chiral condensate $< q\bar{q} >$. There is no *direct* relation between the modification of the hadrons properties in the nuclear medium, such as mass or width, and the quark condensate. However, there is an *indirect* relation which connects the QCD picture to he hadron picture via the QCD sum rules as seen in equation 1.2 where the left-hand side is related to hadrons and the right-hand side to QCD [8]:

$$\frac{Q^2}{\pi}\int_0^{\infty}\frac{\tau m\Pi(s)}{s(s+Q^2)} = \frac{-1}{8\pi^2}(1+\frac{\alpha_s}{\pi})\frac{Q^2}{\Lambda^2}+\frac{m_q\langle q\bar{q}\rangle}{Q^4}+\frac{1}{24}\frac{\langle\frac{\alpha_s}{\pi}G^2\rangle}{Q^4}-\frac{112}{81}\alpha_s\pi\frac{m_q\langle q\bar{q}\rangle^2}{Q^6}+... \tag{1.2}$$

This dependence should be clearly seen under experimental conditions where temperature and density are significantly high like in heavy ions reactions, but to some extent effects should be already seen at zero-temperature and normal nuclear matter density like in the case of pion and photon induced reactions. Fig. 1.12 shows for some experiments the predicted dependence in the Nambu-Jona-Lasinio model (JNL) [9].

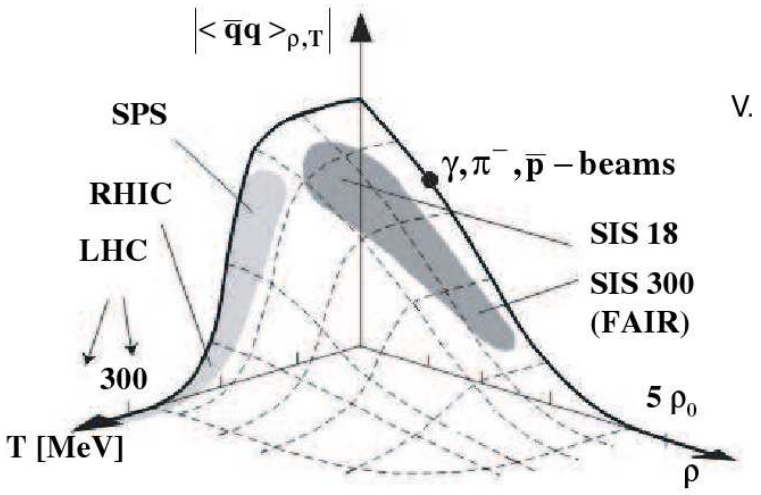

Figure 1.12: *Temperature and density dependence of the chiral condensate in the JNL model.*

The in medium modifications arise from the coupling of mesons to resonance - hole states and the coupling of the modified mesons to resonances. Many models tried to predict the in medium spectral functions of hadrons. Post, Leupold and Mosel calculated the spectral functions of $\pi-$, $\eta-$ and $\rho-$ mesons in vacuum and in medium in a self-consistent coupled channel approach as shown in Fig. 1.13 [10].

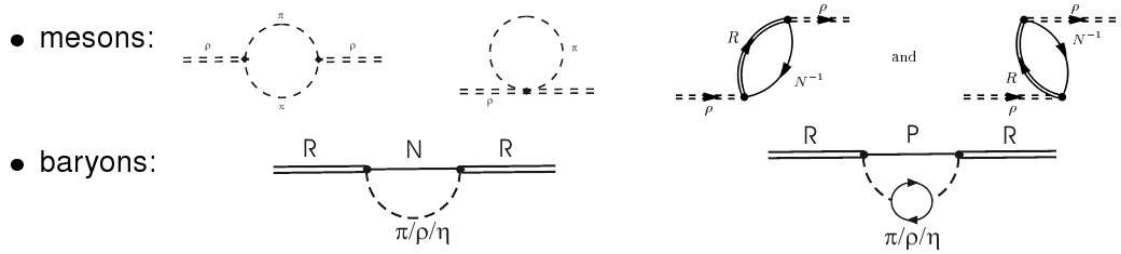

Figure 1.13: *Diagrams for the vacuum and in medium self-energies of mesons and baryons according to [10].*

The spectral functions have been calculated using the corresponding propagator:

$$D = \frac{1}{p^2 - m^2 - \Pi_{vac}} \qquad in\ Vacuum \tag{1.3}$$

$$D = \frac{1}{p^2 - m^2 - \Pi_{vac} - \Pi_{med}} \qquad in\ medium \tag{1.4}$$

Fig. 1.14 shows the spectral functions calculated by Post et al. for the ρ meson and for the S_{11} and D_{13} resonances. The D_{13} resonance is expected to have the largest effects due to its strong coupling to the Nρ channel.

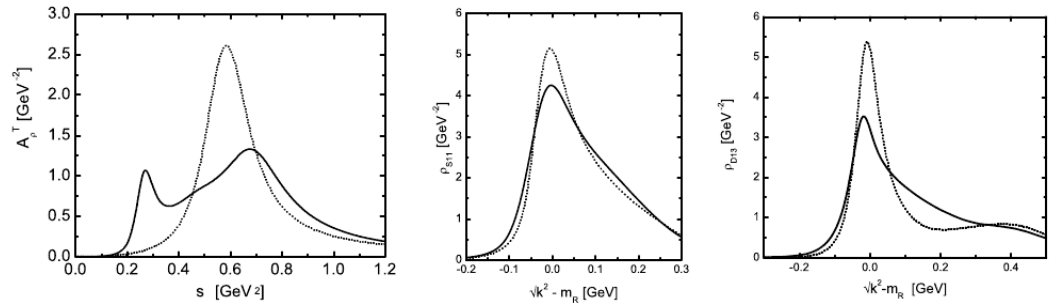

Figure 1.14: *Predicted vacuum (dashed curves) and in medium (solid curves) spectral functions for the $\rho-$meson(left), S_{11}(1535) (center) and D_{13} (right) resonances).*

Experimentally, the excitation of the Δ-resonance and its propagation through the nuclear medium have been intensively studied in heavy ion reactions [21], in pion, electron, and photon induced reactions [19, 50] and in medium effects have been experimentally established since a longtime [16]. This part will be discussed in Chapter II, section 2.

In the second resonance region, predictions from the self-consistent resonance model discussed above give strong broadening for the D_{13} due to the strong coupling to $N\rho$ while only small effects are expected for the S_{11} following [22] :

$$\Gamma^{D_{13}}_{med} \approx \Gamma^{D_{13}}_{vac} + (200MeV)\frac{\rho}{\rho_0} \tag{1.5}$$

$$\Gamma^{S_{11}}_{med} \approx \Gamma^{S_{11}}_{vac} + (30MeV)\frac{\rho}{\rho_0} \tag{1.6}$$

In a first series of data, at most a slight broadening of the D_{13}-resonance in quasi-free single π^0 production or quasi-free inclusive π^0 production was ob-

served. The large broadening is not excluded due to 'sampling' over the nuclear density distribution and FSI [23].

On the other hand the S_{11} resonance has been investigated with TAPS at MAMI with photon energies up to 820 MeV and for energies up to 1.1 GeV at KEK [17] and Tohoku [18]. The first experiment found no in medium broadening of the S_{11} resonance (beyond effects from Fermi smearing and η FSI), the KEK experiment reported some collisional broadening of the resonance and the Tohoku experiment pointed to a significant contribution of a higher lying resonance to the $\gamma n \rightarrow \eta n$ reaction. However, none of these experiments covered the full line shape of the S_{11}. [24]. The S_{11} has been recently re-investigated for different heavy solid targets at ELSA with energies from threshold up to 2.2 GeV. No shift or broadening in the resonance line shape was found. Results agreed with BUU model calculations which included only "trivial" in medium effects such as Fermi smearing, Pauli blocking of final states. At higher incident photon energies, the agreement was less good between experiment and BUU calculations which needs better input for the semi-inclusive ηX channels [25].

To summarize, the in medium modification of resonances may arise from the following effects, some more trivial such as:

- Broadening of the resonance structure by Fermi motion of the nucleons
- Broadening by additional decay channels: NN* $\rightarrow$NN (collisional broadening)
- Narrowing by Pauli-blocking of final states for N* $\rightarrow$Nπ etc.

up to modifications with signs of chiral symmetry restoration which need calculations for the most simple effects.

On the mesons side..

A possible signature of in medium modification of mesons has been investigated in the frame of different experiments. A first evidence for medium modification of the ρ- vector meson from the reaction $\rho \rightarrow e^+e^-$ has been observed in ultra-relativistic heavy-ion collisions with CERES at CERN. Fig. 1.15 shows the dilepton spectra in ultra-relativistic pA and AA collisions where an enhancement is clearly seen in the cross section of heavy targets compared to a proton

target. This enhancement is attributed to the reaction $\pi\pi \rightarrow \rho \rightarrow e^+e^-$ with in medium modified ρ-mesons [11],[12]. Data fit well to a predicted medium-modified ρ spectral function.

Indication for the same medium modifications at normal nuclear matter density from the $\rho \rightarrow e^+e^-$ reaction was observed as well in p+A collisions at 12 GeV at KEK[14] [13].

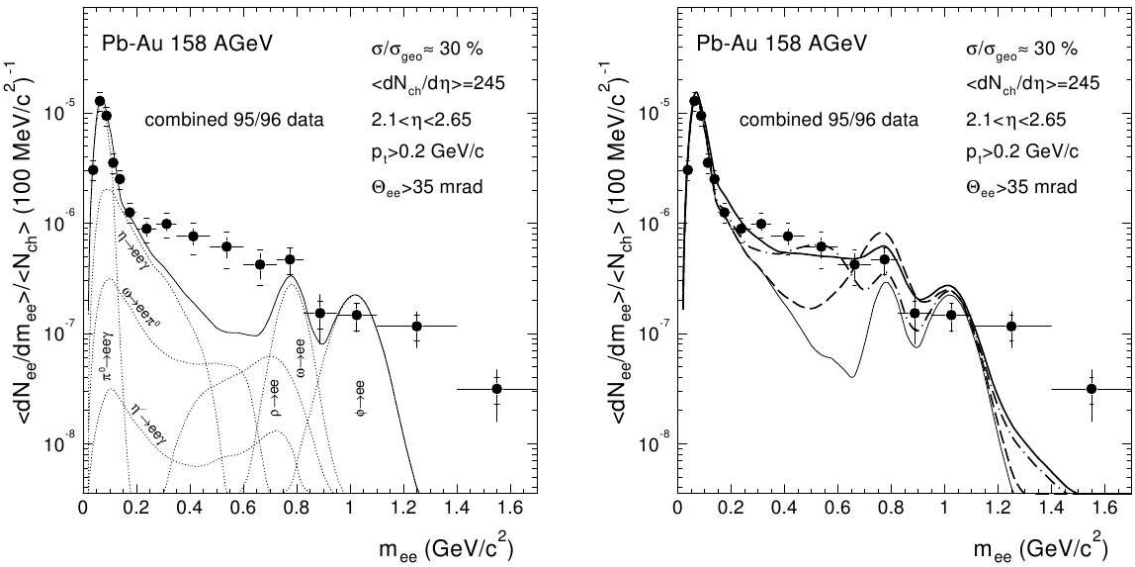

Figure 1.15: *Left: Invariant mass spectrum of e^+e^- pairs emitted in 158 AGeV/c Pb+Au collisions from the combined analysis of two different beamtimes. The solid line shows the expected yield from hadron decays, dashed lines indicate the individual contributions to the total yield. Right: Comparison of the experimental data to i) free hadron decays without ρ decays (thin solid line), ii) model calculations with a vacuum ρ spectral function (thick dashed line), iii) with dropping in medium ρ-mass (thick dash-dotted line, iv) with a medium-modified ρ spectral function (thick solid line). The latter fits almost perfectly to the data as a signature of an in medium modification of the ρ-meson.*

Concerning the σ scalar meson, the evidence for an in medium change of the $\pi\pi$ interaction has been observed in different experiments but without definitive conclusions. The charmed mesons are also in the play, like in the planned

[14]KEK = The High Energy Accelerator Research Organization (Ko Enerugi Kasokuki Kenkyu Kiko) is a high-energy physics research organization in Tsukuba, Japan. Its two major accelerators are the 12 GeV Proton Synchrotron and the KEKB electron-positron collider.

experiments at FAIR (GSI)[15] in view of the in medium modification of the D-meson. A first signature for a possible ω meson mass modification in its $\pi^0\gamma$ decay has been reported by the CB-ELSA/TAPS collaborations, but without conclusive results [15].

The meson-nucleus bound systems

Another hotly debated topic is meson-nucleus bound systems. First experimental evidence of the existence of η-mesic nuclei has been recently reported, among others, by the CB-TAPS collaboration. The existence of ω-meson-nucleus bound system is also under investigation within the CBELSA/TAPS collaborations.

The topics of σ-meson properties in medium and meson-nucleus bound systems, being the major topics of the present work, will be developed with details in Chapter II.

[15] In the years to come, GSI will evolve to an international structure named FAIR for Facility for Antiprotons and Ions Research. The first beam is expected by 2013. Among the improvements, two new synchrotrons, a Super-FRS and several new rings among which one that can be used for antimatter research.

Chapter 2

Theoretical background and previous results

2.1 Introduction

In meson photoproduction experiments on nuclei, three different final states can occur corresponding to three different production mechanisms

- **Coherent production :** $\gamma + A \rightarrow Meson + A$
  In the case of coherent production, the nucleus remains intact and in its ground state. The production amplitudes of all nucleons add up coherently. The total center of momentum energy $\sqrt{s}$ is :

$$\sqrt{s} = \sqrt{(\mathbf{k} + \mathbf{p})^2} = \sqrt{2E_\gamma m_A + m_A^2} \tag{2.1}$$

  where k and p are the four-momenta of the incoming photon and the nucleus, respectively. E_γ stands for the photon energy and m_A for the nucleus mass. The center of momentum energy has to be high enough to produce at least the masses of the outgoing particles:

$$\sqrt{s} \geq m_{meson} + m_A \tag{2.2}$$

  The threshold photon energy can be calculated:

$$E\gamma^{th} = m_{meson} + \frac{m_{meson}^2}{2m_A} \tag{2.3}$$

- **Incoherent production :** $\gamma + A \rightarrow Meson + A^*$
  In the incoherent process, the nucleus remains intact but in an excited state. The nucleus decays then by the emission of photons. The incoherent process is very difficult to observe due to very small cross sections. In light nuclei with only a few excited states, incoherent excitations of the nucleus can be exploited as spin-isospin filters, but their treatment becomes very complicated for heavy nuclei with a high level density.

- **Quasi-free production :** $\gamma + A \rightarrow Meson + A^{'} + N$
  In the case of quasi-free production, the meson is produced off one of the target nucleons. This nucleon is knocked out of the target due to the momentum transfer. The other nucleons are spectators and do not participate in the production process. Here, the energy of the meson is no longer fixed but follows a broad distribution. This is due to Fermi motion of the nucleons inside the nucleus. For the same reason, the threshold energy is reduced compared to the elementary process. This lowering of the threshold is however limited by kinematics. The separation energy of the participating nucleon has to be brought up in addition to the coherent threshold energy.

In the present work, three main reactions will be studied in view of hadron properties in nuclear matter:

- Study of the pion-pion invariant mass distributions for $\pi^0\pi^0$ and $\pi^0\pi^{+/-}$ photoproduction as a tool for in medium behavior of the σ -meson.

- The study of the coherent π^0 -photoproduction aiming at the in medium properties of the Δ resonance. This reaction may be also exploited in view of the nuclear mass distribution.

- The search for η-nucleus bound states.

For each reaction, the coherent and quasi-free thresholds for ^{7}Li are summarized in the table (in MeV). 2.1

Channel	**Coherent th.**	**Quasi-free th.**
$\pi^0\pi^0$	275.5	283
π^0	136.3	144
η	569.3	577

Table 2.1: *Coherent and quasi-free thresholds of the studied reactions on ^{7}Li*

For each channel, a short introduction and the basic theoretical background will be given before previous related results will be shown. The reason for the choice of ^{7}Li and its importance for the different reactions will be discussed.

2.2 Photoproduction of $\pi\pi$ pairs - In-medium properties of σ meson

As stated in the previous chapter, models indicate a strong temperature and density dependence of the chiral condensate which in principle leads to a partial restoration of chiral symmetry at high temperature and/or density.
The case of the σ meson is of particular interest. A calculation by Bernard et al. in the framework of the Nambu-Jona-Lasino model predicted that the $J^\pi = 0^+$ σ -meson should become degenerate with its chiral partner the $J^\pi = 0^-$ pion in the chiral limit [26]. Fig. 2.1 shows how the σ -meson mass drops as function of the nuclear density. According to the model, a significant drop in the σ mass[1] is therefore expected in normal density nuclear matter (like in the case of the photoproduction experiments) compared to the vacuum.

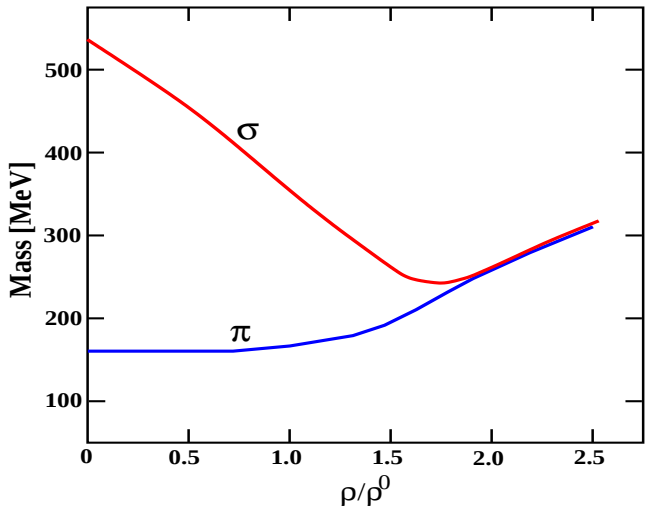

Figure 2.1: *σ mass in Nambu, Jona-Lasino (NJL) model as function of density. ρ_0 is the normal unclear density. If the density is large enough, chiral symmetry is restored and the σ mass is degenerate with its chiral partner, the pion.*

[1]Since the pion approximates a Goldstone boson, the pion mass is not expected to change dramatically with increasing density.

However the σ meson itself, which has not yet been seen experimentally, is still subject of big controversies. Significant discrepancies about its properties can be found in the literature. It is treated as a pure $q\bar{q}$ state in some approaches whereas others treat it as a correlated $\pi\pi$ pair in a $I = 0, J^{\pi} = 0^{+}$ state.
The mass and width of the σ are also still uncertain. In the review of particle properties [33], it is listed as $f_0(600)$ with a mass lying between 400 and 1200 MeV and a full width between 600 and 1000 MeV. However, Caprini, Colangelo and Leutwyler have recently predicted its mass and width within small uncertainties from dispersion relations [34].

Despite the discrepancies, different model approaches agree to predict a strong correlation between the σ meson and the $\pi\pi$ pairs and therefore a clear in medium modification of the invariant mass distributions of the $\pi\pi$ pairs. As seen in Fig. 2.2 even with the restoration parameter set at zero (α = 0), an effect on the $\pi\pi$ mass is expected produced by the interaction of the two pions [27]. The predicted effect can be due to the in medium spectral function of the σ -meson [26, 28, 29]. However, in medium $\pi\pi$ interaction can cause similar effects due to the coupling to nucleon - hole, Δ - hole and N^* - hole states [30, 31, 32].

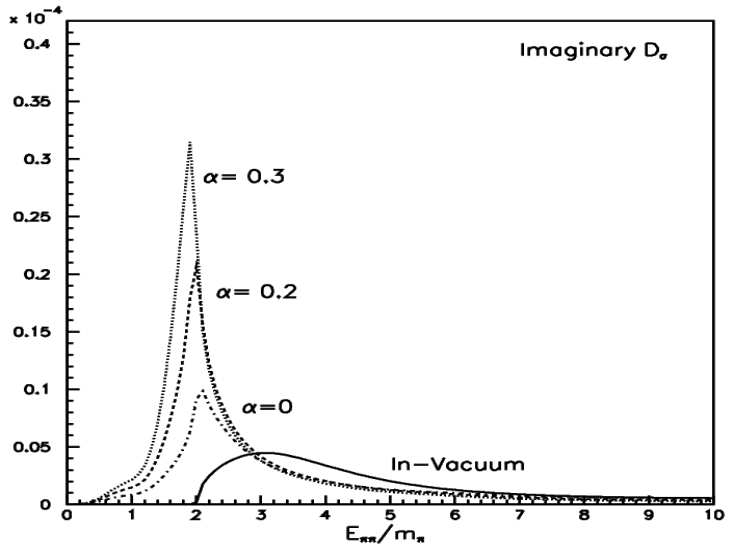

Figure 2.2: *Results for the imaginary part of the in medium σ-meson propagator. Except for the vacuum case (full line curve) the remaining in medium curves are computed at normal nuclear matter density. The dashed-dotted curve is for α=0, dashed for α=0.2 and the dotted for α=0.3 (α is the restoration parameter).*

Experimental evidence of this effect has been claimed in pion-induced and photon-induced reactions. The signal in pion-induced reactions could suffer from the fact that only the low-density surface zone of the nuclei is probed. This effect is due to the final (FSI) and initial (ISI) state interactions of the pions. But in photo-induced reactions, which have the advantage that the pion can be produced in the entire volume (which means no ISI can contribute), the FSI could be significantly decreased by the choice of a low incident photon beam energy. At low energy, produced pions have much larger mean free paths and are less likely re-absorbed by excitation of the Δ-resonance.

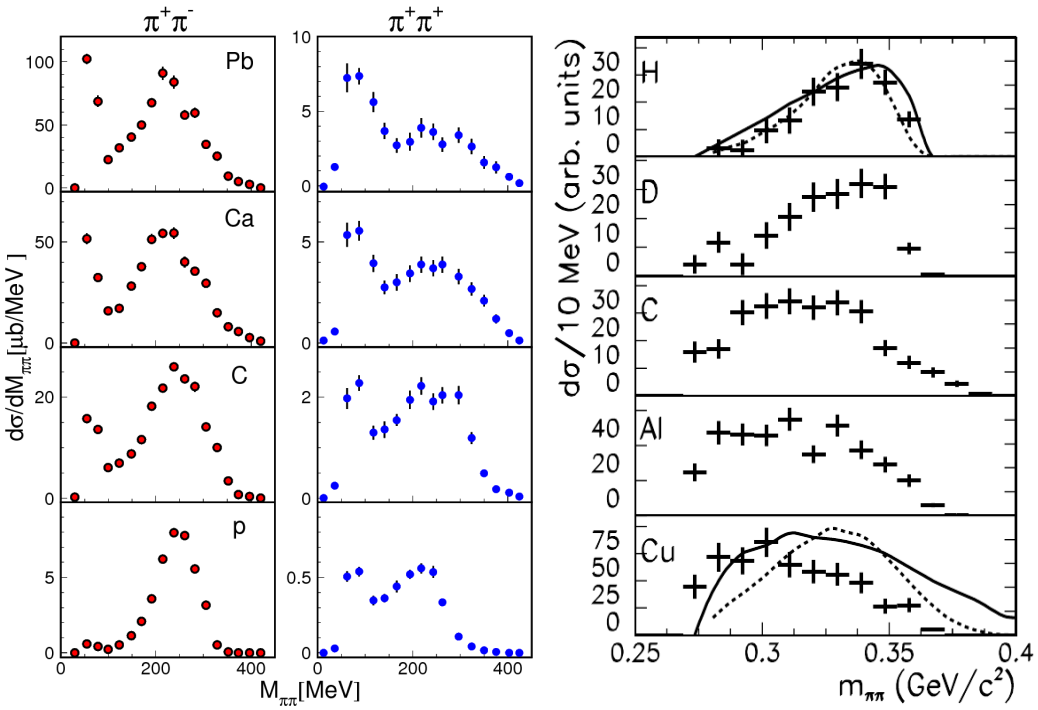

Figure 2.3: *Results using pion-induced beam. Left: Invariant mass distributions for $\pi^+ \rightarrow \pi^+\pi^+$ and $\rightarrow \pi^+\pi^-$ reactions on ^2H, ^{12}C, ^{40}Ca and ^{208}Pb (CHAOS collaboration). Right: Invariant mass distributions for $\pi^- A \rightarrow A'\pi^0\pi^0$ (CB@BNL collaboration).*

The first results came from pion-induced reactions by the CHAOS collaboration [35, 36, 37, 38, 39]. Motivating results have been obtained by the CHAOS collaboration in the isospin zero $\pi^+ \pi^-$ channel compared to a non-zero isospin channel $\pi^+\pi^+$ (see Fig. 2.3). The $\pi^+ \pi^-$ mass distributions show more strength at low mass for heavy targets (large nuclear density) like Calcium or lead than for lighter targets like the proton target. The $\pi^+ \pi^+$ distributions do not show

the same kind of nuclear mass dependency. However, the complicated acceptance of the spectrometer (only a small slice in the azimuthal angle Φ) makes the interpretation of the results difficult. The pronounced peaks at low invariant mass in the original spectra (see Fig. 2.3a) are for example an artifact introduced by the detection acceptance. Therefore only the ratios of invariant mass spectra from different nuclei carry more relevant information.

More interesting results using pion-induced beams followed by the CB@BNL collaboration [41] as shown in Fig. 2.3b where the neutral mass distributions have been compared for H, D, C, Al and Cu and showed a clear shift towards small invariant masses with increasing A.

More recently photon-induced beams brought also motivating results by the TAPS collaboration with noticeable improved statistics [40]. As seen in Fig. 2.4 the normalized ratio of the charged to the neutral mass distributions showed a clear effect for the neutral channel while the mixed charged channel remained almost unchanged.

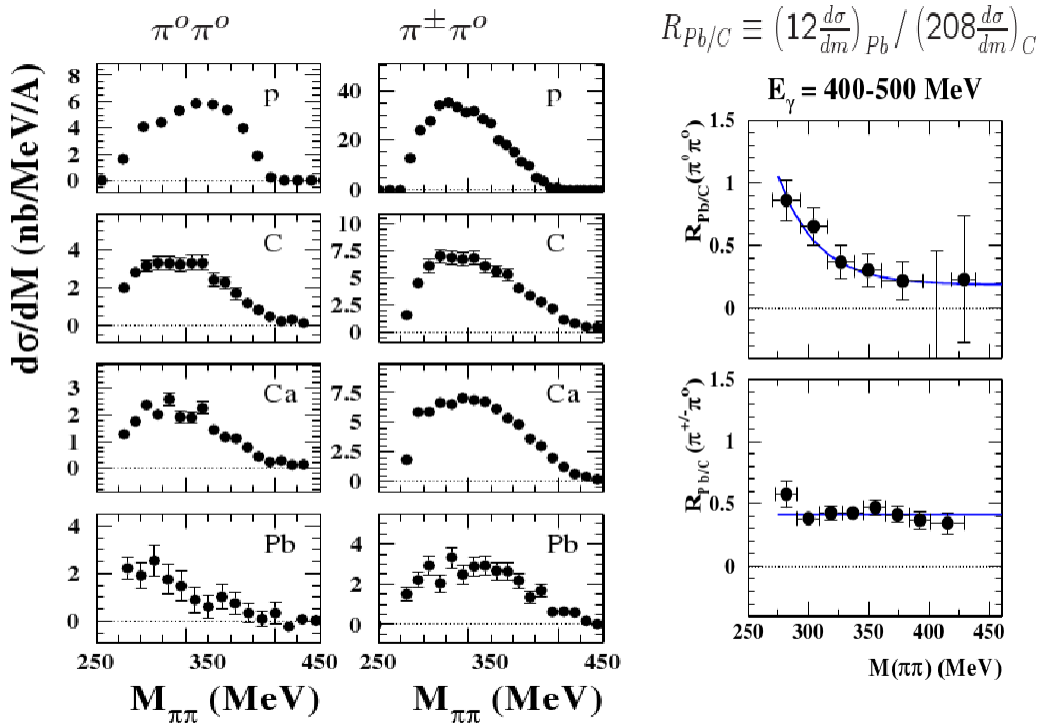

Figure 2.4: *Results using photon-induced beam. Left: Invariant mass distributions for $\gamma A \to \pi^0\pi^0 X$ and $\gamma A \to \pi^+\pi^- X$ reactions on proton, ^{12}C, ^{40}Ca and ^{208}Pb (TAPS collaboration).*

Finally, the photoproduction of $\pi^0\pi^0$ and $\pi^0\pi^{+/-}$ pairs off Ca has been again investigated by the TAPS collaboration [14]. As seen in Fig. 2.5 the $\pi^0\pi^0$ invariant mass distributions showed some relative enhancement with respect to the mixed charged channel. The distributions fit well to the calculations in the framework of the BUU model. However, this model includes only the FSI with no explicit in medium modification of $\pi\pi$ pairs. This means that for Ca, at least, most of the experimentally observed effects are due to FSI.

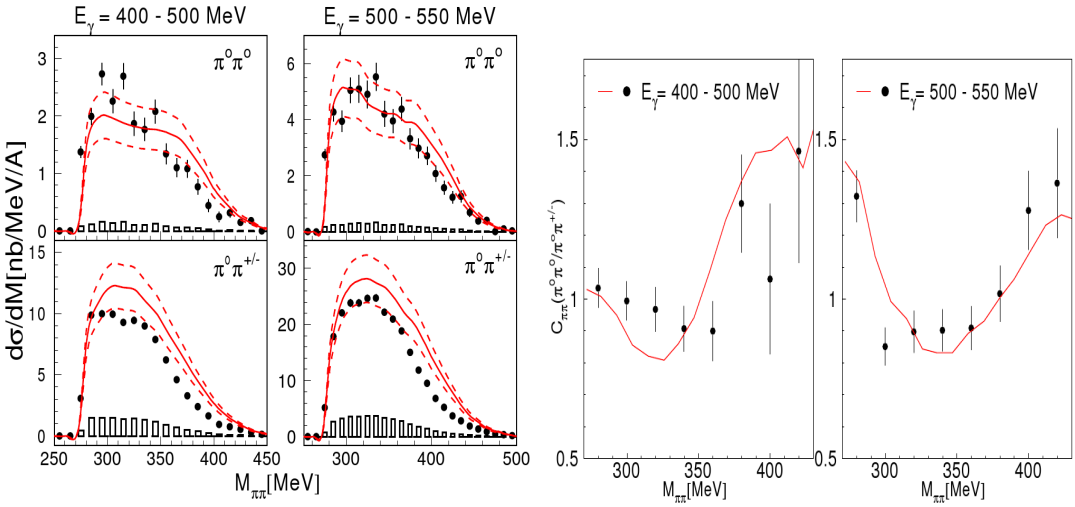

Figure 2.5: *Left: pion-pion invariant mass distributions compared to results of the BUU model [57]. The bars at the bottom represent the systematic uncertainty of the data, the dashed lines represent the error band for the BUU calculation. Right: Cross section ratio $C_{\pi\pi}$ ($\pi^0\pi^0$ / $\pi^0\pi^{+/-}$) compared to the results of the BUU model. Symbols: data, curves BUU results. Left hand side: incident photon energies 400 - 500 MeV, right hand side: incident photon energies 500 - 550 MeV.*

A new series of experiments with improved statistical quality has been done for solid targets in 2005 by the A2 collaboration in Mainz in view of the investigation of a possible downward shift of the strength in the invariant mass in the $\pi^0\pi^0$ channel compared to the $\pi^0\pi^{+/-}$ channel with improved data quality. Data from Carbon, Calcium and Lead are under analysis at the university of Giessen. Data from Lithium have been analyzed in Basel and results will be presented in the present work. Even if it was not expected to see an effect in the neutral channel compared to the mixed charged one, ^{7}Li has been chosen to serve as a new reference point for the comparison between heavy and light nuclei.

2.3 Coherent photoproduction of π^0 mesons - Properties of the Δ-resonance in medium

The in medium modification of the first low-lying excited state $P_{11}(1232)$ (or Δ-resonance) has been definitely experimentally demonstrated. The inclusive break-up cross sections showed a good agreement to the model calculations of the Δ spectral function by Post et al. in which in medium modification terms were accounted for. The in medium broadening of the resonance was found to agree with the model value of approx. 190 MeV [43, 42, 4].

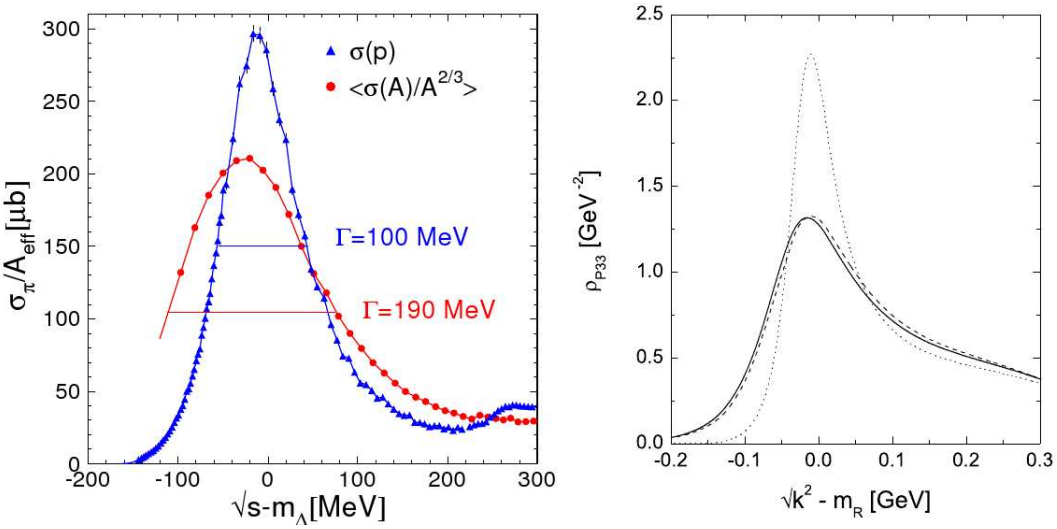

Figure 2.6: *Total cross section in Δ-resonance region of the reaction $\gamma A \rightarrow \pi^0 + X$ with A= (proton/average heavy nuclei) (left) and predicted spectral function of Δ-resonance by Post et al. with in medium modification terms accounted (right).*

The study of the *coherent π^0 photoproduction off nuclei* is also strongly connected to the topic of the in medium properties of the Δ-resonance. The momenta transfered to nuclei in pion photoproduction to forward angles are so small that the coherent process is dominant for heavy nuclei. Furthermore, the elementary photoproduction of neutral pions from the nucleon is well understood in this energy region (200 - 350 MeV) and strongly dominated by the excitation of the Δ-resonance.

In order to investigate the in medium properties of the Δ-resonance and the pion-nucleus interaction in medium, different models have treated the coherent π^0 photoproduction with different approaches. One group of models,

treated the problem with attention to FSI effects of the pion in the nuclear medium but neglected the medium modification of the position and the width of the Δ-resonance. The model used the Distorted Wave Impulse Approximation (DWIA) [43]. On the other hand other models took into account the properties of the Δ-resonance in the nuclear medium in the framework of the Δ-hole approach. These models neglected the non-resonant contributions in the elementary production process but took into account the Δ and pion dynamics [43].

Motivated by the growing interest in the topic of the in medium modification of hadrons, and the experimental progress achieved in the photo- and hadron- induced reactions, several extensions of the models have been proposed. Takaki et al. made calculations for the incoherent contributions from low-lying nuclear excitations. Carrasco et al. tried to extend the Δ-hole calculations to heavy nuclei using a local density approximation. Drechsel et al. tried to improve a model using DWIA approximation including a phenomenological parametrization of the Δ self energy[2]. Peters et al. developed a relativistic non-local model which includes medium modifications in the production operator of the delta resonance [54].

The modification of the Δ-resonance properties have been demonstrated using the coherent π^0 photoproduction by Krusche et al. [57]. Fig. 2.7 shows the differential cross sections for ^{12}C(γ,π^0)C, ^{40}Ca$(\gamma,\pi^0)^{40}$Ca and Pb(γ,π^0)Pb. The data were compared to PWIA, DWIA and DWIA with Δ-self energy. The latter case also called full model, included in addition to pion FSI, the medium modification of Δ-resonance properties due to the Δ-nucleus interaction via a phenomenological parametrization of the Δ self energy. The Δ self energy was fitted to the ^{4}He$(\gamma,\pi^0)^4$He reaction and this paramatrization was used without modification to calculate cross sections for C, Ca and Pb[3] [43]. The Δ-self energy was extracted from the ^{4}He data for the incident photon energy corresponding to the Δ peak position (290 MeV) and gave $Re(V) \approx$ 19 MeV and $Im(V) \approx$ -33 MeV [44], corresponding to a significant effective broadening of the resonance by 66 MeV. Calculations fitted well to the data which indirectly demonstrates the in medium broadening of the Δ-resonance and confirmed results obtained in the break-up cross sections.

[2]The self-energy of a particle represents the contribution to the particle's energy, or effective mass, due to interactions between the particle and the system it is part of.

[3]The comparison of calculations for self-energy between ^{4}He and heavier nuclei agreed which led to establish that the Δ self-energy saturates already for ^{4}He.

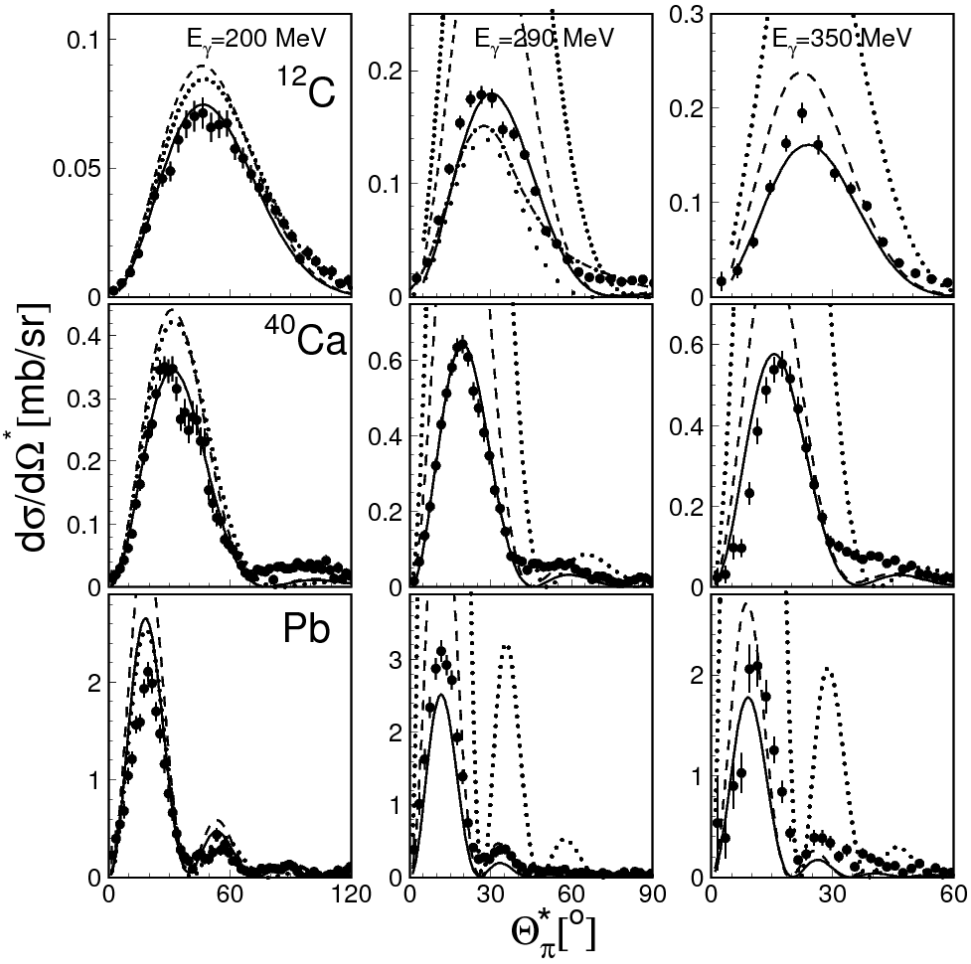

Figure 2.7: *differential differential cross sections for $^{12}C(\gamma,\pi^0)C$, $^{40}Ca(\gamma,\pi^0)^{40}Ca$ and $Pb(\gamma,\pi^0)Pb$ compared to the predictions from Drechsel et al. [52]. Dotted lines: PWIA, dashed lines: DWIA, full lines: DWIA with Δ-self energy fitted to ^{4}He cross sections. For the carbon data at 290 MeV the predictions from [43] for the coherent reaction (wide space dotted) and coherent plus incoherent excitation of low lying states (dash-dotted) are also shown.*

On the other hand, the coherent photoproduction of π^0 mesons is also of interest for the study of nuclear mass distributions. The charge distributions and related parameters (charge radius, skin thickness..) are already known for most nuclei with high precision. They have been studied with elastic electron scattering and via the spectroscopy of X-rays of muonic atoms (see [58, 59, 60, 61]). However, these techniques do not allow the extraction of the neutron density and therefore the total mass distributions in nuclei.

In some experimental methods, results for specific single neutron orbits have been obtained in magnetic electron scattering experiments using the neutron magnetic dipole moment, making use of the magnetic form factor of the neutron [62, 63]. However, most experimental methods used hadron induced reactions (α, proton, pion or kaon). Unfortunately, the uncertainties of these measurements were significant since scattering theories for strongly interacting particles are required in such experiments. An overview over these experiments can be found in [64])

An alternative to overcome these difficulties is the use of coherent π^0 photoproduction. In the energy region where the Δ-resonance strongly dominates the π^0 coherent photoproduction process, protons and neutrons contribute identically with the same amplitude as can be seen in equation 2.4:

$$A(\gamma p \to \pi^0 p) = +\sqrt{\frac{2}{3}}A^{V3} + \sqrt{\frac{1}{3}}(A^{IV} - A^{IS}) \tag{2.4}$$

$$A(\gamma n \to \pi^0 n) = +\sqrt{\frac{2}{3}}A^{V3} + \sqrt{\frac{1}{3}}(A^{IV} + A^{IS}) \tag{2.5}$$

where $A^{IS}, A^{IV} and A^{V3}$ are the isoscalar, isovector, and total isospin changing parts of the total amplitude. However, at incident photon energies in the region of interest in this work (200 - 350 MeV) the reaction is completely dominated by the photo excitation of the $\Delta(1232)$ resonance. Since this is an isospin I = $3/2$ state only the isospin changing vector component A^{V3} can contribute, so that for the Δ excitation :

$$A(\gamma p \to \pi^0 p) = A(\gamma n \to \pi^0 n) \tag{2.6}$$

Therefore, the coherent π^0 photoproduction is the ideal reaction to test the matter distribution, since in addition the photo-induced reactions probes the entire nuclear volume. The study of the coherent and breakup photoproduction of π^0 mesons from the deuteron have confirmed that the elementary cross section for protons and neutrons are equal [66, 67], which means that protons and neutrons contribute identically with the same amplitude in the coherent π^0 cross section from nuclei. Only small background from the nucleon Born terms[4]

[4]The nucleon Born terms correspond to the off-shell nucleons in the intermediate state rather than an excited nucleon.

could contribute. Consequently, this reaction is sensitive to the distribution of nucleons rather than the distribution of charge in the nucleus.

This method has been first used by Schrack, Leiss and Penner in 1962 but was faced to experimental difficulties and the lack of the developed theoretical tools [65]. A second attempt to measure the nuclear mass radii using the coherent photoproduction of ρ_0-mesons was made by H. Alvesleben et al. during the 70s but was not explored for the same reasons [68]. The most precise results have been obtained by the TAPS collaboration a few years ago [69]. The method is summarized in the following :

In the most simple plane wave approximation (PWIA) the coherent cross section from spin zero nuclei can be written as:

$$\frac{d\sigma_{PWIA}}{d\Omega}(E\gamma,\theta_\pi) = \frac{s}{m_N^2}A^2\frac{d\sigma_{NS}}{d\Omega^*}(E\gamma^*,\theta_\pi^*)F^2(q)\cdot sin^2(\theta_\pi) \tag{2.7}$$

$$\frac{d\sigma_{NS}}{d\Omega^*}(E\gamma^*,\theta_\pi^*) = \frac{1}{2}\frac{q_\pi}{k^*} \mid F_2(E\gamma^*,\theta_\pi^*)^2 \mid \tag{2.8}$$

where E_γ and θ_π are incident photon energy and pion polar angle in the photon-nucleus cm-system, m_N is the nucleon mass, q(E_γ,θ_π) the momentum transfer to the nucleus, and F(q) the nuclear mass form factor. The total energy $\sqrt{s}$ of the photon-nucleon pair, the photon energy and momentum Eγ^*, k^*, and the pion angle and momentum θ_π^*, q_π^* in the photon-nucleon cm-system can be evaluated from the average momentum P_N of the nucleon in the factorization approximation $p_N = q(A-1)/2A$. The spin independent elementary cross section $\frac{d\sigma_{NS}}{d\Omega}$ is calculated from the isospin average (for $I \neq 0$ nuclei weighted with N,Z) of the standard Chew-Goldberger-Low-Nambu (CGLN) amplitude F_2 [70] taken from [44]. The extraction of the form factor from the differential cross section in this approximation is straight forward and will be used below for a first approximative determination of the mass radius.

The form factor could therefore be extracted in PWIA approximation as :

$$F^2(q)|_{PWIA} = \frac{d\sigma_{exp}}{d\Omega}/[\frac{s}{m_N^2}A^2sin^2(\theta_\pi)(\frac{d\sigma_{NS}}{d\Omega^*})] \tag{2.9}$$

Once the form factor is determined, the mass rms radii were extracted without

further model assumptions from the slope of the form factor for $q^2 \to 0$ via :

$$F(q^2) = 1 - \frac{q^2}{6} r_{rms}^2 + O(q^4) \tag{2.10}$$

which is done in the usual way by fitting a polynomial

$$F(q^2) = \sum (-1)^n a_n q^{2n} \tag{2.11}$$

to the data. The rms-radius is then given by

$$r_{rms} = \sqrt{6 a_1 / a_0} \tag{2.12}$$

where for a correctly determined form factor a_0 should be unity. Fig. 2.8 show the extracted form factors in PWIA and DWIA approximations and the corresponding mass rms-radius for C, Ca, Nb and Pb nuclei.

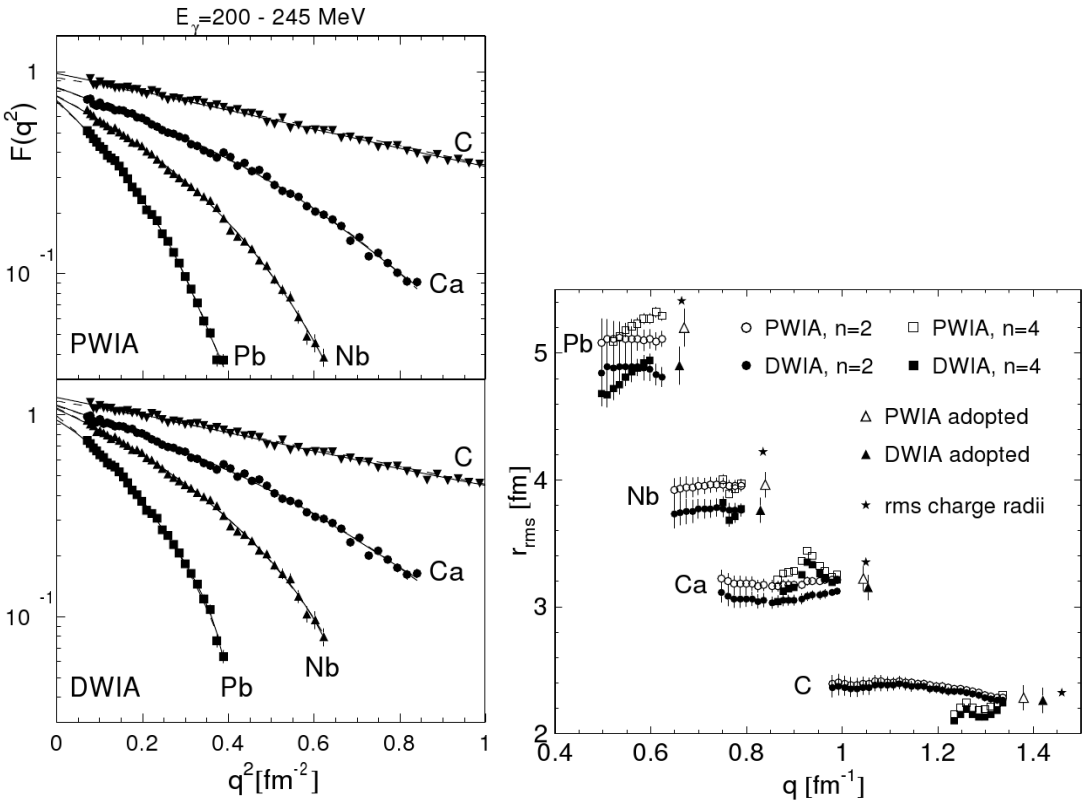

Figure 2.8: *Data from heavy nuclei in PWIA and DWIA approximations [69]. Left: Form factor. Right: Mass rms-radii (triangles) compared to the charge radii (stars)*

To sum up, the coherent photoproduction of the π^0 served for two different aspects. First, the differential cross section confirmed the Δ-resonance broadening found in the break-up cross sections. This was demonstrated via the good agreement to the calculations which took into account the FSI of the pion and the Δ-self energy. Furthermore, the form factors and the mass rms radii could be extracted since the reaction is sensitive to the distributions of the nucleons in the nucleus. The lithium nucleus, well positioned in the middle between light and heavy nuclei, would serve for the confirmation of the Δ-in medium modification and in the investigation of the feasibility to extend the extraction of matter densities using coherent photoproduction of the π^0 - mesons to lighter nuclei.

2.4 Coherent photoproduction of η-mesons - Search for η-mesic nuclei

Interaction of mesons with nucleons and nuclei is a hotly debated topic since it is closely related to the understanding of the strong force. The case of mesons with long lifetime such as charged pions or kaons is much more known than short-lived mesons such as η. In the first case, secondary beams of mesons could be prepared which allowed a direct interaction with the nucleus. It has then been established that the strong interaction does not generate for example bound-pion nucleus states since the pion-nucleon interaction is comparatively weak for small pion momenta.

However, in the case of η-mesons, things are completely different. The interaction of η-mesons with the nucleus is only accessible in indirect ways, η-mesons must be first produced in the nucleus before undergoing FSI in it. In contrast to the pion, the interaction of η-mesons with the nucleon is strongly influenced by the existence of an s-wave N*-resonance S_{11}(1535) which lies close to the η production threshold and couples strongly to the η-N channel (see chapter I) [71]. The existence of a bound η-nucleus system is therefore possible.

During 1985 an attractive s-wave η N-interaction was found by Whaler and Liu while performing calculations for the channels $\pi N \rightarrow \pi N$, $\pi N \rightarrow \eta N$ and $\eta N \rightarrow \eta N$ [72]. Liu and Haider predicted later the existence of strongly bound η-nuclei (which they called η-mesic nuclei system) for nuclei with A>10. Liu and Whaler extracted a η N-scattering length $a = 0.27 + i0.22$ [73]. The strength of the η-nucleus interaction, in particular the scattering length in this system

and the position of possible quasi-bound states is very sensitive to this value of the η-nucleon scattering length [74].

The predictions of Liu motivated the experimentalists towards the investigation of a possible η-bound state in heavy nuclei. Experimental evidence for "heavy" η-mesic nuclei was searched in different reaction processes. The reaction $A(\pi^+, p)\eta(A-1)$ was first investigated [75, 76] without any significant results. Physicists of the Lebedev Institute of physics in Moscow claimed then the observation of an eta-mesic state in the reaction chain :

$$\gamma + A \rightarrow N_1 + (A-1)_\eta \rightarrow N_1 + (N_2 + \pi) + (A-2) \tag{2.13}$$

where the η is produced on the nucleon N_1, captured in the rest nucleus $(A-1)$ which subsequently decays by emission of a nucleon-pion pair [77, 78]. More recently, Sokol et al. claimed the existence of η-mesic states as well in ^{12}C with formation of η-mesic Carbon and Beryllium nuclei in the decay chain from the equation above [79, 80].

However, in a new series of measurements [82] the real part of the scattering length was found to lie in the range between $0.5 - 0.8$, much larger than the value extracted by Liu, which might allow for the existence of lighter η-mesic nuclei.

Since then, the η-nucleus interaction in light nuclei has been intensively studied theoretically and experimentally. The existence of light η-mesic states is controversially discussed in the literature, in particular regarding the necessary strength of the η-N interaction. Most calculations agreed on the existence of light η-nucleus (quasi)bound states. Rakityanski et al. predicted even the existence of such states in all ^{2}H, ^{3}H, ^{3}He and ^{4}He isotopes [83, 84, 85]. They predict in particular for the deuteron the existence of a quasi-bound state for scattering length larger than $0.7 - 0.8fm$. This prediction was confirmed later by Green et al. [74]. However, Grishina et al. estimated $Re(a_\eta N) \leq 0.3$ from an analysis of the threshold behavior of the $pn \rightarrow d\eta$ reaction [86]. Garcilazo and Pena concluded that no bound state η-NN is possible even for very large values of $a_\eta N$ [87].

Experimentally, an enhancement of the cross section relative to the expectation for phase space behavior could be interpreted as presence of a quasi-bound η-nucleus. However, such enhancement could also be due to FSI which do not necessarily involve the η-meson, as in $np-$FSI in case of η-production of the deuteron.

Light quasi-bound η-states were intensively searched near threshold especially in the reactions $pp \to pp\eta$ [88], $np \to d\eta$ [89, 90], $pd \to \eta^3$He [91], $\vec{d}d \to \eta^4$He [93], and $pd \to pd\eta$ [92]. Results showed some enhancements of the cross section near threshold. This enhancement could arise either from a bound state or could be due to FSI which does not necessarily involve the η meson. Therefore no conclusive evidence was found that the final state interaction is strong enough to form a quasi-bound state for the deuteron.

Photoproduction is a useful tool to prepare η-nucleus final states especially since the ISI have not to be cared about. However, in this kind of reaction cross sections are expected to be very low at threshold. In order to know which nucleus is suitable for the investigation of the η-nucleus quasi-bound states, a complete analysis of the S_{11} isospin structure should be done. To do so, the amplitudes of η-photoproduction off the proton and the neutron and in addition, the measurement of coherent photoproduction from an isospin $I = 0$ nucleus is necessary. Since the excitation of the S_{11} resonance via the E_{0+} multi-pole involves a spin-flip transition, the $I = 0$, $J = 1$ deuteron was the ideal target for this purpose. The isospin structure has been extracted from the combined result from the measurement of inclusive and exclusive quasi-free η-photoproduction from the deuteron and ^{4}He and coherent η-photoproduction from the deuteron (of which a summary can be found in [100]) via:

$$\sigma_p \propto |A^{IS} + A^{IV}|^2 = |A^p_{1/2}|^2$$

$$\sigma_n \propto |A^{IS} - A^{IV}|^2 = |A^p_{1/2}|^2$$

$$\sigma_d \propto |A^{IS}|^2 \,,$$

where A^{IS} denotes the isoscalar and A^{IV} the isovector amplitudes of the electromagnetic excitation of the resonance. The combined result from the measurements of inclusive and exclusive quasi-free η-photoproduction from the deuteron and ^{4}He and coherent η-photoproduction from the deuteron indicates the dominance of the isovector amplitude over the isoscalar amplitude by one order of magnitude:

- $\langle \sigma_n / \sigma_p \rangle = (0.67 \pm 0.03)$
- $|A^n_{1/2}|/|A^p_{1/2}| = (0.819 \pm 0.018)$

- $A^{IV}_{1/2}/A^{IS}_{1/2} = (10.0 \pm 0.7)$
- $A^{IS}_{1/2}/A^{p}_{1/2} = (0.09 \pm 0.01)$

From the fact that the dominant S_{11}-excitation proceeds via a spin-flip amplitude with the above isospin structure and the quantum numbers of the nuclei, one expects qualitatively for coherent η-photoproduction from light nuclei:

- ^{4}He: J=0, I=0, only non-spin-flip, isoscalar amplitude: very weak signal
- ^{2}H: J=1, I=0, isoscalar, spin-flip amplitude may contribute: small signal
- ^{3}He J=1/2, I=1/2, isovector, spin-flip amplitude may contribute: "large signal"

More generally, only odd-even or even-odd nuclei are promising candidates. The explication is the following: Since the photon couplings of the S_{11} have different sign but comparable magnitude for proton and neutron, contributions from protons and neutrons cancel to a large extend. In combination with the required spin-flip only unpaired nucleons contribute significantly for such nuclei.

However, in the most simple PWIA approximation, the cross section could be estimated like :

$$\left.\frac{d\sigma}{d\Omega}\right|_A \approx F^2(q) \times \left.\frac{d\sigma}{d\Omega}\right|_N \tag{2.14}$$

where $(d\sigma/d\Omega)_N$ is the free nucleon cross section (proton for odd-even, neutron for even-odd nuclei) and $F^2(q)$ is the nuclear form factor.

A first pilot experiment was conducted by the TAPS collaboration in 2003 at MAMI [97] in view of the reaction : $\gamma +^3 He \rightarrow \eta +^3 He$. Results showed a clear enhancement around the coherent threshold (see Fig. 2.9). A second experiment at MAMI was done few years later with improved experimental conditions and statistical data by the CB-TAPS collaboration at MAMI C[5]. Results confirmed the results of Pfeifer et al. with better statistics. Finally, in an experiment realized at COSY-ANKE in 2004, the same enhancement was seen in the reaction $dp + p \rightarrow \eta +^3 He$ [99].

[5]Paper is in preparation by F. Pheron et al.

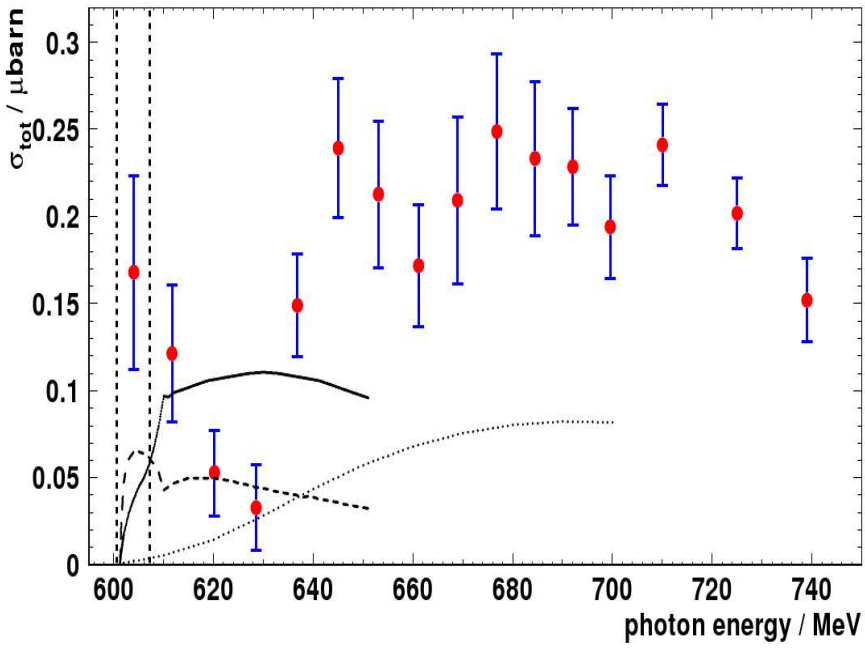

Figure 2.9: *Coherent cross section for the η production off ^{3}He compared to models by Shevchenko et al. (solid lines, dashed lines) and Kamalov et al. (dotted line) Pfeiffer et al.*

Following these predictions, the next heavier candidates are ^{7}Li, ^{9}Be and ^{11}B. All of these nucleus have a unpaired nucleon in their $p_{3/2}$ shell, a proton for Li- and B-isotopes and a neutron in the case of ^{9}Be. Among those three targets, the ^{9}Be is to be excluded since it has a bigger rms-radius and therefore a smaller form factor[6]. In addition, the ^{9}Be would be reduced by a factor 2/3 related to the neutron [94].

Among ^{7}Li and ^{11}B, ^{7}Li is more advantageous. The expected background from quasi-free meson production processes (η and π^o), which scales approximately with $A^{2/3}$ (A = atomic mass number), is smaller for ^{7}Li and the nuclear structure is simpler (only one unpaired proton in the $p_{3/2}$ shell). It is possible that a significant part of the strength leads to the excitation of the ^{7}Li nucleus to the $1/2^-$ state at 478 keV excitation energy (unpaired proton in $p_{1/2}$ shell), which however would not be resolved experimentally.

A very rough approximation in PWIA approximation could be done in order to estimate the cross section of ^{7}Li compared to the ^{3}He. It is in fact established

[6]The charge form factor in the range of interest (q^2 between 3-7 fm^2) $\approx$ 2.4 fm for ^{7}Li against 2.51 fm for ^{11}B. For details, see [58].

that the ^{7}Li form factor is, in the range of interest (q^2 between 3 and 7 fm^2), almost one order of magnitude smaller than the ^{3}He one as shows plots below of ^{7}Li and He form factors [95] and [96] :

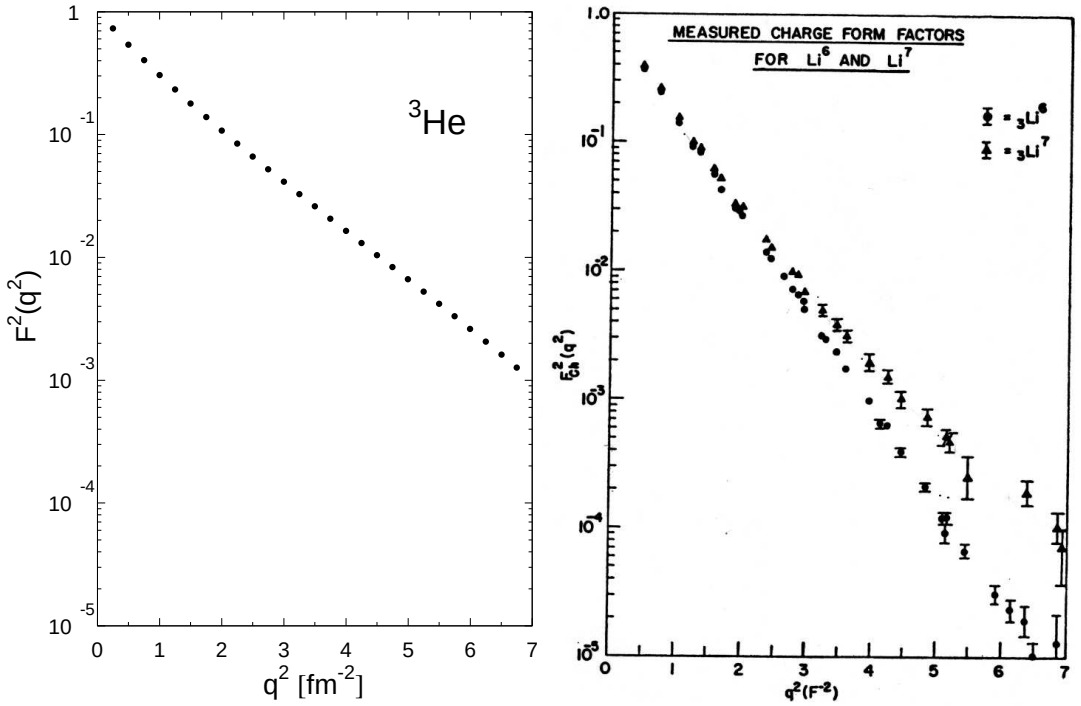

Figure 2.10: *The η coherently produced can be either ejected from the nucleus or reabsorbed by a nucleon. This leads to the emission of a π^0 and a proton back-to-back.*

$$\frac{d\sigma}{d\Omega}_{Li} = \frac{d\sigma}{d\Omega}_{He} \times (\frac{F^2(q^2)_{Li}}{F^2(q^2)_{He}}) \times 3/2 \tag{2.15}$$

With :

- $$\frac{d\sigma}{d\Omega}_{He} \approx 0.1\mu b \text{ (Pfeifer et al.)} \tag{2.16}$$
- $$\frac{F^2(q^2)_{Li}}{F^2(q^2)_{He}} \approx 0.1 \tag{2.17}$$
- The $3/2$ factor is recovered from the fact that in ^7Li the cross section comes from the unpaired proton.

Which gives an extremely small coherent cross section for ^{7}Li about 8-10 times smaller than the ^{3}He coherent cross section.

However, it should be noticed that this estimate comes from the most simple PWIA approximation around the breakup threshold since PWIA is certainly not valid around the coherent threshold. In addition, the influence of the formation of η-nucleus bound states on the threshold cross sections are completely unknown.

The π^0 -proton back-to-back channel

The evidence of the formation of an η-mesic state in photon induced reactions could be investigated as well in its decay via emission of back-to-back nucleon-pion pairs. Fig. 2.11 shows a sketch of the formation of such system.

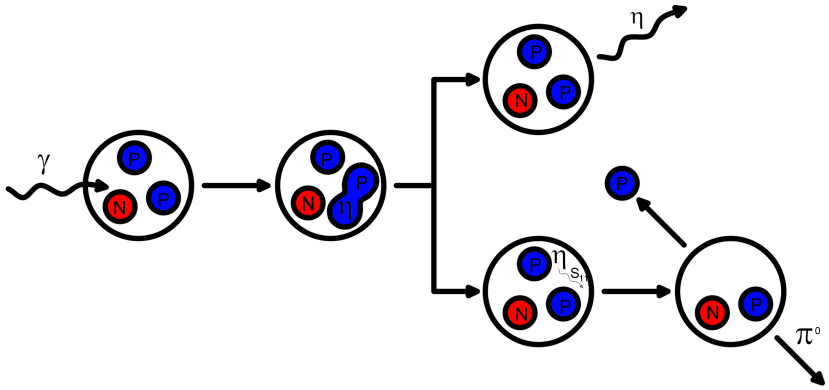

Figure 2.11: *The η coherently produced can be either ejected from the nucleus or reabsorbed by a nucleon. This leads to the emission of a π^0 and a proton back-to-back.*

Such pion-nucleon pairs have been searched for in the experiments performed at MAMI on ^{3}He. Results are not conclusive due to the presence of a competitive residual resonance background from π^0 production in the second and third resonance region. Fig. 2.12 shows, for the most recent experiment, how The created peak-like artifact is moving for different opening angles due to the selection of different kinematics [98].

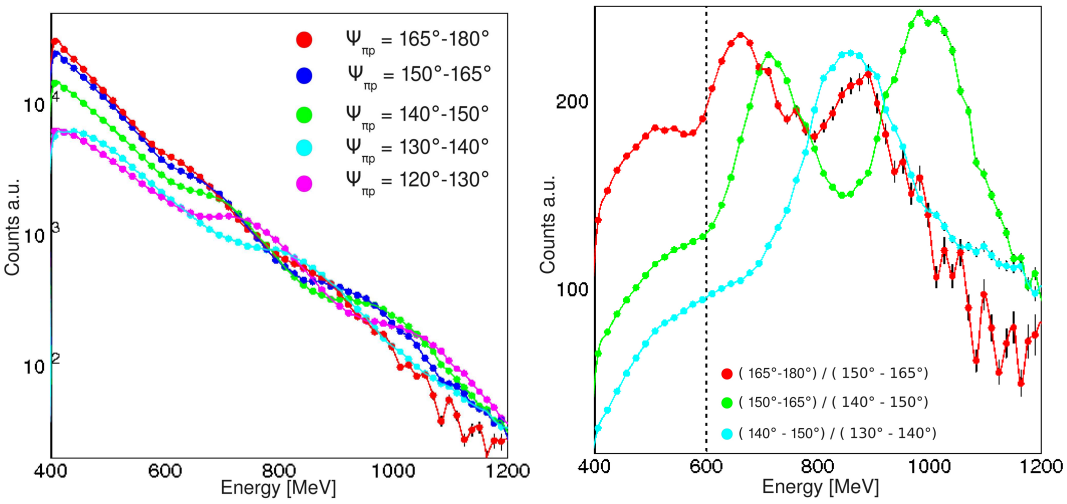

Figure 2.12: *Left: excitation functions of the π^0 -proton back-to-back channel for different opening angles, the resonance is moving to the right hand side with invreasing opening angles. Right: Difference of the excitation functions, an artifact is created and correspond to the coherent η threshold for 165-180°.*

Note that the same analysis could be interesting in view of a possible formation of ω- meson-nucleus quasi-bound states as it could decay in the same way.

Chapter 3

Experimental Equipment

In this chapter the experiment will be described in its different steps and parts, starting from the accelerator used to produce the photons, the target, the detectors that will enable the identification and the reconstruction of the decay products, the electronics and the trigger.

The experiment has been conducted in spring 2005 within the A2 collaboration[1] at MAMI. During this year the new detector setup covering 4π steradians in solid angle was operational. This allowed a big improvement in the data quality.

A simplified sketch of the setup is shown in Fig. 3.1. Bremsstrahlung photons produced by scattered electrons accelerated by MAMI hit the lithium target. The electrons were detected in the focal plane detector of the Glasgow tagging spectrometer and the decay products and the recoil nucleons were detected in the Crystal Ball detector and in the TAPS forward wall.

[1]The A2 collaboration is a nuclear physics research group with members from Germany, Switzerland, Italy, Croatia, Russia, U.S.A, U.K and Canada. It is devoted to experiments using real tagged Bremsstrahlung photon produced at MAMI accelerator in Mainz. MAMI has been built in the 70s at the "Institute fuer Kernphysik" in Mainz.

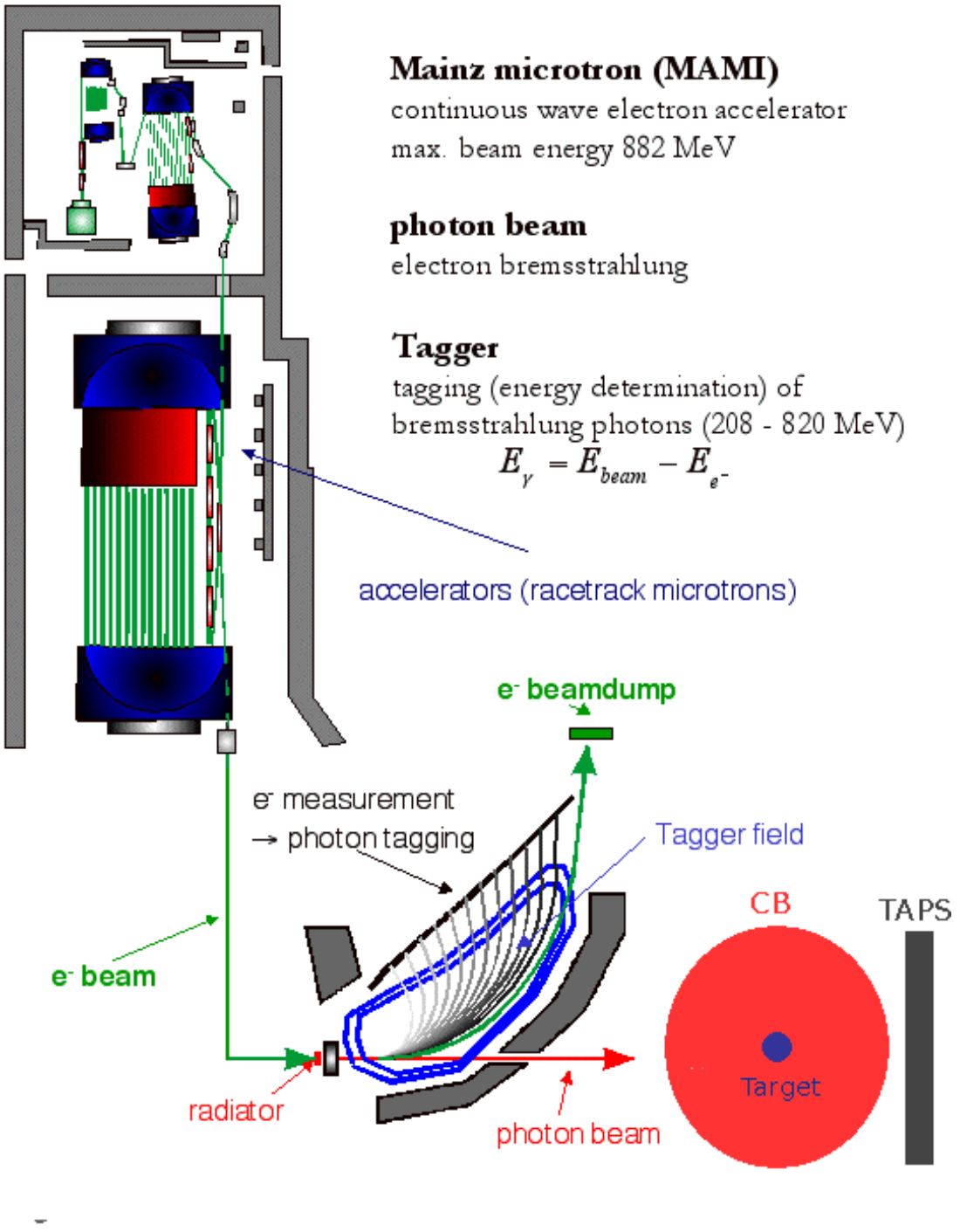

Figure 3.1: *General overview of the experimental setup.*

3.1 MAMI, the accelerator facility

As seen in Fig. 3.2, the MAMI accelerator can feed a couple of experiments set up in different halls : A1 is dedicated to electron scattering, A2 to real photons, A4 for parity violation studies, X1 for X-Ray radiation and others. The present experiment was done in the A2 hall with the MAMI B configuration with an electron beam energy of 883 MeV. In the meantime (2006) MAMI has been upgraded to reach 1558 MeV in electron beam energy.

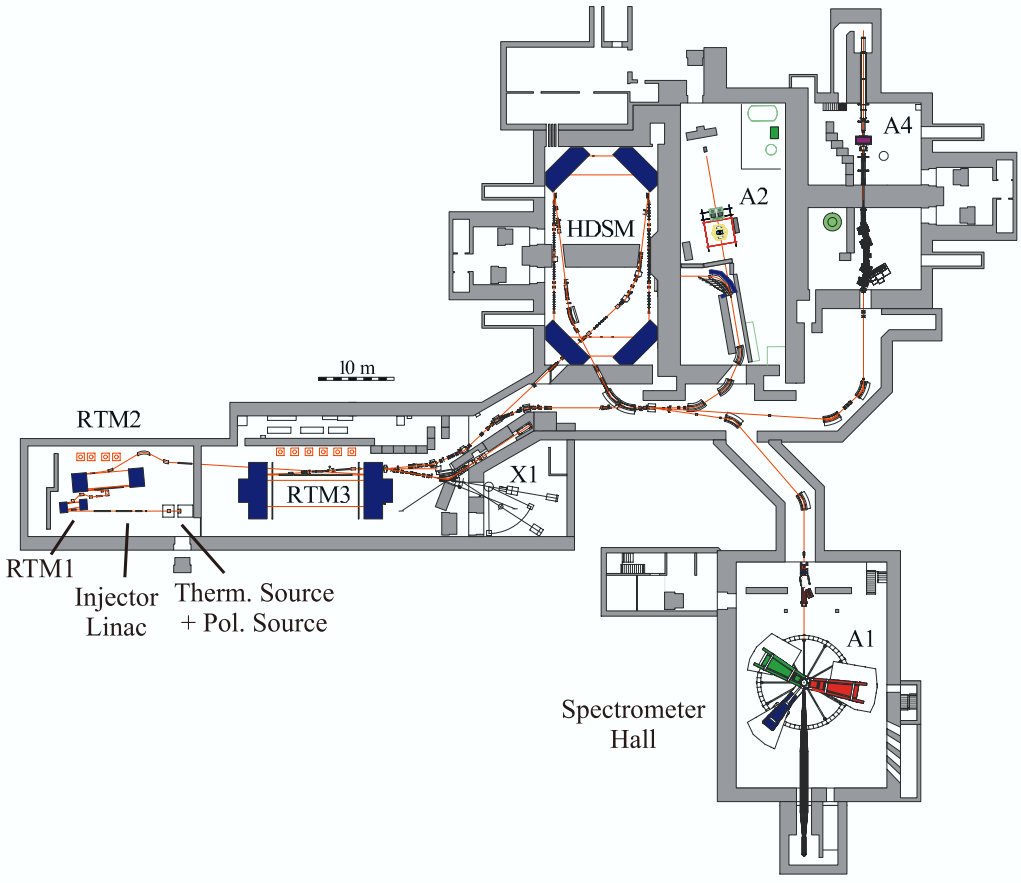

Figure 3.2: *General view of the MAMI accelerator, the experiment was set up in the hall A2*

MAMI is a racetrack microtron accelerator letting pass electrons several times through a linear accelerator completed by a bending magnet at each of its ends. In each passage, electrons gain energy and the radius of their trajectory becomes larger. MAMI consists of three cascade RTMs accelerating electrons up

to 14 MeV, 180 MeV and 883 MeV at each respective stage. The electrons leaving the source are initially accelerated and injected into the first RTM by a 3.5 MeV linear accelerator [101].
Thermal and polarized electron sources are available producing unpolarized or longitudinally polarized electron beams. More informations about the polarized photon production of MAMI can be found in [103].
A general overview of the accelerator is shown in Fig. 3.2 and the principle of a racetrack microtron is sketched in Fig. 3.3.
With its continuous and high intensity, small emittance and excellent beam stability, MAMI is an excellent tool for electron scattering as well as for tagged photon experiments.

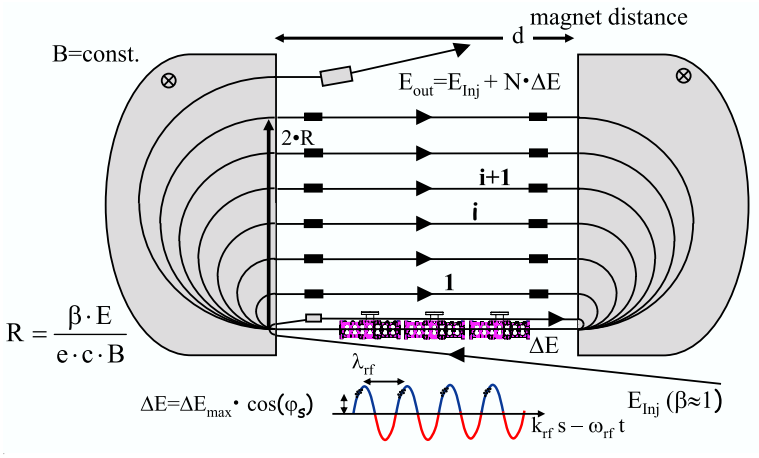

Figure 3.3: *Design of a racetrack microtron. With every loop, an energy ΔE (related to the phase of the oscillation in the cavity, in the present experiment $\Delta E \approx$ 7.5MeV) is added to the beam energy, increasing the radius of the trajectory.*

Th electrons are slowed down by scattering in a radiator foil creating a Bremsstrahlung photon beam. The photons can be either lineraly or circularly polarized. Linearly polarized photons are obtained via coherent bremsstrahlung from a crystalline radiator (typically 100 μm thick diamond foil).
The circular polarization of the photons is obtained by the use of longitudinal polarized electrons in the bremsstrahlung process. A transfer of helicity occurs from the electrons to the emitted photons. Thus, as the helicity of the photon beam depends directly on the spin direction of the electrons, the information concerning the electron polarization delivered by MAMI allows the determination of the helicity status of the corresponding photon.

3.2 The tagging spectrometer

After interaction in the radiator, the electrons loose a fraction of their energy, corresponding to the energy of the emitted photon. Indeed, the energy of a photon produced in the radiator is given by:

$$E_\gamma = E_e - E_{e'} \tag{3.1}$$

With E_e the energy of the MAMI electron beam and $E_{e'}$ the energy of the electron after the photon is produced. This is valid as long as the energy transfered to the recoil nucleus in the Bremsstrahlung process is negligible, which is true since, in 99% of all cases, less than 2.5 keV are transfered to the recoil nucleus. Thus, for the determination of the incident photon energy E_γ, the scattered electron energy $E_{e'}$ has to be measured. This is done using the Glasgow tagging spectrometer (simply called Tagger[2]) [102] .

The Tagger is also used to determine the total number of scattered electrons, which is needed to determine the total number of photons impinging on the target which is essential for the determination of the cross sections (see sect. 6.1).
Fig. 3.4 shows the working principle of the Tagger. After interaction in the radiator, the electrons go through the main body of the Tagger (which includes a magnet of 70 tons producing a magnetic field up to 1 Tesla), the electrons will see their trajectory deflected with a curvature radius proportional to their energy. Hence, the position of the electron at the exit of the magnet will then be directly related to its energy. Knowing this, the electron energy can be determined without ambiguity with a precision of ~ 2 MeV.
In order to measure this position, a set of 352 plastic scintillators is placed in the focal plane of the Tagger called ladder.

[2]The Glasgow photon Tagger is a large magnet build in 1991 by the University of Glasgow to be used with the newly available, at this time, 850 MeV electrons provided by MAMI B.

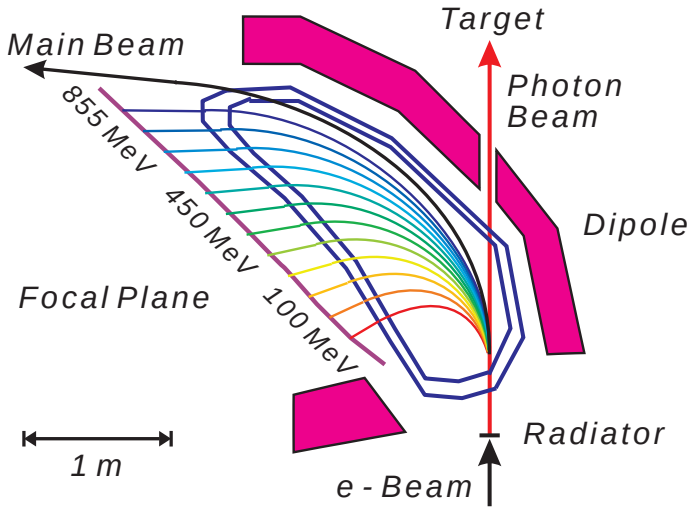

Figure 3.4: *The electron Tagger. Colored lines represent the electrons trajectory depending on their energy*

Fig. 3.5 shows the distribution of the electrons on the focal plane detector as function of the Tagger index. It follows the typical 1/E slope of Bremsstrahlung. The small efficiency fluctuations are corrected with special tagging efficiency measurements, where at reduced beam intensity the direct photon beam is analyzed in coincidence with the Tagger by a lead glass detector. The main purpose of the tagging efficiency measurements is the determination of the fraction of produced photons passing the collimator (see sect. 4.3). Some malfunctioning Tagger channels have been removed from the analysis.

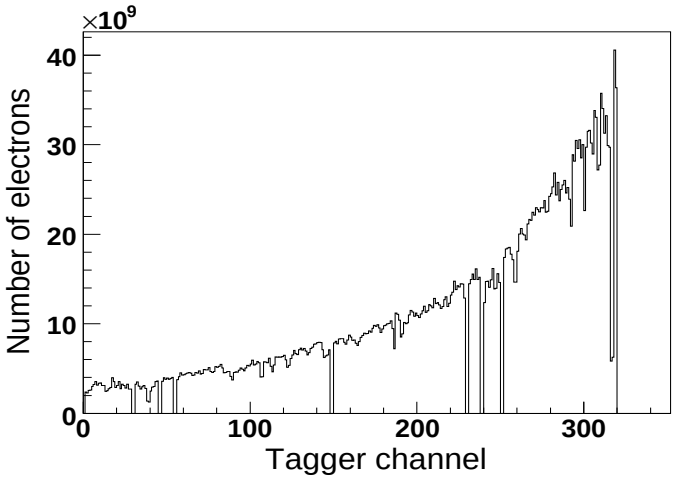

Figure 3.5: *Distribution of the electrons on the focal plane detector.*

3.3 The detectors

In the present experiment, the detection system was composed of a set of different detectors and calorimeters which result in high accuracy data and good detection efficiency. Indeed, the 4π Crystal Ball calorimeter (abbreviated as CB), with its sub-systems PID (Particle Identificator Detector) and MWPC (Multi-Wire Proportional Chamber), combined with the TAPS (Two Arms Photon Spectrometer) forward detector and its veto wall system represent a highly efficient setup, covering almost the full solid angle. The system provides good time and energy resolution and offers various ways for particle identification. It is well adopted for the detection of multi-photon final states such as $\eta \to 3\pi^0 \to 6\gamma$ or $\pi^0\pi^0 \to 4\gamma$.
In the following, each detector and its subsystems will be described and its characteristics and electronics summarized. The trigger used in this experiment and the data acquisition system will be described.

3.3.1 The Crystal Ball and its subsystems

3.3.1.1 The Crystal Ball

The Crystal Ball detector (abbreviated as CB) has been a very good detection tool along its rich history and several travels between accelerators. It has been built at SLAC[3] in the 1970s to be used for J/Ψ measurements at SPEAR[4], then at DESY[5] to study the c quark physics.
After upgrades, it has been used at BNL from 1995 to 2002 where amongst other experiments, one of the first measurements of the in medium modifications of pion pairs produced with a pion beam incident on heavy target nuclei was done (see chapter II). In late 2002 CB was moved to MAMI to be used in combination with TAPS as forward detector. This has opened, together with the excellent beam provided by MAMI, the exciting prospect to measure very precisely a large range of photoproduction reactions. Concerning geometry, CB has a 25.3 cm inner radius and a 66 cm outer radius and is a highly segmented spectrometer made of 672 NaI[6] crystals arranged in a hollow sphere.

[3]Stanford Linear Accelerator Center, USA
[4]Stanford Positron Electron Accelerating Ring
[5]Deutsches Elektronen SYnchrotron, Hamburg, Germany.
[6]Iodide Sodium.

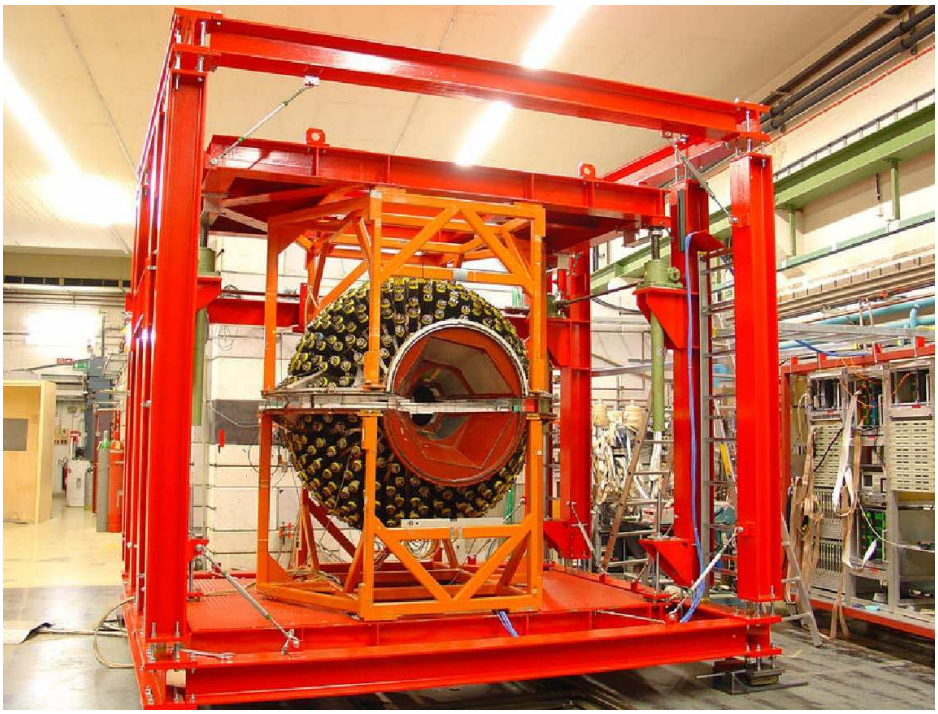

Figure 3.6: *CB and its photomultipliers before cabelling*

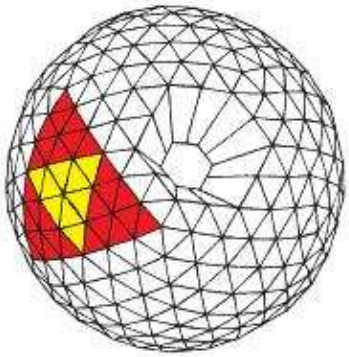

Figure 3.7: *Geometry of CB showing a major triangle (36 crystals) made of 4 minor triangles (9 crystals), the beam hole is also visible.*

The ball geometry is an icosahedron divided in 20 "Major Triangles" that are themselves split into four "Minor Triangles" containing each nine crystals as seen in Fig. 3.3.1.1.
Due to this geometry, the crystals are not exactly identical but each of them is a 40.6 cm long truncated triangular pyramid. In order to leave space for the beam entry ($\sim$ 20 degrees) to exit and to give an easy access to the target, 48 crystal positions have been left empty.

The ball is in reality composed of two hemispheres separated by 0.8 cm. This gap, essential for technical and target needs, induces a small loss in acceptance of $\sim$ 1.6 percent from 4π steradians. For the total detector setup, only $\sim 6\%$ of

the total solid angle are not covered by the detector material. Fig. 3.8 shows a transverse cut of the overall arrangement of the complete CB system with the PID, the MWPC and the target positions.

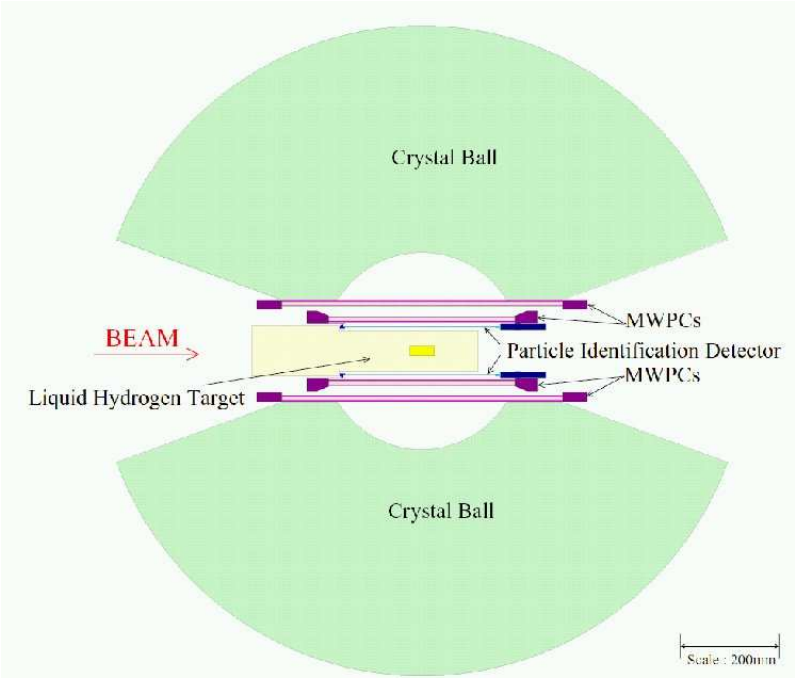

Figure 3.8: *Transverse view of the crystal ball showing the inner detectors (wire chambers and PID) and the Li target.*

3.3.1.2 The MWPC

CB alone has a poor position resolution when detecting charged particles. Indeed, due to the fact that the energy deposition of charged particles in CB occurs most of the time in one or two crystals only, the cluster reconstruction (see section 5.2.1) is inefficient to determine the impact point of the charged particle with a satisfactory accuracy. Thus, the two MWPCs (Multi-Wire proportional Chamber) were added in order to provide a better angular resolution for charged particles. The MWPC served originally in the DAPHNE[7] detector at MAMI between 1990 and 2003. In addition, combining CB and MWPC allows the reconstruction of tracks rather than only impact points.
The MWPC's are filled with a mixtue of Ar(74.5%), ethane (25%) and freon

[7]Détécteur a grande Acceptance pour la PHysique photoNucléaire Expérimentale.

(0.5%). They collect the charge deposited in their substrate gas by charged particles in a combination of fine wire anodes and thin strip cathodes which locate the precise position of the particle's passage through an individual chamber. When such a position is obtained in two or more wire chambers, the particle track can be deduced.
Each of the wire chambers is contained within two coaxial 1 mm thick cylindrical Rohacell walls coated in 25 μm Kapton film. Electrical screening is achieved via 0.1 μm thick Al coating on the external surfaces of the chamber walls.
The hit position can be located by determining the center of gravity of the charges induced in the several strips. The coordinates delivered by the MWPC are given by an azimuthal angle α and a longitudinal coordinate z (cylinder axis direction).
In order to determine the z coordinate when a wire has fired, the inner and the outer cathode strips cross each other twice along the length of the chamber. The location of the same position in two chambers indicates a particle track.
The area covered by the MWPC is 360° in φ and from 21° to 91° in θ. This gives a total of 94% of 4π steradians.
Fig. 3.9 shows a schematic view of one MWPC as well as a picture of it before it was placed inside CB. More informations about the MWPCs and their working principle can be found in [104].

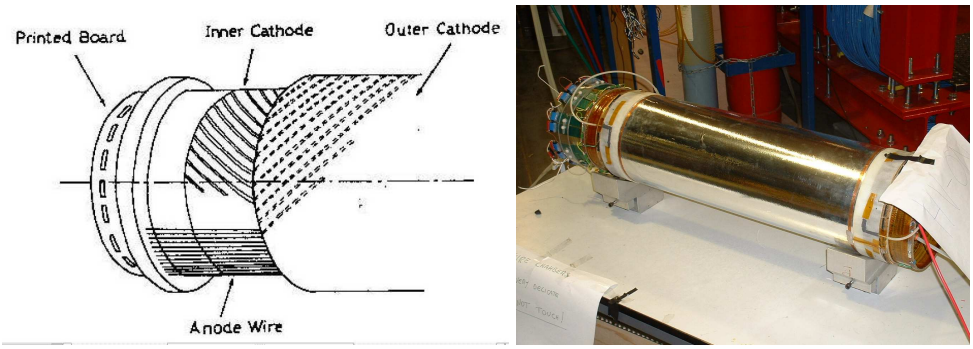

Figure 3.9: *Left: Schematic view of the MWPC, Right: One of the MWPCs before it was placed inside CB.*

In section 5.2.3, it will be explained how the MWPC is used in the tracking and the reconstruction of the charged particles detected in CB.

3.3.1.3 The PID

The Crystal Ball, used with the wire chambers, provides a precise determination of the particle's energy and position. However, the nature of the particle is still unknown. In addition, the very short distance between the target and CB does not allow any time-of-flight measurement. Pulse shape analysis is also not possible since NaI does not have different pulse shapes for different particles (see section 5.2.2). Consequently, another detector in coincidence with CB is needed. Therefore, a Particle Identificator Detector (PID) was built in 2002-2004 by D.Watts at the University of Edinburgh.

Figure 3.10: *The PID detector before it is placed inside the CB.*

The PID consists of a set of 24 EJ204 plastic scintillators (each individual scintillator has 31 cm length, 13 mm width and 2 mm thickness) arranged cylindrically and placed as an inner detector between the target and the CB crystals. The PID has a radius of 100 mm and every scintillating element covers 15° in ϕ.
The unusual location of the PID in front of the wire chamber on the way from the target to the detector is due to a space lack between the wire chamber and the NaI detectors.
Fig. 3.10 shows a picture of the PID and the connectors of its 24 elements before it was placed inside the ball.

The identification of charged particles is obtained by a comparison of their energy E deposited in the NaI, which is supposed to be the total energy, to their energy deposited in the PID scintillators. Typical energy losses of minimum ionizing particles[8] are $\approx$ 400 keV, while protons in the energy range of interest deposit between 1 and 3 MeV. The latter energy is different for particles having the same total energy but a different ionization density.

[8] A minimum ionizing particle (or mip) is a particle whose mean energy loss rate through matter is close to the minimum, such as cosmic ray muons. When a fast charged particle passes through matter, it ionizes or excites the atoms or molecules that it encounters, losing energy in small steps. The mean rate at which it loses energy depends on the material, the kind of particle and also its momentum.

With its sub-detectors, PID and MWPC, CB becomes a good and complete tool for identification of both charged and neutral particles.

In section 5.2.3, the use of the PID in the identification of charged particles and in the distinguishment between protons and charged pions in the CB using the so-called CB-PID banana cuts will be presented.

3.3.1.4 The CB electronics

The scintillation light produced by the interaction of a particle (photon, meson, nucleon..) with a crystal, is converted through the photomultiplier (PM) into an electric pulse. The total charge in the electric pulse is proportional to the energy deposited by the particle in the respective detector module.

As one can see in Fig. 3.11, the analogue output signals coming from the NaI photomultipliers are grouped in bundles of eight and sent to a 'splitter'-module. This module actively splits the original input signal into two output signals, one being integrated in the energy chain and the other sent to a discriminator for the time chain. There are 45 splitter modules, one for every group of signals of two cable bundles, i.e 16 detectors.

The discriminator provides the signals for the trigger, the TDCs and the scalers. Each discriminator channel contains two LED Leading Edge Discriminators (LED) low and high. The amplitude of all 672 crystals is summed and sent to the energy sum trigger (sum threshold). The summed amplitude of each 16-crystal group is also produced and sent to the discriminator which provides a high and a low individual threshold of ~ 20 and ~ 2 MeV respectively.

The number of 16-crystal groups whose energy is above the high threshold is sent to the cluster multiplicity trigger whereas the signals above the low threshold are used to start the TDCs and the scalers. Finally, after a positive trigger decision, the information is digitized in the ADCs and TDCs and sent to the storage computer. The trigger system will be described in more details in 3.3.2.4.

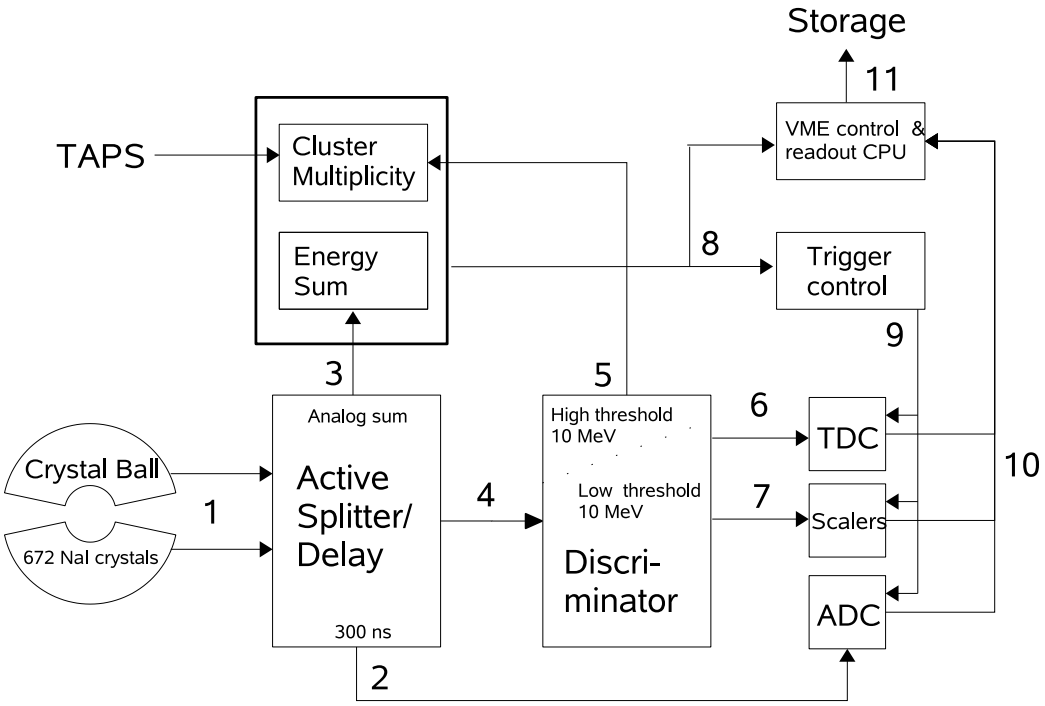

Figure 3.11: *Schematic overview of CB electronics.*

A description of the MWPC and PID electronics can be found in the Ph.D work of D.Krambrich [108]. Further details about the CB electronics can be found in P.Drexler Ph.D thesis [109]. (Both thesis are in German).

3.3.2 The TAPS forward detector system

3.3.2.1 The TAPS detector

The TAPS detector, used in the present experiment as a forward wall, has a long and rich history as well. It has been built in the late 1980s in order to provide, in particular, a better accuracy in the reconstruction of neutral mesons (π^0,η) in their 2γ decay channel.

TAPS has been used at many different laboratories (GANIL[9], GSI, CERN, KVI[10], MAMI, ELSA). Currently a part of TAPS is used at MAMI as forward wall of the Crystal Ball. The other part serves as forward wall combined with the Crystal Barrel at ELSA in Bonn. Informations and published papers which involve TAPS can be found on the TAPS website [107].

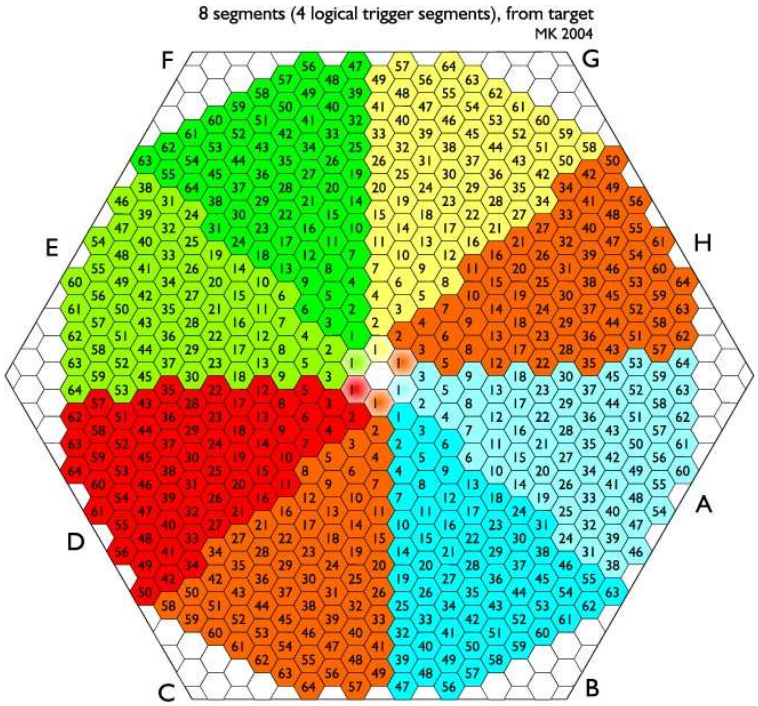

Figure 3.12: *Front view of the TAPS hexagonal wall made of 8 segments of 64 BaF_2 detectors each.*

[9]Grand Accélérateur National d'Ions Lourds, Caen, France.
[10]Kernfysisch Versneller Instituut, Groningen, The Netherlands.

For the present experiment, the TAPS detector was configured as a hexagonal wall of 510 BaF_2 modules placed at a distance of 173.4 cm from the target. For trigger purposes it was logically separated into 8 blocks as shown in Fig. 3.12

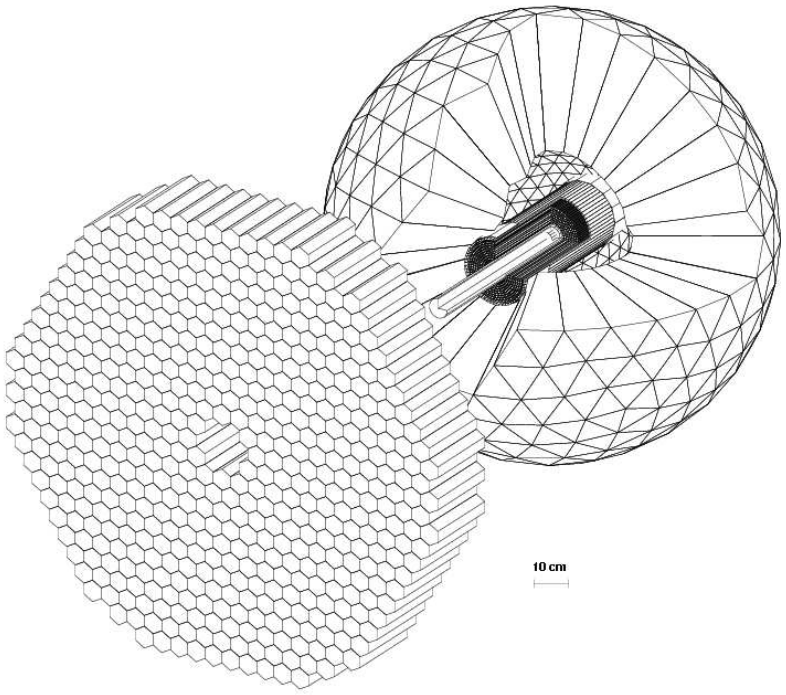

Figure 3.13: *Configuration of the TAPS detectors. The 512 BaF_2 crystals of the TAPS forward wall cover the hole of the Crystal Ball to provide a 4π angle coverage.*

Except for the lowest energies (below few MeVs) where Compton effect and photoeffect are competing, the main interaction mechanism of photons in the BaF_2 is e^+e^- pair production. The e^+ and e^- interact with the scintillators and produce Bremsstrahlung photons which lead to other e^+e^- pairs. This produces a cascade of e^+e^- pairs in addition to photons of decreasing energy, called an electromagnetic shower. When the energy of the particles is low enough, their energy is populating the excited states of the scintillator. The light produced by the de-excitation (the scintillation light) is collected by the photomultipliers linked optically to the back of the scintillators. The electric signals produced by the PMs are proportional to the amount of light and so, proportional to the energy deposited by the particle.

Figure 3.14: *A TAPS BaF2 crystal*

Each detector module is composed of a 250 mm long hexagonal (inner diameter of 59 mm) BaF_2 crystal, whose last 25 mm are spherically shaped, in order to have a better match to the photomultiplier tube. Each crystal owns a quartz fiber to send laser light inside in order to allow the gain monitoring and the calibration of the readout electronics.

In addition to its good energy and time resolutions (Δt<200 ps), a very interesting feature of the barium fluoride scintillators is its sensitivity to the nature of the detected particle. Indeed, BaF_2 scintillators have two different scintillation components with decay times of t = 0.6 ns and t = 620 ns. These components are integrated over short and long electronics gates. The ratio of these two components depends on the ionization density of the particles and therefore, measuring the collected light in two different time windows and comparing their ratio helps to distinguish between particles. In section 5.2.2, the use of this feature in order to distinguish between baryons and electromagnetic particles will be discussed. This technique is called the pulse-shape analysis.

3.3.2.2 The veto detectors

Since TAPS cannot distinguish between proton and neutron as both have the same pulse shape (PSA) and time-of-flight (TOF) signatures, neither between electrons and photons, an additional detector was required to distinguish between charged and neutral particles in the forward direction. For this purpose, a set of 512 plastic scintillators (Veto detectors) was placed in front of the TAPS forward wall, one veto detector in front of each BaF_2 crystal. During the present experiment, the vetos were 5 mm thick, which is too small to record the energy deposited in it. Therefore, the hit in veto is registered as binary digit of a pattern unit, with an efficiency of $\sim 80\%$. This is actually sufficient to provide a discrimination between charged and neutral particles.

The vetos are NE102A scintillating plastic, have 0.025 radiation length and are read out with an optical fiber connected to one of the 32 photomultipliers, a single photomultiplier is responsible for 16 vetos.

A new set of vetos providing a readout of time and energy signals and with

much higher detection efficiency has been developed at the University of Giessen and replaced the veto used in the present experiment since 2006.

3.3.2.3 The TAPS electronics

TAPS electronics have been upgraded during 2004 providing high count rate capabilities, fast digitization, very good resolution, good compatibility to complex trigger architecture and the possibility to be used close to the detector. The main idea of these new electronics is to group four ADCs (Analog) in a single VME module. This VME module is made of two main parts: the Motherboard for the digitization and the VME access in one hand, and the Piggyback[11] for the data collection on the other hand.
But how does the hit recording process in TAPS work? Fig. 3.15 shows a simplified overview of the electronics recording process.

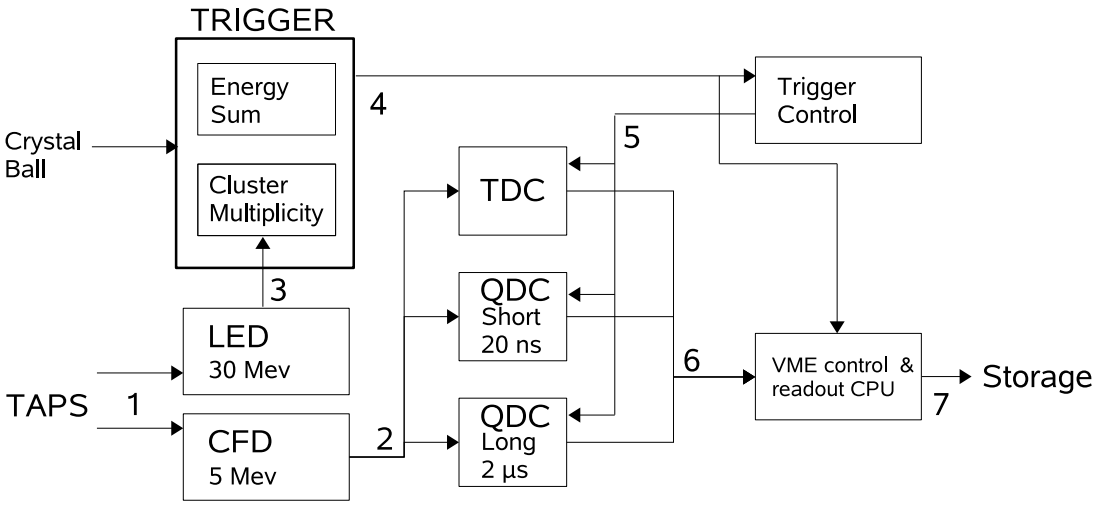

Figure 3.15: *Schematic overview of TAPS electronics.*

This BaF_2 signal is transmitted to a CFD (Constant Fraction Discriminator) with a 5 MeV threshold and it is considered as a hit in the crystal if the signal

[11]Piggyback : A small printed circuit board that plugs into another circuit board in order to enhance its capabilities. It does not plug into the motherboard, but would plug into the boards that plug into the motherboard.
In TAPS electronics, the piggyback is composed of : Active Delay/Passive Split, Test Pulser Generator, CFD, LED1 and LED2, Gate Generator, QACs (Charge to amplitude converter) and TACs (Time to amplitude converter).

is higher than this CFD threshold. If this is the case, it gives the start signal for energy integration in both long and short gate QCDs and for the time measurement in the TDC.
The same signal is sent to a LED low and LED high (Leading Edge Discriminator) and will participate to the trigger if it is higher than the threshold of the LED low or high, depending on the trigger conditions.
There are four ADC channels per detector element which allow the signal integration over different time periods and with different charge to channel conversion gain (see section 4.2). The short gate ADC ($\sim$70 ns) integrates the first fast component of the scintillator light and the long gate ($\sim 2\mu$s) integrate over the whole pulse.
The trigger decision is sent to the QDCs and TDC and stops the time measurement in the TDC. If the Trigger decision is positive, the event energy and time are recorded.

The TAPS veto counter hit patterns were recorded in LeCroy CAMAC pattern units and their signals are compared to the BaF_2 ones in order to distinguish between charged and neutral particles.
More details about the TAPS electronics can be found in [109].

3.3.2.4 The Trigger

In the present experiment, one would like to detect photons from the decay of one or more neutral mesons (π^0 , η, $\pi^0\pi^0$..). Thus, the hardware trigger has been set, depending on the channels of interest, as a filter implemented in the electronics in order to remove the low energy background (due to Compton scattering, electromagnetic background..). The trigger consists of two independent parts: the energy sum of the Crystal Ball and the cluster multiplicity trigger.

As seen above, the CB photomultiplier tubes are connected to fan-out units in groups of sixteen channels. In addition to coping the signal on both ADC and TDC branches, they provide an analog sum of these sixteen inputs which are then summed through a cascade of LeCroy 428 NIM analog Fan In/Out modules to provide an analogue sum of all CB deposited energy signals. If the total energy deposition is below a definite threshold (103 mV or 50 MeV in our experiment) the event will be rejected. This is the "level one" trigger.
However, The TAPS electronic boards have not been designed to provide a

readout of the analog energies and therefore TAPS could not participate to the energy sum trigger.

The second component of the trigger is the cluster multiplicity. It has been used in order to reject or keep events according to the number of desired final state particles, this is explained in the following as seen in Fig. 3.16 :

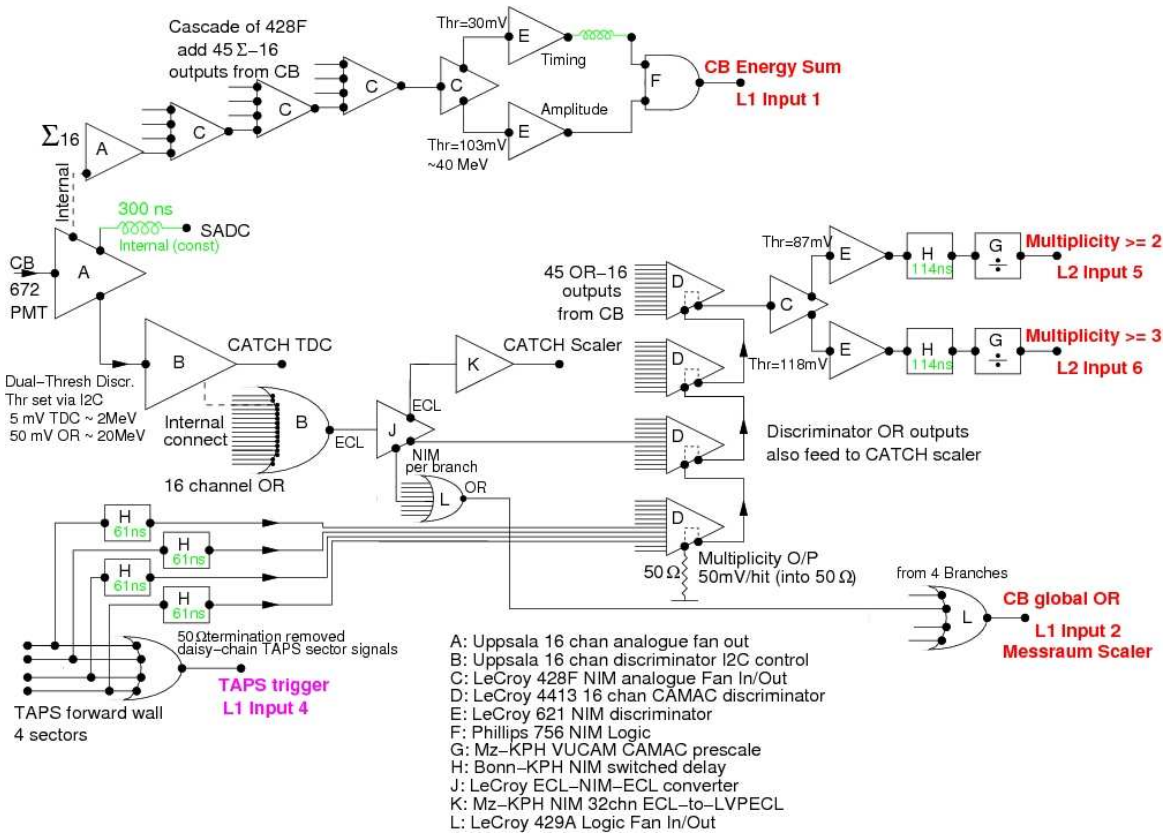

Figure 3.16: *Technical scheme of the trigger. The upper part shows the CB energy sum trigger, the middle part the CB multiplicity trigger and the lower part the TAPS multiplicity trigger.*

The active splitter in the Crystal Ball electronics divides the 672 NaI crystal readout in 45 logical segments made of 16 contiguous crystals and calculates the analog energy sum of each individual segment. The typical size of a single particle energy deposition is small enough to be contained within one logical segment so that one can assume that one firing segment corresponds to one particle .

The high threshold signals from each group of 16 inputs were "OR"ed[12] and the multiplicity of the 45 sector signals were determined using the multiplicity output (50 mV per hit) of four LeCroy 4413 16 channels CAMAC discriminator. The summed multiplicity outputs were fanned out into the discriminator which has a threshold of 87 mV for the "level two" multiplicity two trigger.
In a similar way TAPS has been split in 4 logical segments made of 128 BaF_2 crystals. If any crystal in a segment has an energy deposition above the 20 MeV LED threshold, a multiplicity hit will be recorded.

The trigger multiplicity (M) was set to be M>=2 : at least two hits in CB or one hit in CB and one hit in TAPS. In the present experiment TAPS could not make the trigger alone[13].
Exhaustive technical information about the trigger system can be found in [108].

3.3.2.5 The Data Acquisition

The CB Data Acquisition system (CBDAQ) collects the CB ADCs, TDCs and Scalers arrays and is controlled by two VMEbus[14]. The digital data first pass by the VMEs to receive the slow control functions, like the programmable threshold setting, run start and stop. They are then transferred by the master VME to the A2-counting room computer via an Ethernet connection.

The TAPS DAQ system is made of ten VME crates: Eight for the new 4-channel readout electronics boards, and two for the trigger generation modules (MCU), the HV control modules and the VETOs, TDCs and Scalers readout.
The TAPS DAQ data stream was read out separately from the CB one. The

[12]The OR gate is a digital logic gate that implements logical disjunction. The function of OR finds the maximum between two binary digits, just as the complementary AND function finds the minimum.

[13]In more recent experiments at MAMI, in addition to CB alone and combined CB/TAPS triggers, TAPS alone trigger was needed. Since September 2008 TAPS could make the trigger alone.

[14]The VME(Versa Module Eurocard) is a computer bus standard, originally developed for the Motorola 68000 line of CPUs, which provides a modular means to implement computer-independent systems for real-time data collection.

only direct interaction between CB and TAPS DAQs was for trigger purposes. CB and TAPS data merged then together and have been stored with AcquRoot which provides a basic on-line analysis. This allowed a real-time check of the data quality, detectors response and the synchronization status between TAPS and CB DAQ systems.

The data analyzed in the present work have been taken in March 2005 in the frame of the new series of solid target data (Li, C, Ca and Pb) in the view of the double pion in medium effect investigation as well as for the coherent photoproduction purposes.

The following table summarizes the beam time characteristics.

Target length	5.7 cm
Target density	0.57 g/cm^3
Collimator	4 mm Iron
Radiator	10 μ Iron
Beam Energy	883.25 MeV
Beam Current	6 nA
beam time duration	180 hours
Tagger Range	205-820 MeV

Table 3.1: *Summary of the principal experimental conditions.*

The trigger conditions and the LED thresholds are given in table 3.2. More Detailed informations about the experimental conditions could be found in the A2 logbooks and the run-sheets in Mainz.

Trigger multiplicity	M$\geq$2
Trigger conditions	2γ in CB or 1γ in CB and 1γ in TAPS
CB LED threshold	50 MeV
TAPS LED Low	500 keV
TAPS LED High	20 MeV

Table 3.2: *Summary of the trigger details.*

Chapter 4

Data processing

Once the data taking is done, the signals provided by the detectors (which are nothing but raw digital pulse heights and non synchronized times) should be transformed into physical variables such as masses, energies, and times. To do so, one should be first able to access the data from all parts of the detector using an analysis software. In the present work this was done using the "AcquRoot" tool. In a second step a calibration of every element of each detector should be performed in order to transform the data informations, given in channel format, into physical units.

In the present chapter, the AcquRoot software analysis tool used in the treatment of the data will be first presented. The time and energy calibrations made for the different parts of the detectors will then be summarized.

4.1 The AcquRoot analysis software

AcquRoot is the data acquisition program and analysis tool used for the on-line running and the off-line analysis in CB/TAPS at the A2 collaboration.
AcquRoot has been written by J.R.M Annand (University of Glasgow, UK). It is formed of C++ routines and based on the CERN ROOT high energy physics system used worldwide [110]. AcquRoot combines the full ROOT functionalities and high graphism with the A2 authored classes designed to control the A2 electronics and detectors, data acquisition, storage and analysis. Each of the different functions of AcquRoot runs as a separate thread within the one container program as shown in Fig. 4.1 This allows the four separate threads

to access the same areas of memory while running independently from each other with different levels of priority.

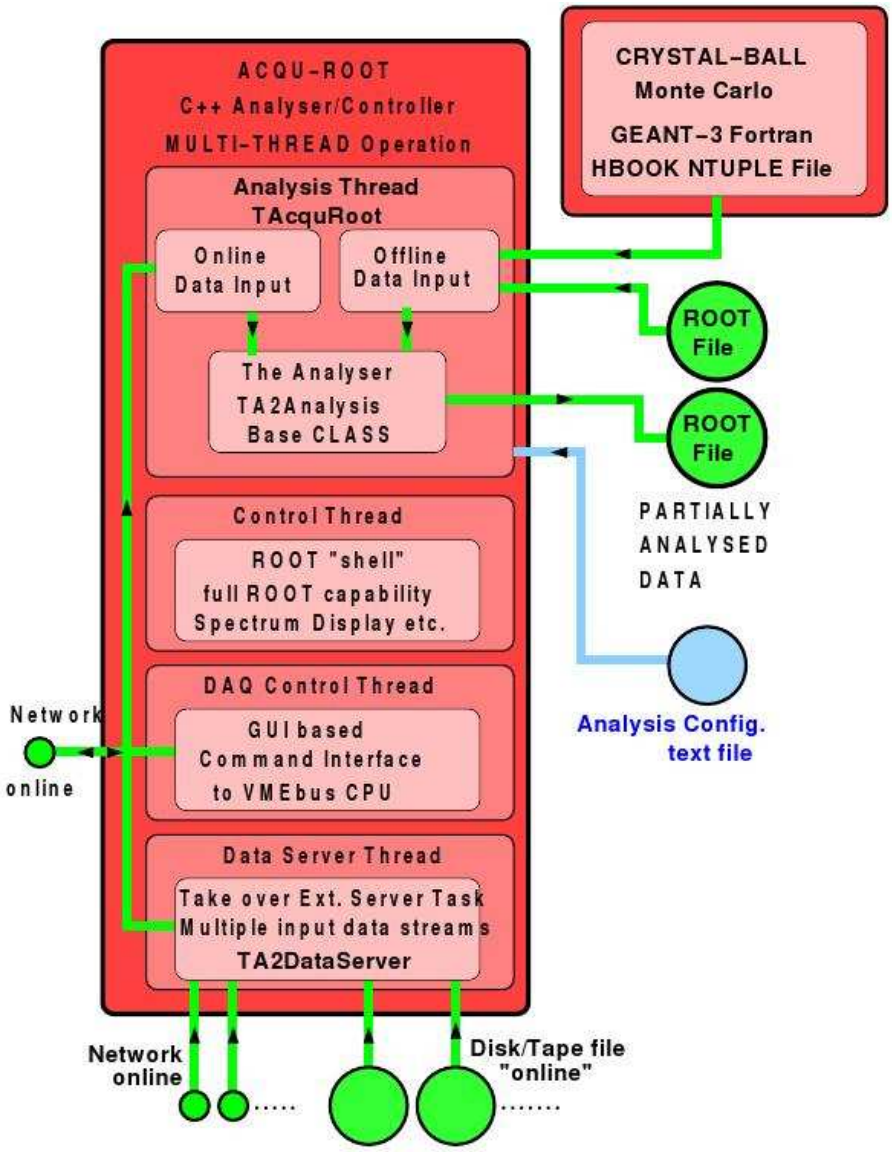

Figure 4.1: *Schematic view of the AcquRoot Data Storage and Analysis System [110].*

The main program TA2Control can be invoked from any ROOT session, but can also be compiled as an executable (used this way in the present analysis).

AcquRoot is using an object-oriented programming language which allows the production of basic templates for functions and data objects to be grouped

together and defined once as a class. The AcquRoot classes are based on the principle of 'inheritance' : the class can be 'inherited from' and the functionality accessed by diverse inherited classes. For example, the conversion of digitally stored pulse heights to energies and times from every single detector is made in the TA2Detector class which forms a part of the AcquSys (the system code of AcquRoot). This class is then inherited by detectors.

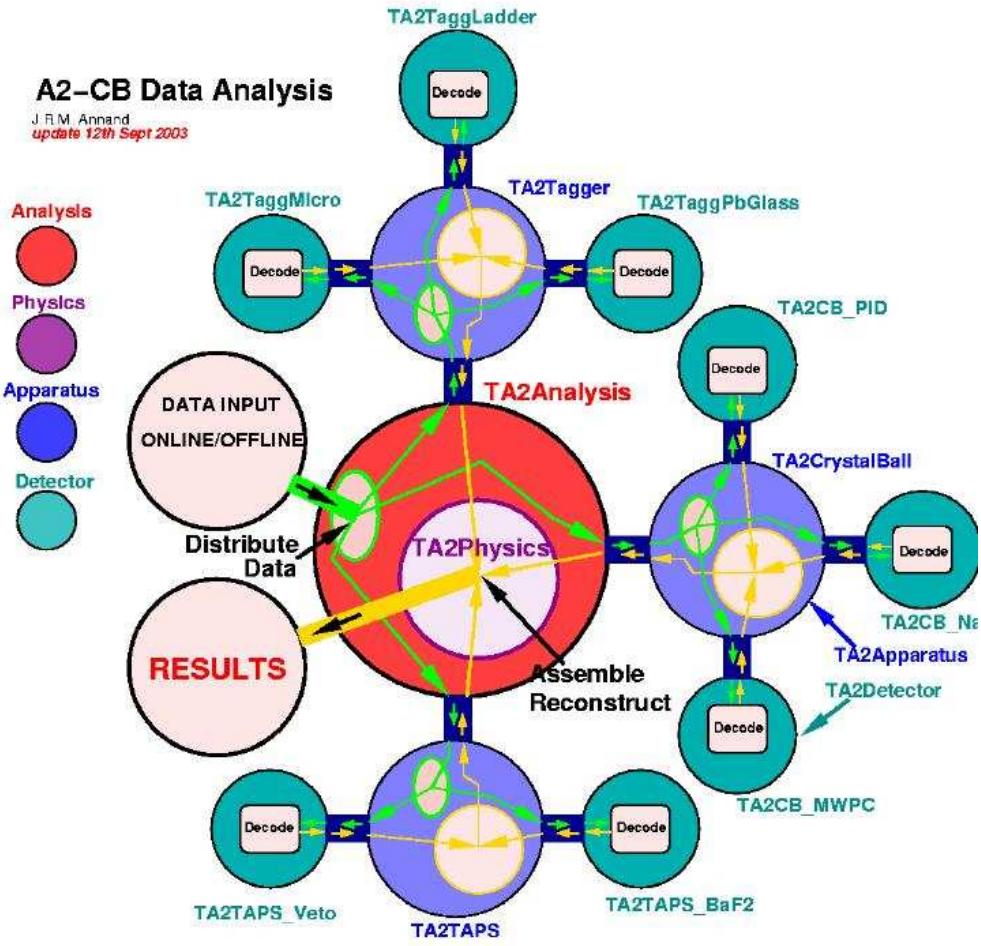

Figure 4.2: *Tree structure of AcquRoot. The path of the data is indicated by the arrows showing where each task is performed [110].*

Further details about the AcquRoot software can be found in [110] and [111].

4.2 The calibrations

Once again, the calibration principle is quite simple and consists of two parts:

- The transformation of raw TDC channels into nanoseconds (time calibration) and ADC channels into MeVs (energy calibration).
- The alignment of all TDCs and ADCs of the detectors in order to optimize the overall time and energy resolution.

In the following, the calibrations for the different elements of the detector setup and for the Tagger will be summarized. However, before going into details, it is important to know which signals are starting and stopping the TDCs of each detector in order to know the total duration of an event. The following table summarizes the start and stop signals.

	START	STOP
Tagger	Tagger Element	Trigger
TAPS	CFD	Trigger
Crystal Ball	Trigger	NaI Element

Table 4.1: *Summary of start and stop signals*

4.2.1 The Tagger calibrations

4.2.1.1 Tagger time calibration

Each Tagger TDC channel has a time conversion of 0.18 ns/channel (based on a calibration done when the Tagger was first installed). It is important that all of the Tagger channels are aligned so that their prompt[1] peaks occurs at the same point in each TDC time spectrum. To do so, the Tagger time alignment has been obtained using Gaussian fits. The TDC spectra were fitted with a Gaussian distribution, which determined the mean position of this Gaussian. Subsequently, offset values have been determined and applied to all spectra in order to align the peaks at the same position. The Tagger versus trigger time resolution (TAPS versus Tagger) obtained in this way was ~ 8 ns.

[1] In a time spectrum there is usually a prompt peak corresponding to the real events under study and a random background. See sect. 5.3.2 for details.

The Tagger time calibration has then been improved in combination with TAPS. The trigger, which controls the detectors timing, has a finite time jitter[2] which gets folded in with the detector times. As the Tagger timing is stopped by the trigger and the TAPS CFD timing is started by it, by subtracting the two times, the trigger width is removed. The individual detector elements are then aligned with an overall resolution determined by the combination of both detectors.

Mathematically, one can write the equation 4.1:

$$t_{Tagger-TAPS} = (t_{trigger} - t_{Tagger}) - (t_{trigger} - t_{CFD}) = t_{Tagger} - t_{CFD} \qquad (4.1)$$

In practice, the calibration is achieved by plotting for each Tagger channel the difference between the Tagger timing and the time of a single photon in a BaF_2 crystal. All these spectra were then fitted with a Gaussian and the position and the mean of the peak are determined. The procedure is repeated until the time resolution can not be improved anymore. The time resolution obtained with this method is better than 1.5 ns. Fig. 4.3 shows the quality of the obtained time calibration of the Tagger. .

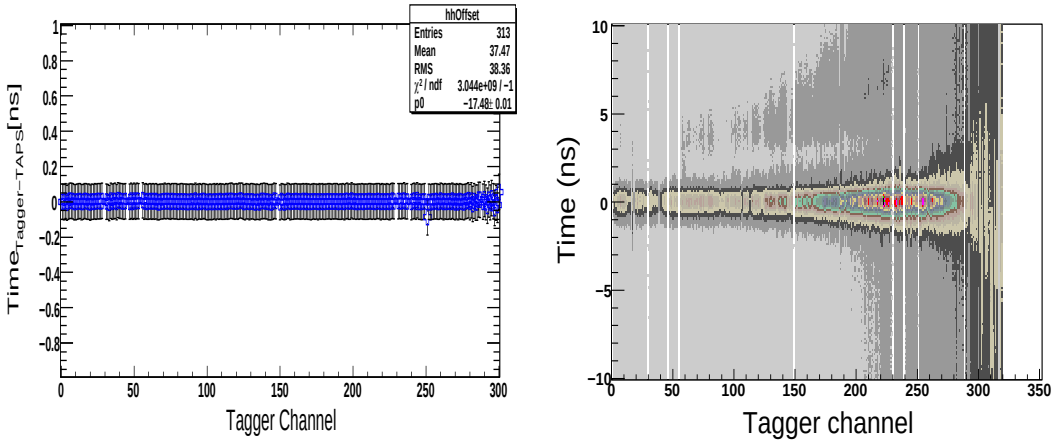

Figure 4.3: *Left: time alignment of all Tagger channels (last iteration). Right: time resolution of the Tagger elements obtained in combination with TAPS, better than 2ns.*

[2]Jitter is the time variation of a periodic signal in electronics, often in relation to a reference clock source. Jitter period is the interval between two times of extrema effects of a signal characteristic that varies regularly with time.

4.2.1.2 Tagger energy calibration

As seen in the previous chapter, the position of the deflected electron in the Tagger focal plane is proportional to its energy and inversely proportional to the photon energy, and therefore the correspondence position-energy has to be calibrated. In order to calibrate the Tagger in energy in the beginning of each beam time a ray tracing is performed, in an equivalent uniform field, monitored with a specific program called TagCal (see [112]). This program, which may be started on-line, is based on the NMR[3] measurement of the Tagger magnetic field and determines the energy of the recoil electron landing in the middle of each Tagger detector. The NMR measurements are monitored throughout each beam time to ensure that there is no drift in Tagger calibration.

4.2.2 TAPS calibrations

4.2.2.1 TAPS time calibration

The TAPS gain used in the present work was chosen to be constant for all TDCs.[4] The TAPS time calibration was similar to the Tagger. The first step consisted in aligning the TDCs using a Gaussian fit. The second step consisted in achieving one further alignment in combination with the Tagger by improving $t_{TAPS-Tagger}$ in order to get a reasonable time resolution. The procedure was repeated until the time resolution can not be improved anymore. The obtained $t_{TAPS-Tagger}$ resolution was better than 1.5 ns (FWHM[5]). The overall time difference between TAPS and the Tagger is shown in Fig. 4.4.

[3]Nuclear Magnetic Resonance.

[4]TAPS TDC start was given by a CFD discriminator and the common stop was based on the trigger decision. Tests showed that choosing a constant gain value for all TAPS TDCs is reasonable. Recently, the new TAPS (Configuration changed during 2007) TDCs gain was measured and gave an almost constant value around 100 ps.

[5]Full width at half maximum. All the values of calibration will be given in term of FWHM. The FWHM and Mean values shown in the following spectra are given in ns.

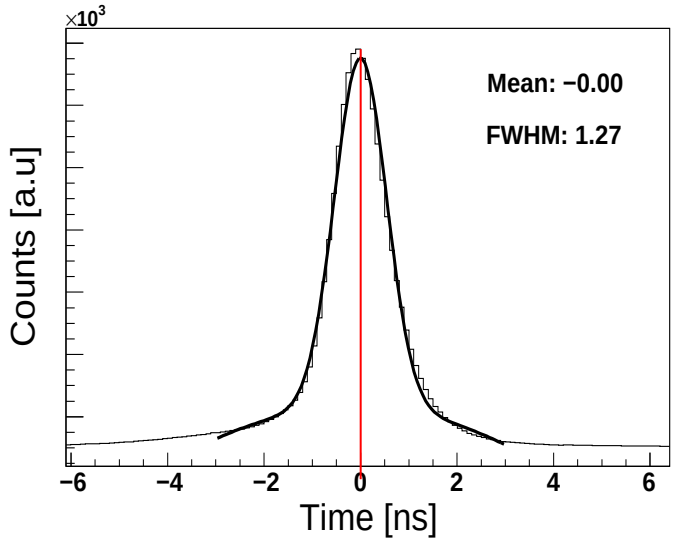

Figure 4.4: *Overall time difference between TAPS and Tagger. A resolution better than 1.5 ns is obtained.*

One further improvement has been achieved by aligning the TAPS-TAPS time resolution (Time difference between two photons in TAPS with a cut on the π^0 invariant mass between 110 and 160 MeV[6]) as seen in Fig. 4.5.

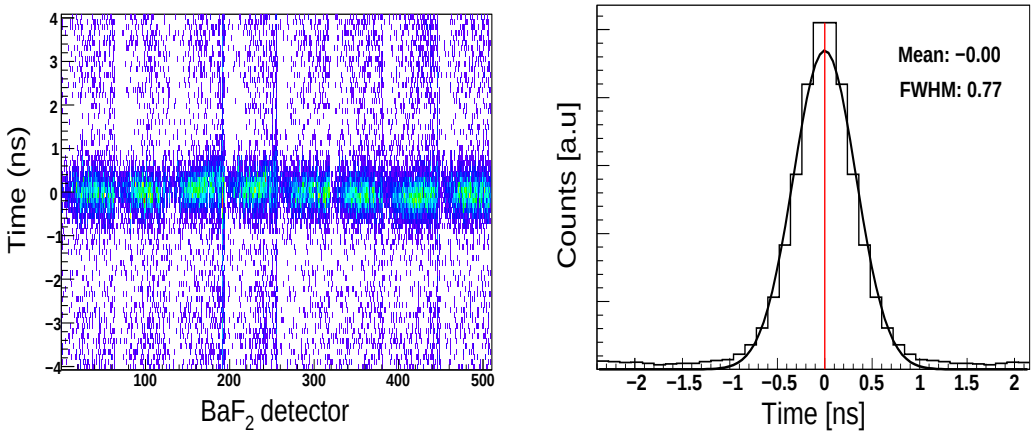

Figure 4.5: *TAPS time calibration quality. Left: Time alignment of all TAPS detectors using TAPS-TAPS timing, resolution is better than 1 ns. Right: 1D-projection of the lefthandness histogram showing the TAPS-TAPS time resolution.*

[6]The invariant mass principle will be introduced in sect. 6.1.

4.2.2.2 TAPS energy calibration

TAPS has been energy calibrated using measurements of cosmic muons at the beginning and the end of the beam time when the beam was off. The purpose is to establish a relationship between ADC channels and the energy deposited in the BaF_2 crystals. Since they are minimum ionizing particles, muons loose approximately 6.45 MeV/cm when passing through BaF_2 crystals. This corresponds to 37.7 MeV in crystals when they are arranged horizontally like in the present experiment. This value was obtained by MC simulations performed with GEANT 3.21 (simulations will be introduced in Chapter IV). Further details can be found in [116].

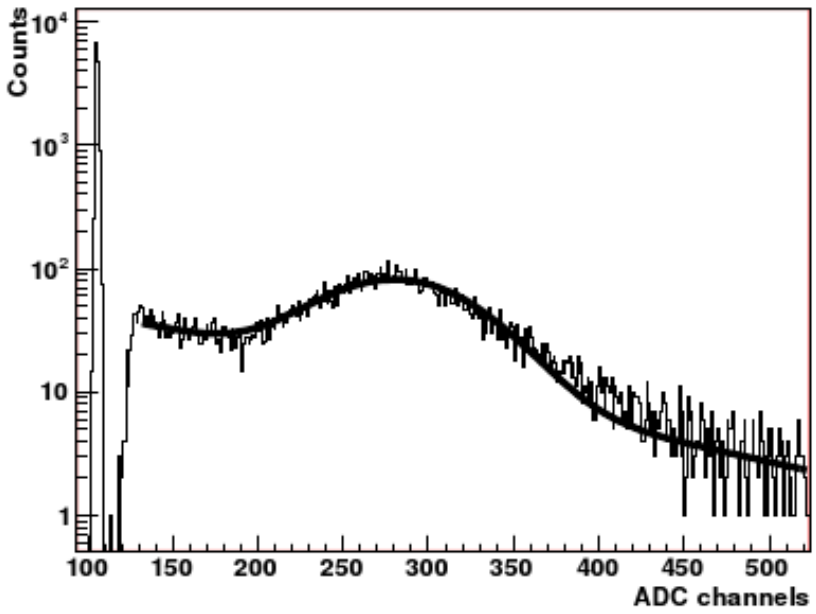

Figure 4.6: *TAPS energy calibration spectrum for a single crystal showing the pedestal peak corresponding to 0 MeV deposited energy and the used fit made of Gauss-peak plus exponential background.*

The fitted peak position shown in Fig. 4.6 was used to calculate the gain. The offset was provided by the TAPS pedestal[7] pulser. The cosmics peak positions

[7]The pedestal is a peak at zero energy created by the electronic module which recorded the readout of all ADCs once per second during cosmic data-taking. Practically, the pedestal position is determined by registering the first highest channel of the spectrum before decreasing again.

were determined by a Gauss-peak plus exponential- background fit.
These two values are then used to establish a linear correspondence between ADC channels and MeVs for each crystal. The procedure was applied twice, once for the long and once for the short integration gate.

Finally, the energy calibration has been improved by aligning the pion invariant mass peak positions in each TAPS BaF2 detector obtained with one photon and one photon in CB in an iterative way. The quality of the energy calibration is shown in Fig. 4.7

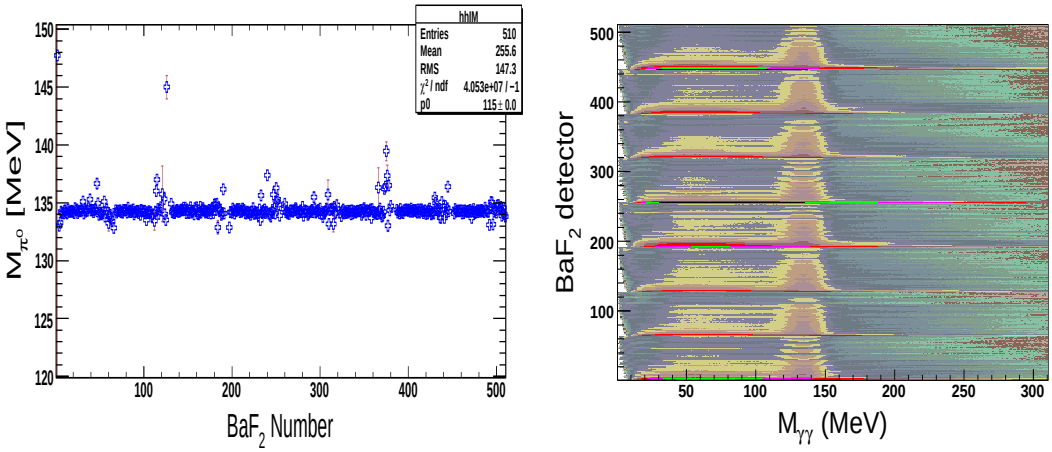

Figure 4.7: *Left: For each BaF2 detector, the energy was aligned to the π^0 mass (last iteration). Right: π^0 mass as function of BaF_2 detector.*

4.2.2.3 The veto calibration

The veto wall was not calibrated in the present experiment as the veto crystals were not able to provide any readout of the energy deposited by the charged particles that pass through. The new veto wall installed since 2006, which provided an energy readout, has been energy calibrated by the author and I.Keshelashvili at the beginning of the beam times using cosmics. The procedure was the same as for TAPS, the veto wall was placed horizontally.

4.2.3 CB calibrations

4.2.3.1 CB time calibration

The CB time alignment was done in a similar way as for TAPS with a channel to time conversion of 117 ps/channel. In case of CB, the electronics are set up in a way that the 'start' is made by the trigger and the 'stop' by the NaI elements. This gives the equation:

$$t_{CB-Tagger} = (t_{trigger} - t_{CB}) + (t_{Tagger} - t_{trigger}) = t_{Tagger} - t_{CB} \tag{4.2}$$

The iterative procedure made for TAPS timing was applied identically, and the best time resolution obtained was better than 2.5 ns (FWHM) as seen in Fig. 4.8

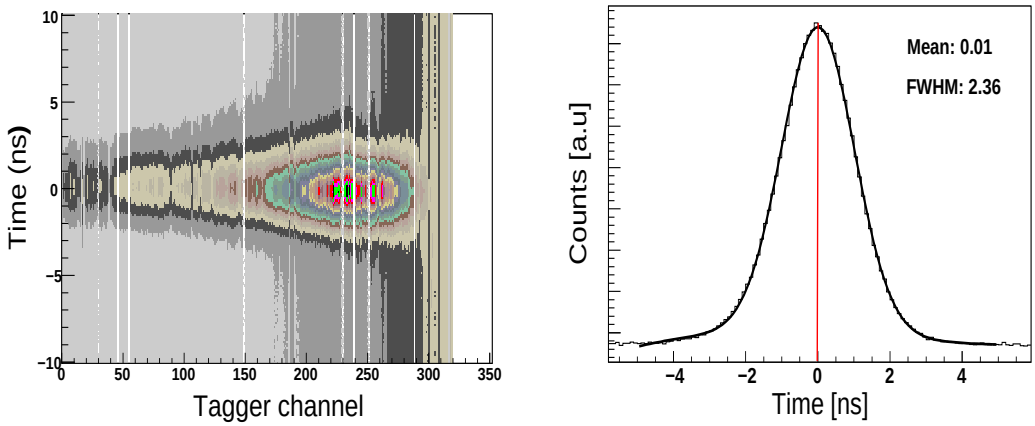

Figure 4.8: *Left: Time alignment of all CB elements, Right: Overall time difference between CB element and Tagger channels, a resolution better than 2.5 ns has been achieved.*

Similarly to TAPS, a further check of the CB time calibration has been achieved through the CB-CB timing (1 photon in CB versus 1 photon in CB with a cut 110-160 MeV on their invariant mass). The result is shown in Fig. 4.9.

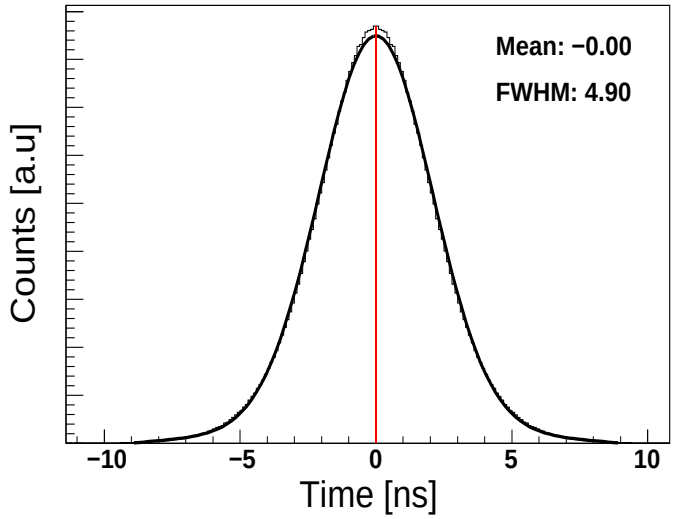

Figure 4.9: *1D-projection of the CB-CB time resolution.*

4.2.3.2 CB Time walk correction

In CB electronics, the time depends on the energy of the measured particle. This is due to the fact that, in contrast to TAPS which uses CFD discriminators, the CB uses LED discriminators so that the CB timing t_{CB} is dependent on the energy seen by the CB module. This means that particles with small energies need more time to activate the trigger and start the measurement. This causes a time difference between signals with different pulse heights, called time walk, and has therefore to be corrected. To do so, as for the energy calibration, the single π^0 channel was used. The time of the π^0 decay photons was plotted against their deposited energy (see Fig. 4.10). The maxima of multiple vertical slices have been determined and the 2D shape was plotted with the function:

$$f(y) = p_0 + p_1(1 - \sqrt{p_2/2}) \tag{4.3}$$

where the offset is adapted with p_2.

Applying the "inverse" function to arrive at a horizontal distribution, the result shown on the right side of Fig. 4.10 is typically obtained. A detailed description of the walk correction can be found in in the Project work of M. Horras [113].

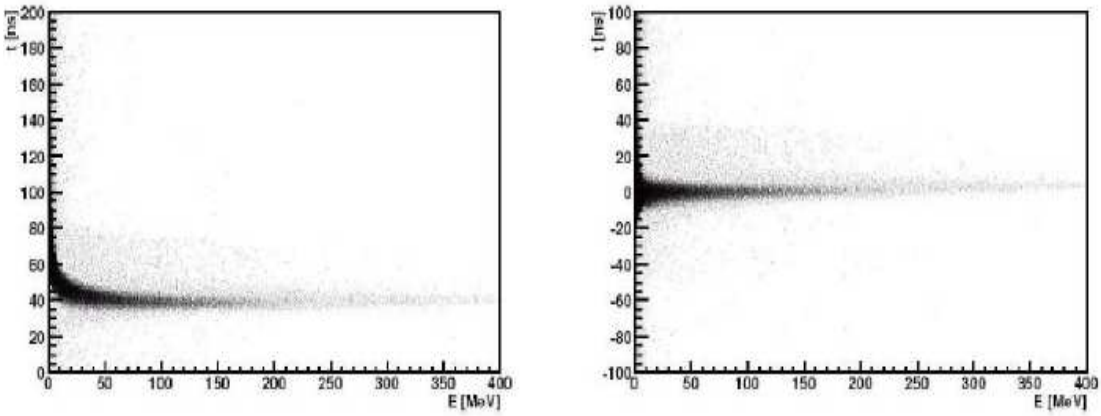

Figure 4.10: *2D walk and alignment CB time. Left: Before correction, Right: after correction.*

4.2.3.3 CB energy calibration

Unlike TAPS, CB could not be calibrated using cosmics muons because of the arrangement of the crystal in a spherical geometry. CB crystals were calibrated individually by irradiation using a $^{241}Am/^{9}Be$ source.

The response of the photomultipliers was adjusted for the peaks produced by the 4.438 MeV decay photons to be aligned for all 720 ADC spectra in order to get the peak within 20 $\%$ of the mean range.

For particles with much higher energy, a fine-tuning of the calibration was done using the $\gamma p \rightarrow \pi^0 p \rightarrow 2\gamma p$ reaction and the energy of the π^0 was determined as function of the incident photon beam. The π^0 energy is then measured experimentally (from its reconstructed decay photons) and the ratio between measured and calculated energy delivers a first MeV/channel value. The correction process was repeated iteratively until obtaining a resolution of 8.3 MeV for the π^0 mass.

The CB energy calibration was improved for each NaI crystal, similarly to TAPS, in an iterative way by considering the invariant mass peak position obtained with two photons in CB. Fig. 4.11 shows the quality of energy calibration for the CB.

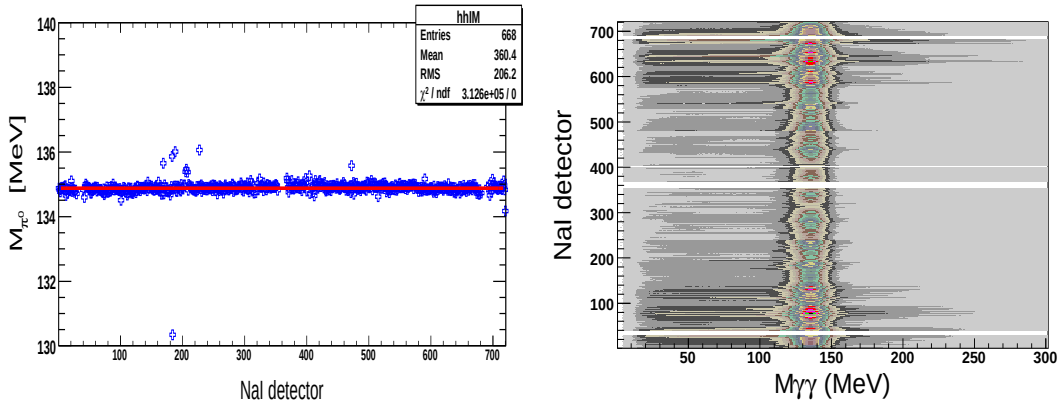

Figure 4.11: *Left: For each NaI detector, the energy was aligned to the π^0 mass (last iteration). Right: π^0 mass as function of NaI detector.*

4.2.3.4 PID calibrations

The calibrations of the PID (time, energy and position) have been done by E. Downie (University of Glasgow). The position calibration determined the azimuthal angle of each PID scintillating element by plotting in a 2D histogram the PID channel versus the ϕ angle of the NaI for synchronized events with one hit in the PID and one in CB. This is necessary in order to link the energy deposits in the PID with the appropriate clusters in CB NaI crystals and thereby build the $\Delta E/E$ plots (ie, energy deposit in CB cluster versus energy deposit in PID element) that provide the basis for charged particle identification in CB.

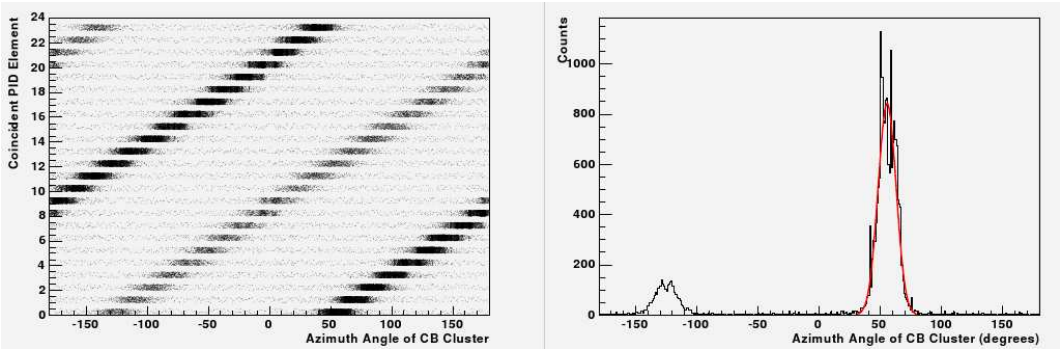

Figure 4.12: *Azimuthal position calibration of the PID taken from [105]. left: Azimuthal angle of CB clusters in coincidence with PID elements for events with one hit in each detector. Right: projection of left panel for PID element 0.*

The highest peak of the projection of these 2D histograms was then fitted by a Gaussian as seen in Fig. 4.12. The results of the fits are then used in order to calculate the mean ϕ position of each individual element.

The quality of the PID position calibration is shown in Fig. 4.13 where the difference between the azimuthal angle of each PID element and the the azimuthal angle of the CB cluster is plotted. Note that two elements (2 and 4) were out of service during the present experiment.

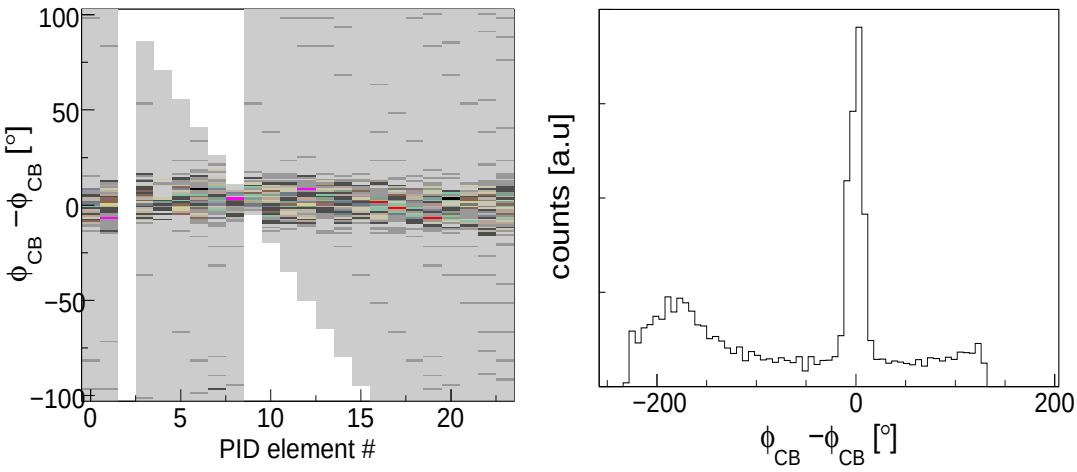

Figure 4.13: *Position calibration of PID element number 1. Left: difference between the azimuthal angle of each PID element and the the azimuthal angle of the CB cluster . Right: Projection of the left histogram for the PID element 1.*

The PID energy calibration was performed by aligning the output of the individual PID elements using MC simulations in order to enable the separation of different charged particles and to deal easier with the few cases were a particle traverses the gap between two neighboring scintillators.

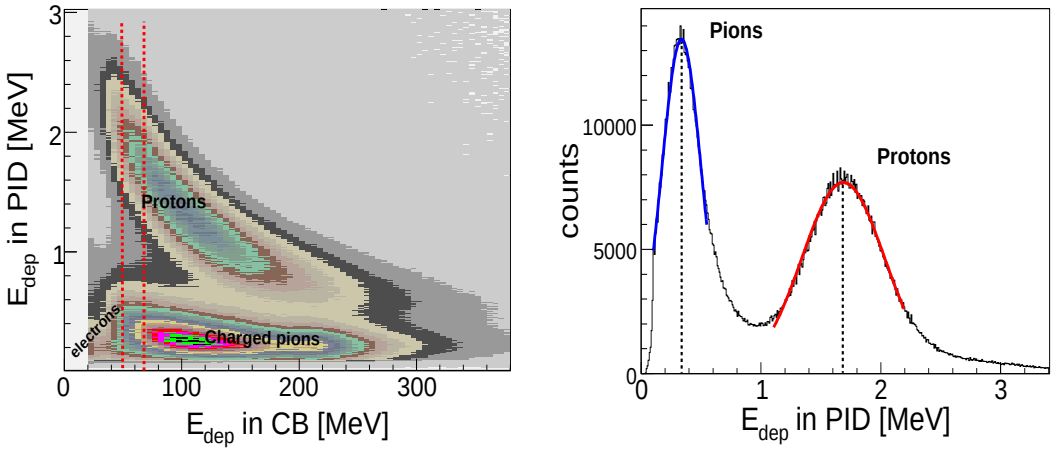

Figure 4.14: *Energy calibration of PID element number 1. Left: $\Delta E/E$ plot showing the regions where sit the different charged particles. Right: Projection of the $\Delta E/E$ plot and Gaussian fits of the pion and the protons peaks.*

The PID time calibration was easy to perform as it is delivered by CATCH TDCs with well-known time/channel ratios. The alignment was done using the usual procedure (Gaussian fit - shift) as the time peaks are very sharp (time resolution of $\sim$5 ns).

Additional information about the PID electronics and calibrations can be found int he PhD work of E. Downie [105].

4.3 The Tagging efficiency

The knowledge of the photon flux is needed for the absolute normalization of the cross sections (see section 6.1). This flux is, however, not equal to the number of the recorded recoil electrons in the Tagger detector. Due to collimation, Moeller scattering and other processes, the number of photons reaching the target is lower than the number of electrons recorded in the Tagger. Thus, the number of emitted photons for a specific beam time period is obtained by the combination of the emitted electrons during this time (scalers) and the efficiency of the tagging system :

$$N\gamma = N_{e^-} \times \epsilon_{tagg} \tag{4.4}$$

To measure the tagging efficiency, the scattered electrons have been detected in the Tagger focal plane detectors. The tagged photons which pass through the collimator have been detected in a Cerenkov lead glass detector.
The ratio of the tagged photon spectrum and the electron spectrum delivers a tagging efficiency for each Tagger channel.

Fig. 4.15 shows examples of individual tagging efficiencies. Most channels show a smooth ϵ_{tagg}. However, some of them, have a low and instable efficiency and therefore they have to be removed.

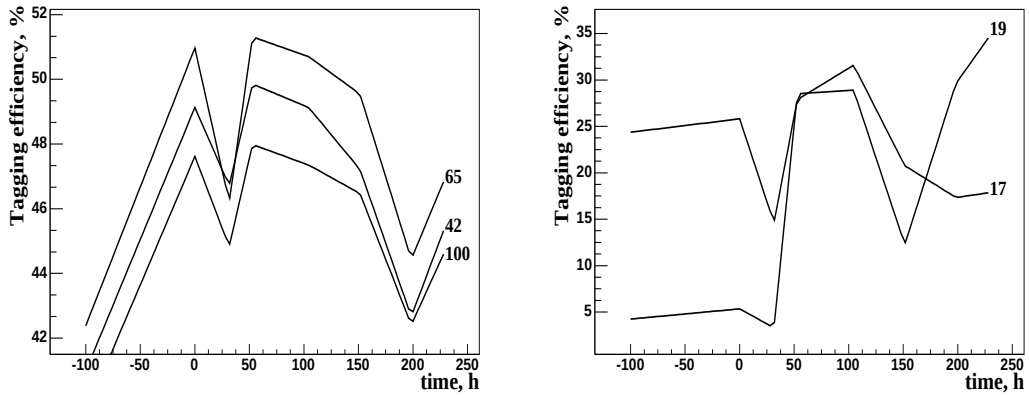

Figure 4.15: *Tagging efficiency versus time. Left: ϵ_{tagg} for Tagger channels 42, 65 and 100. Right: example of Tagger channels to be removed because of bad ϵ_{tagg}.*

The tagging efficiency was estimated approximately daily with dedicated measurements. These recorded tagging efficiencies are then averaged over the beam time duration and one gets only one ϵ_{tagg} per Tagger channel. However, since the tagging efficiency was only measured periodically, approximately once a day, this leaves room for fluctuations between two consecutive determinations. To account for this, a method described in [115] was applied to the experiment. A ionization chamber - called P2 - was placed behind the target to measure the beam intensity. During the runs, the ratio between the counting rates in P2 and in the Tagger was continuously monitored. This P2/Tagger ratio is proportional to the average tagging efficiency, although in arbitrary units.

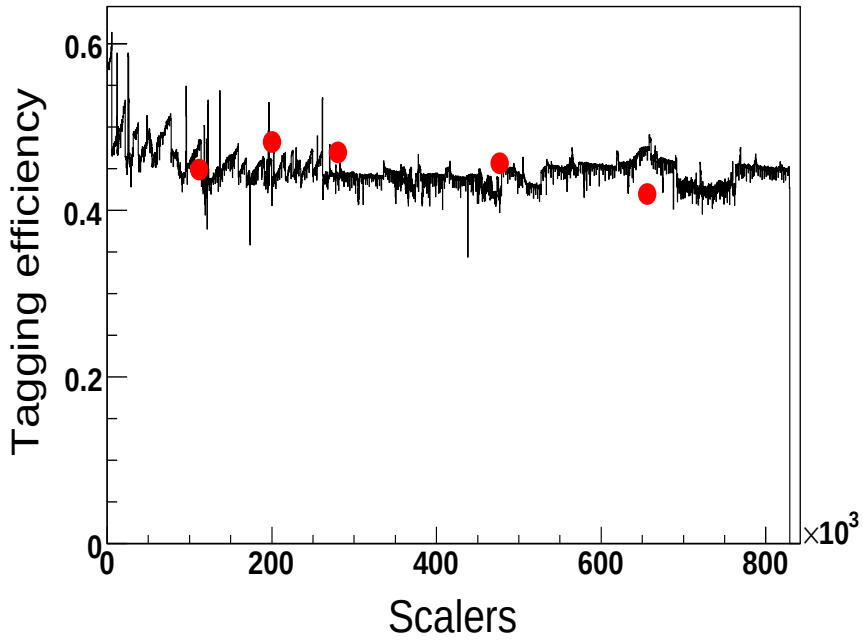

Figure 4.16: *Averaging of tagging efficiency. The ratio P2/Tagger (black line) is compared to the individual measurements (red dots).*

The P2/Tagger ratio as function of time is compared to the measured average tagging efficiencies (see Fig. 4.16) and its absolute scale is fixed such that it agrees with the tagging efficiencies. This calibrated P2/Tagger ratio is then used to control the time dependence of the tagging efficiency. However, as can be seen in Fig. 4.16 the variations are small, typically below the 10% level.

Note that the matching between P2/Tagger ratio and the measured tagging effeciencies is unfortunately not perfect, especially for the one of the highest scalers in Fig. 4.16. This will be accounted for as a systematic uncertainty and a complete paragraph will be dedicated to that in Chapter VII.

The average over the whole beam time of the tagging efficiency is plotted in Fig. 4.17 as function of the Tagger index, with the P2-Tagger correction taken into account.

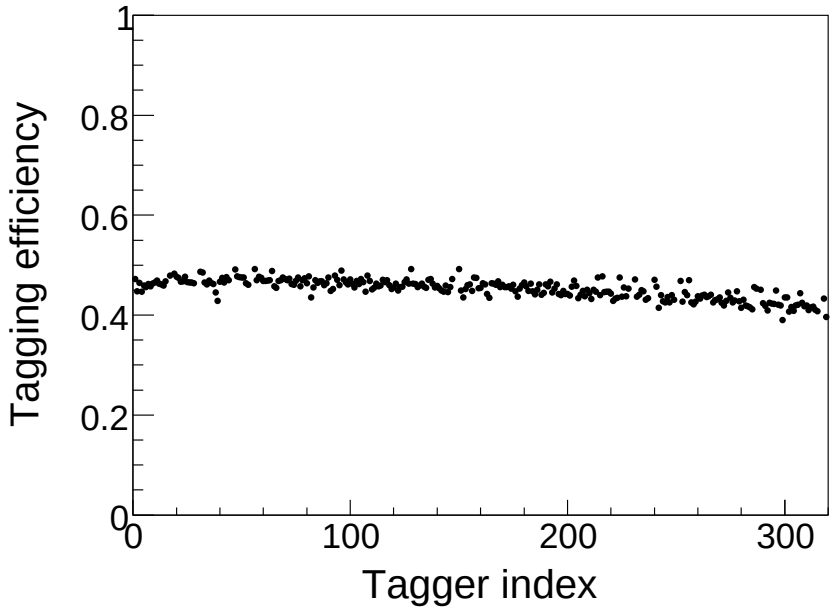

Figure 4.17: *Average tagging efficiency over all beam time.*

Chapter 5

The analysis

After all calibrations have been done, for each hit in the detector system time, deposited energy, and geometrical position are known. In the next step this information must be used to assign the detector hits to particles such as pions, recoil nucleons and photons. For this purpose different analysis tools based on time-of-flight, Δ E/E, pulse-shape-analysis, invariant mass and missing mass spectra are used. The application of these analysis steps is controlled with the help of Monte carlo simulations which take into account all features of the detection system.

5.1 Simulations

Although the detector setup covers almost the full 4π solid angle, not all events will be detected. The probability to reconstruct an event produced in the target, also called detection efficiency, is therefore never equal to one. An event could get lost either in the crystal-free beam holes in TAPS or CB, or if it does not fulfill technical requirements such as detector thresholds, trigger conditions or software analysis cuts. The detection efficiency, which is supposed to represent these effects, can depend on many variables, such as the incident photon energy, or the detected particle angle and energy.
For the extraction of absolute cross sections, it is essential to reproduce this detection efficiency for each channel to be reconstructed (see chapter VI).
To do so, one needs to simulate the experiment as closely to the reality as possible, generate fake events and analyze them. Here, contrarily to the real measured events, these fake events are exactly known. The detection efficiency

could then be easily calculated by dividing the number of analyzed simulated events by the number of the generated simulated events :

$$\epsilon(E_\gamma) = \frac{\text{Number of analyzed events}}{\text{Number of generated events}} \tag{5.1}$$

5.1.1 GEANT simulation package

The simulation of the experimental setup was done using the GEANT[1] tool. GEANT has been developed at CERN since 1974 in order to provide the precise detector simulations that almost all particle physics experiments need. Since then, GEANT has become an essential tool used worldwide in a variety of fields (nuclear, particle, and reactor physics, astrophysics..).
The GEANT simulation package consists of two parts: geometry and tracking. First, the exact geometry of the virtual setup is built including the target, detectors, different structures, cables, and electronics. The dimensions, positions and materials are also taken into account. The tracking consists in passing generated particles into the simulated detector. GEANT simulates the interaction of these particles with the traversed materials and calculates their deposited energy.
In the present work, the GEANT simulation package of the CB setup is called Cbsim and has been created together with the detector. At this time, Cbsim was based on the GEANT 3.21 version written in FORTRAN. Cbsim has been then upgraded to the new version GEANT 4 based on C++ language by the A2 collaboration and developed to fit to the present setup including TAPS, the PID and the MWPC.
More details about Cbsim development and upgrade can be found in the thesis of S. Lugert [114]. Fig. 5.1 shows a sketch of the simulated detector setup in GEANT 4.

[1] GEometry ANd Tracking.

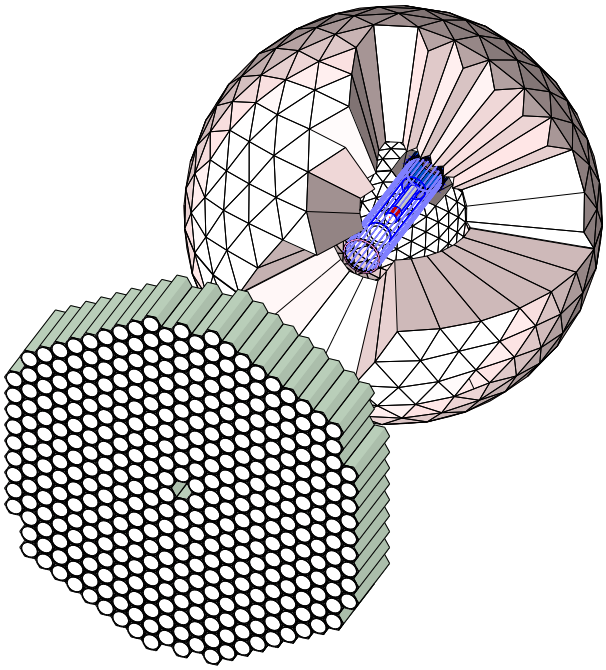

Figure 5.1: *Sketch of the detector setup simulated using GEANT4.*

5.1.2 Particle generation and reconstruction

As mentioned above, one needs to generate "fake" events depending on the studied channel and feed them through GEANT and then pass the reconstructed events through the same conditions and cuts used for the real data in order to get the analyzed events.
The event generator used in most reactions treated in this work, *Evgen*, has been first written, in FORTRAN, by D.Hornidge[2] and then developed and upgraded in the Nuclear physics group in Basel. For the $\pi\pi$ channel, the event generator package *wukin* was provided by the Giessen group and upgraded in Basel (see section 6.2).
Evgen[3] asks first the user for the different desired variables of the reaction (particles number and ID, beam energy, particle energy and angle..), computes the desired decay using GEANT routines, and stocks the decay parameters in

[2]Current location: University of Mount Allison, Sackville, New Brunswick, Canada.
[3]The event generator will be discussed in details (routines, FSI, Fermi momentum..) in Chapter VI for each studied reaction.

a Hbook file in Ntuple format. The Hbook file is then converted into a ROOT file and passed through GEANT4, which asks for the number of desired reconstructed particles and the output ROOT file. Finally, the latter is treated as real data file and the detection efficiency is calculated using the equation 5.1.
The detection efficiency will be described and plotted in the beginning of every studied reaction in chapter IV.
Note that the overall resolution in time and energy of the detectors in MC simulation were adapted in order to be similar to the real data.

5.2 Particle identification techniques

5.2.1 The clustering

A photon interacts with a crystal by creating a cascade of electron-positron pairs and bremsstrahlung photons called electromagnetic shower. The typical Molière radius[4] of such a shower is about 4.3 cm for NaI and 5.9 cm for BaF_2 which is larger than the size of the individual crystals.
The photon energy is usually deposited in a central crystal and additional neighboring crystals. Therefore the total energy of a cluster is calculated by summing the energy deposited in each crystal involved in this cluster. In the present experiment, one considers that a detector is fired when at least 5 MeV for TAPS and at least 2 MeV in CB are deposited, otherwise the crystal will not be considered for the clustering.

The total energy of a cluster was calculated by summing the energy deposited in each member of that cluster. Minimum values were set at least 20 MeV in TAPS and 20 MeV in CB in order to reduce split-offs[5].
A special clustering routine has been implemented in order to perform the clustering in an iterative way. This routine is one of the most important parts of the off-line analysis code.

[4]The Molière radius is a characteristic constant of a material giving the scale of the transverse dimension of the fully contained electromagnetic showers initiated by an incident high energy electron or photon. By definition, it is the radius of a cylinder containing on average 90% of the shower's energy deposition.

[5]Split off is an important source of background and occurs when a particle creates accidentally more than one cluster.

Once the clusters are built, the informations of the individual crystals belonging to the cluster are combined in order to reconstruct the parameters of the original particles. The energy of the particle is the sum of all the cluster crystal energies and its time is the time of the central crystal.
The position of the particle is reconstructed by taking the average of the positions of all modules in the cluster or PED[6], logarithmically weighted by their energy E_i.(cf. equation. 5.2)

$$\vec{r} = \frac{\sum_i \vec{r}_i \sqrt{W_i}}{\sum_i \sqrt{W_i}}, i = (1, .., N_{Crystal}) \tag{5.2}$$

5.2.2 Particle identification in TAPS

5.2.2.1 The time-of-flight

A particle might loose energy and slow down in the different materials that are lying in its flight path depending on its nature. Therefore, its time-of-flight, which is the time it takes to reach a detector while traveling over a known distance, can be used as a technique of identification. This technique might be used in the present analysis to distinguish between nucleons and photons in TAPS since the distance between the target and TAPS is sufficient (173.4 cm). However, the TOF technique cannot be used in CB, since the flight path is too short.

In the present experiment, the time-of-flight is given by the difference between the Tagger time (the time at which an electron hits the Tagger focal place) and the time of the cluster in TAPS. It is therefore possible to distinguish between particles in TAPS by plotting the time-of-flight versus the deposited energy in TAPS. A typical time-of-flight versus energy spectrum for TAPS is shown in Fig. 5.2 where one can clearly see the difference between photons and electrons on the lower side and protons and neutrons on the upper side.

[6]PED = Particle Energy Deposits, designs the sub-clusters.

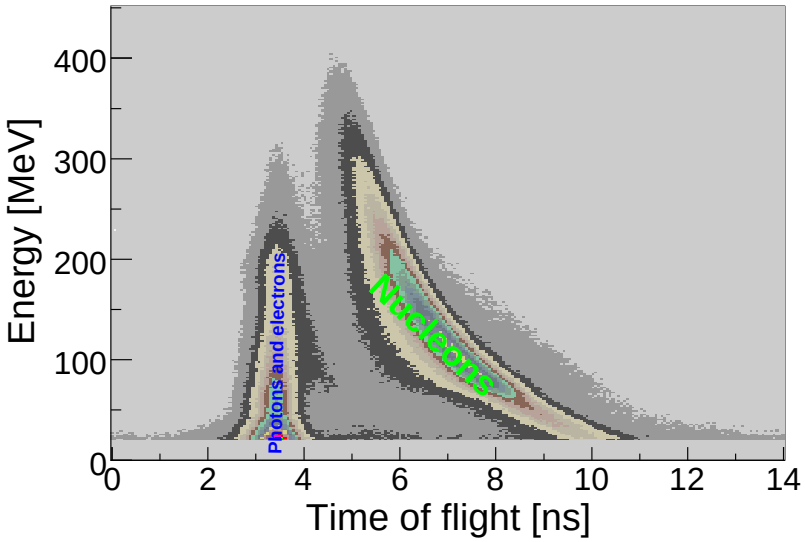

Figure 5.2: *Time difference vs. deposited energy in TAPS. One can clearly distiguish between different charged particles between nucleons and photons electrons*

5.2.2.2 The pulse shape analysis

As described in section 3.3.2, since the BaF_2 crystals have two different light components, by integrating the signal over the short and long time gate, one obtains different energy signatures depending on the nature of the incident particle. This is the principle of the pulse shape analysis used to distinguish between baryons and electromagnetic showers, in particular between nucleons and photons.

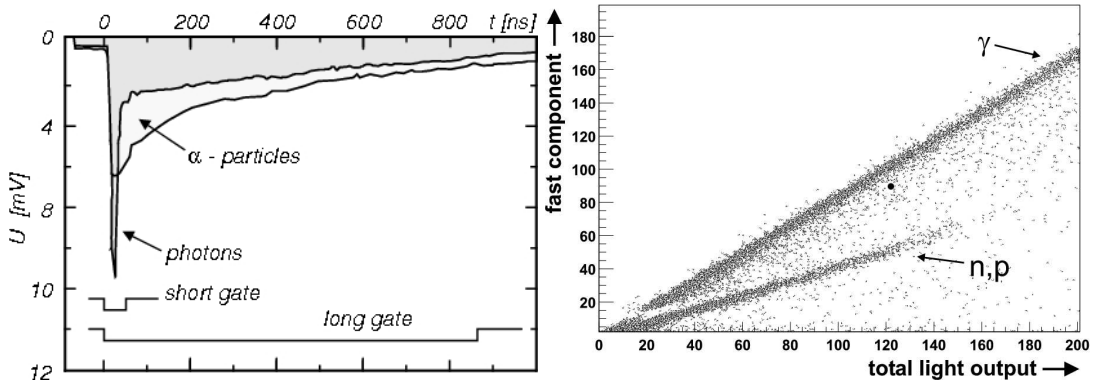

Figure 5.3: *Left: Pulse-shape signal of a γ and alpha in the BaF_2 , Right: Ratio of short (fast light) and long gate (total light).*

Fig. 5.3 shows a plot of the short gate versus long gate energy signals and the clear signature of the different particles. A calibration was made so that the photons appear on a 45° line. In practice, one uses a representation in polar coordinates.

5.2.2.3 The veto decision

As seen in chapter III, the veto wall provides a "yes or no" information to distinguish between charged and neutral particles in TAPS. A cluster will be marked as charged if the veto in front of the central crystal or any of the first ring neighbors had recorded a charged hit.

Now that one has the TOF information (which allows to distinguish between nucleons and photons) as well as the PSA information (which allows to distinguish between electromagnetic shower and baryonic particles), one can combine these informations with the veto decision in order to have a more accurate identification of the particles in TAPS.
It could happen that there is a discrepancy between TOF and PSA informations, making the nature of the particle ambiguous. In this case the event is simply ignored.

5.2.3 Particle identification in CB

5.2.3.1 The MWPC and PID tracking

The PID and the MWPC allow for an identification of charged particles in CB with a good efficiency.
On one hand, one can compare the direction of each track in the MWPC with the direction of the clusters as it is drawn in Fig. 5.4. One can estimate how probable a cluster corresponds to a charged particle by considering the maximum of the cosines of the opening angle between each track and the cluster.

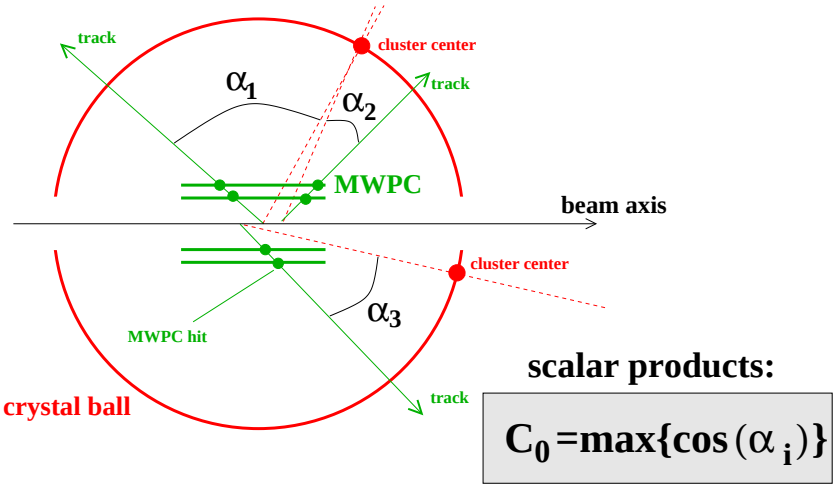

Figure 5.4: *Direction of tracks in the MWPC relative to the position of CB clusters.*

On the other hand, one can also compare the azimuthal angle Φ of each PID element which fired with the Φ angle of the clusters as it is shown in Fig. 5.5. One can estimate how probable a cluster corresponds to a charged particle by considering the minimum of the Φ difference between each PID element and the cluster.

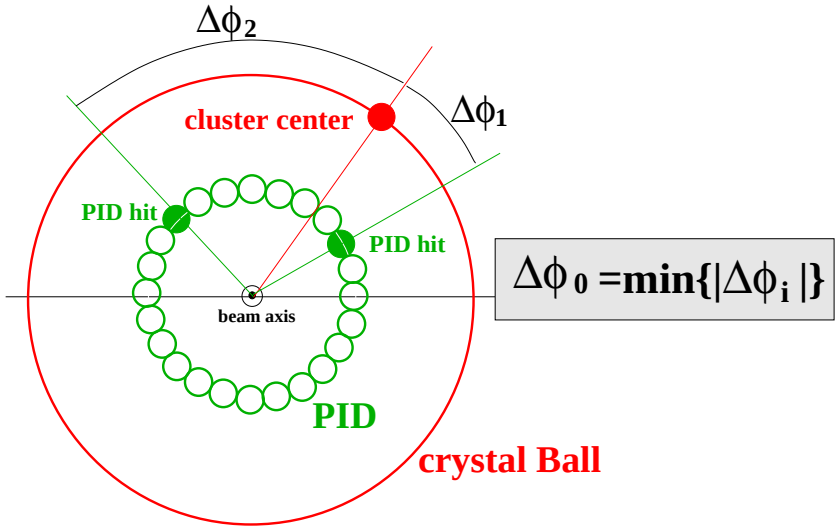

Figure 5.5: *Direction of the PID elements relative to the position of CB clusters.*

5.2.3.2 CB-PID banana cuts

The PID is the principal tool to distinguish between charged particles in the Crystal Ball. Depending on their nature, the particles deposit a certain energy in the PID scintillators before they interact with CB elements and deposit a bigger fraction of energy. A π^+ for example, which can be considered as a minimum ionizing particle, deposits around 400 keV in the PID whereas the proton can deposit from 1 up to 3 MeV. Thus, if one plots for every PID element the energy deposited in the PID against the total energy deposition in CB, one sees that the charged particles have different signatures. As seen in fig 5.6, for one PID scintillating element, protons are located in the upper zone, charged pions in the lower zone of around 400 keV and the background electrons at the lowest energies. One defines then manually a polygon cut in the analysis and in the simulation for every PID element depending on the particle one wishes to separate. This tool was the principal technique used in order to identify the charged pions in the channel $\pi^0\pi^{+/-}$ (cf. section 6.2).

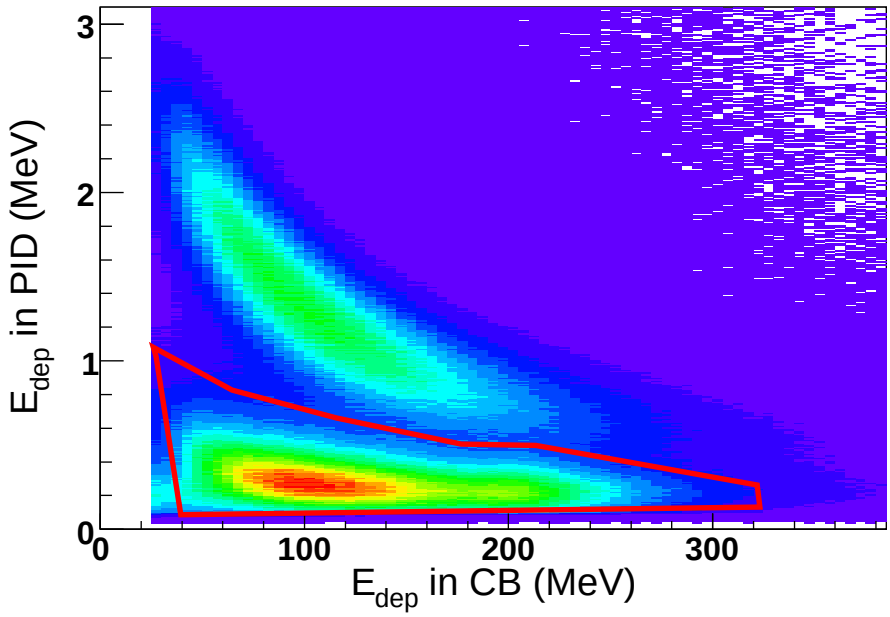

Figure 5.6: *Energy deposition in CB versus PID. Charged pions are separated from protons and electrons using a polygon cut.*

5.3 Event selection

Once the primary particles have been identified, one should be able to reconstruct the reactions and identify the secondary particles (here mesons) that decay into photons. To get a clean and clear reconstruction of those events, some special techniques, summarized in the following part, should be applied.

5.3.1 The software trigger

As seen in chapter III, in the present experiment the hardware trigger was set at a multiplicity 2 or more (two in CB or one in TAPS and one in CB) and an energy sum in CB of 50 MeV. The hardware thresholds are not very precisely known in the analysis and therefore strict conditions are used for data and simulation to be sure that the trigger conditions are correctly implemented. This is called "software trigger" and it consists of two parts:

- A new energy sum threshold is set up and it should be higher than the hardware one depending on the studied channel. In this way, one can be sure that the initial thresholds for data and simulation are taken into account and that both are above the hardware threshold.
- The multiplicity condition must be fulfilled by the registered photons alone. In other words, no other particles such as neutrons (whose energy is randomly deposited) or charged pions must contribute to the trigger. In this way, the analysis becomes cleaner especially since the simulation is much easier to do when only photons are involved in it.

Note that obviously a fraction of good events will be lost when applying the software trigger but this fraction is small in most cases and automatically corrected via the detection efficiency simulation where the same cuts are applied. The software trigger has been applied to all the physics spectra produced in each of the studied channels.

5.3.2 Random background subtraction

During the experiment, a lot of electrons are detected in the Tagger focal plane. Some of these electrons correspond to photons involved in the event under study, the other electrons do match with photons which did not contribute to

the event. One needs therefore to distinguish between the prompt photons (that are related to reactions in the production target) and random ones (those which did not interact in the target) in order to remove background caused by this effect. To do so, the difference between the time of the electron in the Tagger and the photon time detected in TAPS or in CB is calculated as explained in section 4.2.

An example of the obtained spectra is shown in Fig. 5.7 for the $\eta \rightarrow 2\gamma$ channel where a prompt peak centered around zero contains "real" coincident photons (blue region), random background underneath it (red region), and a flat remaining region related to the "pure" random background photons (green region).
To get rid of the random background, another region of the "pure background" flat area is chosen, it is then scaled by the relative widths of the prompt and the pure background regions. That gives a quantity of background equivalent to what one expects to find under the prompt peak. This process is applied to all the produced physical spectra (i.e invariant mass, missing energy, etc..) in order to get a random background free result.

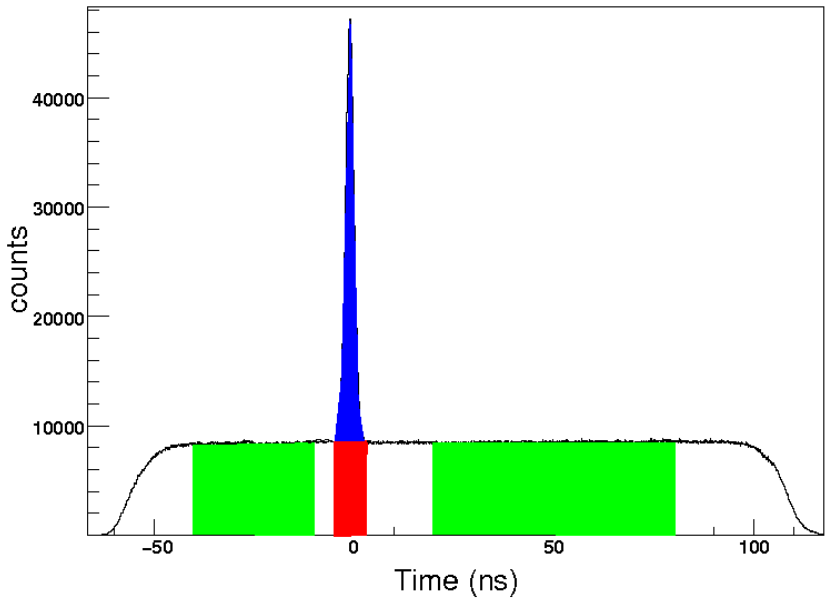

Figure 5.7: *Time difference between CB photons and Tagger electrons for $\eta \rightarrow 2\gamma$ channel. The zones used for random background subtraction are highlighted.*

5.3.3 The χ^2-test

Reactions with two photons or more could include combinational background. This background could come from the combination of photons that do not belong to the desired meson decay reaction. To get rid of the background in reactions with more than two photons, the χ^2-test is applied, based on the test of the different combinations of $\gamma\gamma$ pairs mass. Indeed, in reactions such as $\pi^0\pi^0$ (see sect. 6.2), one can combine photon pairs in different ways and the χ^2-test serves the purpose of finding the best solution.

The χ^2-test is defined by:

$$\chi^2 = \sum_{i=1}^{n_{\gamma\gamma}} \left(\frac{m_{\gamma\gamma}^{th} - m_{\gamma\gamma,i}^{exp}}{\Delta m_{\gamma\gamma,i}^{exp}} \right)^2 \tag{5.3}$$

where :

- $m_{\gamma\gamma}^{th}$ corresponds to the π^o-meson or/and $\eta-$meson mass.
- $m_{\gamma\gamma}^{exp}$ is the experimental $\gamma\gamma$-pair mass given by[7] : $m_{\gamma\gamma}^{exp} = \sqrt{2E_1E_2 \cdot (1 - \cos\phi_{12})}$
- $\Delta m_{\gamma\gamma}^{exp}$ is the uncertainty of the measured $\gamma\gamma$-pair given by:

$$\Delta m_{\gamma\gamma}^{exp} = \tfrac{1}{2} m_{\gamma\gamma}^{exp} \left(\tfrac{\Delta E_1}{E_1} + \tfrac{\Delta E_2}{E_2} - \tfrac{\Delta cos\phi_{12}}{1 - cos\phi_{12}} \right)$$

where :

$\Delta cos\phi_{12} = sin(\theta_1)cos(\theta_2)(cos(\phi_1 - \phi_2) - 1)\Delta\theta_1$
$+ cos(\theta_1)sin(\theta_2)(cos(\phi_1 - \phi_2) - 1)\Delta\theta_2$
$- sin(\theta_1)sin(\theta_2)sin(\phi_1 - \phi_2)(\Delta\phi_1 - \Delta\phi_2)$
$- sin(\theta_1 - \theta_2)(\Delta\theta_1 - \Delta\theta_2)$

Where ϕ_{12} is the azimuthal opening angle between the two photons and θ_1 and θ_2 are their polar angles in lab.

[7] $M_{inv} = \sqrt{\mathbf{P}^2} = \sqrt{(\mathbf{P}_1 + \mathbf{P}_2)^2} = \sqrt{\mathbf{P}_1^2 + \mathbf{P}_2^2 + 2\mathbf{P}_1\mathbf{P}_2}$
with for photons: ${\mathbf{P}_1}^2 = {\mathbf{P}_2}^2 = {M_\gamma}^2 = 0$

The best combination corresponds to the lowest χ^2. Once the best combination is selected, the $\gamma\gamma$-pair masses are constrained to the theoretical value.

For example, for the : $\eta \to \pi^o\pi^o\pi^o \to \gamma\gamma\gamma\gamma\gamma\gamma$ channel, equation 5.5 becomes

$$\chi^2 = \left(\frac{m^{th}_{\pi^o} - m^{exp}_{\pi^o,1}}{\Delta m^{exp}_{\pi^o,1}}\right)^2 + \left(\frac{m^{th}_{\pi^o} - m^{exp}_{\pi^o,2}}{\Delta m^{exp}_{\pi^o,2}}\right)^2 + \left(\frac{m^{th}_{\pi^o,3} - m^{exp}_{\pi^o,3}}{\Delta m^{exp}_{\pi^o,3}}\right)^2 \tag{5.4}$$

which is evaluated for all possible combinations of six photons to three π^0 - mesons.

5.3.4 The invariant mass analysis

Most of the neutral mesons can be identified only through their photon decay products. When a meson decays, its four-vector is conserved. By applying the principle of energy and momentum conservation, the four-vector of the meson can be reconstructed by summing the four-vectors of the decay photons and the meson can be identified and reconstructed via an invariant mass analysis. For example, in the case of a π^0 or an η which decays into two photons, if $\mathbf{P}$ is the four-vector of the meson and $\mathbf{P}_1$ and $\mathbf{P}_2$ are the four-vectors of the two photons :

$$M_{inv} = \sqrt{2\mathbf{P}_1\mathbf{P}_2} = \sqrt{2E_1E_2.(1 - cos\phi_{12})} \tag{5.5}$$

where E_1 and E_2 being the energies of the two photons and ϕ_{12} is the opening angle between them.
Fig. 5.8 shows the invariant mass of two photons. Two peaks can be seen, a first around 135 MeV corresponds to the π^0 and a second one around 547 MeV correspond to the η.

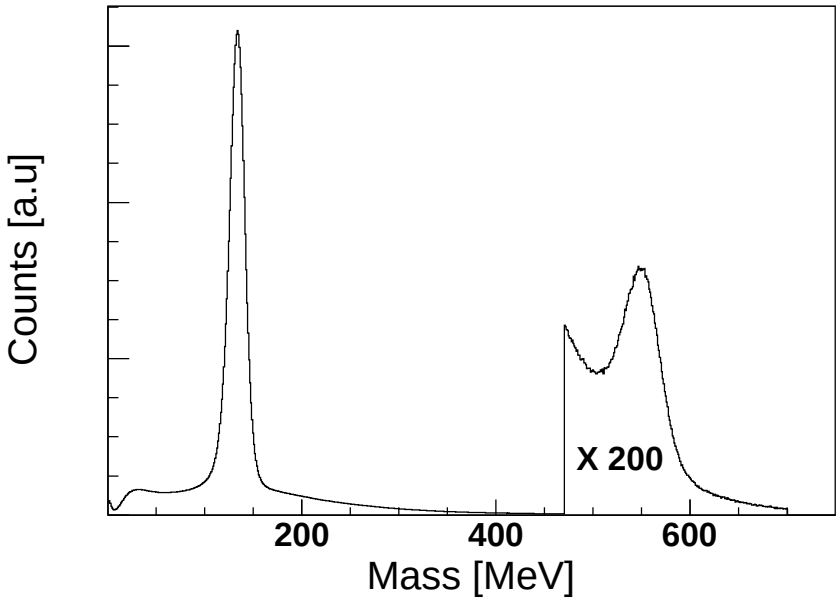

Figure 5.8: *Invariant mass of photon pairs, π^0 and η peaks can be seen, plus background coming from combination of uncorrelated photons*

5.3.5 The missing mass and missing energy principle

The missing mass analysis

The missing mass technique is used to test events for particles that have escaped detection. For this purpose the difference of the initial and final state four-vectors is computed and its magnitude is interpreted as the mass of the missing particle. If no particle or only a photon is missing its value is zero, if one massive particle is missing in the final state the missing mass equals the mass of that particle. If two or more particles are missing, the missing mass is a broad distribution.

For example, the missing mass analysis could be a good tool to remove background of the competitive channel $\gamma N \rightarrow \eta N \rightarrow \pi^0\pi^0\pi^0 N$ from which the reaction $\gamma N \rightarrow \pi^0\pi^0 N$ could suffer. Indeed, if one π^0 from the second reaction gets lost, only four gammas will be detected and could be identified as $\pi^0\pi^0$ event. So the reaction is $\gamma N \rightarrow \eta N \rightarrow \pi^0\pi^0\pi^0 X$ where X is not detected. If

one applies the conservation rules (supposing the nucleon is at rest inside the nucleus) :

$$\mathbf{P}_X = \mathbf{P}_\gamma + \mathbf{P}_N - \mathbf{P}_{\pi_1^0} - \mathbf{P}_{\pi_2^0} \tag{5.6}$$

The missing mass of X is therefore :

$$m_X = \sqrt{(\mathbf{P}_\gamma + \mathbf{P}_N - \mathbf{P}_{\pi_1^0} - \mathbf{P}_{\pi_2^0})^2} \tag{5.7}$$

if m_X is the mass of a nucleon, this is a good event for $\gamma N \rightarrow \pi^0\pi^0 N$, if not, this is a bad event of, for example $\gamma N \rightarrow \gamma\eta \rightarrow \pi^0\pi^0\pi^0 N$ where the undetected part X is a pion plus a nucleon.
The initial nucleon is actually not at rest as it is part of the lithium nucleus, which is at rest, so it has a Fermi momentum. This effect broadens the missing mass of the non-light nuclei, in contrast to a hydrogen target for example. One still can use the missing mass technique but the separation of background is less efficient as without Fermi motion.

The missing energy analysis

The missing energy principle is similar to the missing mass: compare the energy of a detected particle to the value determined from over determined reaction kinematics and calculate the difference in order to identify a reaction. In this work, the missing energy principle was essential in order to identify the coherent reactions. The missing energy of a meson in the center of mass, in case of a coherent process is :

$$E_{miss} = E_{meson}^{CM,\text{meas}} - E_{meson}^{CM}. \tag{5.8}$$

where :

$$E_{meson}^{CM} = \frac{\mathrm{s} + M_{meson}^2 - M_{^7Li}^2}{2\sqrt{s}}, \tag{5.9}$$

with s the squared available CM energy :

$$s = 2 \cdot E_\gamma M_{^7Li} + M_{^7Li}^2, \tag{5.10}$$

and E_γ the energy of the incoming photon.
The measured energy in the Center of mass frame is :

$$E_{meson}^{CM,\text{meas}} = \gamma \left(E_{meson}^{\text{lab}} - p_\gamma \cdot \beta \cdot \cos(\theta_{meson}^{lab}) \right), \tag{5.11}$$

with

$$\vec{\beta} = \frac{E_\gamma}{E_\gamma + M_{^7Li}} \cdot \vec{e_z}, \tag{5.12}$$

$$\gamma = \frac{E_\gamma + M_{^7Li}}{\sqrt{s}}, \tag{5.13}$$

θ_{meson}^{lab} and E_{meson}^{lab} being the laboratory polar angle and energy of the meson respectively.

In a missing energy spectrum, coherent processes give a peak around zero. Breakup events give a contribution at negative missing energies. Because of Fermi motion, a coherent peak would be mixed with the breakup peak and therefore cannot be easily distinguished.

Chapter 6

Results and discussion

In the previous chapter, the different techniques and procedures used to identify reactions and remove background have been discussed. The simulations used to calculate the detection efficiencies have been introduced. In this chapter the results of the reactions investigated in this work will be presented and compared to the existing ones and possibly, compared to theoretical predictions.

For each studied channel, the general procedure was similar. First, the channel is identified as well as the possible sources of background. The signal and the background are estimated and reproduced by Monte-Carlo simulations. The detection efficiencies are then calculated. Finally the differential and total cross sections are extracted.

As seen in chapter II, the following table summarizes the motivation of the studied reactions in this work.

Channel	motivation
$\gamma +^7 Li \rightarrow \pi^0 +^7 Li$	Δ-resonance, ^{7}Li form factor and mass-radius
$\gamma +^7 Li \rightarrow \pi\pi + X$	in medium behavior of $\pi\pi$ pairs and σ meson
$\gamma +^7 Li \rightarrow \eta +^7 Li$	coherent η photoproduction and η-mesic nuclei

Table 6.1: *Reminder of the investigated channels in the present work*

6.1 The cross section

The differential cross section can be expressed as function of any important observable (angle, mass..) depending on the studied reaction. The angular distribution is given by the following formula :

$$\frac{d\sigma}{d\Omega}(E_\gamma,\theta) = \frac{N(E_\gamma,\theta)}{\epsilon_\gamma \cdot (E_\gamma) \cdot \rho \cdot N_{scaler} \cdot (E_\gamma) \cdot \Delta\Omega \cdot \Gamma_m \cdot \epsilon_r(E_\gamma,\theta)} \tag{6.1}$$

Where :

- N is the number of events detected of the desired reaction at a given energy E_γ and in a solid angle $\Delta\Omega$ cell at an angle θ . (θ is the polar angle in the center-of-momentum system of the incident photon beam and the target).
- ϵ_γ is the tagging efficiency for that E_γ.
- ρ is the target number surface density given by :

$$\rho = \frac{N_A \cdot \rho_{Li} \cdot l_{target}}{A_{Li}} = 2.64 \cdot 10^{23} nuclei/cm^2 \tag{6.2}$$

  With :
  N_A is the Avogadro number ($N_A = 6.022136.10^{23}$ mol^{-1}),
  ρ_{Li} is the lithium target density (ρ_{Li} =0.534 g/cm^3),
  l_{target} is the target length (l = 5.7 cm) and,
  A_d is the atomic weight (A_{Li} = 6.941 g/mol).

- N_{scaler} is the number of Tagger scaler counts.
- $\Delta\Omega$ is the solid angle of the angular bin [sr].
- Γ_m is the branching ratio of the decay.
- ϵ_r is the reaction detection efficiency in a (E_γ,θ) cell.

ϵ_r is obtained by comparing the initial number, N started, created in the simulation with the number of detected events, N detected, after the analysis:

$$\epsilon_r = \frac{N^{detected}}{N^{started}} \tag{6.3}$$

The total cross section is then obtained by integrating the differential cross section :

$$\sigma = \frac{N(E_\gamma)}{\epsilon_\gamma \cdot (E_\gamma) \cdot \rho \cdot N_{scaler}(E_\gamma) \cdot \Gamma_m \cdot \epsilon_r(E_\gamma)} \tag{6.4}$$

$$\sigma = \int \frac{d\sigma}{d\Omega}(E_\gamma, \theta) d\Omega \sim 2\pi \sum_{\theta\ bin} \frac{d\sigma}{d\Omega}(E_\gamma, \theta) sin\theta \Delta\theta \tag{6.5}$$

The total cross section can be obtained as well by using the formula :

$$\sigma = \frac{N_X}{N_{e^-} \cdot \epsilon_{tagg} \cdot \epsilon_{det} \cdot N_{target} \cdot \Gamma_{X \to Y}} \tag{6.6}$$

where N_X is the absolute number of reconstructed events, N_{e^-} is the number of electrons measured by the Tagger and the denominator factors allow the normalization of σ to the conditions of the experiment.

6.2 The double pion photoproduction off lithium

As discussed in chapter II, models predict the existence of an in medium effect of the σ -meson, which consists of a shift towards small invariant masses in its decay channel $\pi^0\pi^0$. The higher the mass of the investigated nucleus, the more significant this shift is expected to be. Since the σ meson is not supposed to decay into $\pi^0\pi^{+/-}$, an efficient tool to investigate this in medium effect would be to compare the mass distributions of the neutral channel to the mixed charged ones for different nuclei.

The analysis will combine two separate parts. The first part consists in the analysis of the neutral channel and the mixed charged channel for ^{7}Li. The comparison of the two results will establish or rule out a different behavior of this channels. The second part of the analysis -and the most important- will consist in comparing the mass distributions of ^{7}Li and the heavy targets. However, in the present work, only results from ^{7}Li will be presented as results from the heavy targets[1] were not yet ready when writing this thesis. A final analysis followed by a common publication is expected to follow.

The analysis should be made for fine incident photon energy bins and close to the threshold in order to minimize the FSI effects. In the present work, two incident photon beam energy bins have been selected to show in details the obtained invariant mass distributions: [400-460] (the usual E_γ range used in the previous work) and [460-520] MeV. In order to minimize the FSI and get closer to threshold, the E_γ = [300-400] MeV range will be investigated as well but with much lower statistics.

For both channels, the reaction identification will first be presented. The MC event generator and the detection efficiency will then be shown. Mass distributions will be plotted for the different E_γ ranges then normalized in order to obtain the ratio of the two channels. Finally, mass distributions will be integrated over the whole incident photon beam energy range in order to get the total cross section which will be compared to existing results from Deuterium, Calcium and Lead.

[1] Data of C, Ca and Pb are under analysis at University of Giessen, Germany.

6.2.1 The neutral channel

6.2.1.1 The reaction identification

In order to identify the reaction, the quasi-free inclusive channel was studied where three cases were taken into account and combined :

case	**Relative contribution**
$\gamma +^7 Li \rightarrow \pi^0\pi^0 + (pn)$	50.26%
$\gamma +^7 Li \rightarrow \pi^0\pi^0 + p(n)$	28.1%
$\gamma +^7 Li \rightarrow \pi^0\pi^0 + n(p)$	21.64%

Table 6.2: *Cases considered and combined in the neutral channel and their relative contributions. Particles in brackets are not detected.*

For the first case, events with four photons were accepted, for the second four photons and one proton and for the third four photons plus an additional neutral hit. In each case, the best combinations of two photon pairs were selected using a χ^2-test (see sect. 5.3.3). The nominal mass of the pion was then used to improve the experimental resolution by recalculating the pion momenta using:

$$\mathbf{P}' = \mathbf{P}\frac{m_{th}}{m_{\gamma\gamma}} \tag{6.7}$$

where $m_{\gamma\gamma}$ refers to the measured invariant mass and m_{th} to the theoretical value of π^0 mass.

The obtained pion four vectors were then added up. In the following, a cut on each π^0 mass between 110 and 160 MeV was applied.

Fig. 6.1 and 6.2 show the invariant mass of the pions in a 3D-plot and 2D-plot.

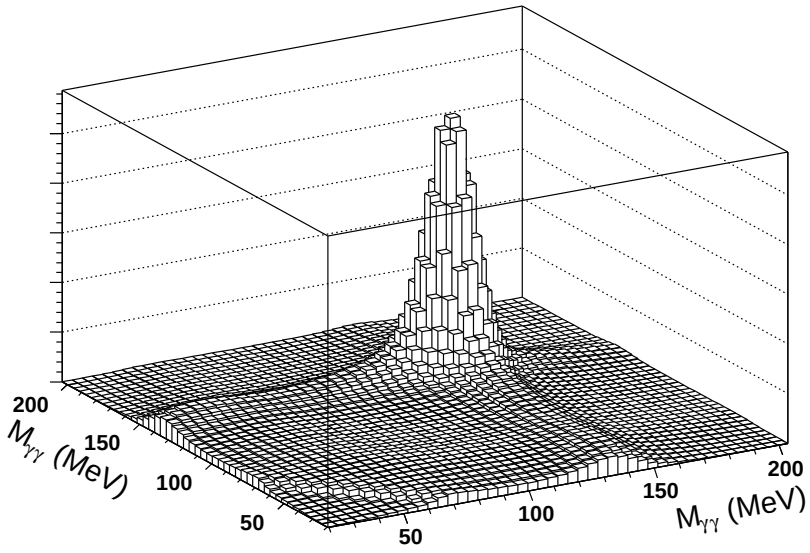

Figure 6.1: *Invariant mass distribution of two pions.*

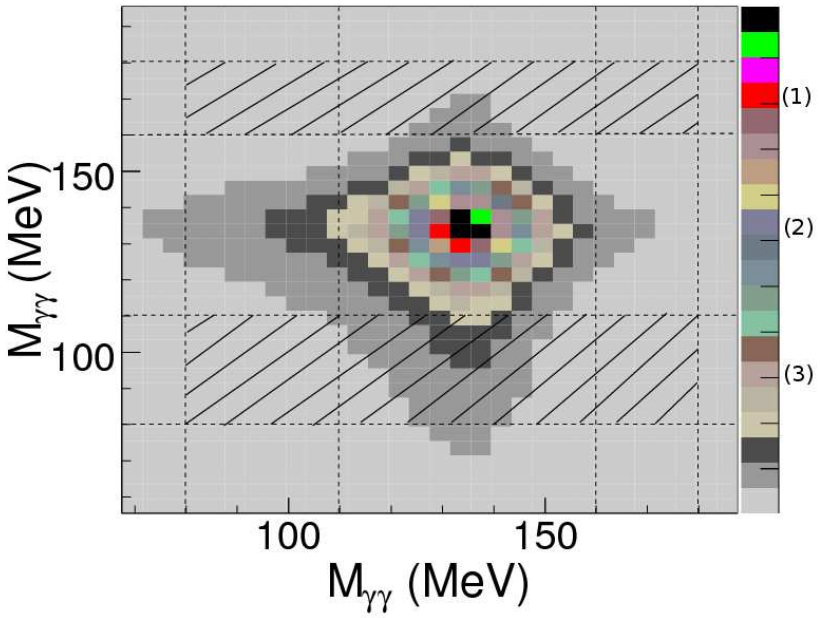

Figure 6.2: *Side bin signal to be removed from the hatched areas.*

In order to extract the mass distributions the number of $\pi^0\pi^0$ "good" events

(i.e background removed and signal extracted) must be estimated. For this purpose, in addition to the cuts between 110 and 160 MeV applied on each π^0 invariant mass, an additional so-called "side bin" background had to be removed from the hatched areas shown in Fig. 6.2 where the pion masses are plotted one against the other. In other words some ”fake signal“ is sitting below (region 1) and above (region 2) the area where the $\pi\pi$ signal is supposed to be (region 3). The side bin region have been defined so that it is equal to the signal region[2]. This fake signal has been then subtracted from the true signal.

Despite this treatment, an additional combinational background is still sitting under the pion peaks. It has been eliminated by fitting the pions invariant masses using a *Gaussian + polynomial* function. This was done for each bin in the $M_{\pi\pi}$ invariant mass distributions. An example of the fitting procedure is shown in Fig. 6.3 for one single bin of $M_{\pi\pi}$ for a defined E_γ range. The signal has been estimated by integrating the Gaussian distribution between 110 and 160 MeV.

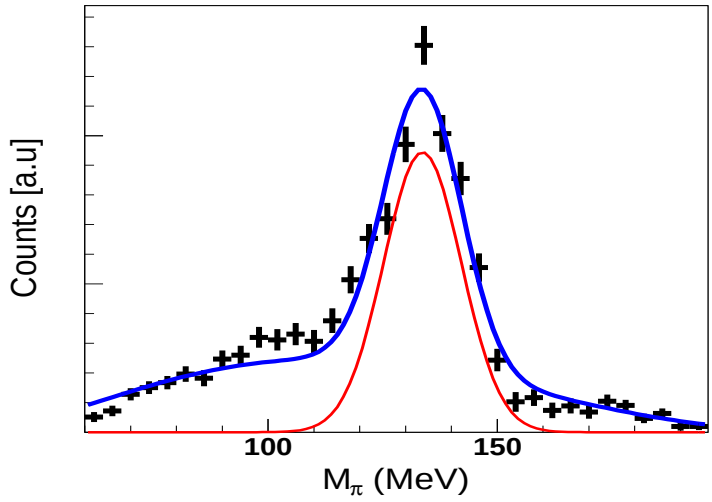

Figure 6.3: *Example of fit for E_γ = [400 - 460] MeV. The (signal + background) was fitted by (Gauss + pol4) function (blue histogram). The integral of the Gaussian (red) represent the signal corresponding to one point of the mass distribution.*

However, the obtained mass distributions would fluctuate due to the fits. To minimize these fluctuations, the position and the width of the Gaussian have been plotted versus $M_{\pi\pi}$ fitted using a *polynomial* as shown in Fig. 6.4. The signal was then recalculated using the same *Gaussian + polynomial* function

[2]Region (1) has 30 MeV + Region (2) has 20 MeV = Region (3) which has 50 MeV.

but with fixed parameters extracted from the fits of the *Gaussian* width and position.

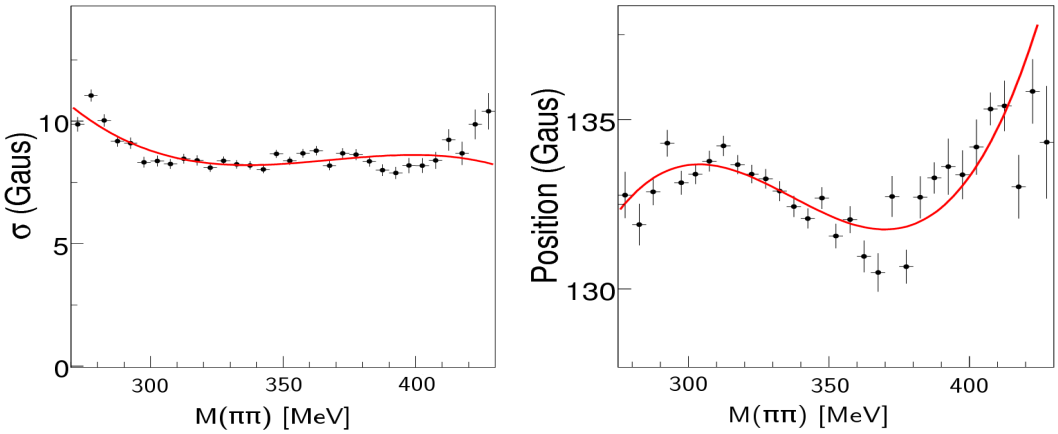

Figure 6.4: *The width (left) and the position (right) of the Gaussian have been fitted in order to minimize the fluctuations.*

An additional possible source of combinational background is the reaction $\eta \rightarrow \pi^0\pi^0\pi^0$. This background is non existing below the η production threshold (570 MeV) and increases with increasing E_γ. However, due to the large solid angle coverage of the detectors ($\sim$98%), this background is very small as shows the comparison between data and simulation in Fig. 6.5 (the $\pi\pi$ simulation will be presented in the next paragraph) and it only matters at high energies. Therefore no cuts have been applied.

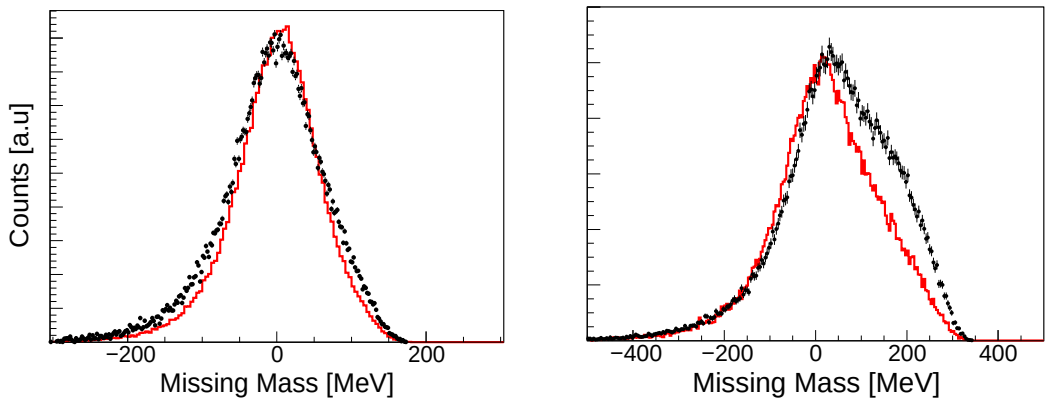

Figure 6.5: $\pi^0\pi^0$ *missing mass for data (points) and simulation (red histogram). Left: at* E_γ *= 550 MeV (below* η *production threshold) Right: at* E_γ *800 MeV (above* η *production threshold) .*

6.2.1.2 Channel simulation and detection efficiency

Two reactions have been simulated using the GEANT4 simulation package :

- $\gamma +^7 Li \rightarrow \pi^0\pi^0 + p(n)$
- $\gamma +^7 Li \rightarrow \pi^0\pi^0 + n(p)$

The event generator produced four photons in the final state from the decay of two neutral pions. The initial state was an incident photon of a given energy in the z-axis direction and a nucleon at rest. Theoretical four-momenta of the incident photon and the target nucleon were added up and three particles (two π^0 and one nucleon) were produced by the GEANT routine GDECA3 in the center of momentum. The produced particles were after that boosted into the lab frame. The same routine GDECA3 was then used for the decay of each π^0 into two photons. The event generator simulated the FSI in a special routine *nFSI*:

$$nFSI(pos, radnuc, dismfp, disfer, \mathbf{P}_{\pi^0}, M_{\pi^0}) \tag{6.8}$$

The FSI routine is described in the following:

Depending upon the radius of the nucleus (radnuc), a π^0 is generated at a position (pos) of coordinates (x,y,z) uniformly chosen in the nucleus. The pion will then travel a path length obtained from its decay width. The resulting position is returned to the calling program, which corresponds to the initial position of the pions.

Given the kinetic energy of the pion, the mean-free path (dismfp) is taken from another program and the traveling path L of the pion is calculated. The pion will then travel a distance L from (x, y, z) to $(x^{'}, y^{'}, z^{'})$. For this new position it is checked whether the pion is outside or inside the nucleus. In case it is outside, no FSI interaction will occur and the function returns. In case the pion is inside the nucleus the FSI occurs according to the reaction $\pi^0 + N \rightarrow \pi^0 + N$ (Phase-Space). The momentum of the initial nucleon (disfer) is chosen from the Fermi distribution shown in fig 6.6 [117]. The Delta mass is also taken from a distribution. The function returns how often the pion has rescattered and uses the GEANT routine GENBOD to simulate interaction with

the nucleon. Finally, it boosts the pion momenta into lab, thereby replacing the old momenta $\mathbf{P}_{\pi^0}$. It neglects effects on the nucleon.

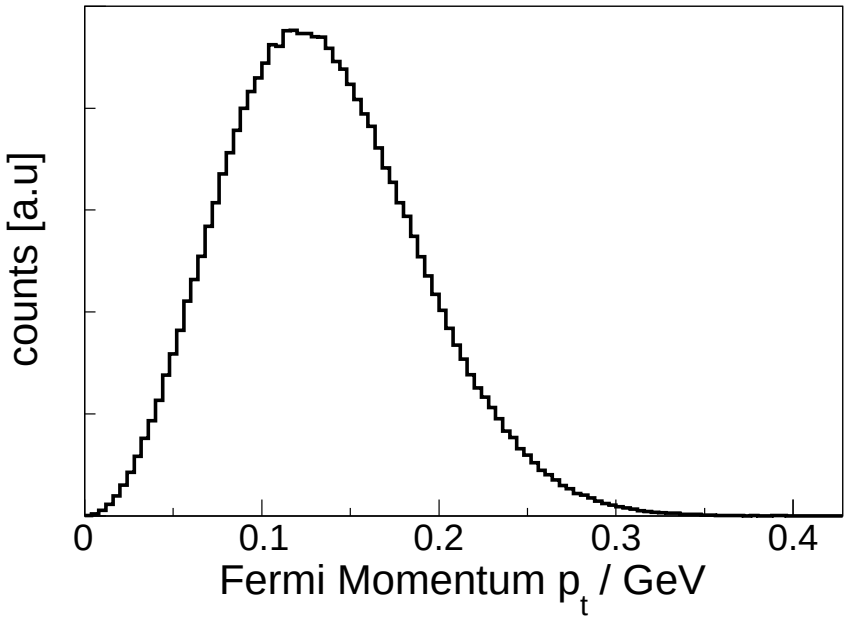

Figure 6.6: *Fermi momentum distribution of nucleons in the ^{7}Li nucleus used for the simulation of $\pi\pi$ events [117].*

The final state of four photons and one nucleon is then sent to GEANT to be tracked in the simulated detector setup and the obtained output is of the same kind as for a real event.

Data and simulation have been analyzed using the same program, including the same cuts and steps leading to the identification and the reconstruction of a $\pi\pi$ (time and invariant mass cuts , software trigger..). Fig. 6.7 shows the invariant mass distribution of the simulated events for E_γ = [400 - 460] MeV. The simulated events will be classified in this way: The events originally produced by the event generator are called *start events*. For events that have been tracked with GEANT and passed all reconstruction steps and analysis cuts one distinguishes two different types: *tracked events* are those which have passed the analysis as detected events, but for all particles the four vectors generated by the event generators are kept. *Reconstructed events* are those where in addition the four-vectors have been taken from the analysis. This means *tracked events* correspond to detected events ignoring effects from detector resolution for the final state four-vectors.

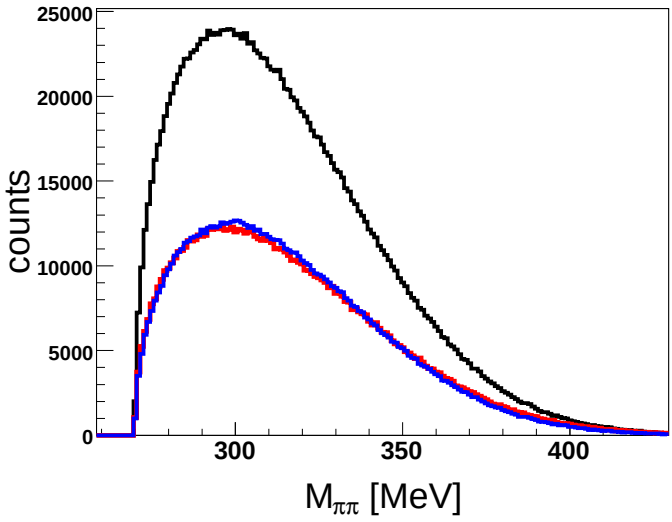

Figure 6.7: *Invariant mass distribution of simulated events for E_γ = [400 - 460] MeV. In black the start distribution, in blue the distribution of the tracked events and in red the distribution of the reconstructed events.*

In order to check the quality of the simulations, the invariant mass of one of the two π^0 has been plotted and the background has been fitted using a *polynomial* and added to the simulated line shape. The agreement is good as seen in Fig. 6.8 where the applied cut is also shown.

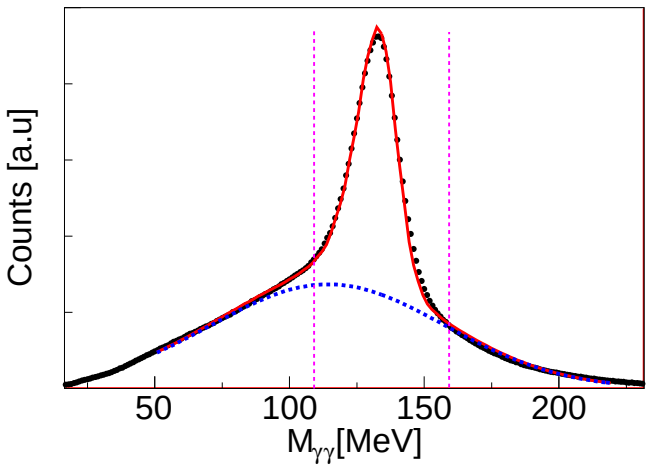

Figure 6.8: *The Invariant mass of one of the two pions is plotted to crosscheck the simulations: Background (blue) was fitted using a polynomial and added to simulated line shape and the sum (red) is compared to data (black points). The applied cut can be seen (dashed lines). E_γ = [400 -460]*

In order to compute the invariant mass distributions, the detection efficiency has been calculated using eq. 5.1. It has been calculated in two ways: using the tracked events and using reconstructed events as shown in Fig. 6.9 and plotted as function of the invariant mass of the $\pi\pi$ pairs for the two E_γ ranges. The difference between both detection effeciencies arise from the detector resolution limitations. By using the efficiency calculated using the reconstructed events, the detector resolution effects are partly corrected.

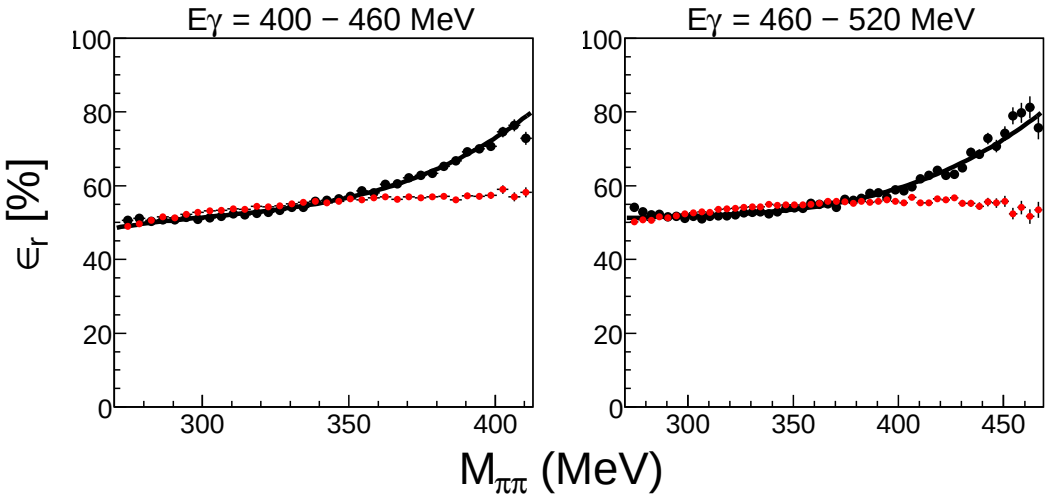

Figure 6.9: *Neutral efficiency vs $M_{\pi\pi}$ invariant mass for different E_γ for reconstructed events (black) and tracked events (red). The detector resolution effects are corrected by using the black one.*

The detection efficiency has been plotted as well as function of the incident photon beam energy as shown in Fig. 6.10.

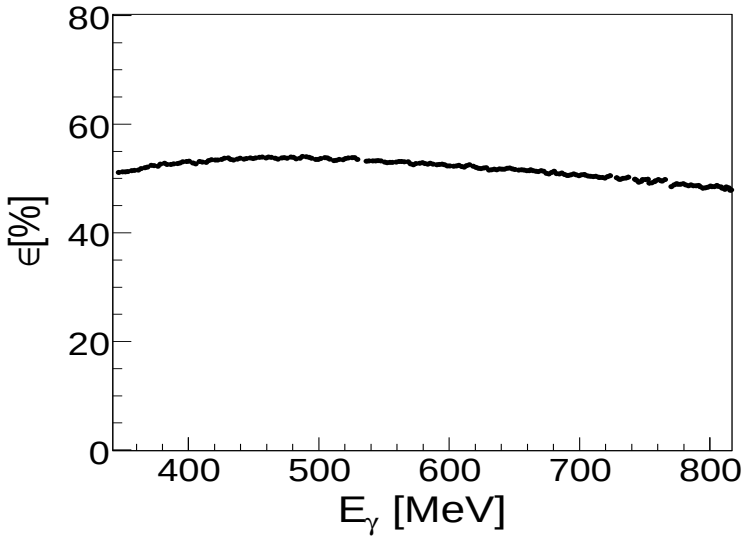

Figure 6.10: *Neutral efficiency vs incident photon beam energy.*

6.2.1.3 The cross sections

Neutral mass distributions were obtained by applying the equation 6.1 and plotted in Fig. 6.11 for the energy ranges [400 - 460] MeV and [460 - 520] MeV.

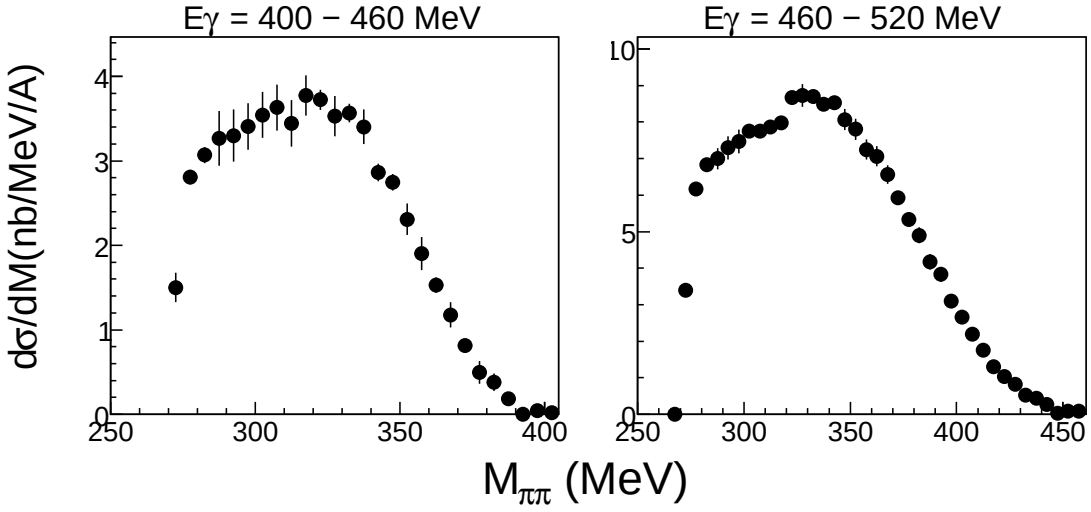

Figure 6.11: *Neutral mass distributions.*

The total $\pi^0\pi^0$ cross section was obtained by integrating the mass distributions over the whole E_γ range. The obtained total cross section is plotted in Fig. 9.1a.

It has been normalized to $A^{2/3}$ to be compared to the Calcium and deuterium cross sections from [14], as seen if Fig. 9.1b. The region of interest (E_γ < 500 MeV) is plotted in Fig. 6.13.

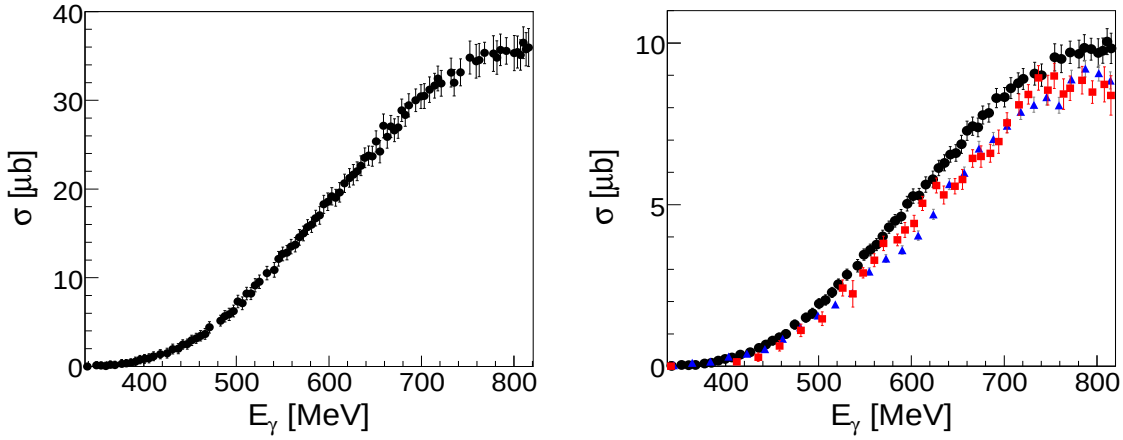

Figure 6.12: *Left: Neutral total cross section. Right: Total cross section normalized to $A^{2/3}$ compared to Calcium (blue triangles) and deuterium (red squares).*

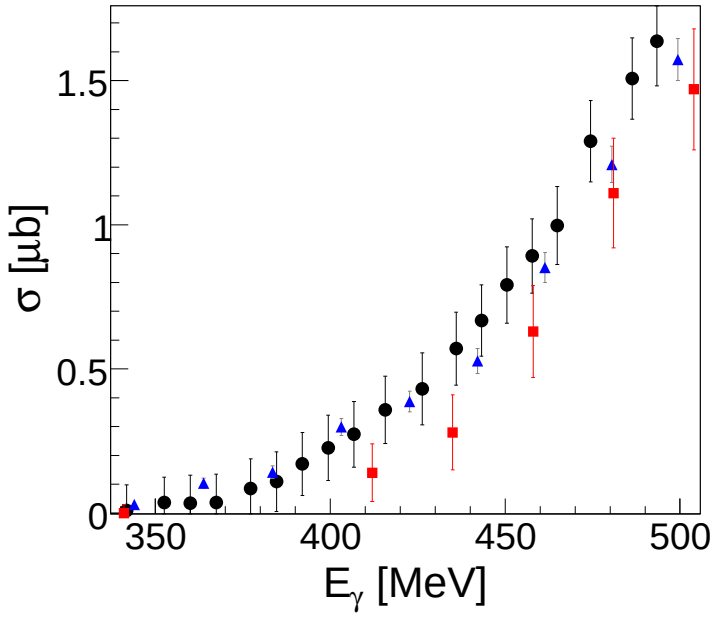

Figure 6.13: *Total cross section normalized to $A^{2/3}$ compared to Calcium (blue triangles) and deuterium (red squares) for E_γ up to 500 MeV .*

6.2.2 The mixed charged channel

6.2.2.1 The reaction identification

For the mixed charged channel, the quasi-free inclusive channel has been studied where three cases were taken into account:

case	**Relative contribution**
$\gamma +^7 Li \rightarrow \pi^0\pi^{+/-} + (pn)$	49.34%
$\gamma +^7 Li \rightarrow \pi^0\pi^{-} + p(n)$	32.53%
$\gamma +^7 Li \rightarrow \pi^0\pi^{+} + n(p)$	18.13%

Table 6.3: *Cases considered and combined in the mixed charged channel and their relative contributions. Particles in brackets are not detected.*

For the first case, events with two photons and one charged pion were accepted, for the second case two photons, one charged pion and one proton and for the third case two photons, one charged pion and one additional neutral hit. In the two first cases, the neutral pion was reconstructed by adding up the four-vectors of the two photons. In the third case with three neutral hits (π^0 decay photons and a neutron) the best combination of a photon pair was selected using a χ^2-test. The neutral pion momentum was constrained using eq. 6.7 to improve the experimental resolution.

The charged pion has been identified using the polygon cut in the $E - \Delta E$ spectra (PID versus CB) as explained in Fig. 5.6. The momenta of the neutral and the charged pions were then added up.

In the following a cut between 110 and 160 MeV has been applied on the π^0 invariant mass in order to remove a part of the combinational background (see Fig. 6.21 and sect. 6.2.2.3).

Since a charged pion is more difficult to identify than a neutral one, an additional important background had to be removed before computing the mass distributions. The principal source of background was related to the events where a proton is miss-identified as a charged pion (the reaction $\gamma p \rightarrow \pi^0 p$) and was mostly removed using the missing mass principle. This miss-identification is due to the overlapping between the protons and the charged pions in the "banana" cuts (Fig. 5.6). This background is important at low energy, close to

the $2\pi^0$ production threshold as the single pion cross section is large compared to the double pion cross section. Fig. 6.14 shows the π^0 missing mass for two incident beam energies, E_γ = [400 - 460] and [800 - 820] MeV and after subtraction of the nucleon mass. A missing mass analysis was therefore made for the hypothesis $\gamma N \rightarrow \pi^0 p$. The peak of the background is located around 0 and the one at large missing mass correspond to the signal. The broadening of the background is due to the Fermi smearing[3]. Requesting this missing mass to be higher than 140 MeV highly improves the agreement between data and simulation.

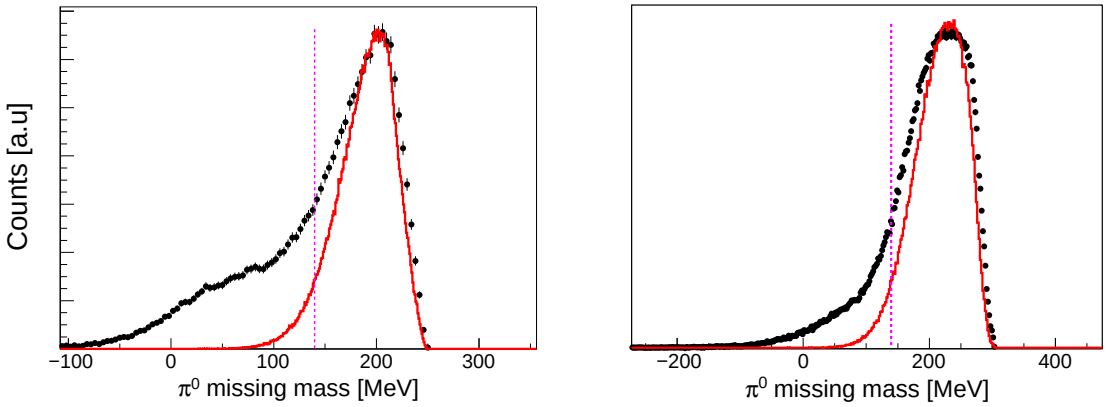

Figure 6.14: *π^0 Missing mass spectra for E_γ = [400 - 460] (left) and [550 - 600] MeV (right) after subtraction of the nucleon mass. The solid curve is a simulation of $\pi^0\pi^{+/-}$ (see next paragraph) and the points are experimental data. Events with a π^0 missing mass smaller than 140 MeV are assumed to be background due to events where a proton is miss-identified a charged pion.*

Further background due to the reactions where the detected $\pi^0\pi^{+/-}$ belong to another channel and where one or more other particles have not been identified had to be removed. Fig. 6.15 shows the correspondent missing mass spectra at E_γ = [400 - 460] and [800 - 820] MeV after application of the first π^0 missing mass cut. Requesting the $\pi^0\pi^{+/-}$ missing mass to be larger than -80 MeV (after subtracting the nucleon mass) removes an important part of this background in an efficient way.

A typical background in this case could be related, at high photon energies, to the reaction $\eta \rightarrow \pi^0\pi^+\pi^-$ but it is completely suppressed by these missing mass cuts .

[3]In the case of a H target for example, in the same missing mass analysis, the background and the signal are clearly separated (See [103]).

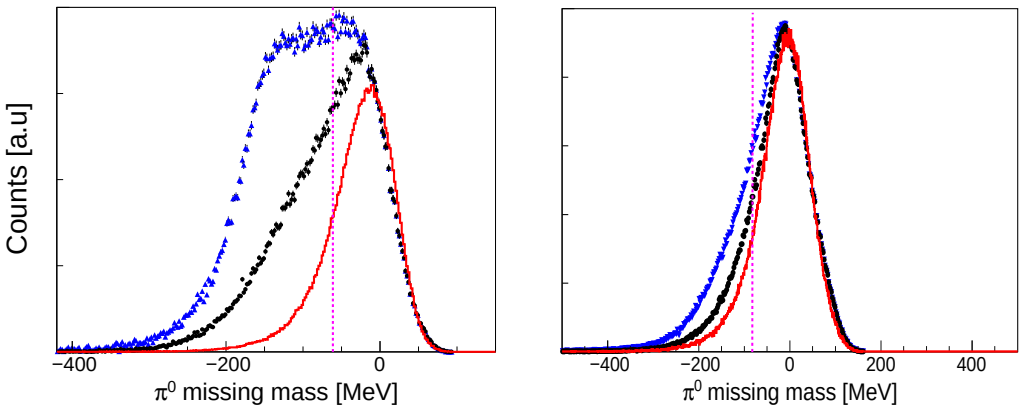

Figure 6.15: $\pi^0\pi^{+/-}$ *Missing mass spectra for* E_γ *= [400 - 460] (left) and [550 - 600] MeV (right) after subtraction of the nucleon mass. The solid curve is a simulation (see next paragraph). The blue triangle points are experimental data before applying the first* π^0 *missing mass cut and the black points are the same after the cut. Events with a missing mass bigger than -80 MeV (dashed line) are accepted in order to remove background belonging to another channel. a Fraction of signal is removed as well but corrected with the simulations.*

Note that after these cuts, a small fraction of background, about 5%, will be included in the signal. This will be accounted for in the calculation of the systematic uncertainties (see chapter VII).

6.2.2.2 Channel simulation and detection efficiency

Two reactions have been simulated using the GENAT4 package:

- $\gamma +^7 Li \rightarrow \pi^0\pi^- + p(n)$
- $\gamma +^7 Li \rightarrow \pi^0\pi^+ + n(p)$

The event generator was similar to the one in the case of the neutral channel with the difference of the final state which contained one charged and one neutral pion. The Fermi momentum was considered and the charged pions suffered from the same FSI as in the neutral channel. The neutral pion decayed into two photons using the GDECA3 GEANT routine and given to GEANT to be tracked whereas the charged pion was directly given to GEANT.

A specific problem was related to the π^+ simulation. While the π^- get absorbed by nuclei after they deposited their energy, the π^+ decay into anti-muons. Once the anti-muons deposited their small energy, they are trapped and decay after $2.2 \cdot 10^{-6} s$ into electrons and neutrinos. This muons decay in the experiment after the electronics gates are closed. So no trace of the deposited energy from the muon decay products exist in the data. This is not the default case of the simulation. It was then needed to stop the tracking of the particles in the simulation after 1 μs and therefore get rid of extra deposited energy and extra detector hits in π^+ clusters.

Another problem occurred while calculating the charged detection efficiency. Charged particles were more difficult to be correctly identified than the meson decay photons. Indeed, energy and time calibrations in MC simulations were made using photons. While photons see their energy entirely recorded, charged particles suffer from additional interactions and deposit less energy. The difficulty manifested principally in the energy of the charged pion recorded in CB which was slightly bigger than its kinetic energy, which is non-physical. In addition, as shown in the figures below, the π^- is more concerned by the problem than the π^+ . This can be due to the fact that the π^- continue interacting with nucleons after it is absorbed by the nuclei of the detector elements.
To get rid of this problem, an empirical correction has been applied in the simulation and extrapolated to the data. For each case, the energy of the charged pion in CB was plotted against its kinetic energy and adjusted using a linear fit in order to get :

$$E^{dep}_{\pi^{+/-}} = E^{kin}_{\pi^{+/-}} \tag{6.9}$$

The plots below show the initial situation and the correction made for each case :

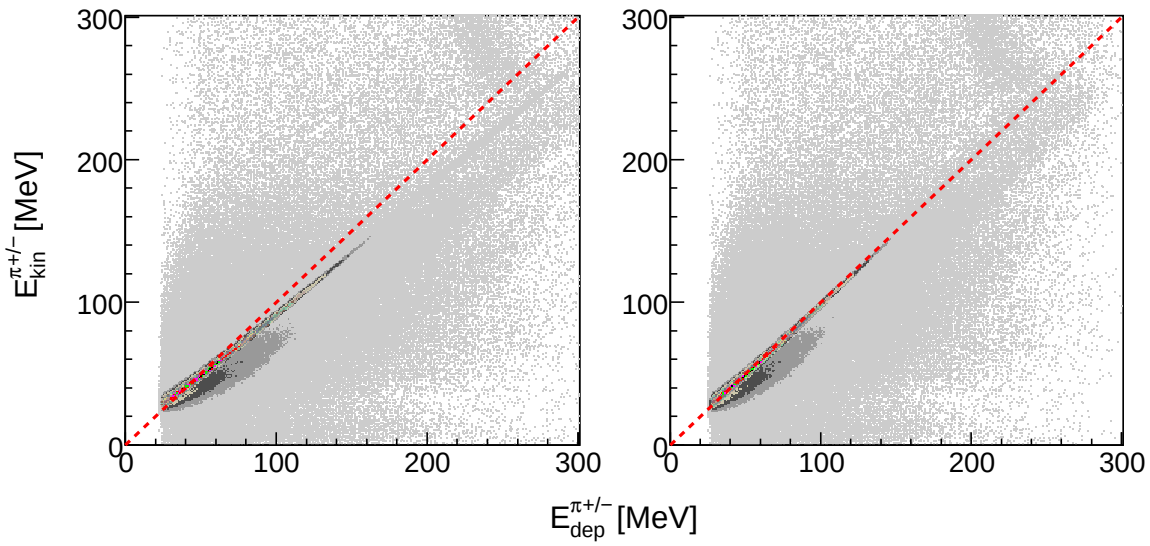

Figure 6.16: *Deposited energy in CB versus the kinetic energy of a simulated π^0 in the case $\gamma +^7 Li \rightarrow \pi^0\pi^{+/-} + (pn)$. Left: before correction, right: after correction.*

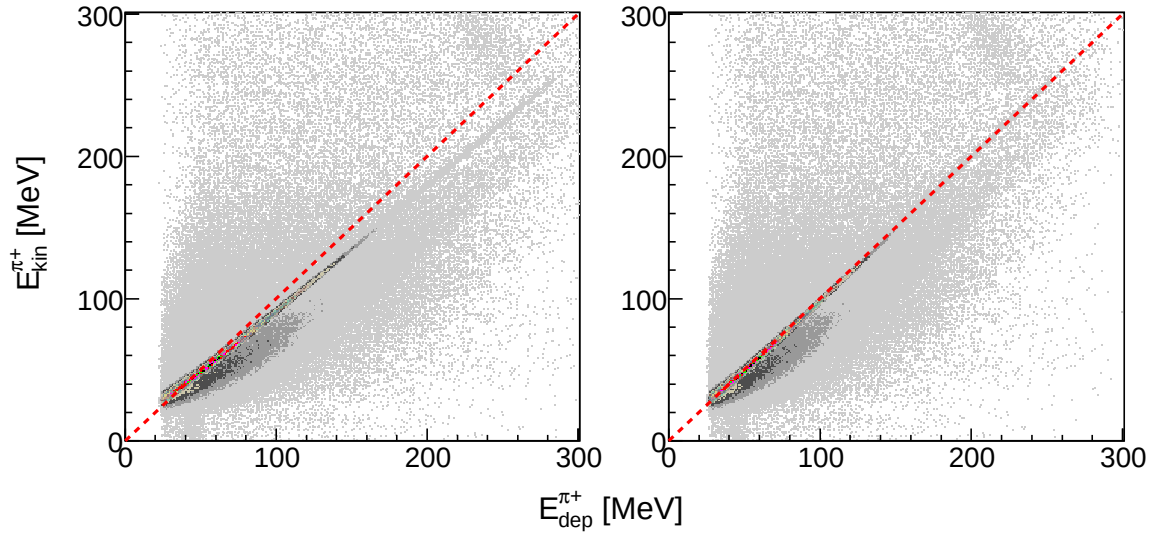

Figure 6.17: *Deposited energy in CB versus the kinetic energy of a simulated π^0 in the case $\gamma +^7 Li \rightarrow \pi^0\pi^{+} + n(p)$. Left: before correction, right: after correction.*

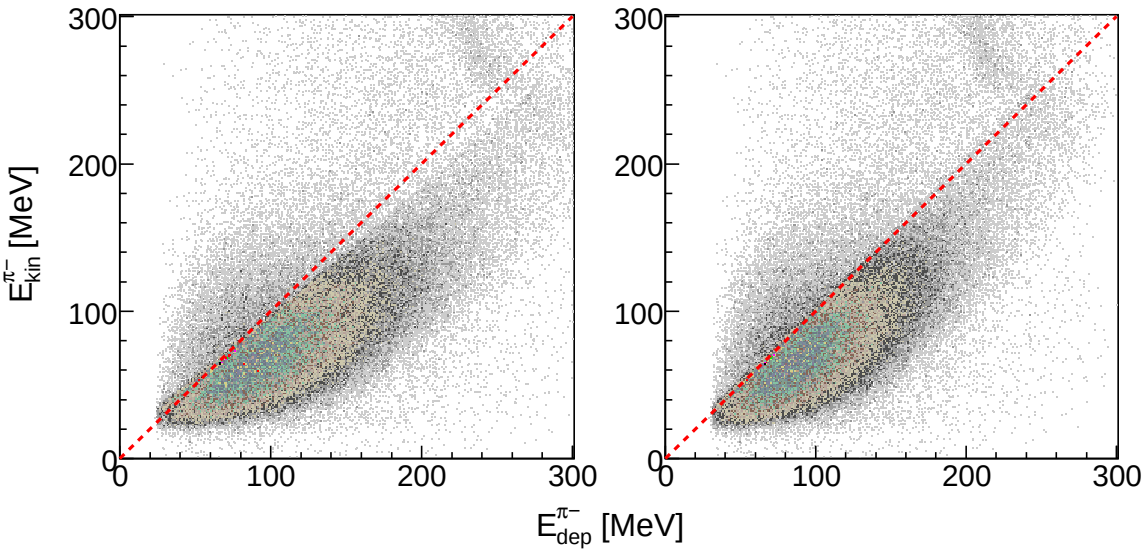

Figure 6.18: *Deposited energy in CB versus the kinetic energy of a simulated π^0 in the case $\gamma +^7 Li \rightarrow \pi^0\pi^- + p(n)$. Left: before correction, right: after correction.*

After these corrections have been applied, the simulated events could be analyzed and the detection efficiency calculated. Fig. 6.19 shows the invariant mass distribution of the simulated events.

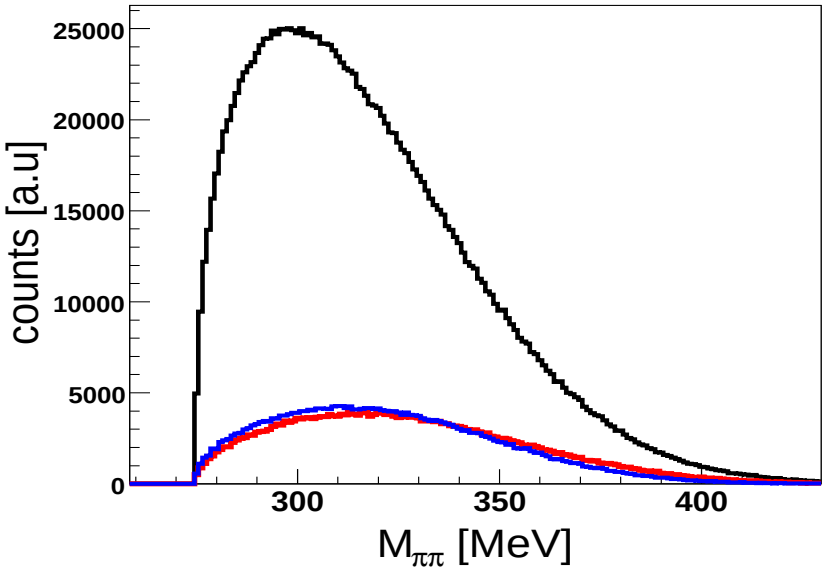

Figure 6.19: *Invariant mass distribution of simulated events. In black the start distribution, in blue the distribution of the tracked events and in red the distribution of the reconstructed events.*

Note that different fits have been tested and the shown ones were the best. The choice of these fits would obviously induce a certain systematic uncertainty, especially in the last case where the distribution looks difficult to fit. This systematic uncertainty will be discussed in chapter VII.

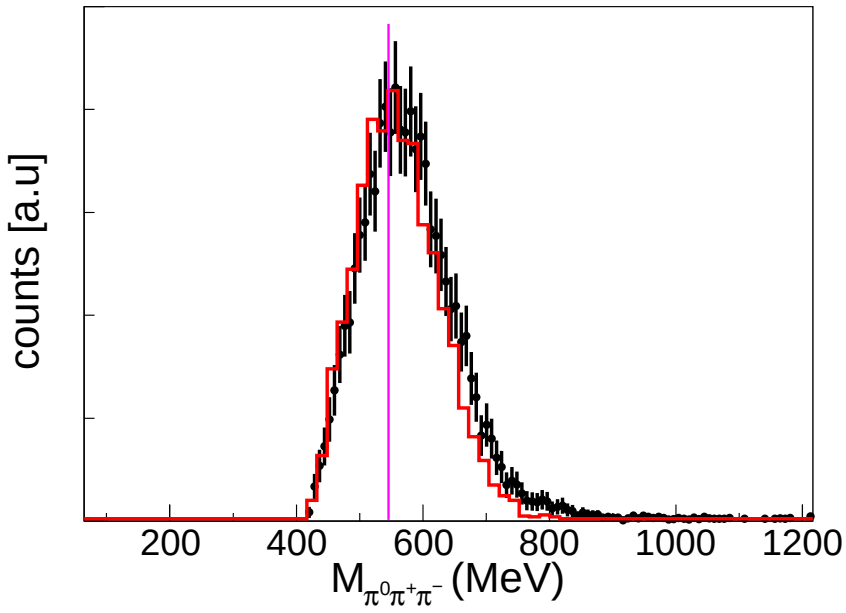

Figure 6.20: *Invariant mass of $\pi^0\pi^+\pi^-$ pion triples. It served as a calibration check for the charged pion in MC (red histogram) and data (black points).*

A crosscheck of the quality of the calibrations in data and simulations was made by verifying if the peak position of the invariant mass distribution of $\pi^0\pi^+\pi^-$ corresponds to the η mass as shown in 6.20.

A further check was made by comparing the shapes in MC and data of the invariant mass of the neutral π^0 detected in coincidence with the charged pion. As seen in Fig.6.21, the background in data has been fitted using a polynomial and added to the simulated line shape. and the sum was plotted together with the data. The applied cut in MC and data between 110 and 160 MeV mass can be seen.

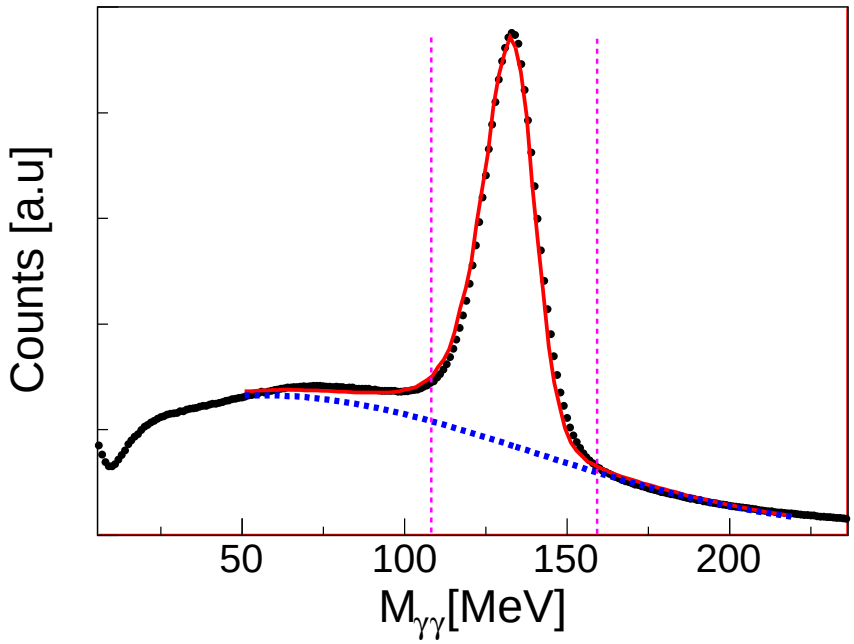

Figure 6.21: *MC simulations quality check: Invariant mass of the neutral pion detected in coincidence with a charged pion. Background (blue) was fitted using a polynomial and added to simulated line shape and the sum (red) is compared to data (black points). The region where the cut has been applied is represented by the dashed lines. For background fit, see sect. 6.2.2.3.*

In order to compute the invariant mass distributions, the detection efficiency has been calculated using eq. 5.1 and plotted as function of the invariant mass of the $\pi\pi$ pairs. The detection efficiency is shown for E_γ = [400 - 460] and [460 - 520] MeV in Fig. 6.22 together for the tracked and the reconstructed events.

Again, the efficiency obtained using the reconstructed events was selected in order to correct the detector resolution effects.

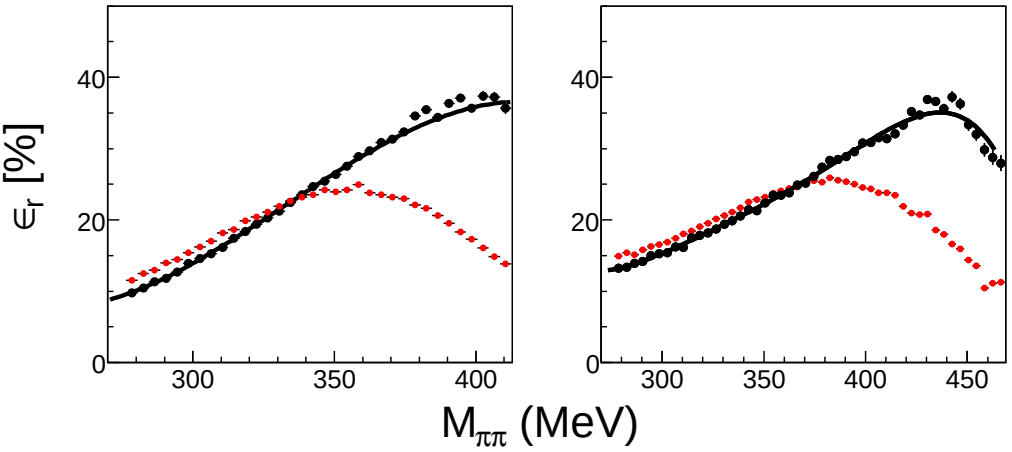

Figure 6.22: *Charged efficiency vs $M_{\pi\pi}$ invariant mass for E_γ = 400 -460 MeV (left) and E_γ = 460 -520 MeV (right) plotted for the reconstructed events (black) together with the tracked events (red).*

The detection efficiency has been plotted as well as function of the incident photon beam energy as shown in Fig. 6.23.

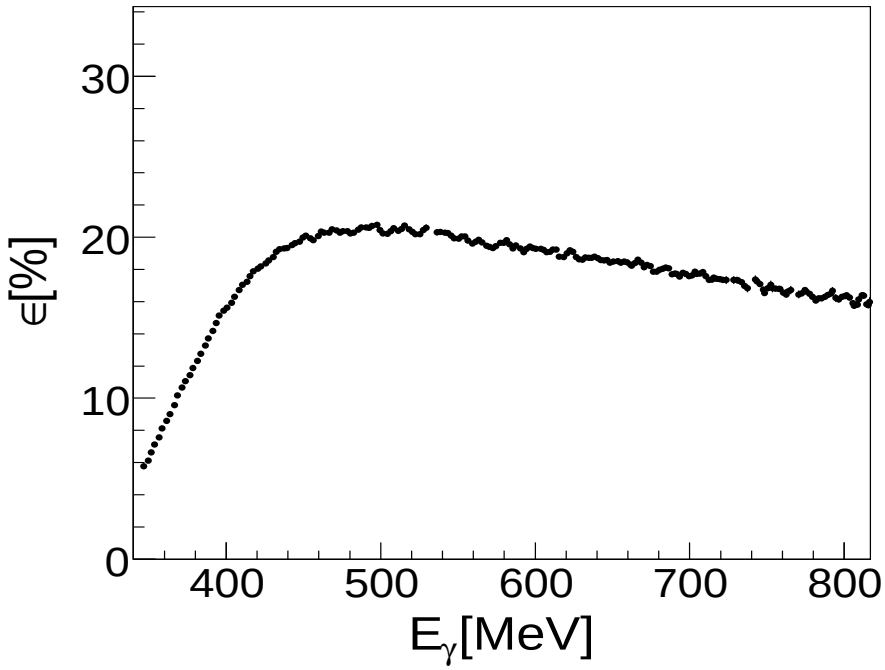

Figure 6.23: *Charged efficiency vs incident photon beam energy.*

6.2.2.3 The cross sections

The charged signal was extracted similarly to the neutral one. The π^0 was fitted for each bin of $M_{\pi\pi}$ of the defined E_γ range as seen in Fig. 6.24. The position and the width of the Gaussian have been again fitted using a polynomial function to minimize the fluctuations. The signal was determined by integrating the Gaussian.

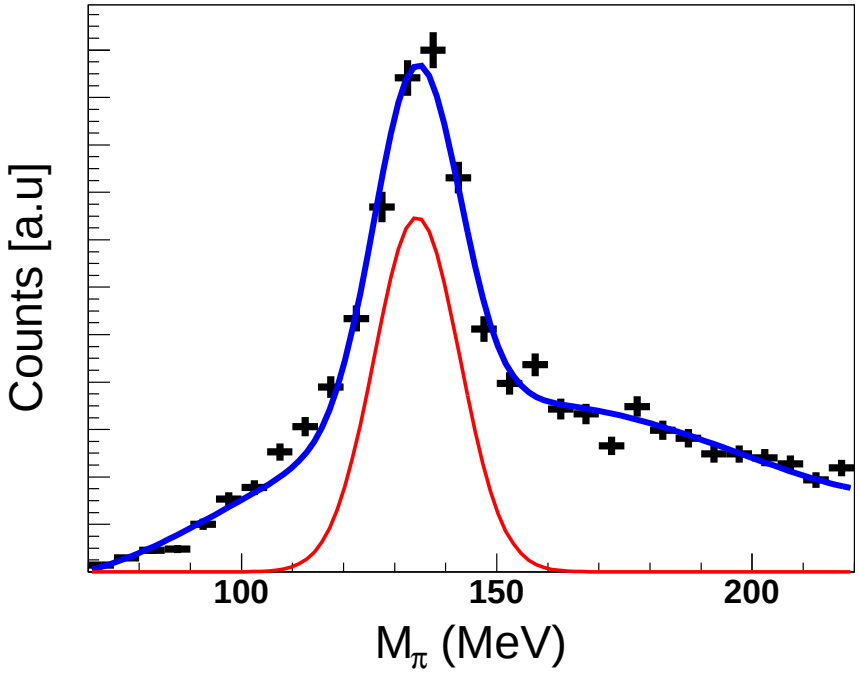

Figure 6.24: *Example of invariant mass fit for E_γ = [400 - 460] MeV. The (signal + background) was fitted by (Gauss + pol4) function (blue histogram). The integral of the Gaussian (red histogram) represent the signal corresponding to one point of the mass distribution.*

Once the signal is extracted, the charged mass distributions were calculated by applying the equation 6.1 and plotted in Fig. 6.25.

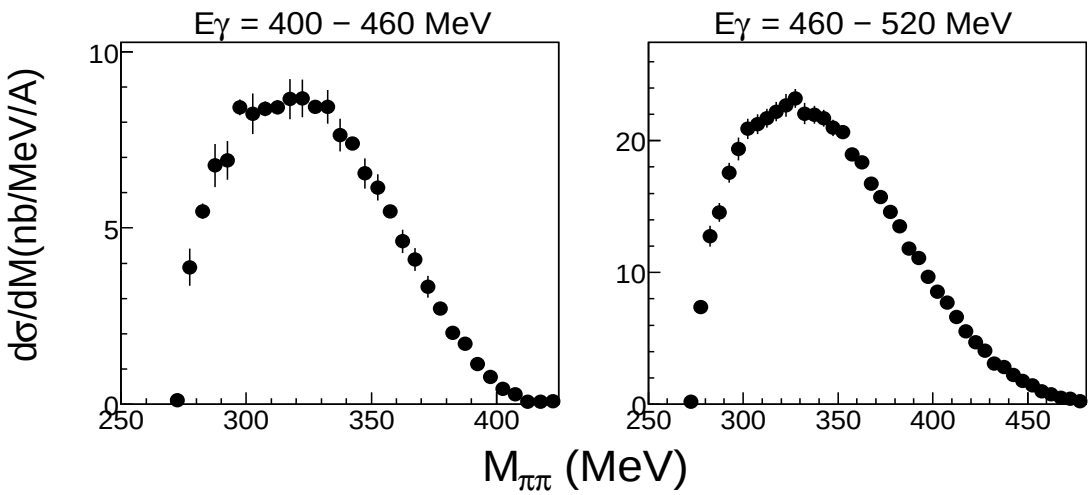

Figure 6.25: *Charged mass distributions for E_γ = [400 - 460] MeV and E_γ = [460 - 520] MeV.*

The charged total cross section has been obtained by integrating the mass distributions over the whole E_γ range. The obtained total cross section is plotted in Fig. 6.26a. It has been normalized to $A^{2/3}$ to be compared to the Calcium and deuterium cross section from [14], as seen if Fig. 6.26b. The region of interest (E_γ < 500 MeV) is plotted in Fig. 6.27.

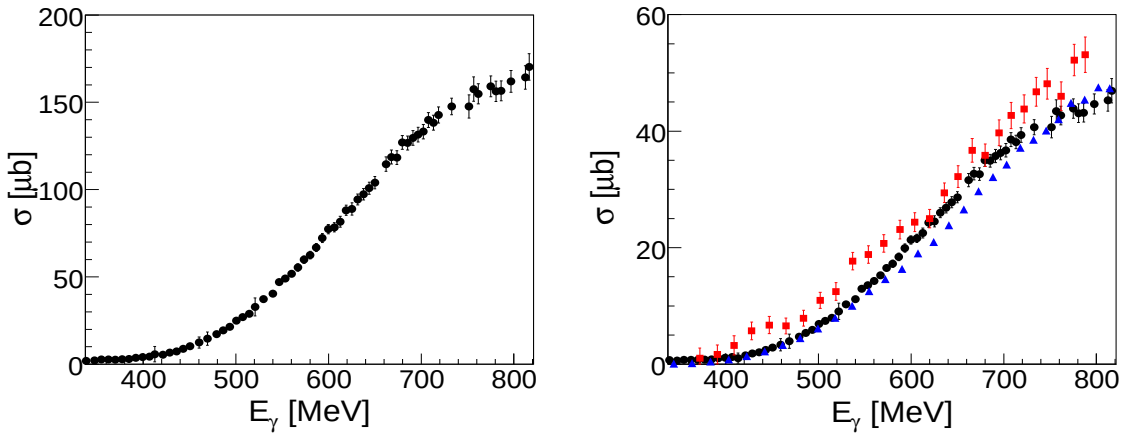

Figure 6.26: *Left: Charged total cross section. Right: Total cross section normalized to $A^{2/3}$ compared to Calcium (blue triangles) and deuterium (red squares).*

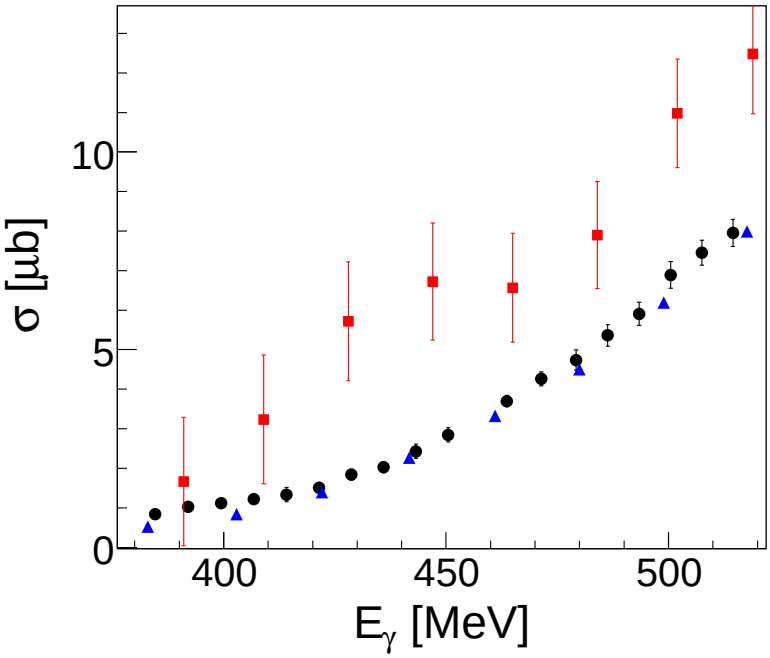

Figure 6.27: *Total cross section normalized to $A^{2/3}$ compared to Calcium (blue triangles) and deuterium (red squares) for E_γ up to 500 MeV.*

6.2.3 Discussion

Concerning the $\pi^0\pi^0$ and $\pi^0\pi^{+/-}$ total cross sections normalized to $A^{2/3}$, they agree well with calcium (normalized to $A^{2/3}$) and deuterium (normalized by a factor 2). It is already discussed in literature (see e.g [55] and [56]) that such a scaling holds for all so far investigated exclusive meson production reactions in the second resonance region. The scaling of the cross sections of the medium-heavy nuclei is what is expected when only the nuclear surface contributes to the reactions and therefore an indication for strong FSI.

In order to investigate a possible σ in medium effect for ^{7}Li, the mass distributions of $\pi^0\pi^0$ and $\pi^0\pi^{+/-}$ channels calculated above have been normalized to their respective total cross sections and plotted together as seen in Fig. 6.28.

The ratio of the two mass distributions has then been calculated for each E_γ range:

$$R_{(\pi^0\pi^0/\pi^0\pi^{+/-})} = \frac{d\sigma(\pi^0\pi^0)}{\sigma(\pi^0\pi^0)dM} / \frac{d\sigma(\pi^0\pi^{+/-})}{\sigma(\pi^0\pi^{+/-})dM} \tag{6.10}$$

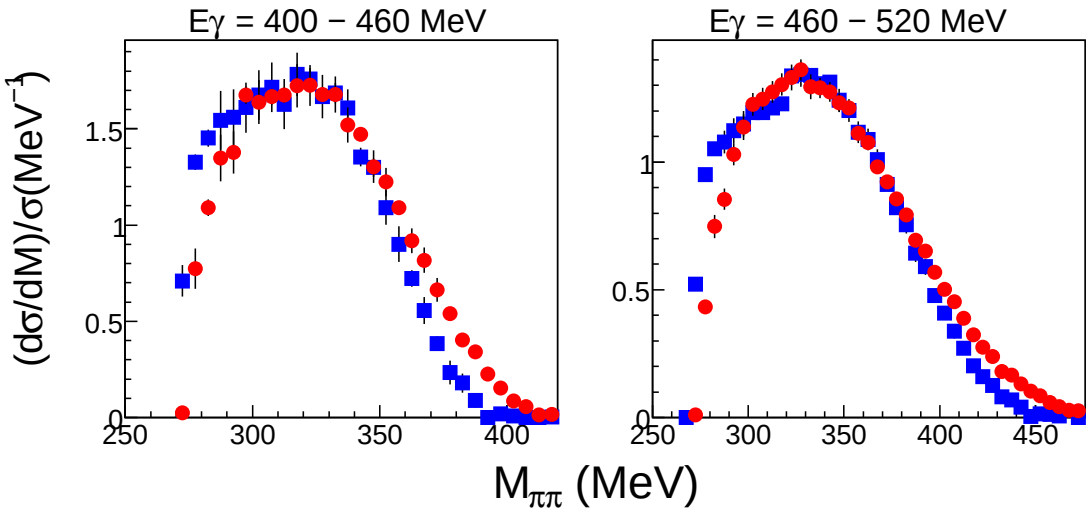

Figure 6.28: *Neutral (blue squares) and charged (red full circles) normalized to their respective total cross sections for E_γ = [400 - 460] MeV and E_γ = [460 - 520] MeV.*

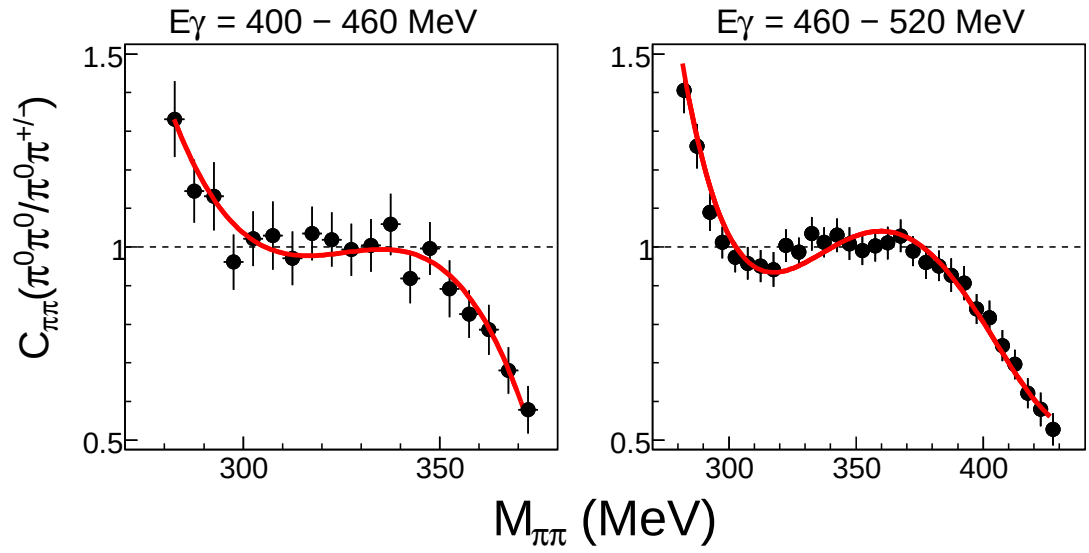

Figure 6.29: *Ratio of neutral and charged mass distributions fitted with a polynomial of degree 3.*

As seen in Fig. 6.29 the obtained ratios showed a slight shift in the neutral mass distribution compared to the charged one (the ratio rises for small $M_{\pi\pi}$).

However, this shift could arise from the direct effect related to the $\sim$ 4.6 MeV difference between a charged and a neutral pion. In order to account for this

effect, the neutral invariant mass distributions were shifted by 4.6 MeV. The invariant mass spectra obtained in this way are compared in Fig. 6.30 and their ratio shown in Fig. 6.31.

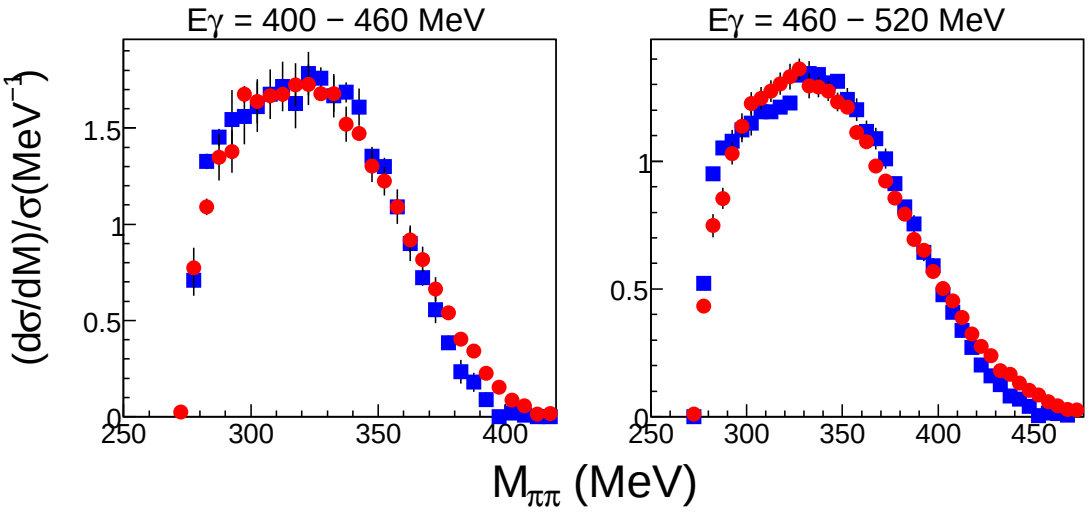

Figure 6.30: *Neutral (blue squares) and charged (red full circles) normalized to their respective total cross sections for E_γ = [400 - 460] MeV and E_γ = [460 - 520] MeV. The neutral distributions were shifted by 4.6 MeV.*

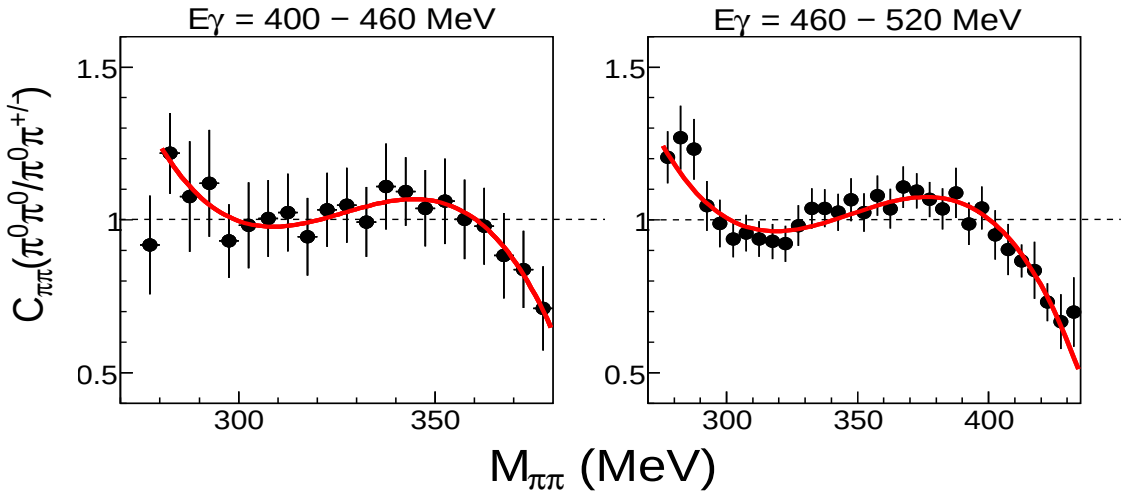

Figure 6.31: *Ratio of neutral (shifted by 4.6 MeV) and charged mass distributions fitted with polynomial of degree 3.*

The observed shift of the neutral invariant masses compared to the ones of the

mixed charged channel could also arise from the FSI as discussed in chapter II. In order to minimize the FSI, the E_γ = 300 - 400 MeV, much closer to threshold, has been investigated. However, at this low energy the mass distributions suffered from low statistics. Fig. 6.32 shows the normalized neutral and charged mass distributions and the corresponding ratio between both of them.

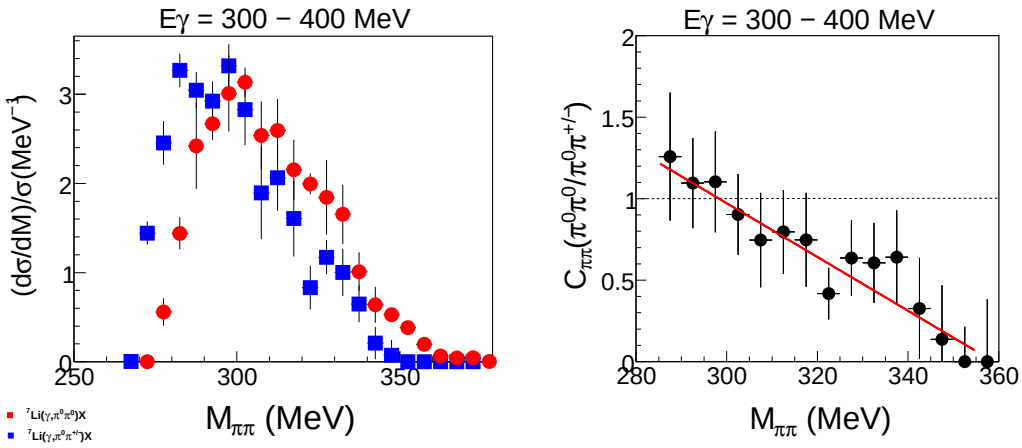

Figure 6.32: *Left: Neutral (blue squares) and charged (red full circles) mass distributions normalized to their respective total cross section, for E_γ = [300 400] MeV. Right: ratio of both fitted with linear polynomial.*

The neutral mass distribution has then been shifted by 4.6 MeV in order to account for the difference between a charged and a neutral pion as seen in Fig. 6.33 where a relative effect can still be seen nevertheless.

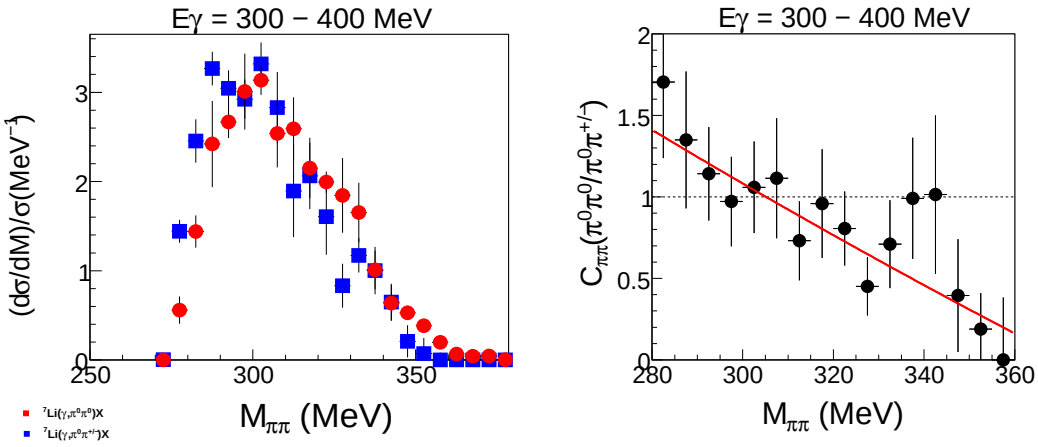

Figure 6.33: *Same as the previous picture with neutral points shifted by 4.6 MeV.*

6.3 The coherent π^0 photoproduction off lithium

As discussed in chapter II, the coherent π^0 photoproduction from nuclei is interesting for the investigation of the in medium modification of the Δ-resonance and for the extraction of the mass distributions. This analysis aims to extend the study into "medium" nuclei such as ^{7}Li.

The procedure for ^{7}Li was the following. The reaction was first identified and reconstructed. It was then simulated and analyzed using the same program. The differential cross sections were then plotted for the E_γ energy ranges : $[180-200]$, $[200-220]$, $[220-240]$ and $[240-260]$ MeV. The total cross section was then deduced. In the second part, the ^{7}Li form factor was extracted for E_γ = $[180-220]$ MeV in PWIA approximation. The choice of such low incident photon energy bin for the extraction of the form factor was motivated by the minimization of the FSI effects. Finally, the mass rms-radius was extracted as described in chapter II.

6.3.1 Reaction identification and simulation

Coherent photoproduction of π^0 -mesons from ^{7}Li is the reaction :

$$\gamma +^7 Li \rightarrow \pi^0 +^7 Li \tag{6.11}$$

For the reconstruction of this reaction, events with exactly two photons with no hit in the PID, in the MWPC or in the veto wall were considered. The four-vectors of the two photons were summed up and the coherent neutral pion was reconstructed. A cut between 110 and 160 MeV on its invariant mass has been applied.

As described sect. 5.3.5, the reaction can be identified via its missing energy spectra. For this purpose two reactions have been simulated using the GEANT simulation package :

- $\gamma +^7 Li \rightarrow \pi^0 +^7 Li$
- $\gamma +^7 Li \rightarrow \pi^0 + N + X$

The second reaction has been simulated in order to plot the quasi-free contribution and was made with a proton in the final state. Since the masses of proton and neutron are close, results do not differ significantly.

The event generator produced two photons in the last step from the decay of one neutral pion. The initial state was an incident photon of a given energy in the z-axis direction and a ^{7}Li nucleus at rest. The four-momenta of the incident photon and the target nucleus were added up and two particles (a π^0 and a ^{7}Li nucleus) were produced by a special routine called DECAY in the center of momentum. The produced particles were after that boosted into the lab frame. The same routine DECAY was then used for the decay of the π^0 into two photons. The final state of two photons and one ^{7}Li nucleus is then sent to GEANT to be tracked and the obtained output is of the same kind as for one real event. Data and simulation have then been analyzed using the same program including the same cuts and steps leading to the identification of the reaction. The quality of the simulated events is shown in the figures below. Fig. 6.34a shows the distribution of the start events of coherent π^0 as function of their polar angle θ in the photon-nucleus cm-system and their kinetic energy and Fig. 6.34b shows the same distribution for the reconstructed events (the generated events which passed through the same analysis as for real data).

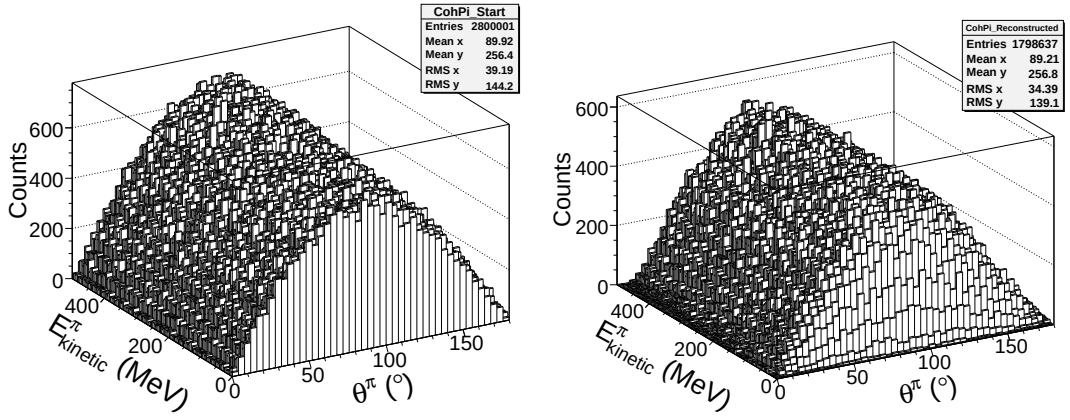

Figure 6.34: *Distribution of the π^0 events as function of their polar angle θ in the photon-nucleus cm-system and their kinetic energy. Left: Start events, Right: Reconstructed events.*

In the following, a cut on the π^0 invariant mass (110 - 160 MeV) has been applied in data and simulations as seen in Fig. 6.35a. Most results will be plotted

as function of the momentum transferred to the nucleus defined as:

$$q = p_{\gamma}^{lab} - p_{\pi}^{lab} \tag{6.12}$$

where the p_{γ}^{lab} stands for the momentum of the incident photon and p_{π}^{lab} for the momentum of the pion, both in the laboratory frame.

For the present analysis, this is more instructive than results shown as function of the incident photon beam energy.

Fig. 6.35b shows the distribution of the simulated events as function of the momentum transfer q. The start events are shown together with the distribution of the tracked events (given by GEANT) as well as the distribution of the reconstructed events after different cuts and conditions have been applied (event selection, π^0 invariant mass, trigger, coincidence time..). The figure has been made for incident photon energies between 180 and 220 MeV.

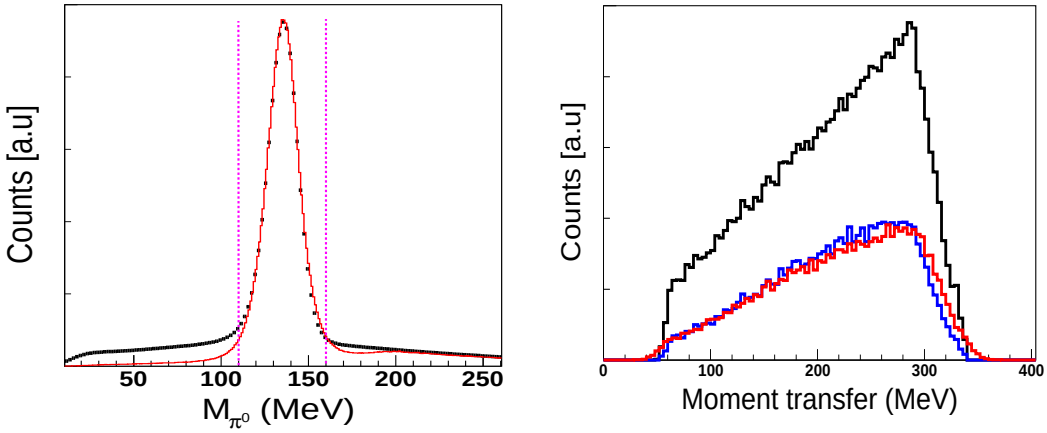

Figure 6.35: *Left: A cut on the π^0 invariant mass $110 < M_{\pi^0} < 160$ MeV has been applied to data (black points) and MC simulations (red histogram). Right: Distribution of the coherent π^0 events as function of the momentum transfer q, in black the start distribution, in red the distribution of the tracked events and in blue the distribution of the reconstructed events. Plots are made for E_{γ}= [180-220] MeV.*

The coherent π^0 photoproduction was identified via its pion energy difference spectra. As shown in Fig. 6.36, the missing energy spectra showed a clear narrow peak centered around zero for incident photon beam energies close to threshold (137 MeV).

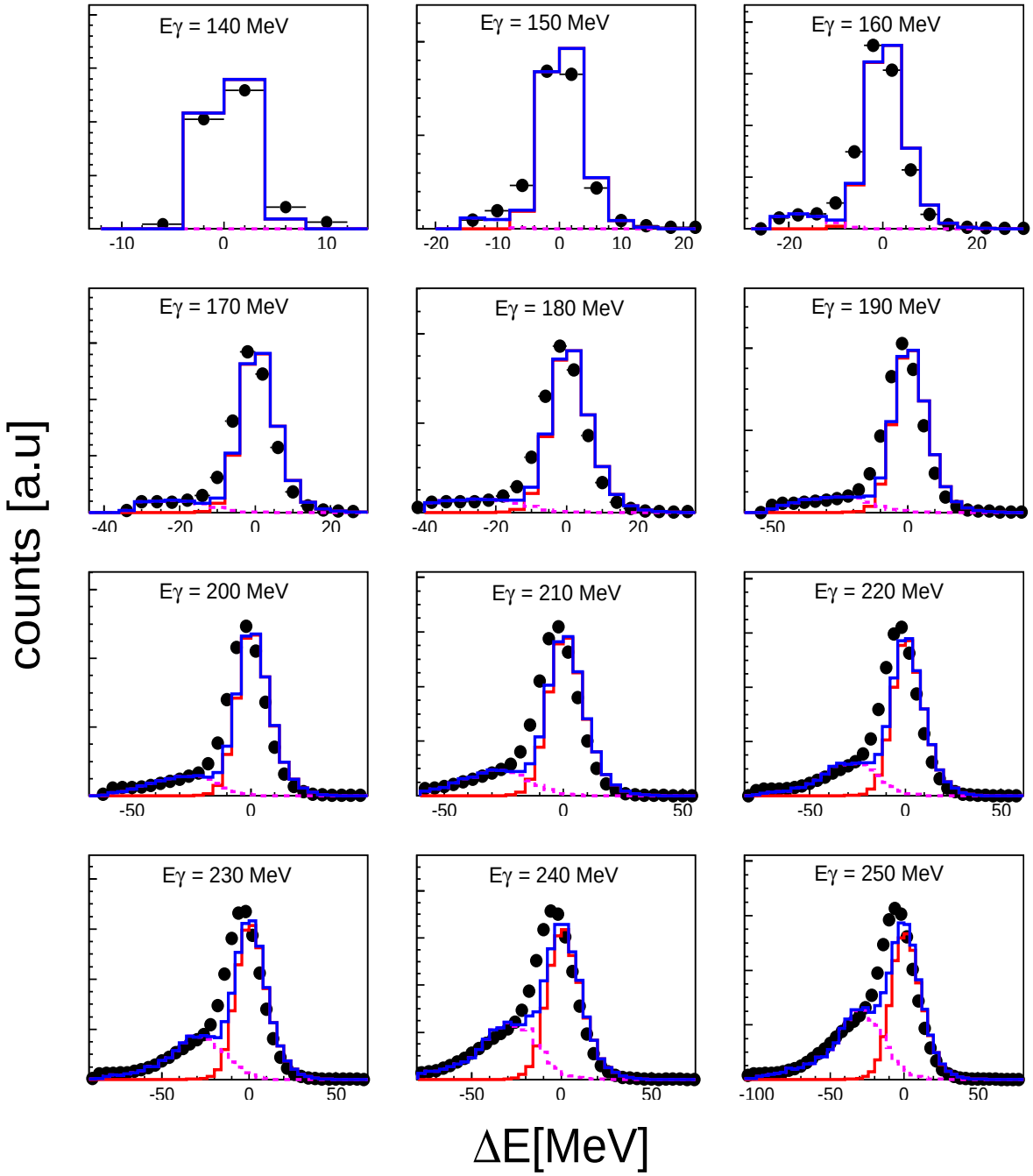

Figure 6.36: *Pion energy difference spectra for the reaction* $(^7Li\gamma\pi^0)X$. *Full points represent the data, the red line a monte-carlo simulation of the coherent reaction* $Li(\gamma\pi^0)Li$ *and the dashed magenta line a monte-carlo simulation of the break-up process* $Li(\gamma\pi^0)p$. *The sum of the simulated coherent and break-up reactions are represented by the blue line. In the following, a cut* $\Delta E > 0$ *has been applied in order to remove contributions from incoherent* $(\gamma +^7 Li \rightarrow \gamma + \pi^0 +^7 Li)$ *and break-up* $(\gamma +^7 Li \rightarrow \pi^0 + N + X)$ *reactions.*

At higher energies, contributions from the non-coherent reactions (break-up and incoherent) become visible at negative values. Therefore, only data with positive values of the pion energy difference were taken into account. Contributions from break-up reactions are almost completely removed in this way but incoherent excitations to low-lying nuclear states are incompletely suppressed. Due to the shape of the angular distributions and the A^2-dependence of the cross sections of the coherent process [57], residual background is mainly a concern for light nuclei and large pion angles.

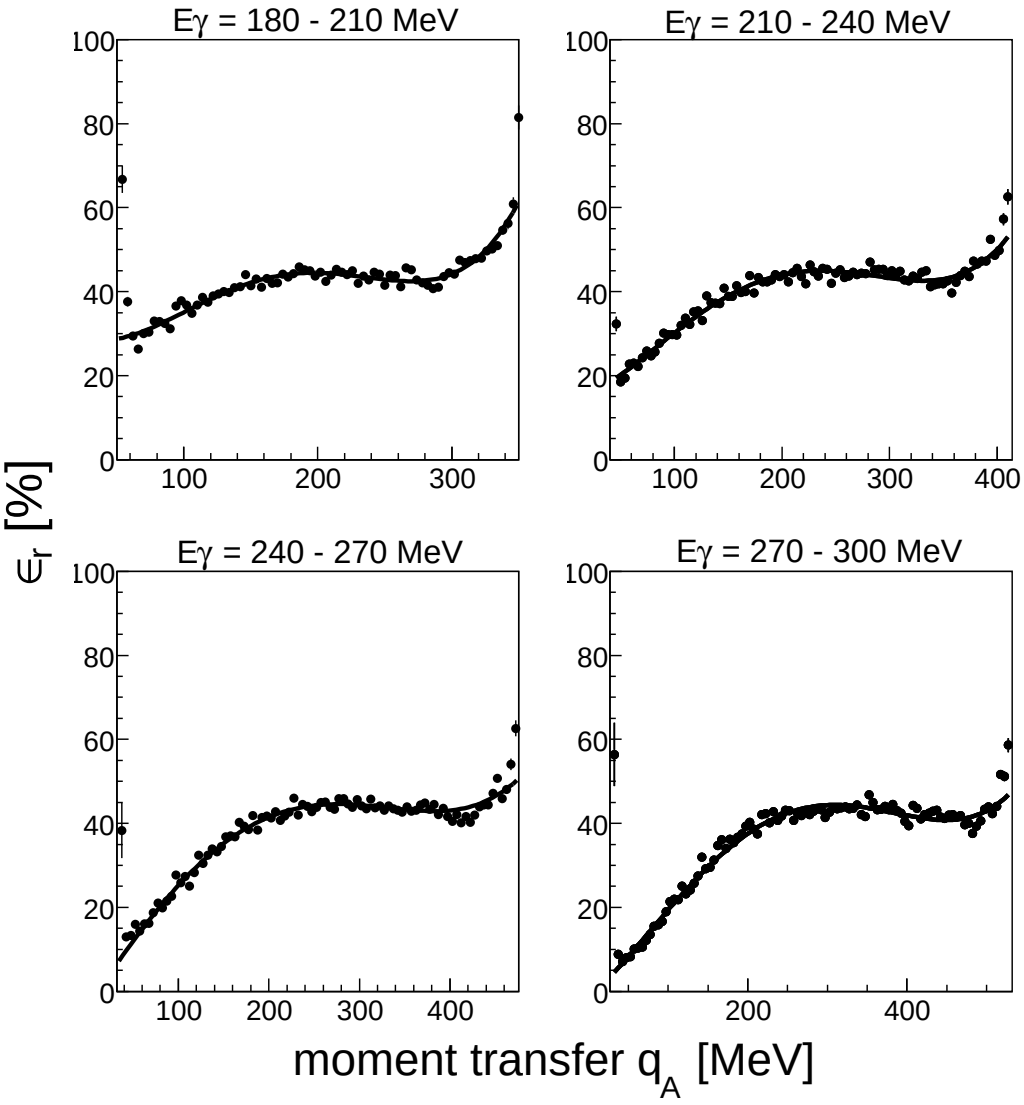

Figure 6.37: *Coherent π^0 detection efficiency as function of the momentum transfer q.*

In order to compute the differential cross sections, the detection efficiency has been calculated as function of the momentum transferred to the nucleus respectively as function of θ_π (polar angle of the coherent π^0 in the photon-nucleus cm-system). Fig. 6.37 and Fig. 6.38 show the detection efficiency for different E_γ.

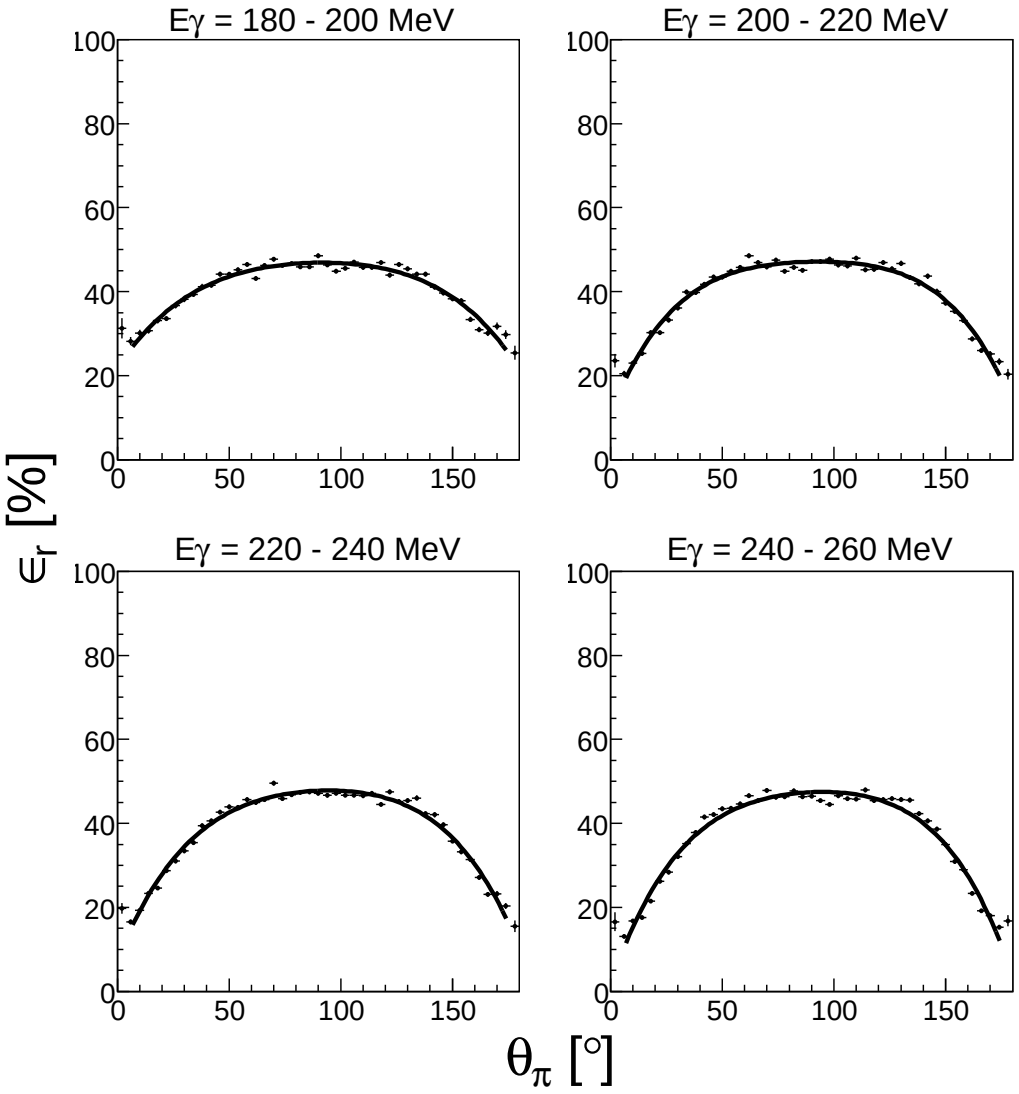

Figure 6.38: *Coherent π^0 detection efficiency as function of θ_π for different E_γ.*

6.3.2 The cross sections

The quality of the obtained data is shown in the figures below where the differential cross sections averaged over photon energies are plotted versus the momentum transfer q_A (Fig. 6.39) and versus θ_π (Fig. 6.40) for different E_γ.

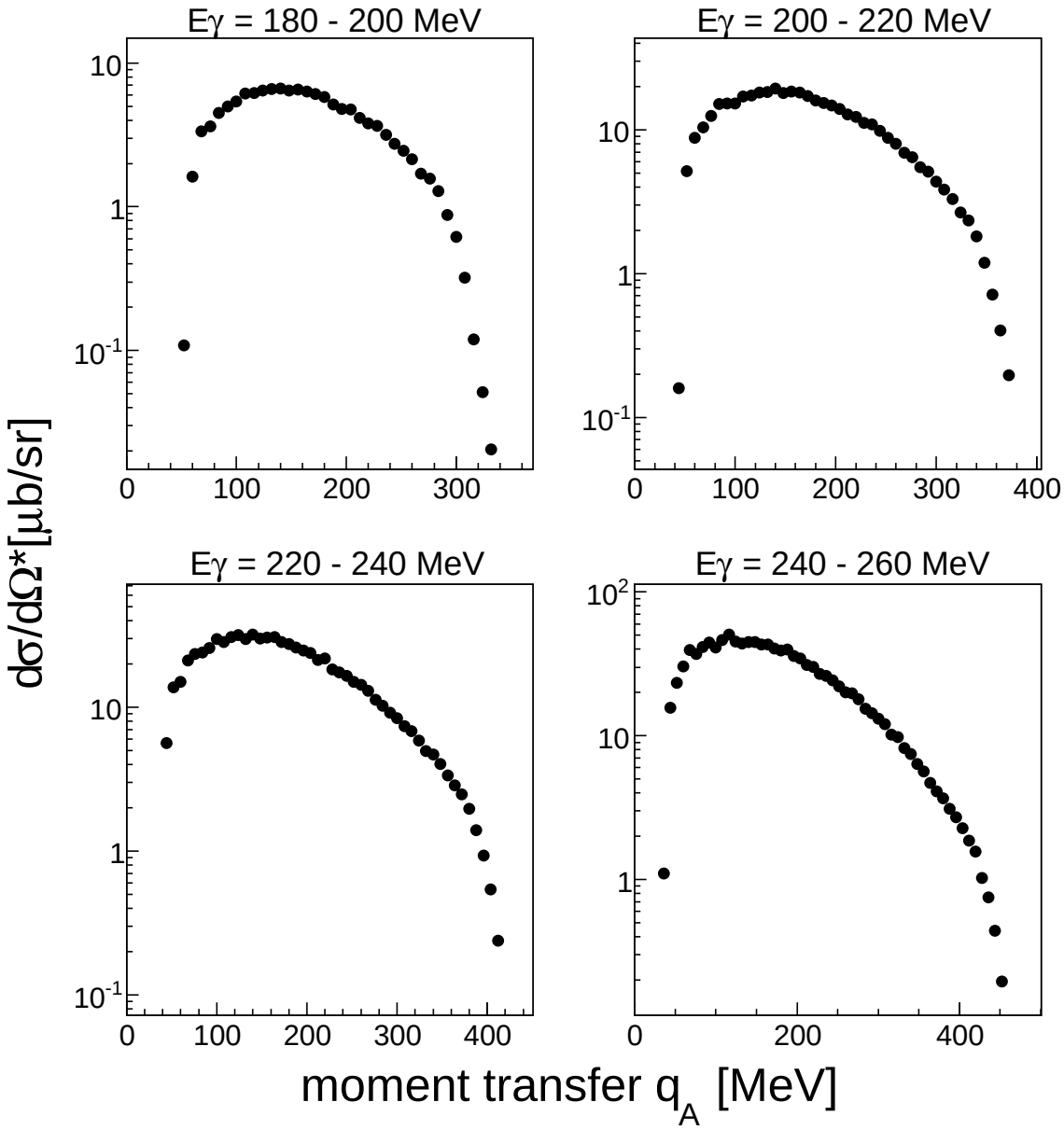

Figure 6.39: *Differential cross sections for $A(\gamma, \pi^0)A$ averaged over different incident photon energies as function of the momentum transfer.*

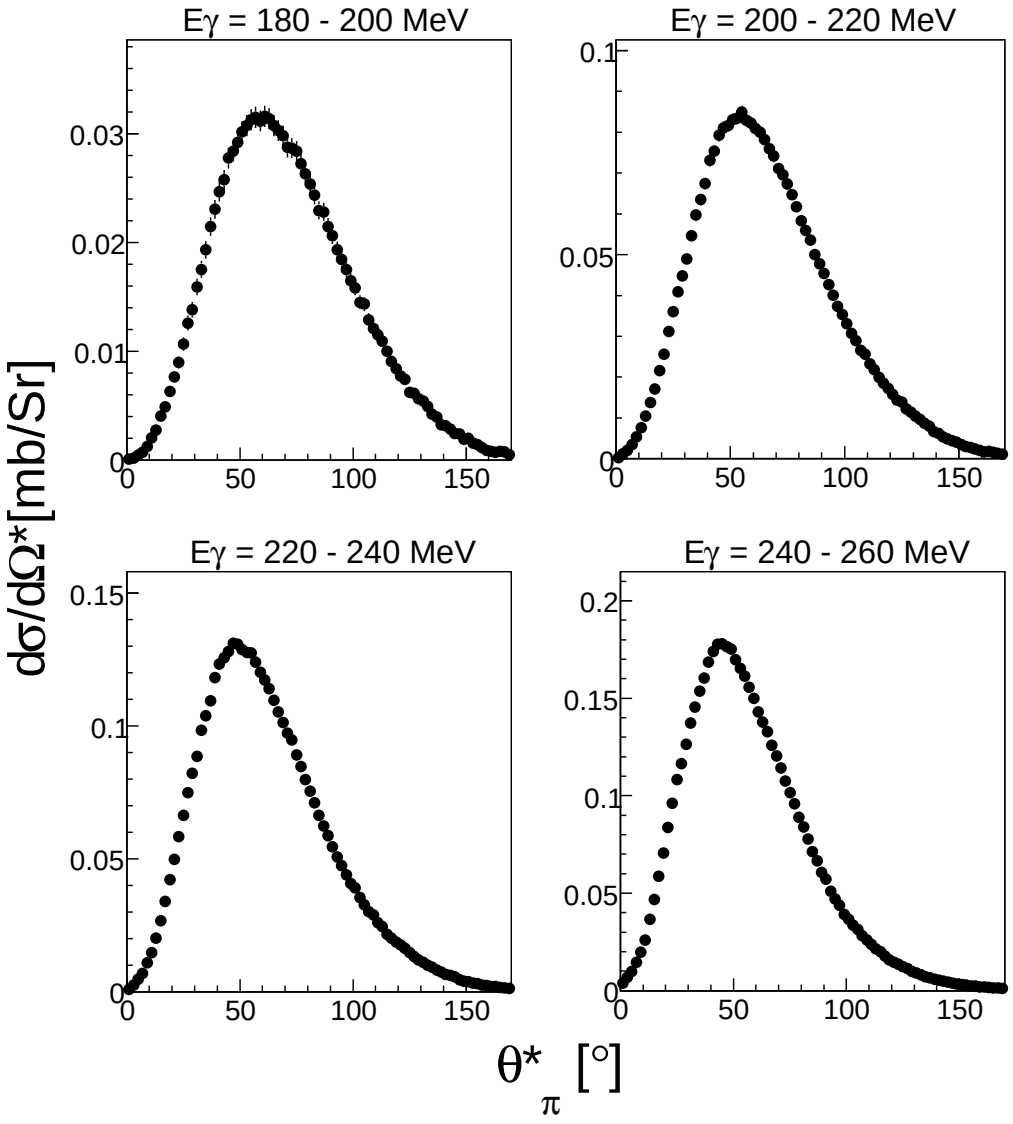

Figure 6.40: *Differential cross sections for $A(\gamma, \pi^0)A$ averaged over different incident photon energies as function of the polar angle of the coherent pion in the photon-nucleus cm-system.*

The total cross section of the $A(\gamma, \pi^0)A$ reaction was obtained by integrating the differential cross sections function of the momentum transfer. The same result can obtained by integrating the angular distributions. The total cross section has been normalized by A and plotted as function of E_γ together with the total cross sections from Carbon, Calcium and Lead published in [57] as seen in Fig. 6.41.

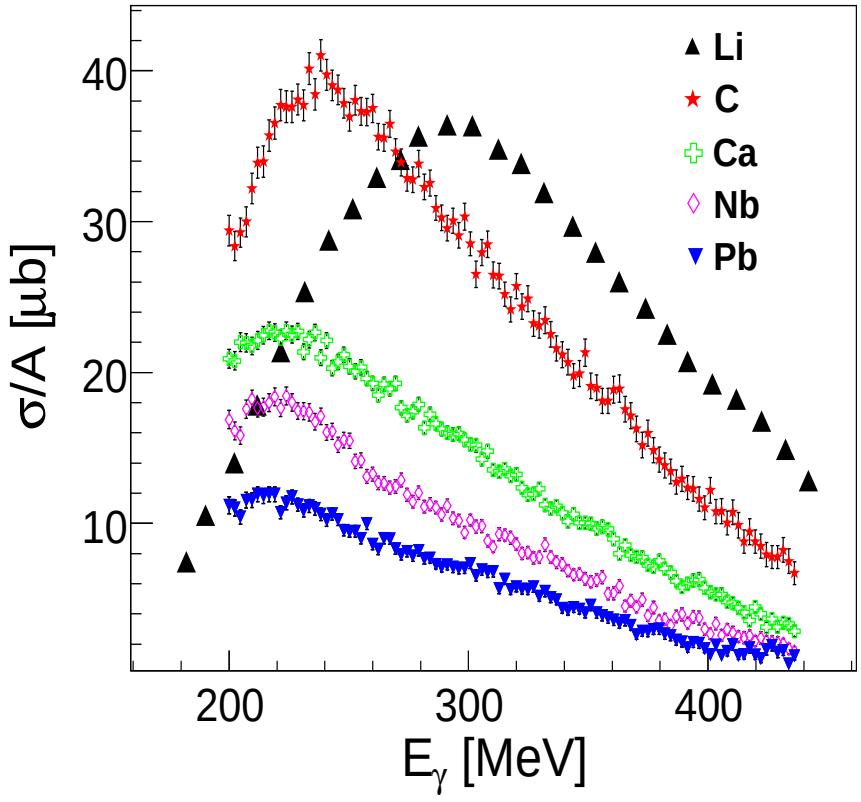

Figure 6.41: *Total cross section for $Li(\gamma,\pi^0)Li$ versus E_γ normalized by A and plotted together with the total cross sections from Carbon, Calcium [57].*

6.3.3 The extraction of the ^{7}Li form factor in PWIA

As described in chapter II, the ^{7}Li nuclear form factor could be extracted in the most simple plane wave approximation (PWIA) using the equation eq. 2.9. For each E_γ range, two cuts on q^2 (lower and upper limits) have been applied depending on the detection efficiency. Figures below show the obtained ^{7}Li form factor plotted together with the measured differential cross section (Fig. 6.42) for E_γ = [200 - 245] MeV. The ^{7}Li form factor has been plotted for different E_γ bins between 180 and 260 MeV as seen in Fig. 6.42.

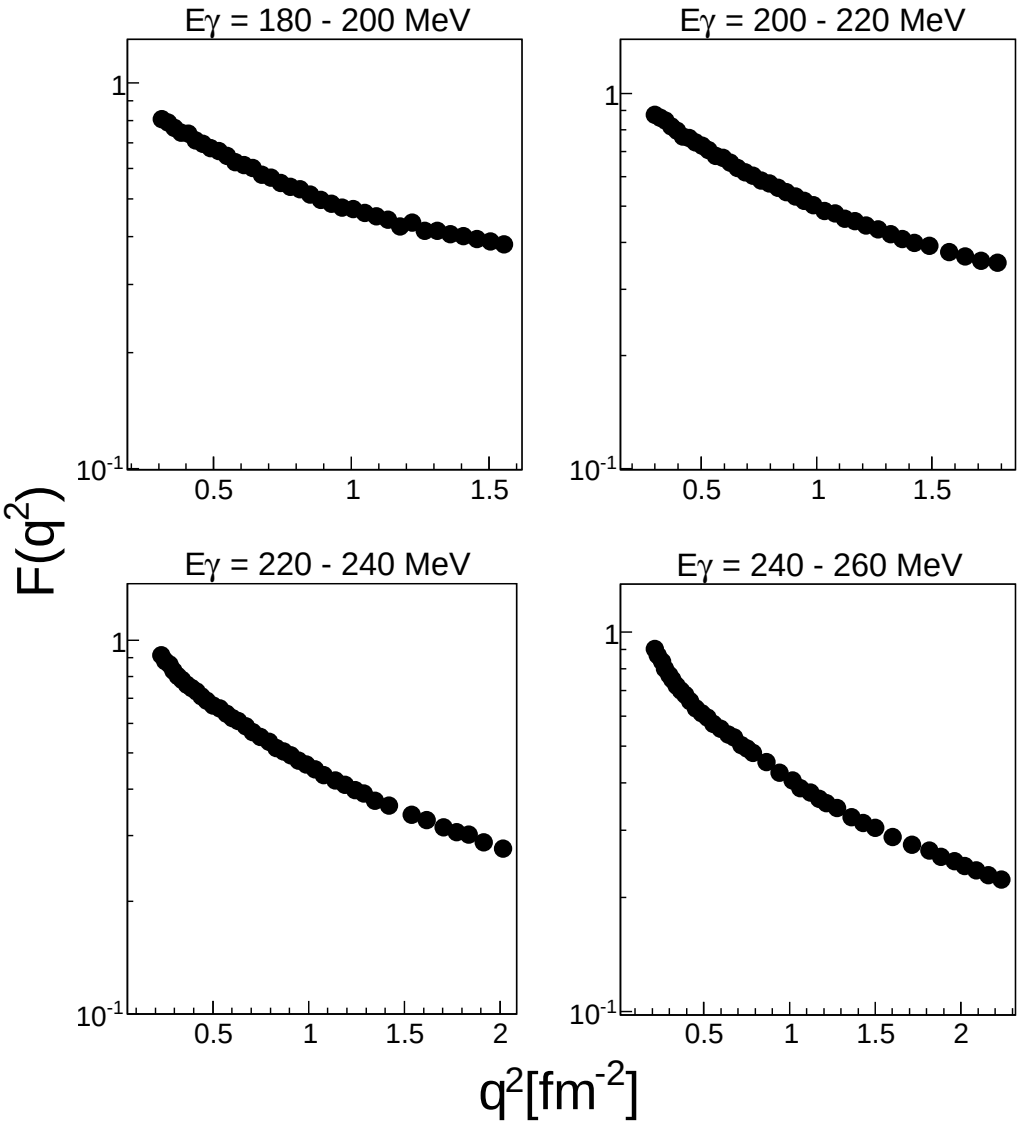

Figure 6.42: *^{7}Li Form factor extracted in PWIA approximation for different E_γ.*

6.3.4 The extraction of the ^{7}Li rms-radius

The root-mean-square (rms) mass radius has been extracted using the nuclear mass form factor $F(q^2)$ calculated above. As discussed in chapter II the rms extraction has been made in PWIA without further model assumption from the slope of the form factor for $q^2 \to 0$ via :

$$F(q^2) = 1 - \frac{q^2}{6} r_{rms}^2 + O(q^4) \tag{6.13}$$

which is done in the usual way by fitting a polynomial

$$F(q^2) = \sum_{i=0}^{N} (-1)^i a_i q^{2i} \tag{6.14}$$

to the data. The rms-radius is then given by:

$$r_{rms} = \sqrt{6 a_1 / a_0} \tag{6.15}$$

where for a correctly determined form factor a_0 should be unity. This is not exactly true in the present case as the form factor was extracted in PWIA approximation and the FSI effects should be taken into account.

The form factor has been fitted using eq. 6.15 for N = 1 and N = 2. Since the FSI increase with increasing E_γ, the mass radius has been extracted for a low energy range ($[180 - 220] MeV$). The quality of the fits is shown in Fig. 6.43.

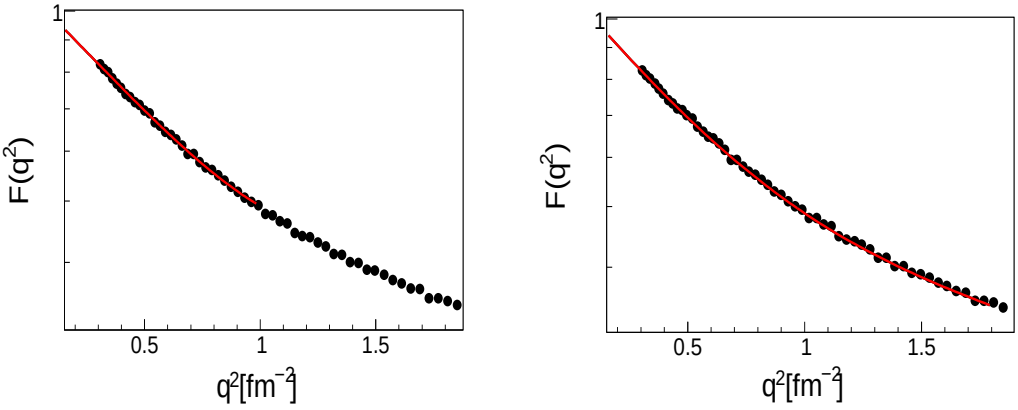

Figure 6.43: *Example of fit of the form factor extracted in PWIA using eq. 6.14 with N = 1 (left) and N =4 (right) for E_γ = [180-220] MeV.*

The rms-radius was then calculated using 6.15. The obtained rms-radius is shown in the figures below where it is plotted as function of the upper limit of the fit range for N = 1 for $q = [0.83, 096] fm$ and N = 2 for $q = [1.26, 138] fm$. The study was limited to the lowest energy range.

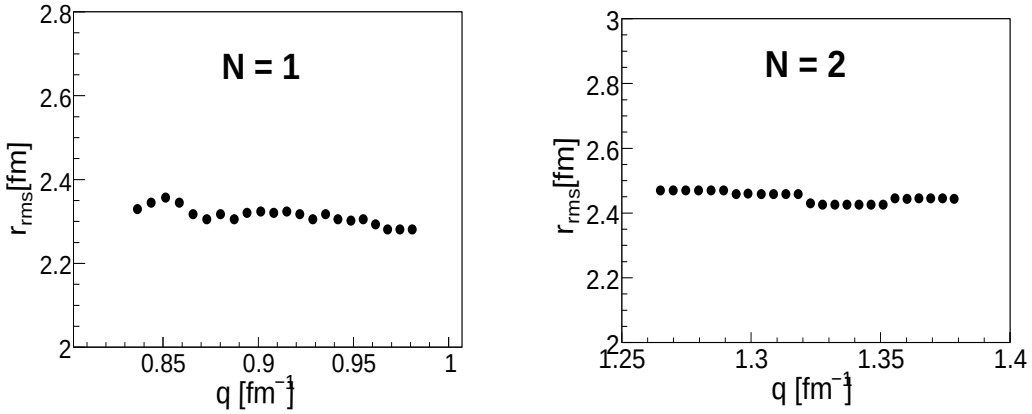

Figure 6.44: *Fit results for the rms-radius extracted from eq. 6.14-6.15. They are plotted as function of the upper limit of the fitted q-range for fits with polynomials of degree 2 (left) and degree 4 (right) in PWIA approximation.*

6.3.5 Discussion

The obtained cross sections are in line with the previous results, where the A^2 and the form factor dependence is clearly seen. A more detailed discussion of the Δ-resonances properties in ^{7}Li needs model calculations as in [43] which are not yet available.

The form factor extracted in PWIA approximation seems reasonable since the a_0 parameter approaches unity at low energies. At higher E_γ results become slightly overestimated. This is expected since the FSI become larger with increasing E_γ.

The average of the extracted mass rms-radius at E_γ = [180 - 220 MeV] was $\sim$ 2.3 fm using a N = 1 fit and $\sim$ 2.45 using a N = 2 fit. These values were compared to values found in literature. Table 6.45 shows charge and matter radii for the lithium isotopes given by Tomaselli et al [118].

	^{5}Li	^{6}Li	^{7}Li	^{9}Li
Theor. charge radius (fm)	2.54	2.55	2.41	2.42
Expt. charge radius (fm)		2.56(5) [2,20]	2.39(3) [20]	
Theor. matter radius (fm)	2.59	2.41	2.36	2.42
Expt. matter radius (fm)		2.35(3) [13] 2.44(7) [12]	2.35(3) [13]	2.32(2) [13]

Figure 6.45: *Charge and matter radius for the lithium isotopes taken from [118].*

Results seem to be in quite good agreement with the table above but slightly larger especially for N=2. However, the fits appear to be more stable for N=2. Again, the rms radius was extracted only for the lowest E_γ range. For higher energies results become large and the PWIA approximation seems to become unusable.

To sum up, calculations for ^{7}Li which includes the FSI effects and the Δ-self energy are needed for further discussion of the obtained results. In addition, since statistics are very good for the coherent π^0 channel, the presented results will be recalculated in the near future using finer bins and the mass rms radius will be extracted as well for N = 3 and above. Finally, the form factor extracted in this chapter will be calculated also for higher incident photon beam energies in order to be compared to results obtained in [95] shown in Fig. 2.10.

6.4 The η photoproduction off ^{7}Li

This section presents the results of the $\gamma(^7Li, \eta)$ reaction motivated by the investigation of the η-meson coherent photoproduction discussed in section 2.4. First, the inclusive channel $\gamma(^7Li, N\eta)X$ will be discussed and cross sections will be shown. The $\gamma(^7Li, \eta)^7Li$ will be then investigated through the η missing energies spectra and the coherent cross section will be presented. For both inclusive and coherent processes, the same analysis has been made for the two η- decay modes. Finally, the π^0 -proton back-to-back channel will be discussed.

6.4.1 The inclusive η production

6.4.1.1 The reaction identification

The η meson has to principal decay modes :

- $\eta \rightarrow \gamma\gamma$, with $\Gamma \sim 39\%$
- $\eta \rightarrow \pi^0\pi^0\pi^0 \rightarrow \gamma\gamma\gamma\gamma\gamma\gamma$, with $\Gamma \sim 32\%$

Where Γ is the branching ratio of the decay.

In the following the first case will simply be called the 2γ channel and the second the 6γ channel.

For both decay modes, the fully inclusive reaction has been studied :

$$\gamma + Li \rightarrow \ \eta \ + X \tag{6.16}$$

For the 2γ channel events with two or three neutral hits were considered. The four-vectors of the best combination of two photons (The ηn case selected by a χ^2-test) were summed up and a cut between 500 and 600 MeV on the invariant mass has been applied. For the 6γ channel events with six or seven neutral hits were considered and the four-vectors of the best combinations of three photon pairs selected by a χ^2-test were summed up. A cut between 110 and 160 MeV on the invariant mass of each pion has been applied. The four-vectors of the three pions were then summed up and the η reconstructed. For both channels, a constraint has been applied to the momentum of each of the $\gamma\ \gamma$ pairs in order to improve the experimental resolution :

$$\mathbf{P}' = \mathbf{P}\frac{m_{th}}{m_{\gamma\gamma}} \tag{6.17}$$

where $m_{\gamma\gamma}$ refers to the measured invariant mass and m_{th} to the mass of π^0 or η depending on the channel.

6.4.1.2 Reaction simulation and detection efficiency

For the inclusive reaction, the mechanism leading to the production of η-mesons in the nuclear target is unknown. Simulations taking into account the Fermi smearing only would be unrealistic. An alternative is to use the so called "grid efficiency" method, where the η detection efficiency is determined in the laboratory frame as function of its measured polar angle θ and its measured kinetic energy E_{kin}. For both channels 2γ and 6γ , the η particles were randomly generated in the event generator for a given interval of θ and E_{kin}. The η meson decayed using the DECAY routine of GEANT into two photons for the 2γ channel or into $3\pi^0$ then again into six photons using the same routine for the 6γ channel. A set of start distributions $N^{start}[\theta, E_{kin}]$ which contains the number of emitted η per interval of $[\theta, E_{kin}]$ has then been obtained for each channel. The start events were then passed through GEANT than analyzed using the same program used for real data with the usual analysis process (best combinations, cuts, trigger..) and a second distribution $N^{reconstrcut}[\Theta, E_{kin}]$ of the generated η events was obtained.

The η detection efficiency is then simply obtained by dividing both quantities:

$$\epsilon_\eta = \frac{N^{reconstrcut}[\theta, E_{kin}]}{N^{start}[\theta, E_{kin}]} \tag{6.18}$$

Fig. 6.46 shows the efficiency distributions as function of the η polar angle θ in the lab frame and its kinetic energy.

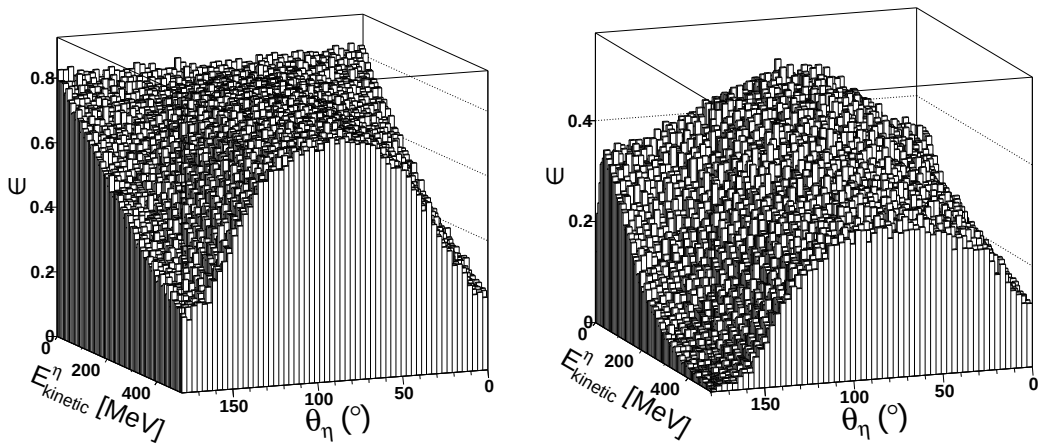

Figure 6.46: *Grid efficiency for the 2γ (left) and the 6γ channels (right).*

Fig. 6.47 shows the obtained detection efficiency as function of the incident photon beam energy. The effeciencies of the 2γ and the 6γ channel are plotted together. In order to extract the angular distributions the detection efficiency has been plotted for different E_γ between the quasi-free production threshold (578 MeV) and the maximum of E_γ (820 MeV), as function of the cosine of the η polar angle in lab frame as seen in Fig. 6.48.

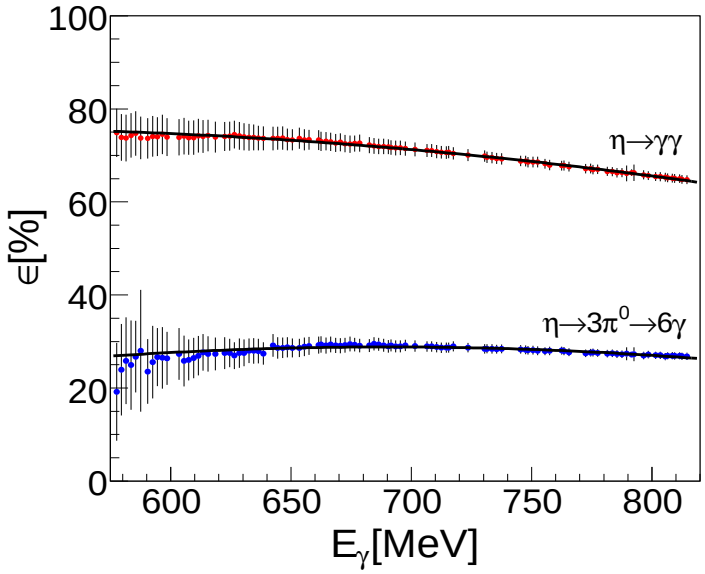

Figure 6.47: *η detection efficiency as function of the incident photon beam energy.*

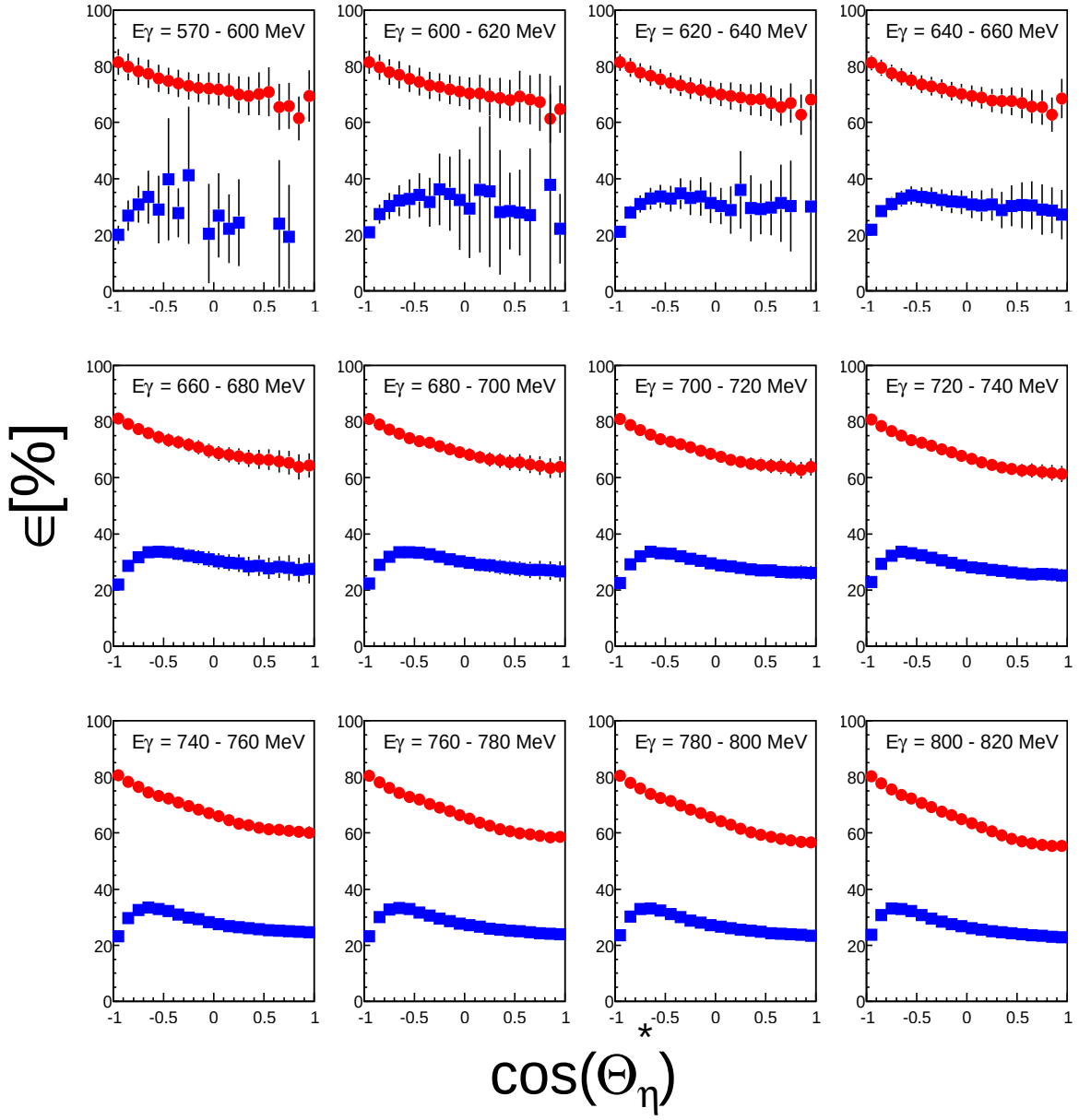

Figure 6.48: *Detection efficiency of the η mesons in its 2γ (red points) and 6γ (blue squares) decay channels. They have been obtained using experimental distributions.*

6.4.1.3 The inclusive cross sections

In the following, a cut has been applied on the η invariant mass in both data and simulation in order to remove a part of the combinational background.

The remaining background would be eliminated before computing the cross sections, in the usual way, by fitting the invariant masses in order to estimate the signal and the background. Fig. 6.49 shows the invariant masses spectra for the 2γ and the 6γ channels and the regions where the cuts are applied. The background has been fitted using a polynomial and added to the simulation line shape in order to compare data and simulations.

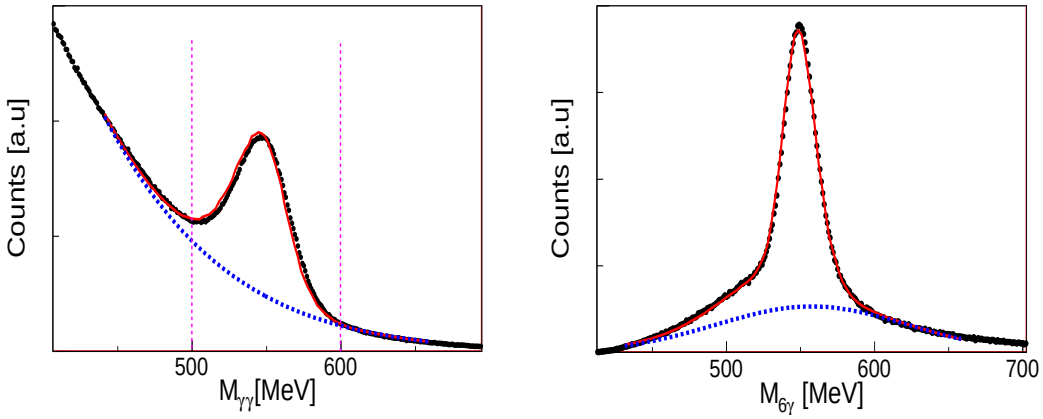

Figure 6.49: *η invariant mass integrated over the whole E_γ range for the 2γ (left) and 6γ channels (right). Background (blue) has been added to simulation line shape and the sum of both (red) is compared to data (black). The applied cuts are represented by the dashed line.*

As seen in Fig. 6.49, the 2γ channel comes with a lot of combinational background whereas the 6γ is almost background-free. For the 2γ channel, most events were recoded in CB alone. As shown in Fig. 6.50 the case where one photon detected in CB and one in TAPS counted almost one order of magnitude less events than the case where two photons are detected in CB. The case where both photons are detected in TAPS alone is almost inexistent due to the large opening angle of the decay photons.

In order to extract the signal, the η invariant mass was fitted for each bin of $cos(\theta_\eta)$ and for each defined E_γ range by *Gaussian + polynomial* function. The obtained fit parameters were injected in the same fit function whose integral (between the cuts discussed above) correspond to the signal. An example of these fits is shown for the 2γ channel (Fig. 6.51a) and the 6γ channel (Fig. 6.51b).

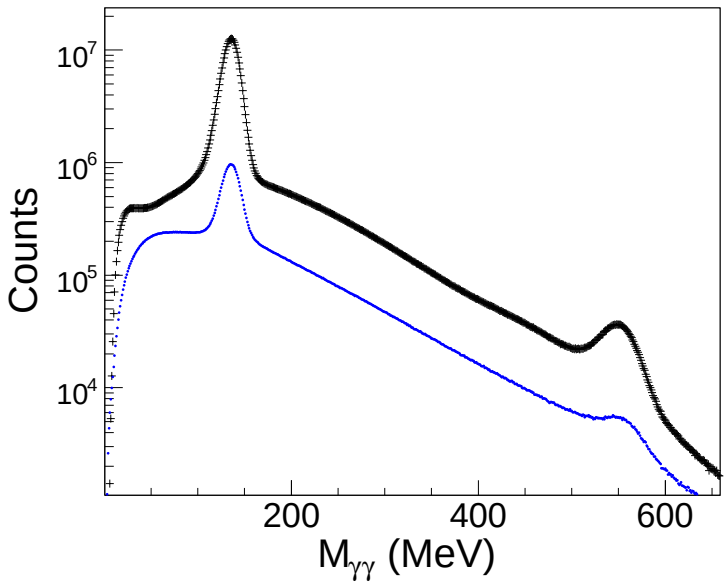

Figure 6.50: *Invariant mass of 2γ in logarithmic scale. The pion and the η peaks can be seen. in black the case with 2γ detected in CB and in blue the case with one γ detected in CB and one γ in TAPS.*

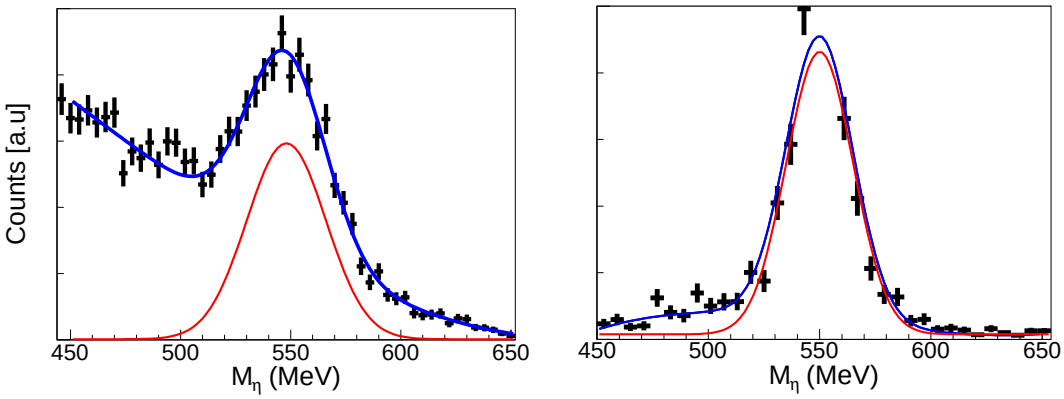

Figure 6.51: *In order to extract the signal, the η invariant mass spectra for the 2γ (left) and the 6γ (right) channels were fitted using a (Gauss+pol). The black points represent the data, the blue line a fit of the signal+background and the red histogram represent the obtained signal.*

The η angular distributions were obtained by applying eq. 6.1. Fig. 6.52 shows the obtained angular distributions as function of $cos(\theta_\eta)$ in γ -N cm-system and Fig. 6.53 shows the obtained angular distributions as function of $cos(\theta_\eta)$ in γ -^{7}Li cm-system.

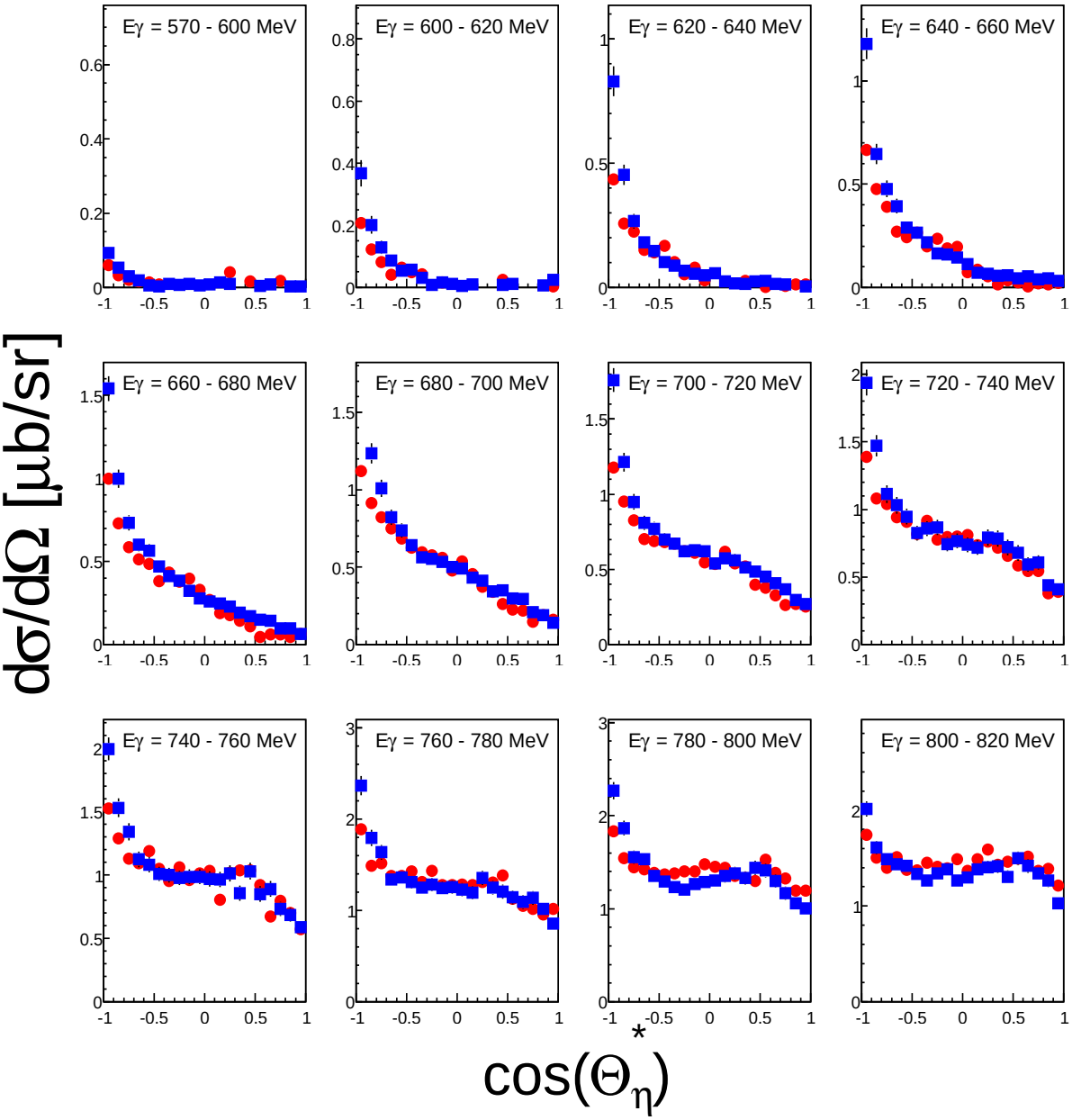

Figure 6.52: *η inclusive angular distributions for different E_γ for the 2γ channel (red points) and 6γ (blue squares) channel as function of $cos(\theta_\eta)$ in the γ -N cm-system.*

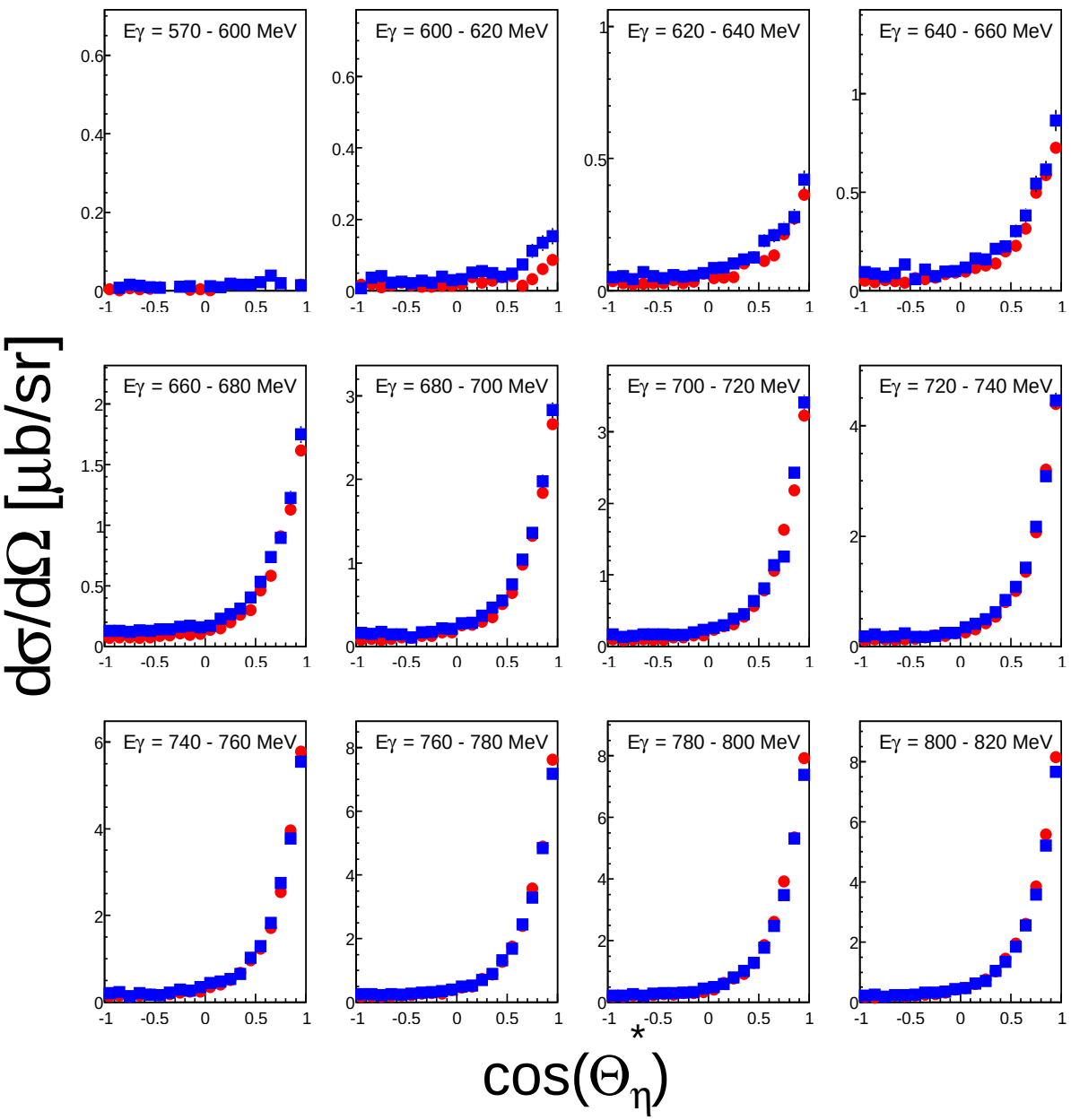

Figure 6.53: *η inclusive angular distributions for different E_γ for the 2γ channel (red points) and 6γ (blue squares) channel as function of $cos(\theta_\eta)$ in the γ -Li cm-system.*

The differential cross sections have then been integrated over the whole incident photon beam energy in order to extract the total cross section shown in Fig. 6.54 where 2γ and 6γ cross sections are plotted together. The total cross sections were then normalized to $A^{2/3}$ and compared to the Ca cross section

taken from [14].

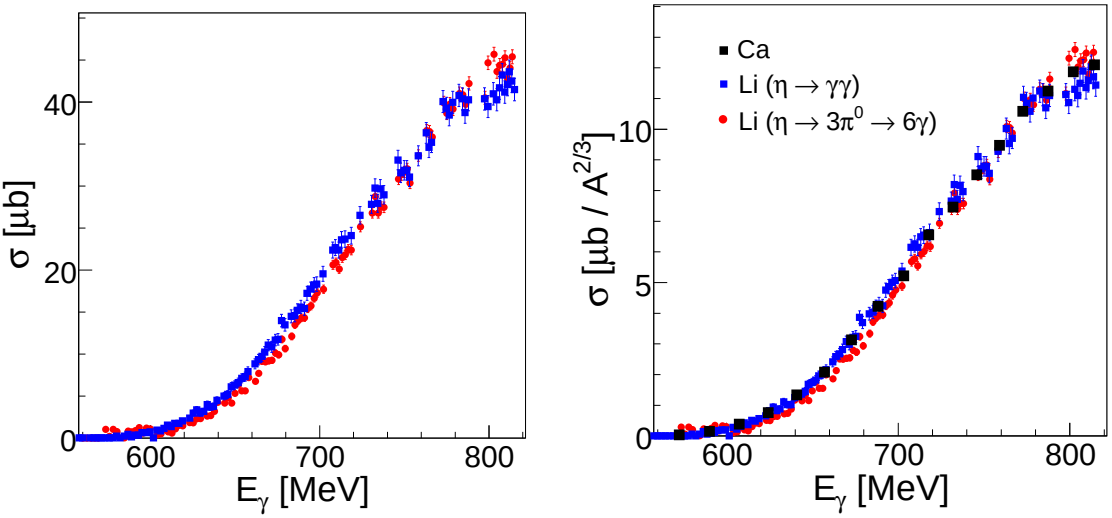

Figure 6.54: *Left: Total η inclusive total cross section for 2γ (red points) and 6γ (blue squares) decay modes. Right: Total cross section normalized to $A^{2/3}$ and compared to Ca (black points) taken from [14].*

6.4.2 The coherent η production

As described in chapter II, the ^{7}Li is the next best candidate after ^{3}He for the investigation of the coherent η production and the search for the η-mesic nuclei. However, as seen in 2.4 the coherent η production off ^{7}Li cross section is expected to be very small.

Coherent photoproduction of η-mesons from ^{7}Li is the reaction :

$$\gamma +^7 Li \rightarrow \eta +^7 Li \tag{6.19}$$

For the two η principal decay modes :

- $\eta \rightarrow \gamma\gamma$
- $\eta \rightarrow \pi^0\pi^0\pi^0 \rightarrow \gamma\gamma\gamma\gamma\gamma\gamma$

As for the coherent π^0 , the coherent reaction can be identified via the η energy difference spectra, for this purpose the above reaction has been identified and

simulated. On the data side, events with exactly two or six photons with no hit in the PID, in the MWPC or in the veto wall.

For the 2γ channel, the four-vectors of the two photons were summed up and the η reconstructed. The η was corrected using eq. 6.7 a cut between 525 and 575 MeV on its invariant mass has been applied. For the 6γ channel, the best combinations of three photon pairs were selected by a χ^2-test. The obtained photons pairs were corrected using eq. 6.7 and a cut between 110 and 160 MeV on the invariant mass of each pion has been applied. The four-vectors of the three pions were then summed up and second cut between 525 and 575 was applied.

On the simulation side, similarly to the coherent pion the coherent and the break-up reactions were simulated. For the 2γ coherent channel, the event generator was exactly the same as for the coherent pion with an η instead of a pion. For the 6γ coherent channel, the event generator produced six photons in the last step from the decay of three neutral pions. The initial state was an incident photon of a given energy in the z-axis direction and a ^{7}Li nucleus at rest. The four-momenta of the incident photon and the target nucleon were added up and four particles (3 π^0 and 1 nucleus) were produced by the GEANT routine DECAY in the center of momentum. The produced particles were after that boosted into the lab frame. The same routine DECAY was then used for the decay of each π^0 into two photons. The final state of 6 photons and a ^{7}Li nucleus (two photons and a ^{7}Li nucleus for the 2γ channel) was then sent to GEANT to be tracked in the simulated detector setup and the obtained output is of the same kind as for one real event.

Concerning the break-up reactions. three reactions have been simulated :

- $\gamma +^7 Li \rightarrow \pi^0 + p + X$
- $\gamma +^7 Li \rightarrow \pi^0 + n + X$
- $\gamma +^7 Li \rightarrow \pi^0 + d + X$

These reactions were simulated in the usual way using the same event generator and the same DECAY routine of GEANT. The mass of the recoil nucleon X was approximated to (mass[Li] - mass[p]) in the first case, (mass[Li] - mass[n]) in the second case and (mass[Li] - mass[d]) in the third case. This is of course a simple approximation and needs a much more advanced event generator

which includes the correct recoil nucleus masses and their Fermi momenta. Therefore, the simulated missing energies were not expected to fit exactly to the data.

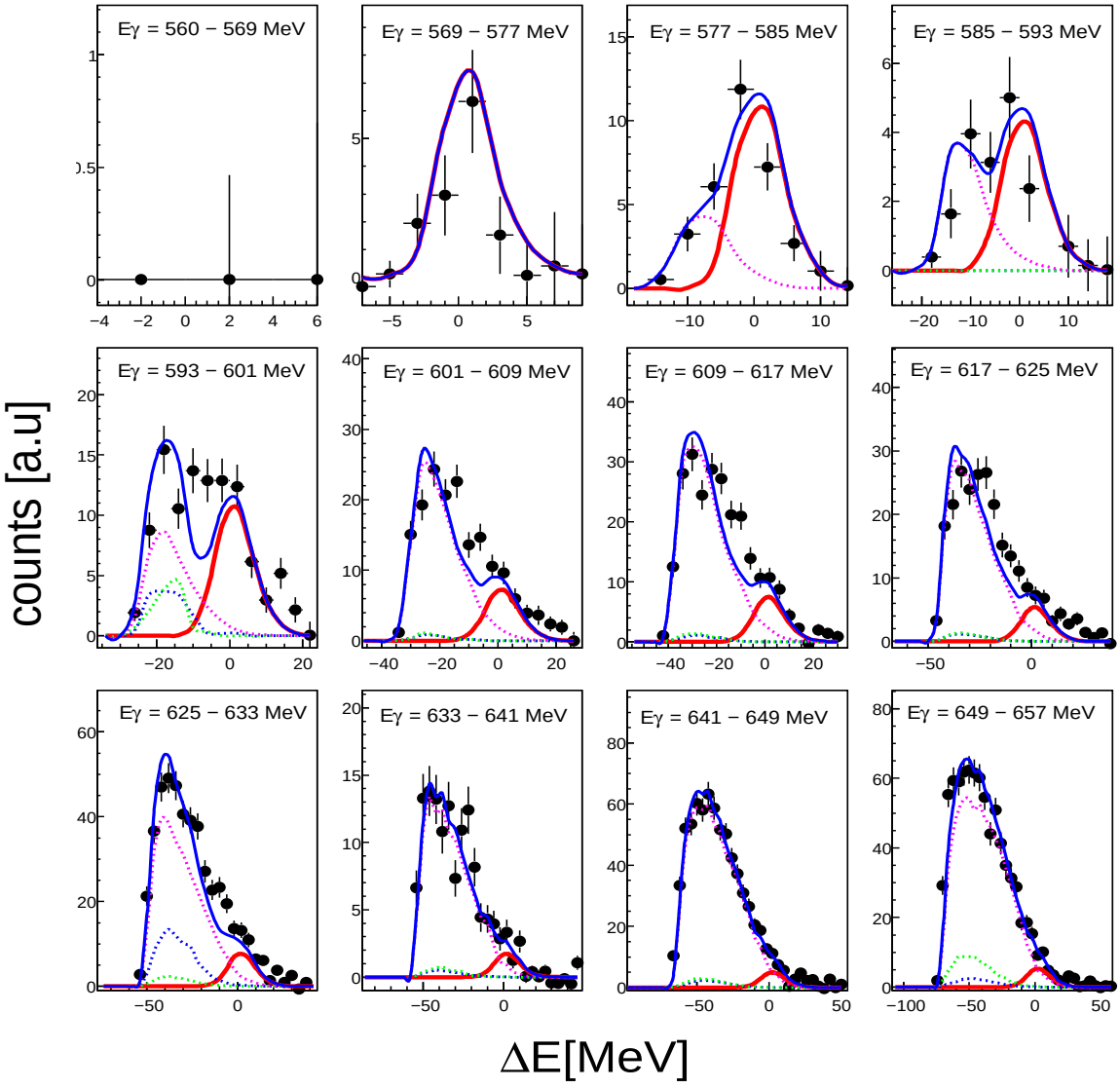

Figure 6.55: *$\eta(2\gamma)$ energy difference spectra for the reaction ($^7Li\gamma\eta X$). Full points represent the data, the red line a monte-carlo simulation of the coherent reaction Li($\gamma\eta$)Li, the dashed magenta line a monte-carlo simulation of the deuteron contribution Li($\gamma\eta$)d, the dashed green line a simulation of the neutron contribution Li($\gamma\eta$)n and the dashed blue line a simulation of the proton contribution Li($\gamma\eta$)p. The sum of the simulated coherent and break-up reactions are represented by the solid blue line.*

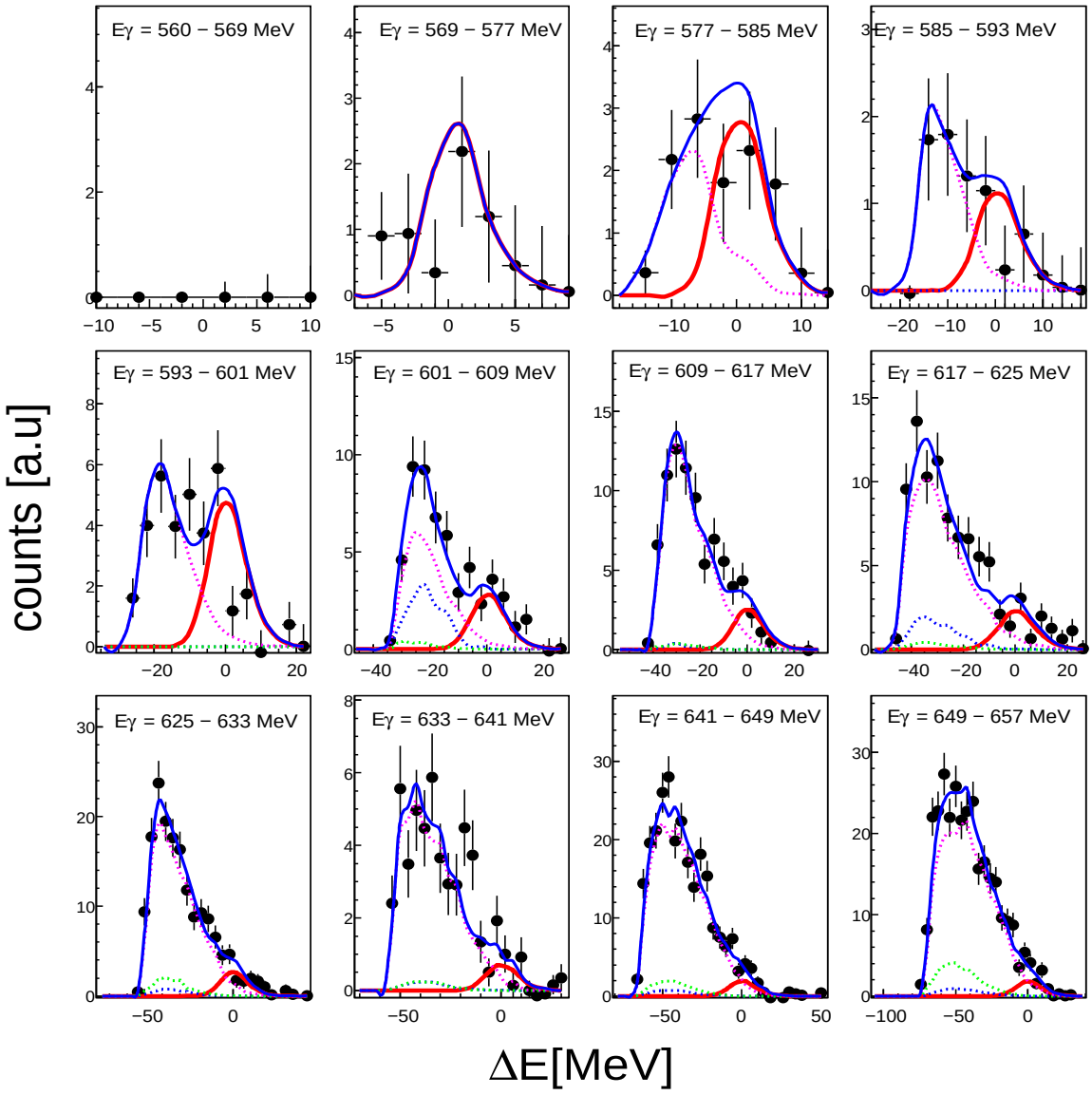

Figure 6.56: *$\eta(6\gamma)$ energy difference spectra for the reaction ($^7Li\gamma\eta X$). Full points represent the data, the red line a monte-carlo simulation of the coherent reaction Li($\gamma\eta$)Li, the dashed magenta line a monte-carlo simulation of the deuteron contribution Li($\gamma\eta$)d, the dashed green line a simulation of the neutron contribution Li($\gamma\eta$)n and the dashed blue line a simulation of the proton contribution Li($\gamma\eta$)p. The sum of the simulated coherent and break-up reactions are represented by the solid blue line.*

The obtained missing energies of the four simulated reactions were plotted together and scaled to match to the data as seen in Fig. 6.55 for the 2γ channel

and in Fig. 6.56 for the 6γ channel. The missing energies were plotted for different E_γ ranges from threshold (569 MeV) up to 660 MeV. The simulation contributions fitted mostly well in spite of the lack of statistics but sometimes the fits were not good. The deuteron contribution was surprisingly quite significant for both channels which needs advanced investigation. More improvement will be brought up before publishing the data.

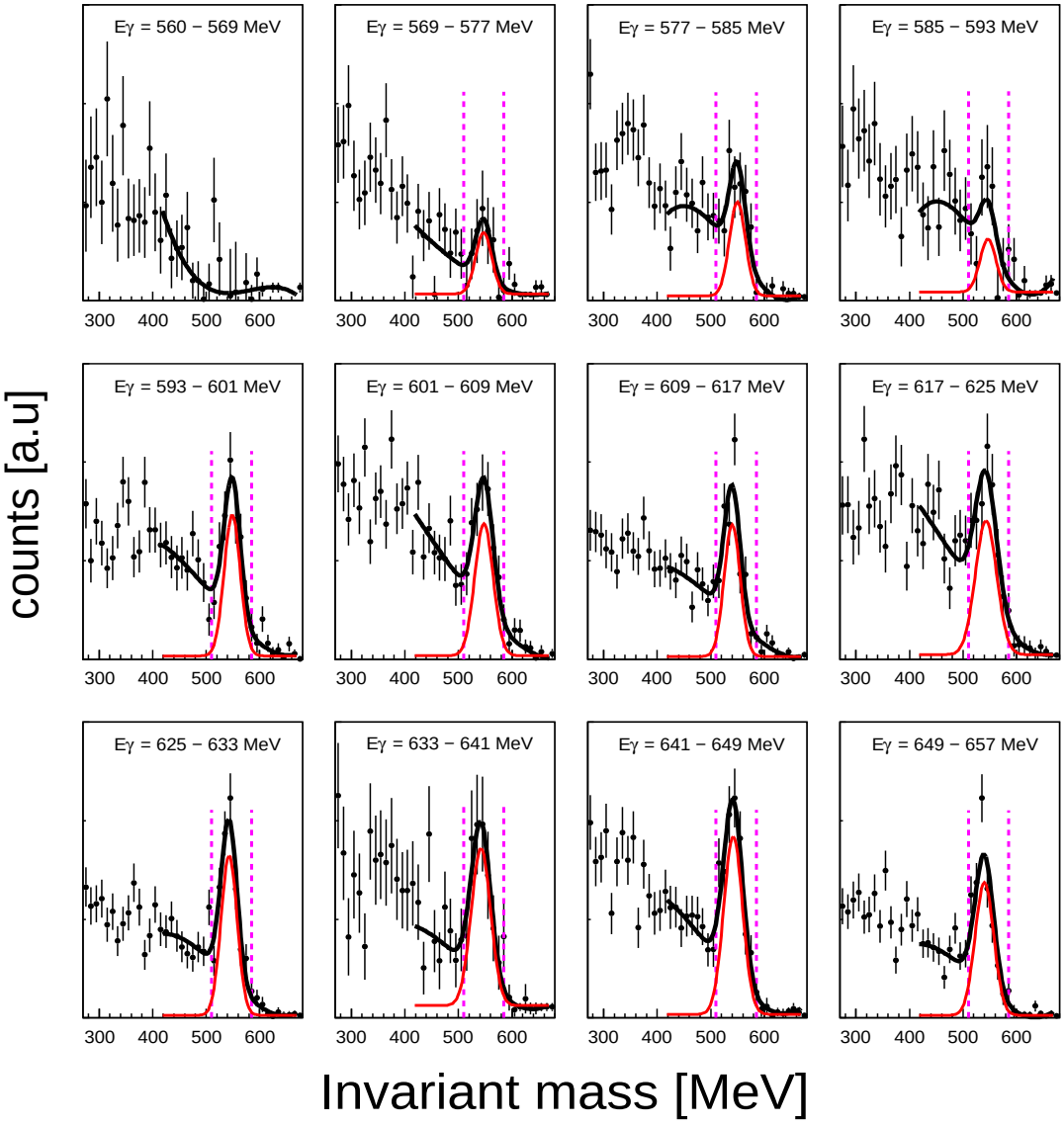

Figure 6.57: *Coherent $\eta(2\gamma)$ invariant mass for different E_γ with -10<ΔE<10 MeV (see text). The applied cuts are represented by the dashed lines. The signal to background ratio was estimated using a Gaussian+polynomial fit.*

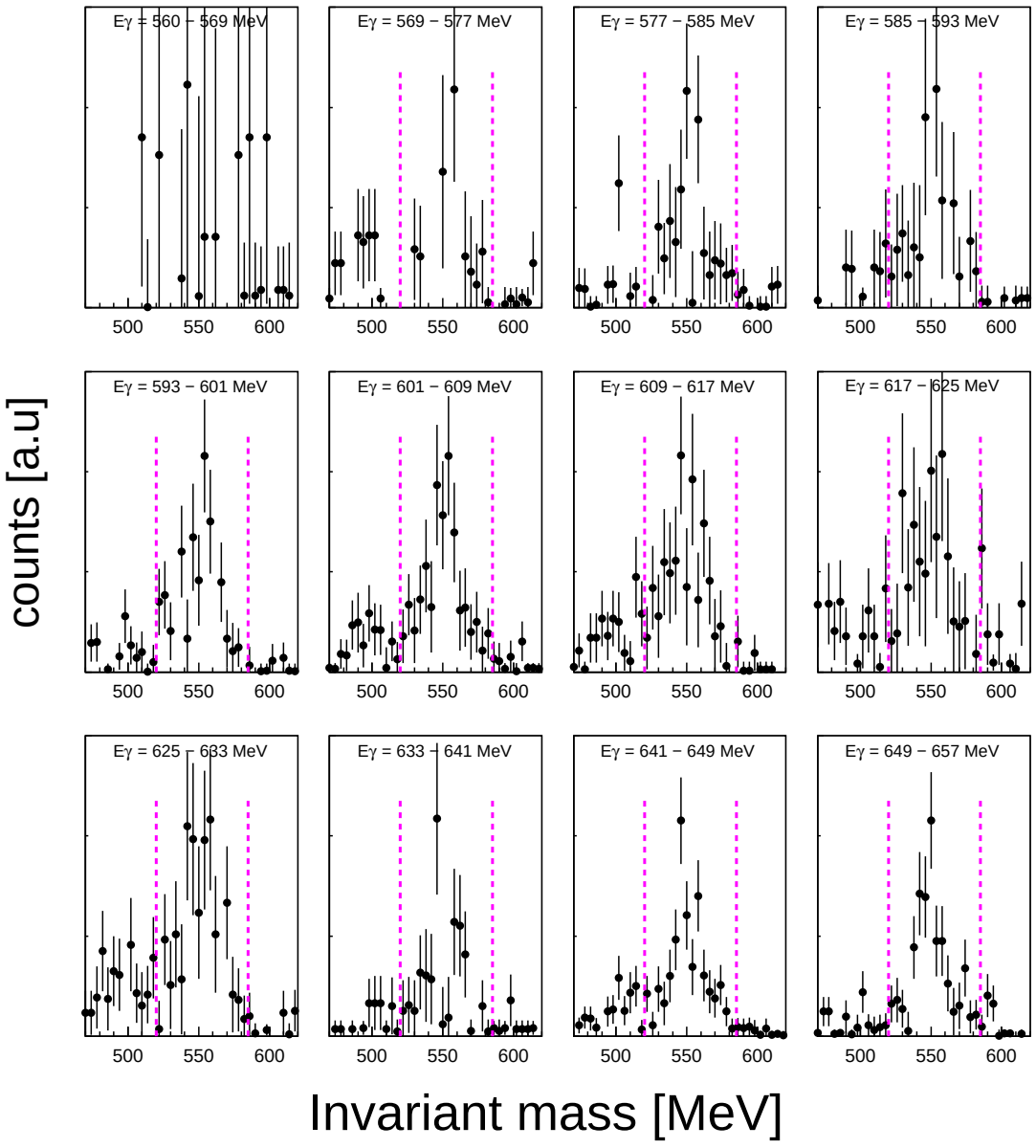

Figure 6.58: *Coherent $\eta(6\gamma)$ invariant mass for different E_γ with -10<ΔE<10 MeV (see text). The applied cuts are represented by the dashed lines. This channel is almost background free.*

Before estimating the coherent signal, the invariant mass spectra have been plotted for both channels with a cut on the missing energy -10<ΔE<10 MeV. The spectra show a non-negligible combinational background for the $\eta(2\gamma)$ channel whereas the $\eta(6\gamma)$ is almost background free. The invariant mass spec-

tra of the 2γ channel were fitted using *Gaussian+polynomial* fit. The spectra are shown in Fig. 6.57 and Fig. 6.58 where the applied cuts can also be seen.

The total cross sections were obtained by application of eq. 6.1. For the 2γ channel, for each bin of Eγ, the signal was obtained by considering the integral of the coherent simulated contribution divided by the peak-to-background ratio. The peak-to-background ratio was obtained by:

$$\frac{S}{S+B} = \frac{\text{Integral of the Gaussian}}{\text{Integral of the invariant mass}} \text{ between 500-600 MeV.} \tag{6.20}$$

For the 6γ channel, the signal was simply given by the integral of the Gaussian inside the cuts as it is almost background-free.

The detection efficiency was plotted as function of E_γ. Fig. 6.59 shows the detection efficiency plotted together for the 2γ and the 6γ channels.

Fig. 6.60 shows the obtained cross sections plotted together for the 2γ and the 6γ channels.

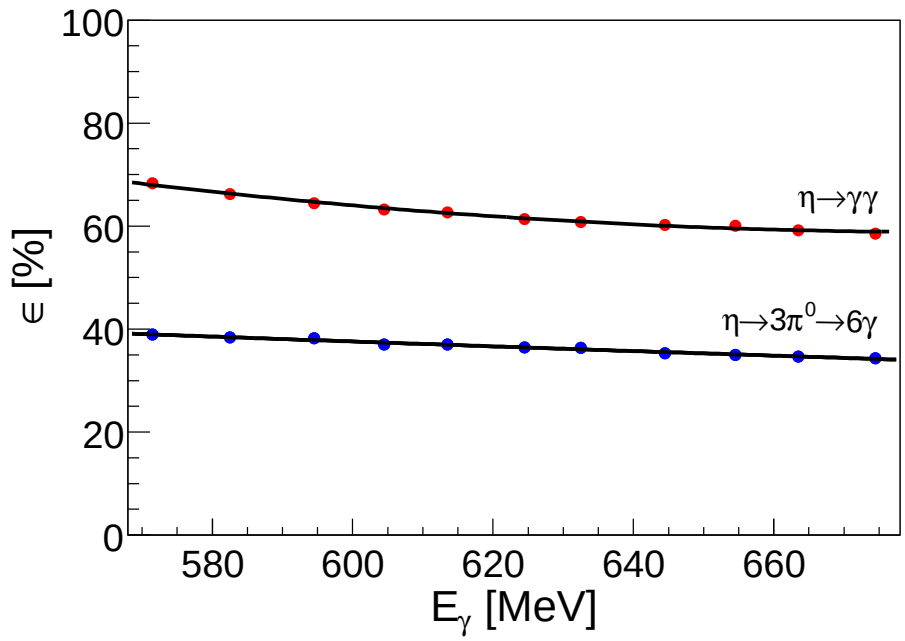

Figure 6.59: *Coherent η detection efficiency vs. E_γ for 2γ channel (red) and 6γ channel (blue).*

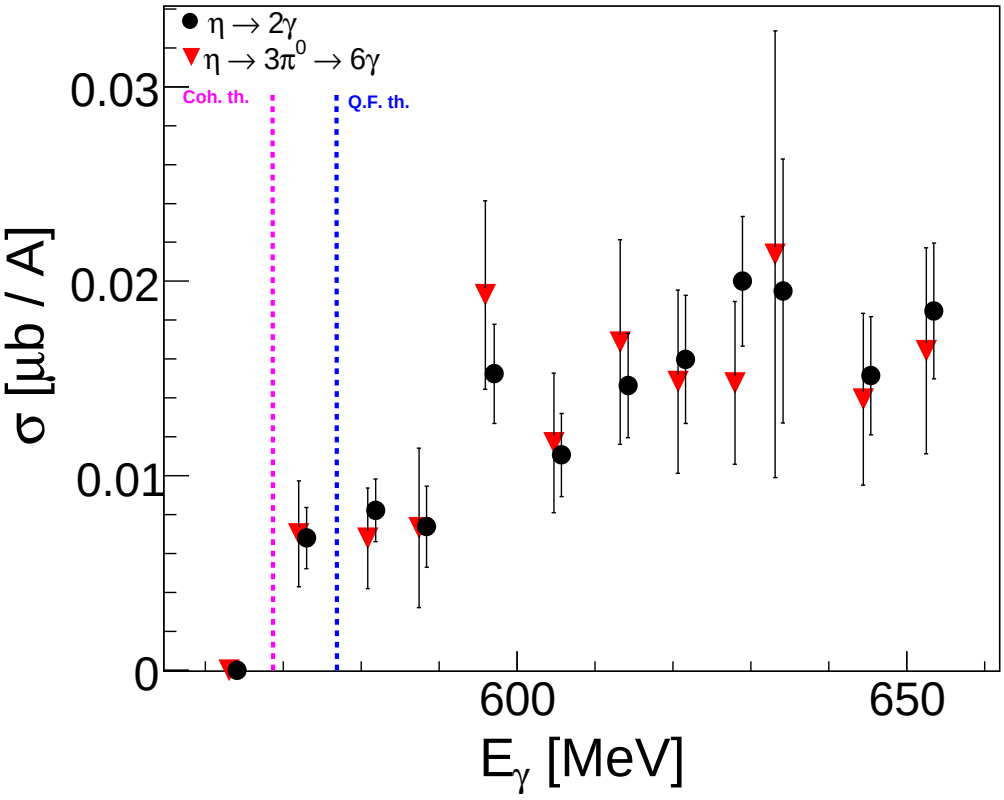

Figure 6.60: *Total coherent cross section versus E_γ for 2γ channel (black points) and 6γ channel (red triangles) obtained by the integration of the simulated coherent contributions.*

6.4.3 The topic of η-mesic nuclei

As described in chapter II, an enhancement of the coherent cross section around the coherent production threshold could be interpreted as presence of quasi-bound state η-nucleus (or η-mesic nucleus). The evidence of the formation of an η-mesic in ^{7}Li could be investigated as well in its decay via emission of back-to-back nucleon-pion pairs. For this purpose, the following reaction has been investigated :

$$\gamma +^7 Li \rightarrow (\eta +^7 Li) \rightarrow \pi^0 + p + X \tag{6.21}$$

In order to identify this reaction, a π^0 and a proton were detected in the final state. The proton was identified in TAPS using the Time-of-flight (see sect. 5.2.2) and in CB using a banana cut (see). The π^0 was identified in the usual way. A cut between 110 and 160 MeV has been applied to the invariant mass of the π^0 .

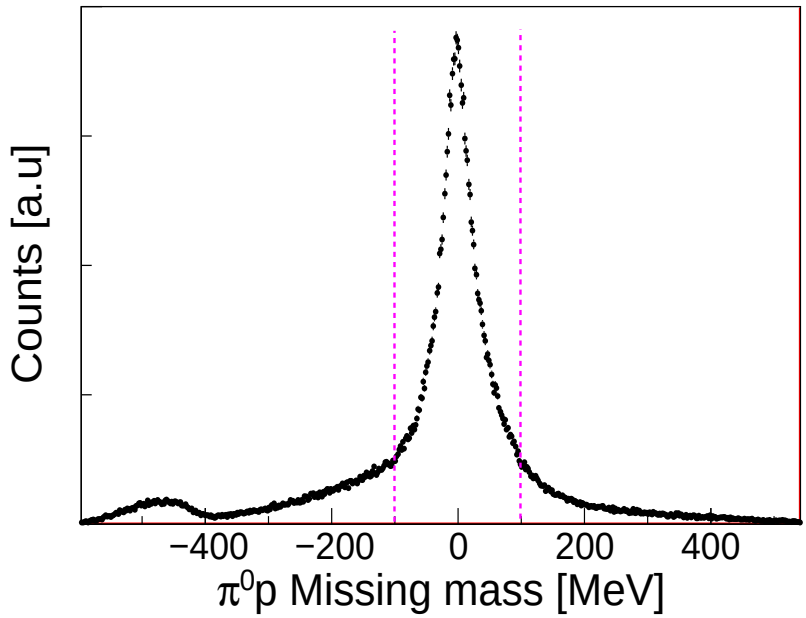

Figure 6.61: *Example of missing mass distribution assuming the quasi-free π^0 production of ^{7}Li ($\gamma +^7 Li \rightarrow \pi^0 + p +^6 Li$) for E_γ = 800 MeV. Some background related to the double pion production can contribute. The applied cut are showed by the dashed line.*

Some background for the single π^0 final state due to the double pion production had to be removed. This was done using a missing mass cut for the reaction $\gamma + ^7 Li \rightarrow \pi^0 + p + ^6 Li$. Fig. 6.61 shows the resulting distribution for E_γ around 800 MeV. The double pion channel contribution is reflected especially at high energy. By selecting events with missing masses between -100 and 100 MeV, the major part of the double pion background can be eliminated.

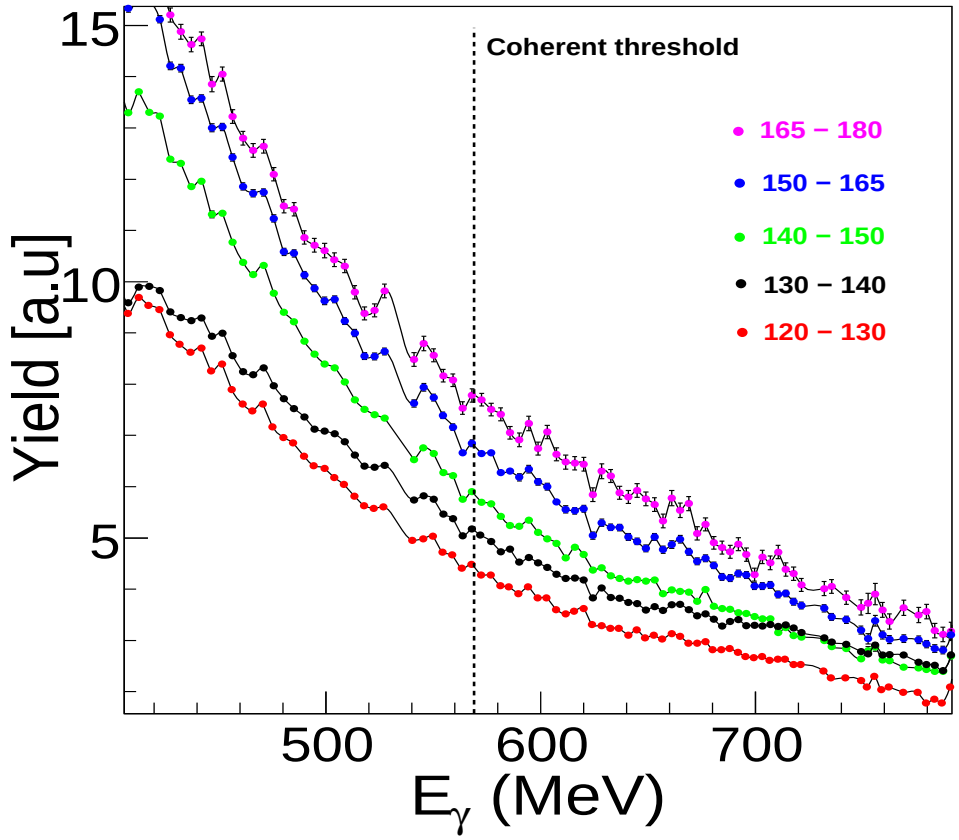

Figure 6.62: *Excitation function of the reaction* $\gamma + ^7 Li \rightarrow (\eta + ^7 Li) \rightarrow \pi^0 + p + X$ *in the* (γ ,^{7}*Li) center of momentum for different* (π,*p) opening angles.*

The next step was to plot the excitations functions for the π^0 +p final state for different opening angles of the pion and the proton in the γ -^{7}Li center of momentum frame. The distributions are dominated by the single π^0 production via the-Δ resonance. Some resonances of the second resonance region might be also partly seen. A possible signature of η-quasi bound state would be an enhancement in the excitation function at high opening angle around the coherent η threshold. These excitation functions are plotted for ^{7}Li in Fig. 6.62.

The difference between excitation functions for different opening angles has been established as shown in Fig. 6.63. These results could not be conclusive without a complete cross section study which needs further analysis and detection efficiency calculation. In addition, some dead Tagger channels in the threshold region made the analysis more difficult. However, a complete study would benefit from the possible use of the *microscope* which was implemented during the beam time of the present experiment but not yet used in the present analysis.

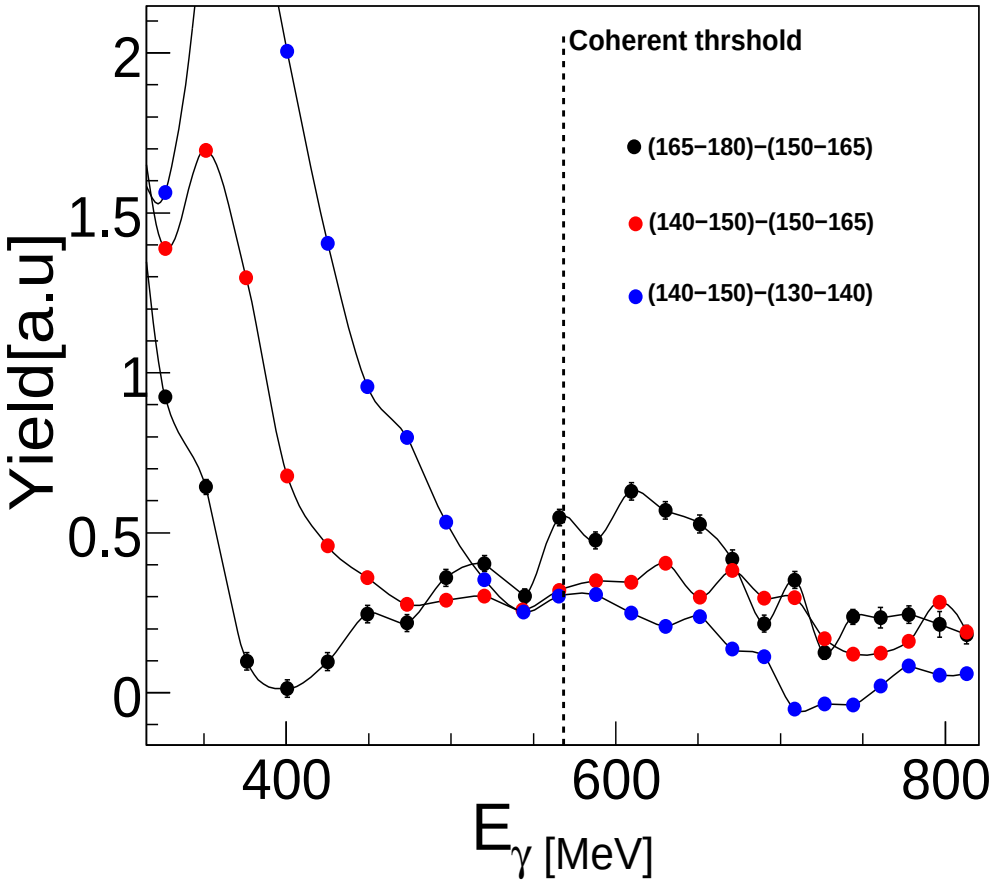

Figure 6.63: *Difference of excitation functions for different (π,p) opening angles. In black is the difference between the opening angles [165-180] and [150-165]°, in blue the difference between the opening angles [140-150] and [150-165]° and in red the difference between the opening angles [130-140] and [140-150]°.*

6.4.4 Discussion

The obtained coherent cross section was normalized and compared to the cross section extracted for ^{3}He by F. Pheron. The normalization of the form factors was very roughly approximated by dividing the ^{7}Li by 10 as discussed in 2.4.

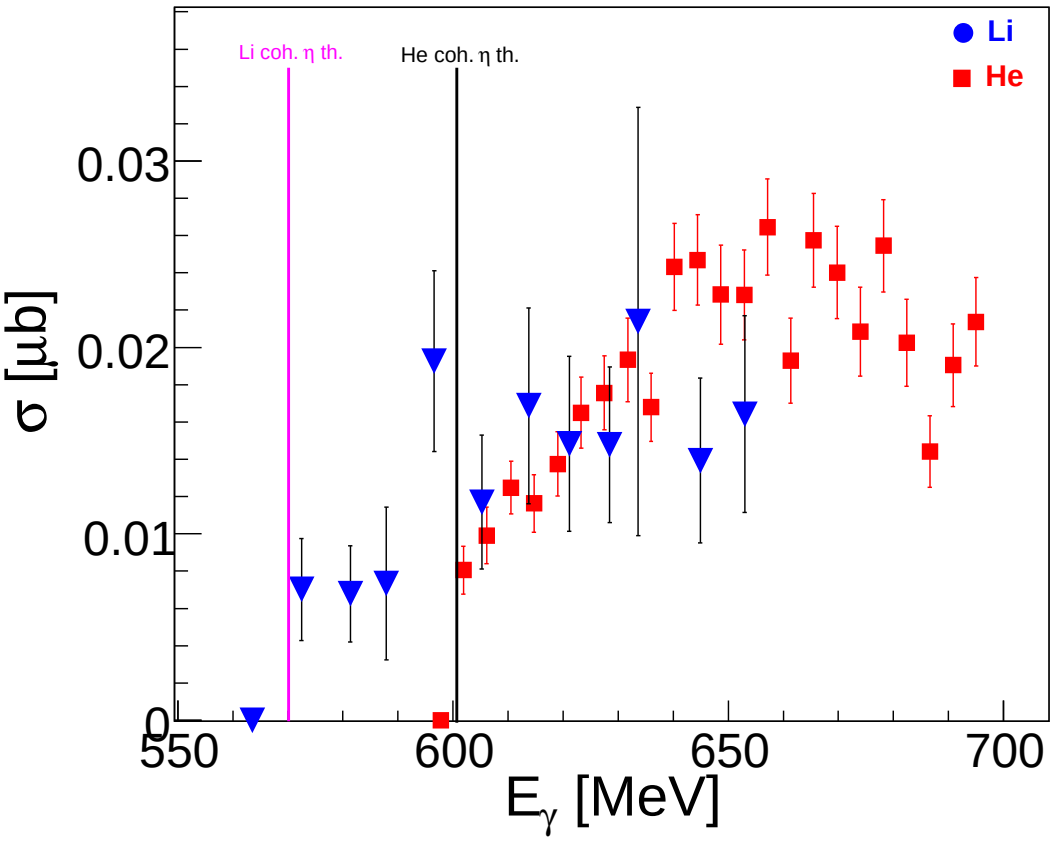

Figure 6.64: *Total coherent cross section of $\eta(2\gamma)$ normalized and compared to ^{3}He. For normalization see text.*

Comparison shows a quite good agreement between both results. The ^{7}Li is expected to show a softer rise at threshold due to the fact that the pole of the η quasi-bound state is further away in ^{7}Li compared to ^{3}He [106]. Further discussion is needed especially regarding the normalization (the form factors should be averaged over q depending on the incident photon energy) as well as the difference between the nature of the FSI in Li and He.

Chapter 7

Systematic uncertainties

7.1 Overview

The calculation of the cross sections presented in this work would not be complete without a rigorous study of the systematic uncertainties which do not affect the interpretation of the results. The main sources of these uncertainties are summarized in the following points:

- **Systematic error related to the photon flux:**
  This is due to the effects of the tagging efficiency measurements during the beamtime and the P2/Tagger ratio (see sect. 4.3). The effect of the tagging efficiency variation had been estimated in [105]. It was done by recording the extrema values of the tagging efficiency for every single Tagger channel for each beamtime. The obtained value of 2.5% can be held in the present experiment.
  In addition, as seen in Fig. 4.16, the matching between the P2/Tagger ratio and the individual tagging efficiency measurement is not perfect and would induce an additional error. This error was estimated by calculating the difference, averaged over five distinct tagger channels, between the P2/tagger ratio and the tagging efficiency values as shown in Fig. 7.1. The absolute obtained uncertainty is oscillating around 5%.

- **Systematic error related to the target:**
  The systematic uncertainty on the measurement of a solid target (surface thickness measurement) is usually small and is more accurate than a gas one. However, the ^{7}Li target was not well shaped. One would estimate

here the total systematic uncertainty on the target to be around 3%. Note that the systematic uncertainty related to the impurities present in the target are negligible.

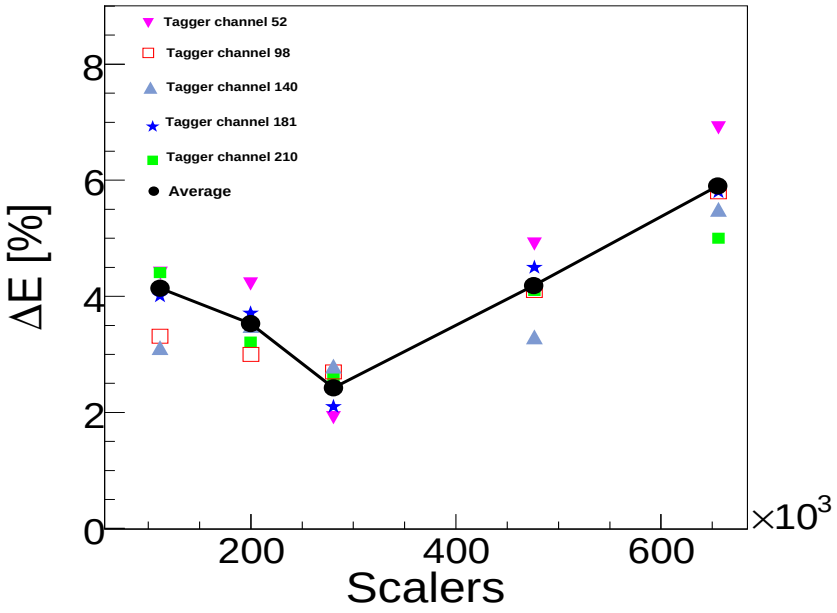

Figure 7.1: *Systematic uncertainty of to the P2/Tagger ratio. It was obtained by calculating the difference between the P2/tagger ratio and the tagging efficiency values averaged over five distinct tagger channels with* $\Delta E = 100 \cdot \frac{(P2/tagger)}{\epsilon}$ *(ϵ is the tagging efficiency).*

- **The detector efficiency uncertainty**:
  The systematic error on the detector efficiency might be estimated by studying the effect of a slight modification of the start distribution. The parameters to be modified in the start distributions depend on the studied channel. For the quasi-free η channel for example, this can be estimated by studying the effect on the angular distributions of a slight modification of the η kinetic energy and/or the η polar angle. For the double pion channel, a study of the effect of the simulated FSI seems judicious (see below).

- **Effects related to the off-line analysis:**
  The cuts and the fits used in the off-line analysis for the extraction of the cross sections might induce some systematic uncertainties. The effects of the usual π^0 and η invariant mass cuts (e.g $110 < M_{\pi^0} < 160$) have been

tested and are negligible. However, other effects are not negligible such those related to the side-bin background subtraction in the double pion channel (Fig. 6.2) or to the signal extraction from the invariant mass fits (e.g. Fig. 6.51).

The two last points have to be treated depending on the studied reaction. In the following only the systematic uncertainty of the double pion channel will be discussed in details.

7.2 The systematic effects of the $\pi\pi$ channel

For the double pion channel, the uncertainty of the detector efficiency was estimated by testing different start distributions in the event generator. This was done by varying the strength of the pion FSI. This choice is also justified by the fact that FSI have a direct impact on the slight difference between data and simulation in the missing mass spectra (see Fig. 6.5) especially at low energy. To do so, the effect on the detection efficiency of varying the nuclear radius parameter in the nFSI function (see sect. 6.2.1) has been studied.

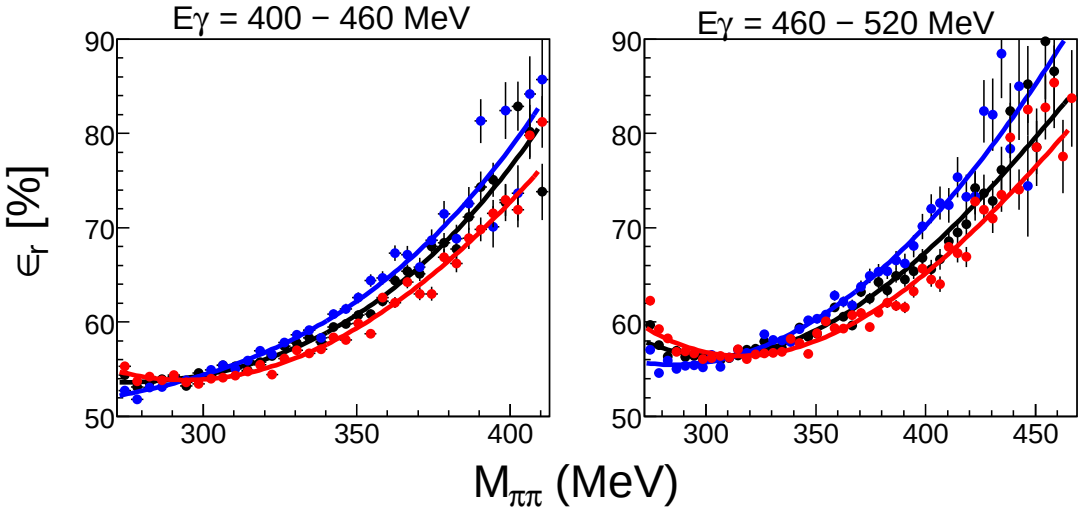

Figure 7.2: *Neutral detection efficiency for E_γ = [400-460] MeV (left) and [460-520] MeV (right) calculated using different values of nuclear radius (radnuc) of the nFSI function. In black radnuc = 2.3 fm (Li original value), in blue radnuc = 4 fm and in red radnuc = 1 fm.*

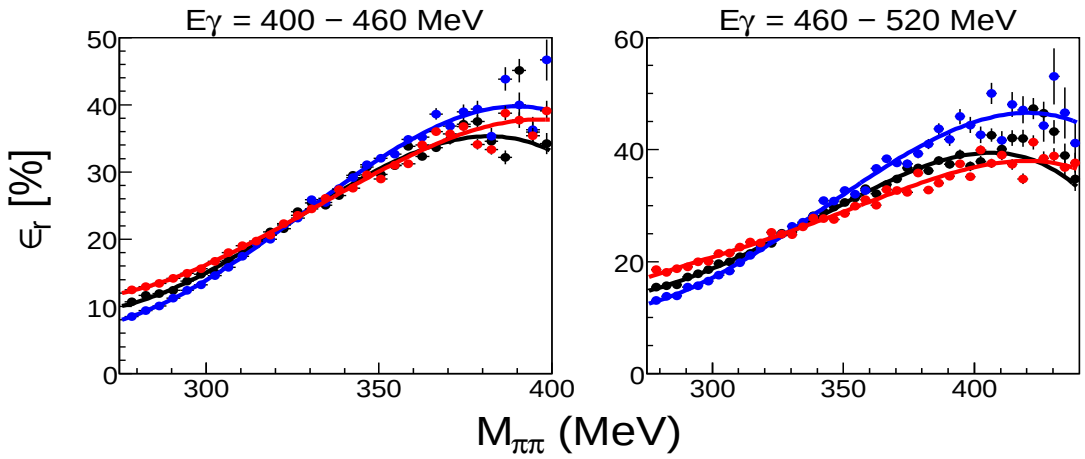

Figure 7.3: *Charged detection efficiency for E_γ = [400-460] MeV (left) and [460-520] MeV (right) calculated using different values of nuclear radius (radnuc) of the nFSI function. In black radnuc = 2.3 fm (Li original value), in blue radnuc = 4 fm and in red radnuc = 1 fm.*

Fig. 7.2 and 7.3 show the detection efficiency obtained by considering different nuclear radius in the nFSI function. The systematic uncertainty of the detection efficiency was then obtained by considering the difference between the invariant mass distributions obtained in the usual way and the average of those obtained by varying the start distributions. The result for the neutral channel is shown in Fig. 7.4.

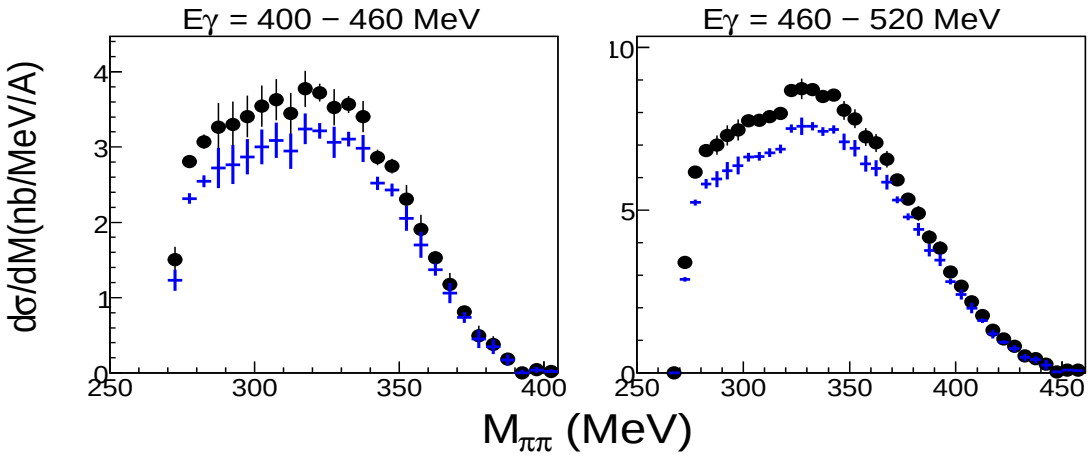

Figure 7.4: *Neutral mass distributions (black) plotted together with those corresponding to the systematic uncertainties on detection efficiency (blue), for details see text.*

In addition to the above common systematic effects, each channel had non-negligible further systematic effects to be accounted for. For the neutral channel, one had to estimate to the systematic effect of the "side-bin background" elimination. The invariant mass distributions were recalculated using different "side-bin" cuts (60-110 instead of 80-110 and 160-200 instead of 180-200 MeV). The uncertainty thereby obtained was normalized so that the side bin region was still proportional to the true signal region. The result is shown in 7.5.

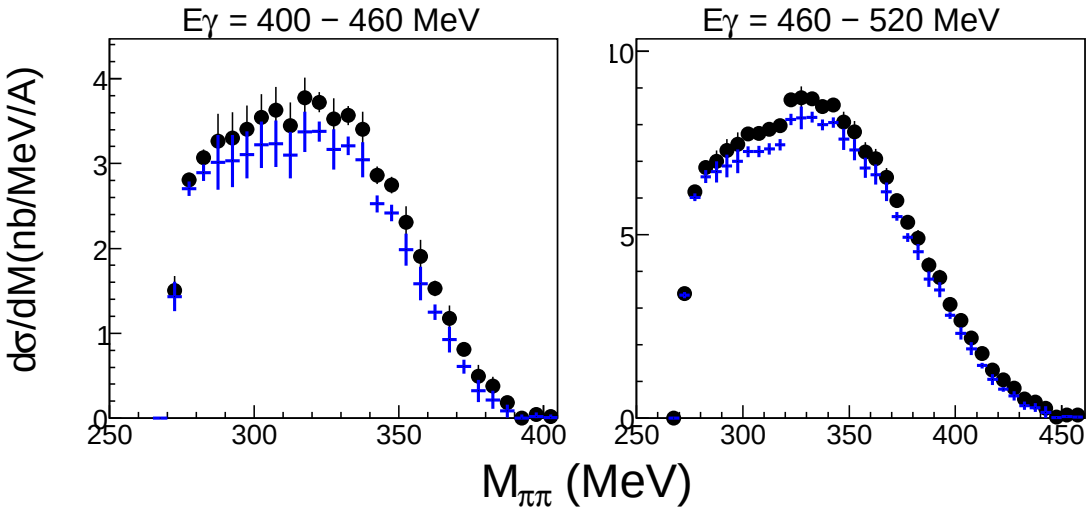

Figure 7.5: *Neutral mass distributions (black) compared to the ones obtained by varying the side bin background regions (blue). For details, see text.*

The systematic uncertainty was after that estimated on the fits used in the signal to background estimation (see Fig. 6.3 and 6.24). For this purpose, the fit properties were slightly modified (fit limits of the Gaussian and degree of the polynomial) following :

- Fit function: Gaussian + pol3 instead of Gaussian + pol4.
- Fit range: [50,210] MeV instead of [20,240] MeV.

The invariant mass distributions were then recalculated and subtracted from the original ones which gave the systematic error on the fit. Fig. 7.6 shows the invariant mass distributions compared to the ones obtained using different fit parameters.

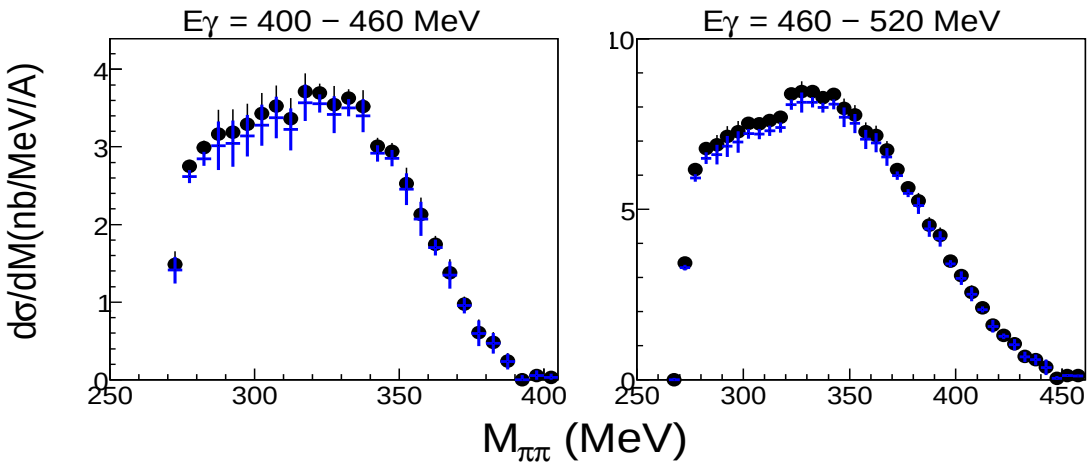

Figure 7.6: *Neutral mass distributions compared to the ones obtained using different fit parameters.*

The systematic uncertainty of the neutral channel is finally obtained by combining the different sources via:

$$\Delta E = \sqrt{(\Delta E^{Eff.})^2 + (\Delta E^{Fit})^2 + (\Delta E^{sidebin})^2} \tag{7.1}$$

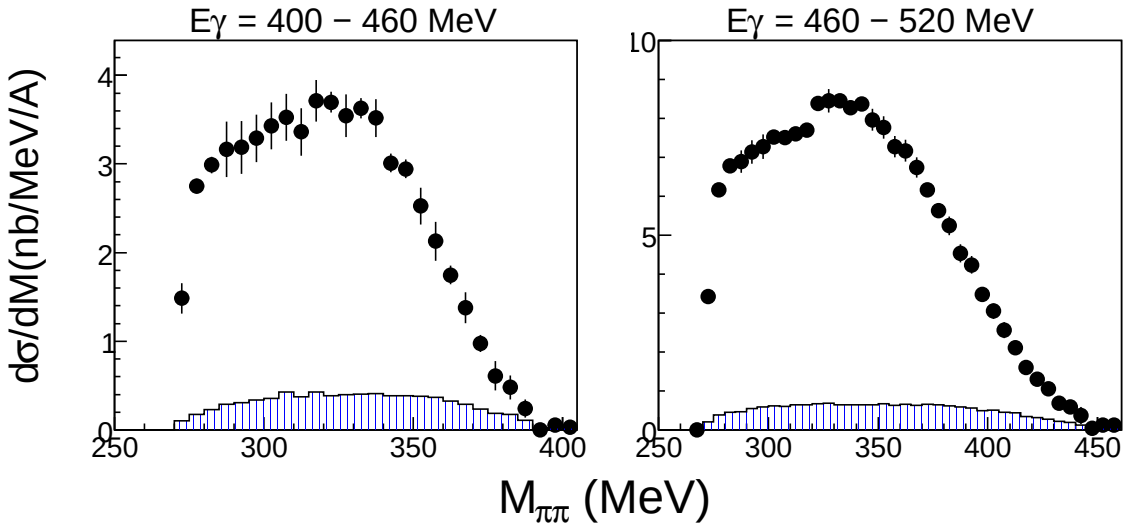

Figure 7.7: *Neutral mass distributions plotted together with systematic uncertainties.*

The obtained systematic uncertainty is shown in Fig. 7.7 together with the

neutral mass distributions for E_γ = [400 - 460] and [460 - 520] MeV. The systematic uncertainty is shown as well as function of E_γ in Fig. 7.8 together with the total cross section.

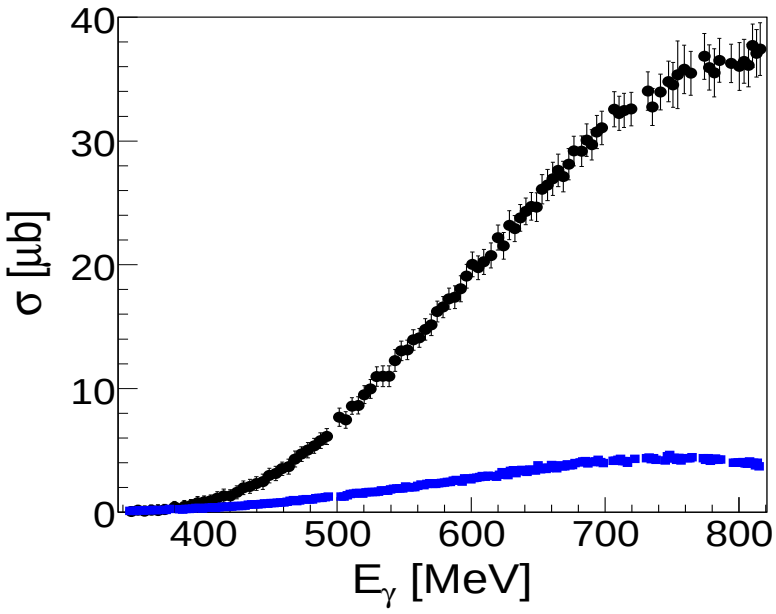

Figure 7.8: *Neutral total cross section (black points) and systematic uncertainties (blue squares) obtained from the combination of the effects discussed above.*

The mixed charged channel

For the mixed charged channel, a systematic study for the effect of the linear calibration of the $\pi^{+/-}$ kinetic energy made in sect. 6.2.2.2 seemed indispensable. To do so, the charged mass distributions were recalculated using a different calibration (i.e. a different linear fit in each case) and subtracted from the original one, which gave the systematic uncertainty of the $\pi^{+/-}$ calibration.

Furthermore, the uncertainty of the missing mass cuts seen in Fig. 6.14 and 6.15 were estimated in a similar way by testing the effect on the mass distributions obtained using 10% smaller missing mass cuts.

Finally, the systematic uncertainty of the mixed charged channel was obtained from the combination of these different effects via (similarly to the neutral channel):

$$\Delta E = \sqrt{(\Delta E^{Eff.})^2 + (\Delta E^{Fit})^2 + (\Delta E^{Calib.})^2 + (\Delta E^{\text{Miss. mass}})^2} \qquad (7.2)$$

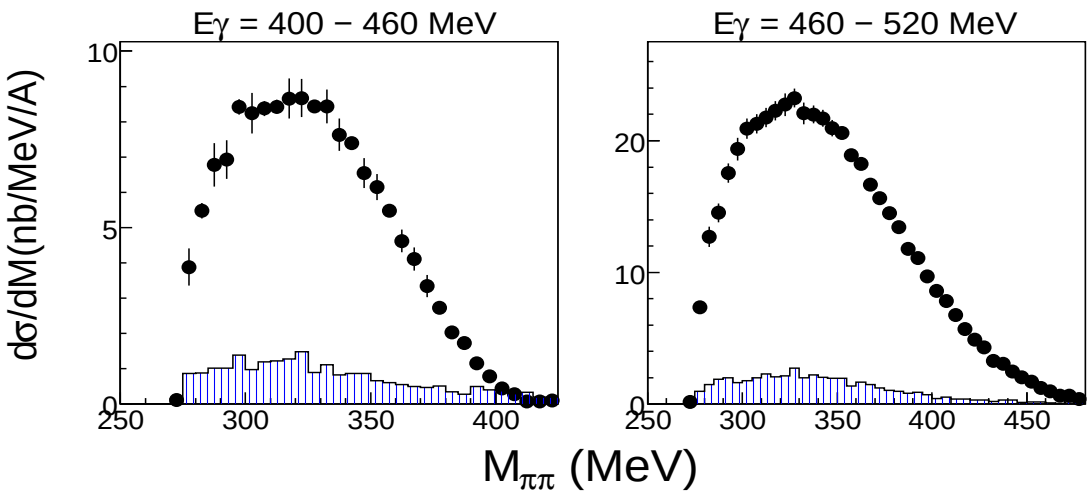

Figure 7.9: *Charged mass distributions plotted together with systematic uncertainties.*

The result is shown in Fig. 7.9 together with the charged mass distributions for E_γ = [400 - 460] and [460 - 520] MeV. The systematic uncertainty is shown as well as function of E_γ in Fig. 7.10 together with the total cross section.

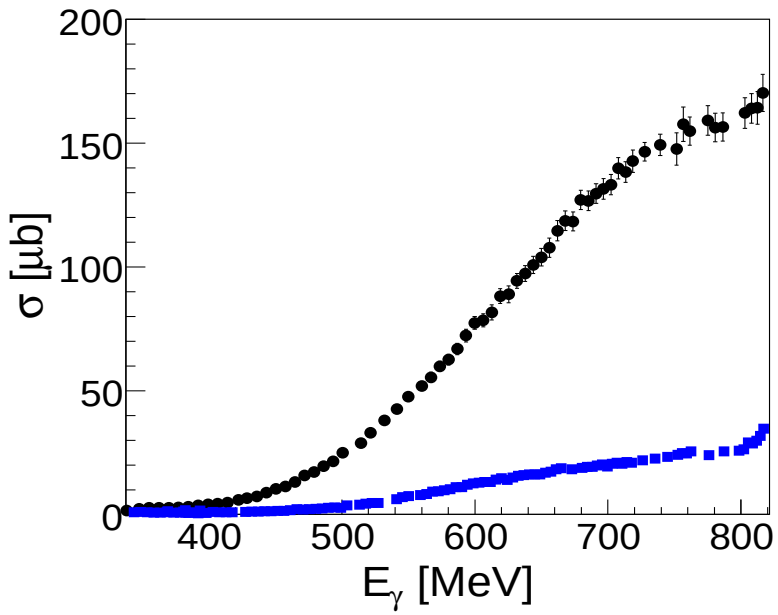

Figure 7.10: *Charged total cross section (black points) plotted together systematic uncertainties (blue squares) obtained from the combination of the different effects.*

7.3 Discussion

For the double pion channel, systematic effects appear quite large especially for the mixed charged channel. This is expected since various conservative cuts have been tested and combined.

Concerning the systematic uncertainty of the coherent π^0 cross section, the major effect would arise from the detection efficiency. The applied cuts on the missing energy and on the invariant mass have no significant impact. However, a systematic uncertainty should be accounted for the fit results on the Form Factor. A first estimation of $\sim 10\%$ of error on the obtained mass radius seems reasonable.

Concerning the coherent η channel, a precise systematic effects study will be done for the final results. It will mainly include the error on the detector efficiency and on the missing energy cuts.

Chapter 8

Conclusions and outlook

The photoproduction of neutral and charged mesons off ^{7}Li have been studied at MAMI with a maximum electron beam energy of 883 MeV. Apart from some minor problems (two broken PID elements, 25% of data were not utilizable ..) the analyzed data enjoyed high statistics and 4π solid angle of detector setup. The presented work aimed to investigate the properties of hadrons in nuclear matter through the analysis of different reactions.

The central part of this work focused on the double pion channel in view of the σ properties in medium which decays into $\pi^0\pi^0$ but not into $\pi^0\pi^{+/-}$. The absolute normalization of the obtained differential and total cross section are in good agreement with previous results on other targets.
We compared the invariant mass distributions of both channels for different incident photon beam energies in view of a possible shift of the neutral channel compared to the charged one. A relative shift was indeed observed at [400 - 460] and [460 - 520] MeV. Thanks to the quality of the statistics, the energy range of [300 - 400] MeV, much closer to the $\pi\pi$ quasi-free production threshold, could be analyzed. In this energy range, the FSI are supposed to be significantly smaller. The mass difference between a neutral and a charged pion was also taken into account. We observed the same shift at this energy range although it can still be due to the FSI. This shift can also be due to an effect of charge exchange between pions.

With the complete systematic effects presented at the end of this work, we consider the double pion results to be final. As an outlook, the combined analysis of ^{7}Li and heavy target (C, Ca and Pb) high statistics data originally analyzed

in the Giessen group is supposed to bring more conclusive informations. This is supposed to follow in the next few months.

In the second part we discussed the results of the coherent π^0 photoproduction off ^{7}Li. For this reaction, statistics were very high. We extracted the differential cross sections as function of the momentum transfer and as function of θ_π in the (γ,^{7}Li) center of momentum. This reaction served also to extract informations about the ^{7}Li mass distribution. We extracted the ^{7}Li form factor in PWIA and calculated the mass rms radius. The obtained results are in good agreement with values we found in literature. However, results were obtained for E_γ = [180 - 220] MeV. FSI prevented averaging the mass rms-radius with results obtained at higher energies. Therefore, DWIA and other calculations are needed for ^{7}Li before going further in the analysis.

Finally, we observed a coherent η signal for the first time in an A>3 nucleus. We extracted the total coherent cross section by integrating the coherent contributions in the missing energy spectra. The cross section was then normalized to the ^{3}He by considering an approximative difference in form factors. Results from both nuclei appear to be in good agreement even if some combinational background was included.
The η-bound states were also investigated via the (π^0 ,p) excitation functions. No conclusive results were obtained. However, a second analysis can be done with the microscope activated. The results presented for the coherent η channel this part are therefore preliminary and still promising.

During the present analysis, in addition to the presented results, different other reactions have been approached. We had unfortunately not enough time to make a complete analysis for these reactions within the PhD work. Most of them are focused on the coherent production. The missing energy spectra are plotted below for the following reactions:

Reaction	Threshold [MeV]
$\gamma +^7 Li \rightarrow \pi^0 + \pi^0 +^7 Li$	275.53
$\gamma +^7 Li \rightarrow \pi^0 + \pi^0 + \pi^0 +^7 Li$	417.477
$\gamma +^7 Li \rightarrow \eta + \pi^0 +^7 Li$	717.899

Table 8.1: *Other potential coherent reactions and their thresholds.*

All of these spectra show a coherent-like peak close to threshold. Obviously, no conclusions can be made without a complete simulation of the reaction (coherent and breakup). However, these reactions seem very promising, since most

of them are already observed and analyzed in our group (Papers by I. jaegle for the coherent $\pi\pi$ and coherent $\pi\pi\pi$ and $\eta\pi$ on D and ^{3}He and I. Keshelashivili for $\eta\pi$ on ^{12}C are in preparation).

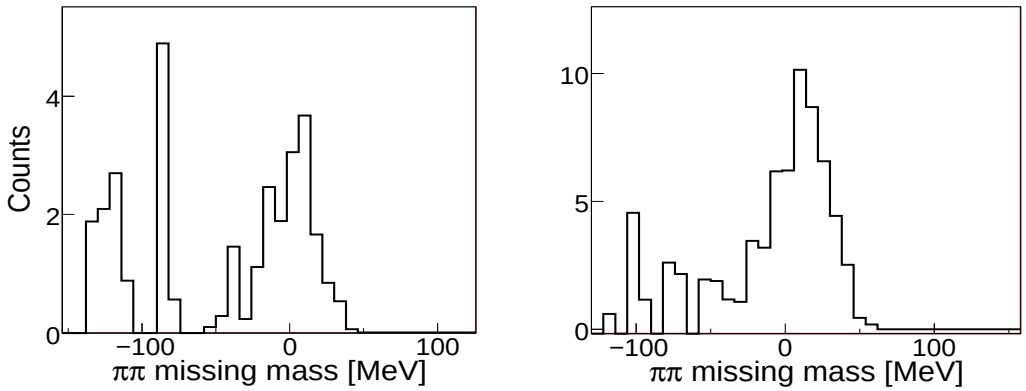

Figure 8.1: *$\pi\pi$ missing mass for E_γ = [270 - 325] (left) and [325 - 345] MeV (right).*

The coherent $\pi\pi$ channel could also be very interesting for the in medium properties of hadrons. Calculations made by Kamalov and Oset [119] for $\pi^0\pi^0$ and $\pi^0\pi^{+/-}$ coherent cross sections on ^{12}C showed that the reaction can serve as a source of information about Δ properties in medium, similarly to the (γ ,π^0) reaction. The reaction could also be useful for the σ -meson in medium by comparing the coherent $(\gamma, \pi^0\pi^0)$ and $(\gamma, \pi^+\pi^-)$ mass distributions. (coherent $(\gamma, \pi^0\pi^{+/-})$ reaction is forbidden for charge conservation reasons).

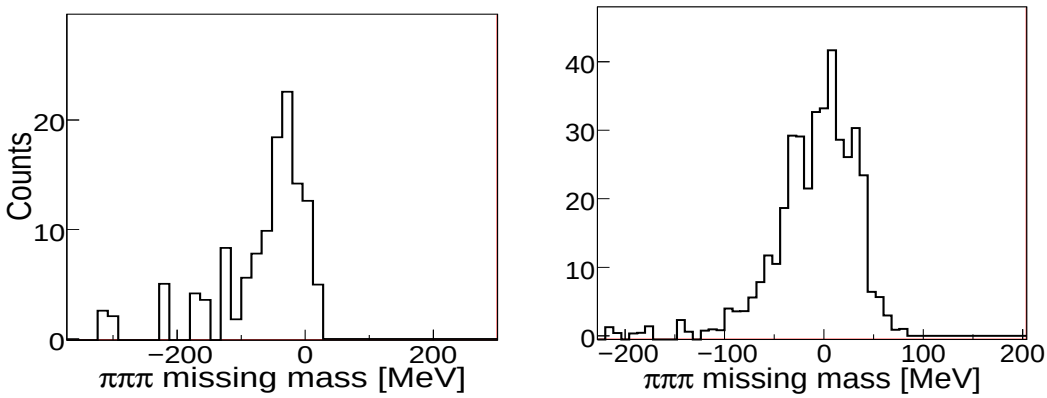

Figure 8.2: *$\pi\pi\pi$ missing mass for E_γ = [414 - 670] (left) and [670 - 720] MeV (right).*

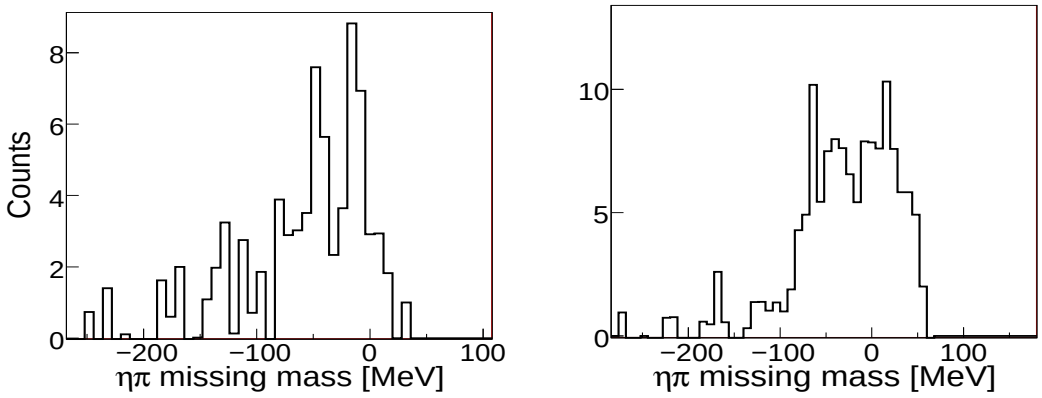

Figure 8.3: *$\eta\pi$ missing mass for E_γ = [700 - 766] (left) and [766 - 820] MeV (right).*

To sum up, the ^{7}Li data are promising for the $\pi\pi$ in medium studies as they will serve as a new reference for the comparison between light and heavy nuclei. These ^{7}Li data have demonstrated a large potential for various studies. Diverse other studies could perhaps be investigated such as the very exciting topic of the incoherent π^0 photoproduction off ^{7}Li. The idea is to use this reaction to measure the decay photons of the ^{7}Li energy levels[1]. That would provide new data for high beam energies without having to worry too much about the energy resolution.

[1]First result on Carbon can be found in [120].

Chapter 9

Tables

This chapter summarizes the values of the cross sections obtained in chapter VI and the tagger calibration file (Tagger channels and the corresponding incident photon beam energies). Only the $\pi\pi$ cross sections are presented. Data (ascii files) for the coherent π^0 channel and the η channel will follow later on. They will be available (as well as the cross sections of the $\pi\pi$ channel) at the following location :

http://jazz.physik.unibas.ch/ yasser/thesis/XXXX.dat

Table 9.1: $\pi^0\pi^0$ *Total cross section*

E_γ [MeV]	σ (μb)	E_γ [MeV]	σ (μb)
816.45	35.99±2.99	639.81	24.61±1.47
813.81	36.24±2.70	635.68	23.55±1.50
810.97	37.33±2.39	631.54	22.52±1.40
807.92	36.06±2.40	627.41	23.39±1.81
804.67	37.07±2.34	623.23	21.87±1.39
801.25	36.16±2.63	619.02	21.93±1.46
797.66	35.09±2.81	614.78	21.04±1.58
793.96	10.93±1.29	610.53	20.26±1.52
790.17	13.22±1.20	606.28	19.69±1.38
786.34	36.22±2.56	601.99	20.28±1.45
782.52	35.96±2.89	597.68	18.82±1.26
778.76	36.49±2.63	593.32	18.33±1.60
775.10	36.58±2.51	588.97	17.43±1.30
764.85	35.01±2.32	584.62	17.88±1.21
761.59	34.49±2.65	580.23	16.54±1.21
758.31	35.02±2.48	575.82	16.43±1.18
754.99	36.47±3.98	571.36	15.11±1.21
751.65	34.07±2.63	566.91	15.20±1.26
748.28	34.31±2.51	562.47	14.17±1.07
744.89	35.30±2.12	557.98	14.03±1.12
738.02	32.59±1.95	553.47	12.96±1.08
734.58	32.80±2.08	548.95	13.22±1.05
731.09	33.69±2.12	544.38	12.71±1.33
720.48	32.44±1.98	539.85	10.99±1.18
716.89	32.89±1.84	535.28	10.99±1.18
713.28	32.67±2.01	526.08	10.17±1.10
709.64	33.00±2.00	521.43	9.53 ±1.014
705.95	32.23±2.02	516.79	8.63 ±1.036
702.26	30.58±1.82	512.17	8.69 ±0.965
698.57	31.76±1.89	507.50	7.66 ±0.957
694.83	30.43±1.89	502.82	7.86 ±1.021
691.06	29.22±1.76	498.13	6.71 ±0.990
687.25	30.80±1.87	493.39	6.31 ±0.923
683.45	28.89±1.85	488.70	5.74 ±0.840
679.61	28.25±1.68	483.96	5.32 ±0.917
675.74	27.49±1.64	479.22	5.10 ±0.884
671.82	28.29±1.77	474.46	4.71 ±0.824
667.90	27.47±1.71	469.66	4.56 ±0.908
663.98	27.29±1.77	464.88	3.69 ±0.895
656.02	25.01±1.67	460.11	3.57 ±0.783
651.99	26.95±1.61	455.31	3.24 ±0.824
647.96	24.05±1.64	450.49	3.13 ±0.834
643.90	24.81±1.56	445.67	2.37 ±0.983

E_γ [MeV]	σ (μb)	E_γ [MeV]	σ (μb)
440.80	2.42±0.783	392.02	0.58±0.671
435.99	1.98±0.824	387.10	0.50±0.675
431.13	2.14±0.743	382.14	0.45±0.704
426.27	1.57±0.744	377.25	0.19±0.685
421.40	1.26±0.704	372.31	0.21±0.584
416.52	1.50±0.744	367.37	0.22±0.635
411.61	1.12±0.740	362.42	0.23±0.617
406.74	0.83±0.675	357.47	0.08±0.579
401.84	0.89±0.665	352.48	0.15±0.568
396.94	0.74±0.667		

Table 9.2: $\pi^0\pi^{+/-}$ *Total cross section*

E_γ [MeV]	σ (μb)	E_γ [MeV]	σ (μb)
815.16	174.58±12.72	604.14	78.01±4.39
810.97	162.74±10.74	597.68	73.98±4.24
806.32	162.78±10.56	591.15	70.15±4.28
801.25	157.87±11.34	584.62	68.50±3.97
784.43	159.47±9.63	578.03	62.27±3.73
778.76	159.88±10.33	571.36	58.19±3.61
773.32	160.92±10.64	564.70	52.74±3.26
763.22	159.65±9.80	551.21	47.87±2.89
758.31	150.42±9.66	537.57	39.20±2.83
753.32	147.85±14.27	523.7	33.91±2.20
748.28	148.41±9.87	516.79	29.09±2.11
743.19	150.86±8.67	509.84	28.82±1.92
738.02	145.96±7.91	502.82	25.85±2.28
732.84	149.02±8.25	495.75	22.11±2.07
722.24	142.15±7.71	488.70	20.26±1.65
716.89	140.50±8.19	481.59	18.27±1.65
711.46	134.85±6.91	474.46	16.20±1.48
705.95	136.20±7.61	467.27	13.76±1.30
700.43	131.26±7.20	460.11	11.87±1.13
694.83	133.44±6.70	452.90	10.97±1.03
689.15	128.62±6.85	445.67	9.331±1.39
683.45	125.45±7.27	438.38	7.800±0.77
677.68	132.38±7.01	431.13	7.142±0.98
671.82	118.10±6.72	423.84	5.919±0.77
665.96	119.05±7.27	416.52	5.026±0.71
660.01	118.35±7.06	409.16	4.491±0.40
654.00	104.58±6.58	401.84	4.434±0.59
647.96	101.19±5.92	394.48	3.722±0.34
641.86	99.53±5.76	387.10	3.378±0.34
635.68	93.92±5.38	379.68	2.853±0.31
629.49	93.28±5.18	372.31	2.744±0.32
623.23	88.14±5.42	364.9	2.628±0.34
616.91	86.18±4.97	357.47	2.650±0.33
610.53	79.55±5.19	350.00	2.549±0.34

Table 9.3: *$\pi\pi$ invariant mass distributions for E_γ = [400 - 460] MeV*

$M_{\pi\pi}$ [MeV]	$d\sigma/dM(\pi^0\pi^0)$ (nb/MeV)	$d\sigma/dM(\pi^0\pi^{+/-})$ (nb/MeV)
272.5	1.50±0.17	0.11±0.05
277.5	2.80±0.08	3.88±0.52
282.5	3.07±0.09	5.47±0.21
287.5	3.26±0.32	6.77±0.61
292.5	3.29±0.30	6.92±0.54
297.5	3.40±0.27	8.41±0.22
302.5	3.54±0.27	8.23±0.57
307.5	3.63±0.27	8.37±0.21
312.5	3.44±0.27	8.42±0.20
317.5	3.77±0.23	8.65±0.56
322.5	3.72±0.11	8.67±0.53
327.5	3.52±0.23	8.43±0.17
332.5	3.56±0.11	8.43±0.47
337.5	3.40±0.20	7.63±0.45
342.5	2.86±0.10	7.39±0.15
347.5	2.74±0.09	6.54±0.42
352.5	2.30±0.18	6.14±0.37
357.5	1.90±0.19	5.47±0.12
362.5	1.52±0.09	4.62±0.32
367.5	1.17±0.14	4.10±0.32
372.5	0.81±0.08	3.33±0.31
377.5	0.49±0.13	2.71±0.09
382.5	0.37±0.10	2.02±0.08
387.5	0.18±0.07	1.72±0.07
392.5	0.00±0.04	1.14±0.17
397.5	0.04±0.04	0.77±0.13
402.5	0.02±0.03	0.43±0.11
407.5	0	0.27±0.11
412.5	0	0.07±0.04
417.5	0	0.07±0.08
422.5	0	0.09±0.07
427.5	0	0.02±0.06

Table 9.4: *$\pi\pi$ invariant mass distributions for E_γ = [460 - 520] MeV*

$M_{\pi\pi}$ [MeV]	$d\sigma/dM(\pi^0\pi^0)$ (nb/MeV)	$d\sigma/dM(\pi^0\pi^{+/-})$ (nb/MeV)
272.5	3.39±0.08	0.18±0.17
277.5	6.16±0.10	7.38±0.30
282.5	6.83±0.17	12.7±0.77
287.5	6.99±0.29	14.5±0.71
292.5	7.29±0.31	17.5±0.74
297.5	7.46±0.32	19.3±0.85
302.5	7.74±0.15	20.8±0.75
307.5	7.75±0.15	21.2±0.74
312.5	7.86±0.15	21.7±0.72
317.5	7.97±0.15	22.2±0.73
322.5	8.67±0.15	22.6±0.85
327.5	8.72±0.31	23.1±0.70
332.5	8.69±0.15	22.0±0.82
337.5	8.48±0.14	21.9±0.67
342.5	8.52±0.14	21.7±0.64
347.5	8.06±0.28	20.9±0.62
352.5	7.80±0.28	20.6±0.26
357.5	7.24±0.27	18.9±0.25
362.5	7.06±0.27	18.3±0.24
367.5	6.56±0.25	16.7±0.23
372.5	5.92±0.11	15.7±0.22
377.5	5.33±0.11	14.5±0.21
382.5	4.89±0.22	13.5±0.20
387.5	4.17±0.21	11.8±0.44
392.5	3.83±0.20	11.0±0.17
397.5	3.09±0.09	9.67±0.40
402.5	2.65±0.17	8.53±0.35
407.5	2.18±0.17	7.71±0.33
412.5	1.75±0.07	6.63±0.13
417.5	1.30±0.15	5.52±0.28
422.5	1.03±0.06	4.69±0.23
427.5	0.81±0.12	4.07±0.09
432.5	0.52±0.11	3.07±0.21
437.5	0.44±0.12	2.81±0.21
442.5	0.26±0.16	2.22±0.17
447.5	0.03±0.04	1.76±0.16
452.5	0.08±0.03	1.44±0.10
457.5	0.07±0.01	0.99±0.05
462.5	0.03±0.01	0.73±0.04
467.5	0	0.47±0.07
472.5	0	0.43±0.08
477.5	0	0.23±0.02
482.5	0	0.17±0.04
487.5	0	0.08±0.01

Table 9.5: $\pi^0\pi^0$ *invariant mass distributions for* E_γ *= [300 - 400] MeV, with the difference between a* π^0 *and* $\pi^{+/-}$ *mass (4.6 MeV) taken into account (see Chapter VI, sect 6.2.3).*

$M_{\pi\pi}$ [MeV]	$(d\sigma_{\pi^0\pi^0}/dM)/\sigma_{\pi^0\pi^0}(MeV^{-1})$	$(d\sigma_{\pi^0\pi^{+/-}}/dM)/\sigma_{\pi^0\pi^{+/-}}(MeV^{-1})$
277.5	1.44±0.12	0.55±0.15
282.5	2.45±0.24	1.43±0.18
287.5	3.26±0.18	2.42±0.48
292.5	3.04±0.20	2.66±0.18
297.5	2.92±0.21	3.00±0.42
302.5	3.31±0.24	3.13±0.16
307.5	2.82±0.39	2.53±0.38
312.5	1.89±0.51	2.59±0.35
317.5	2.06±0.37	2.15±0.33
322.5	1.60±0.42	1.99±0.11
327.5	0.83±0.24	1.84±0.41
332.5	1.17±0.19	1.65±0.33
337.5	1.00±0.26	1.01±0.21
342.5	0.64±0.20	0.63±0.19
347.5	0.20±0.18	0.52±0.07
352.5	0.07±0.17	0.38±0.05

Table 9.6: *Tagger energy calibration.*

Channel	E_γ [MeV]	ΔE_γ [MeV]	Channel	E_γ [MeV]	ΔE_γ [MeV]
1	818.90	1.17	40	753.32	1.65
2	817.70	1.20	41	751.65	1.64
3	816.45	1.25	42	749.97	1.64
4	815.16	1.30	43	748.28	1.63
5	813.81	1.35	44	746.59	1.63
6	812.42	1.40	45	744.89	1.63
7	810.97	1.45	46	743.19	1.62
8	809.47	1.51	47	741.48	1.62
9	807.92	1.55	48	739.74	1.66
10	806.32	1.60	49	738.02	1.66
11	804.67	1.65	50	736.29	1.65
12	802.98	1.69	51	734.58	1.70
13	801.25	1.73	52	732.84	1.69
14	799.47	1.77	53	731.09	1.69
15	797.66	1.80	54	729.34	1.69
16	795.83	1.83	55	727.58	1.68
17	793.96	1.85	56	725.79	1.72
18	792.07	1.87	57	724.02	1.72
19	790.17	1.88	58	722.24	1.71
20	788.26	1.89	59	720.48	1.75
21	786.34	1.89	60	718.69	1.75
22	784.43	1.89	61	716.89	1.74
23	782.52	1.88	62	715.09	1.74
24	780.63	1.86	63	713.28	1.74
25	778.76	1.84	64	711.46	1.73
26	776.92	1.81	65	709.64	1.73
27	775.10	1.78	66	707.81	1.73
28	773.32	1.75	67	705.95	1.77
29	771.56	1.71	68	704.11	1.77
30	769.85	1.68	69	702.26	1.77
31	768.15	1.67	70	700.43	1.81
32	766.47	1.62	71	698.57	1.81
33	764.85	1.58	72	696.70	1.80
34	763.22	1.61	73	694.83	1.80
35	761.59	1.62	74	692.95	1.80
36	759.95	1.63	75	691.06	1.80
37	758.31	1.64	76	689.15	1.83
38	756.65	1.65	77	687.25	1.83
39	754.99	1.65	78	685.34	1.83

Channel	E_γ [MeV]	ΔE_γ [MeV]	Channel	E_γ [MeV]	ΔE_γ [MeV]
80	681.53	1.86	120	599.84	2.04
81	679.61	1.86	121	597.68	2.03
82	677.68	1.86	122	595.52	2.03
83	675.74	1.85	123	593.32	2.07
84	673.79	1.85	124	591.15	2.07
85	671.82	1.89	125	588.97	2.06
86	669.87	1.88	126	586.81	2.11
87	667.90	1.88	127	584.62	2.10
88	665.96	1.92	128	582.43	2.10
89	663.98	1.92	129	580.23	2.09
90	662.00	1.91	130	578.02	2.09
91	660.01	1.91	131	575.82	2.08
92	658.02	1.91	132	573.60	2.08
93	656.02	1.90	133	571.36	2.12
94	654.00	1.94	134	569.14	2.12
95	651.99	1.93	135	566.91	2.11
96	649.97	1.93	136	564.70	2.16
97	647.96	1.96	137	562.47	2.15
98	645.93	1.96	138	560.22	2.15
99	643.90	1.96	139	557.98	2.14
100	641.86	1.95	140	555.73	2.13
101	639.81	1.95	141	553.47	2.13
102	637.76	1.94	142	551.21	2.12
103	635.68	1.99	143	548.95	2.11
104	633.61	1.98	144	546.65	2.16
105	631.54	1.98	145	544.38	2.16
106	629.49	2.02	146	542.10	2.15
107	627.41	2.02	147	539.85	2.20
108	625.32	2.01	148	537.57	2.19
109	623.22	2.01	149	535.28	2.19
110	621.13	2.00	150	532.98	2.18
111	619.02	2.00	151	530.69	2.17
112	616.91	1.99	152	528.39	2.16
113	614.78	2.03	153	526.08	2.16
114	612.65	2.03	154	523.77	2.15
115	610.53	2.02	155	521.43	2.20
116	608.42	2.06	156	519.11	2.19
117	606.28	2.05	157	516.79	2.19
118	604.14	2.05	158	514.50	2.24
119	601.99	2.04	159	512.17	2.23

Channel	E_γ [MeV]	ΔE_γ [MeV]	Channel	E_γ [MeV]	ΔE_γ [MeV]
160	509.84	2.22	200	414.05	2.30
161	507.50	2.22	201	411.61	2.29
162	505.17	2.21	202	409.16	2.28
163	502.82	2.20	203	406.74	2.33
164	500.48	2.19	204	404.29	2.32
165	498.13	2.18	205	401.84	2.31
166	495.75	2.24	206	399.39	2.30
167	493.39	2.23	207	396.94	2.28
168	491.03	2.22	208	394.48	2.28
169	488.70	2.27	209	392.02	2.27
170	486.33	2.27	210	389.56	2.25
171	483.96	2.26	211	387.10	2.24
172	481.59	2.25	212	384.60	2.31
173	479.22	2.24	213	382.14	2.29
174	476.84	2.23	214	379.68	2.28
175	474.46	2.23	215	377.24	2.35
176	472.07	2.22	216	374.78	2.34
177	469.66	2.26	217	372.31	2.32
178	467.27	2.25	218	369.84	2.31
179	464.88	2.24	219	367.37	2.30
180	462.51	2.29	220	364.89	2.29
181	460.11	2.28	221	362.42	2.28
182	457.71	2.27	222	359.95	2.27
183	455.31	2.26	223	357.47	2.26
184	452.90	2.26	224	354.96	2.32
185	450.49	2.25	225	352.48	2.31
186	448.08	2.24	226	350.00	2.30
187	445.67	2.23	227	347.56	2.36
188	443.22	2.28	228	345.08	2.35
189	440.80	2.28	229	342.60	2.34
190	438.38	2.27	230	340.12	2.33
191	435.99	2.32	231	337.63	2.32
192	433.56	2.31	232	335.15	2.31
193	431.13	2.31	233	332.67	2.30
194	428.70	2.30	234	330.18	2.29
195	426.27	2.29	235	327.70	2.27
196	423.84	2.28	236	325.18	2.33
197	421.40	2.27	237	322.70	2.32
198	418.96	2.26	238	320.21	2.31
199	416.52	2.25	239	317.76	2.36

Channel	E_γ [MeV]	ΔE_γ [MeV]	Channel	E_γ [MeV]	ΔE_γ [MeV]
240	315.27	2.35	280	215.83	2.27
241	312.78	2.34	281	213.35	2.25
242	310.29	2.33	282	210.87	2.24
243	307.80	2.32	283	208.40	2.23
244	305.32	2.30	284	205.89	2.29
245	302.83	2.29	285	203.42	2.28
246	300.34	2.28	286	200.94	2.26
247	297.85	2.27	287	198.51	2.32
248	295.33	2.32	288	196.04	2.31
249	292.84	2.31	289	193.57	2.30
250	290.35	2.30	290	191.10	2.29
251	287.89	2.36	291	188.64	2.28
252	285.40	2.35	292	186.17	2.26
253	282.91	2.33	293	183.71	2.25
254	280.42	2.32	294	181.24	2.24
255	277.94	2.31	295	178.78	2.23
256	275.45	2.30	296	176.29	2.27
257	272.96	2.29	297	173.83	2.26
258	270.47	2.27	298	171.37	2.25
259	267.98	2.26	299	168.95	2.30
260	265.46	2.32	300	166.49	2.29
261	262.97	2.31	301	164.04	2.28
262	260.48	2.30	302	161.58	2.26
263	258.03	2.35	303	159.13	2.25
264	255.54	2.34	304	156.68	2.24
265	253.06	2.33	305	154.23	2.23
266	250.57	2.32	306	151.78	2.21
267	248.08	2.30	307	149.34	2.20
268	245.60	2.29	308	146.86	2.25
269	243.11	2.28	309	144.42	2.24
270	240.63	2.27	310	141.98	2.23
271	238.15	2.26	311	139.57	2.28
272	235.63	2.30	312	137.13	2.26
273	233.15	2.29	313	134.69	2.25
274	230.67	2.28	314	132.26	2.24
275	228.22	2.33	315	129.82	2.23
276	225.74	2.31	316	127.39	2.22
277	223.26	2.30	317	124.96	2.20
278	220.78	2.29	318	122.53	2.19
279	218.30	2.28	319	120.10	2.18

Channel	E_γ [MeV]	ΔE_γ [MeV]	Channel	E_γ [MeV]	ΔE_γ [MeV]
320	117.67	2.17	337	76.709	2.22
321	115.22	2.22	338	74.316	2.20
322	112.80	2.20	339	71.925	2.19
323	110.38	2.19	340	69.536	2.18
324	107.99	2.25	341	67.148	2.17
325	105.57	2.23	342	64.763	2.15
326	103.16	2.22	343	62.380	2.14
327	100.74	2.21	344	59.999	2.13
328	98.334	2.20	345	57.620	2.12
329	95.924	2.18	346	55.243	2.11
330	93.516	2.17	347	52.834	2.16
331	91.109	2.16	348	50.461	2.15
332	88.704	2.15	349	48.090	2.14
333	86.302	2.13	350	45.755	2.19
334	83.868	2.19	351	43.388	2.18
335	81.469	2.17	352	40.925	2.36
336	79.072	2.16			

Bibliography

[1] http://www.rikenresearch.riken.jp/

[2] T. Muta *Foundations of quantum chromodynamics: an introduction to perturbative methods in gauge theories* (3rd ed.). World Scientific. (2009) ISBN 978-981-279-353-9

[3] B. Krusche: *Photoproduction of π^0 and η mesons from nucleons and nuclei in the second resonance region.* Habilitation Thesis, Gießen Universität (1995)

[4] B. Krusche: *In-medium properties of nucleon resonances.* Acta Phys. Hungarica A26 (2006) 105, nucl-ex/0412006

[5] B. Krusche et al.: *Photoexcitation of Baryon Resonances on Nucleons and Nuclei.*. Proceedings of the IV International Conference on Quarks and Nuclear Physics, Madrid, Spain, 5. - 10. June 2006, Eur. Phys. J. A31 (2007) 485

[6] N. Bianchi et al.: *Total hadronic photoabsorption cross section on nuclei in the nucleon resonance region.* Phys. Rev. C54 1688 (1996).

[7] B. Krusche: *Photoproduction of Mesons off Light Nuclei.* Proceedings of International Conference Nuclear Reactions on Nucleons and Nuclei, October 5.-9. 2009, Messina, Italy, Int. J. Mod. Phys. E19 (2010) 916

[8] V. Metag: *In-Medium Properties of Hadrons - the experimental status.* Workshop on the in-Medium Hadron Physics of the International Graduate School Complex Systems of Hadrons and Nuclei, Giessen, 2004

[9] M. Lutz et al.: *Meson properties at finite temperature and baryon density.* Nucl. Phys. A542 (1992) 521

[10] M. Post et al.: *Hadronic Spectral Functions in Nuclear Matter.* Nucl.Phys. A741 (2004) 81-148

[11] G. Agakichiev et al.: *Enhanced Production of Low-Mass Electron Pairs in 200 GeV/Nucleon S-Au Collisions at the CERN Super Proton Synchrotron.* Phys. Rev. Lett. 75 (1995) 1272-1275

[12] Johannes P. Wessels et al.: *Latest Results from CERES/NA45.* Nucl.Phys. A715 (2003) 262-271

[13] E. L. Bratkovskaya: *ρ/ω properties from dilepton spectra in pA reactions at 12 GeV.* Phys. Rev. Lett B529 (2002) 26-35

[14] F. Bloch et al.: *Double pion photoproduction off ^{40}Ca .* Eur. Phys. J. A32 (2007) 219

[15] D. Trnka et al.: *First observation of in medium modifications of the ω meson.* Phys. Rev. Lett. 94 (2005) 192303

[16] J.Arends, P.Detemple, N.Floss, A.Hegerath, S.Huthmacher, B.Mecking, G.Noldecke, R.Stenz, and V.Werler. : *Measurement of total cross sections for π^0 photoproduction on nuclei in the Δ-resonance region.* Nucl. Phys. A544 (1986) 579-588

[17] T. Yorita et al., Phys. Lett. B 476 (2000) 226.

[18] T. Kinoshita et al., Phys. Lett. B 639 (2006) 429.

[19] F.Lenz and E.J.Moniz, *Com. Nucl. Part. Phys.* **9** (1980) 101

[20] J.H.Koch, E.J.Moniz, and N.Ohtsuka, *Ann. Phys.* **154** (1984) 99

[21] W.Cassing, V.Metag, U.Mosel, and K.Niita, *Phys. Rep.* **188** (1990) 363

[22] W. Peters et al.: *The spectral function of the ρ meson in nuclear matter.* Nucl. Phys. A632 (1998) 109-127

[23] B. Krusche, J. Ahrens, R. Beck, I.J.D. MacGregor, J.C. McGeorge, V. Metag, H. Ströher: *In-medium properties of the D_{13}(1520) nucleon resonance.* Phys. Rev. Lett. 86 (2001) 4764

[24] B. Krusche: *In-medium properties of hadrons.* Proceedings of the Meson2006 IX Int. Workshop on Production, Properties and Interaction of Mesons, Cracow, Poland 09 - 14 June, 2006, Int. J. Mod. Phys. A22 (2007) 406

[25] T. Mertens et al.: *Photoproduction of η-mesons off nuclei for E_γ < 2.2 GeV.* Eur. Phys. J. A38 (2008) 195

[26] V. Bernard et al.: *Properties of the scalar σ -meson at finite density.* Phys. Rev. Lett. 59 (1987) 966

[27] P. Schuck et al.: *Dropping σ -meson mass and in medium s-wave $\pi\pi$ correlations.* nucl-th/0002031

[28] T. Hatsuda, T. Kunihiro, and H. Shimizu: *Precursor of Chiral Symmetry Restoration in the Nuclear Medium.* Phys. Rev. Lett. 82 (1999) 2840

[29] Z. Aouissat et al.: *Reduced σ -meson mass and in medium S-wave $\pi - \pi$ correlations.* Phys. Rev. C61 (2000) 012202

[30] H.C. Chiang et al.: *Chiral non-perturbative approach to the isoscalar s-wave $\pi\pi$ interaction in a nuclear medium.* Nucl. Phys. A644 (1998) 77

[31] L. Roca et al.: *The σ -meson in a nuclear medium through two pion photoproduction.* Phys. Lett. B 541 (2002) 77

[32] G. Chanfray et al.: *Two-pion production processes chiral symmetry and NN interaction in the medium.* Eur. Phys. J. A27 (2006) 191

[33] W-M. Yao et al. Phys. G33 (2006) 1

[34] I. Caprini, G. Colangelo and H. Leutwyler: *Mass and Width of the Lowest Resonance in QCD* Phys. Rev. Lett. 96 (2006) 132001

[35] F. Bonutti et al.: *$\pi\pi$ pairs in nuclei and the σ -meson.* Phys. Rev. C 60 (1999) 018201

[36] F. Bonutti et al.: *A Dependence of the $(\pi^+, \pi^+\pi^{+/-})$ Reaction near the $2m\pi$ Threshold.* Phys. Rev. Lett. 77 (1996) 603

[37] F. Bonutti et al.: *The $\pi\pi$ interaction in nuclear matter from a study of the $\pi^+ + A \to \pi^+\pi^{+/-}A'$ reactions.* Nucl. Phys. A677 (2000) 213

[38] P. Camerini et al.: *General properties of the pion production reaction in nuclear matter* Nucl. Phys. A735 (2004) 89

[39] N. Grion et al.: *The $\pi \to \pi\pi$ process in nuclei and the restoration of chiral symmetry* Nucl. Phys. A763 (2005) 80

[40] J. G. Messchendorp et al.: *In-Medium Modifications of the $\pi\pi$ Interaction in Photon-Induced Reactions.* Phys. Rev. Lett. 89, 222302 (2002)

[41] A. Starostin et al.: *Measurement of $\pi^0\pi^0$ Production in the Nuclear Medium by π^- Interactions at 0.408 GeV/c.* Phys. Rev. Lett. 85, 5539 (2000)

[42] F. Rambo et al.: *Coherent π^0 photoproduction from ^{4}He.* F. Rambo et al., Nucl. Phys. A660 (1999) 69

[43] D. Drechsel et al.: *Medium effects in coherent pion photo- and electroproduction on ^{4}He and ^{12}C.* Nucl. Phys. A660 (1999) 423

[44] D. Drechsel et al.: *A unitary isobar model for pion photo- and electroproduction on the proton up to 1 GeV.* Nucl. Phys. A645 (1999) 423

[45] A. A. Chumbalov, R. A. Eramzhyan, and S. S. Kamalov: *WIA in the momentum space for (γ, π^0) reaction near threshold.* Z. Phys. A 328 (1987) 195

[46] S. Boffi et al.: *Coherent π^0 Photoproduction Near Threshold On Closed Shell Nuclei.* Nucl. Phys. A448 (1986) 637

[47] S.S. Kamalov et al.: *On the contradictory situation in coherent $^{12}C(\gamma, \pi^0)$ and $^4He(\gamma, \pi^0)$ reactions.* Phys. Lett. B (1985) 162

[48] V. Girija et al.: *Coherent pion photoproduction.* Phys. Rev. C 27 (1983) 1169

[49] E. Oset and W. Weise. Nucl. Phys. A 402 (1983) 612.

[50] J. H Kochet al.: *Coherent π^0 photoproduction at intermediate energy.* Phys. Rev. C 27 (1983) 751

[51] B. Körfgen et al.: *Longitudinal and transverse spin response of C12 in the Δ-resonance region.* Phys. Rev. C 50 (1994) 1637

[52] T. Takaki et al.: *Photoproduction of neutral pions to discrete nuclear states .* Nucl. Phys. A443 (1985) 570

[53] R. C. Carrasco et al.: *Coherent (γ ,π^0) photoproduction in a local approximation to the Δ-hole model.* Nucl. Phys., A565:797-817, 1993.

[54] W. Peters, H. Lenske and U. Mosel: *Coherent photoproduction of pions on spin-zero nuclei in a relativistic, non-local model.* Nucl. Phys. A 640 (1998) 89

[55] B. Krusche et al.: *Surface and volume effects in the photoabsorption of nuclei.* Eur. Phys. J. A22 (2004) 347

[56] B. Krusche et al.: *Photoproduction of π^0 -mesons from nuclei.* Eur. Phys. J. A22 (2004) 277

[57] B. Krusche et al.: *Coherent π^0 -photoproduction from atomic nuclei.* Phys. Lett. B526 (2002) 287

[58] C. W. De Jager, H. De Vries, and C. De Vries: *Nuclear charge- and magnetization-density-distribution parameters from elastic electron scattering.* At. Data Nucl. Data Tables 14, 479 (1974)

[59] H. de Vries, C. W. de Jager and C. de Vries: *Nuclear charge-density-distribution parameters from elastic electron scattering.* At. Data Nucl. Data Tables 36, 495 (1987)

[60] B. Frois, C. N. Papanicolas, and S. E. Williamson, in Modern Topics in Electron Scattering, edited B. Frois and I. Sick (World Scientific, Singapore, 1991), p. 352

[61] G. Fricke et al.: *Nuclear Ground State Charge Radii from Electromagnetic Interactions.* At. Data Nucl. Data Tables 60, 177 (1995)

[62] I. Sick et al.: *Radial Distribution of Valence Neutrons from Elastic Electron Scattering.* Phys. Rev. Lett. 38 (1977) 1259

[63] S. K. Platchkov et al.: *Magnetic electron scattering and valence nucleon radial wave functions.* Phys. Rev. C 25 (1982) 2318

[64] C.J. Batty, E. Friedman, H.J. Gils, and H. Rebel, Advances in Nucl. Phys. 19 (1989)

[65] R.A. Schrack, J.E. Leiss, and S. Penner: *Neutral Meson Photoproduction from Complex Nuclei.* Phys. Rev. 127 (1962) 1772.

[66] B. Krusche et al.: *Single and double π^0 -photoproduction from the deuteron* , Eur. Phys. J. A6 (1999) 309.

[67] E.M. Darwish, H. Arenhvel, M. Schwamb: *Influence of final-state interaction on incoherent pion photoproduction on the deuteron in the region of the Δ-resonance* Eur. Phys. J. A16 2003 111.

[68] H. Alvesleben et al.: *Determination of Strong-Interaction Nuclear Radii.* Phys. Rev. Lett. 24 (1970) 792.

[69] B. Krusche: *Nuclear mass form factors from coherent photoproduction of π^0 mesons.* Eur. Phys. J. A26 (2005) 7, nucl-ex/0509003

[70] G.F. Chew et al.: *Relativistic Dispersion Relation Approach to Photomeson Production* Phys. Rev. 106 (1957) 1345.

[71] B. Krusche et al.: *Near threshold photoproduction of eta-mesons off the proton.* Phys. Rev. Lett. 74 (1995) 3736

[72] R. S. Whaler and L. C. Liu: *Off-shell model for threshold pionic η production on a nucleon and for ηN scattering.* Phys. Rev. Lett. 54, 865 (1985)

[73] L. C. Liu and Q. Haider: *Signature for the existence of η-mesic nucleus.* Phys. Rev. C 34, 1845 (1986)

[74] A.M. Green et al.: *η-deuteron scattering.* Phys. Rev. C54 (1996) 1970

[75] R.E. Chrien et al.: *Search for Bound States of the η-meson in Light Nuclei.* Phys. Lett. B 60 (1988) 2595

[76] Johnson et al.: *Search for an η bound state in pion double charge exchange on 18O.* Phys. Rev. C 47 (1993) 2571

[77] A. I. Lebedev and V. A. Tryasuchevet.: *Cross sections for production of η nuclei by photons.* J. Phys. G: Nucl. Part. Phys. 17 (1991) 1197

[78] A. I. Lebedev and G. A. Sokol.: *Photoproduction of light η nuclei.* Preprint No. 34, Lebedev Physical Institute, Russian Academy of Sciences, Moscow

[79] G.A. Sokol et al.: *First experimental results on creation and decay of η-mesic nuclei.* nucl-ex/0011005v1 (2000)

[80] G.A. Sokol et al.: *Observation of eta-mesic nuclei in photoreactions : results and perspectives.* nucl-ex/0106005)(2001)

[81] B. Krusche et al.: *Near threshold photoproduction of η-mesons from the deuteron.* Phys. Lett. B358 (1995) 40

[82] Sibirtsev et al.: *ηN final state interaction in incoherent photoproduction of η mesons from the deuteron near threshold.* Phys. Rev. C 65 (2002) 044007

[83] S. A. Rakityanski et al.: *Threshold scattering of the η-meson off light nuclei.* Phys. Lett. B359 (1995) 33

[84] S. A. Rakityanski et al.: *Quasibound states of η-nucleus systems.* Phys. Rev. C 53

[85] N.V. Shevchenko, V.B. Belyaev, S.A. Rakityansky, W. Sandhas and S.A. Sofianos: *Low-energy ηd-resonance.* Eur. Phys. J. A 9 (2000) 143

[86] V.Y. Grishina et al.: *η- and $\eta^{'}$-meson production in the reaction $pn \to dM$ near threshold.* Phys. Lett. B475 (2000) 9

[87] H. Garcilazo and M.T. Pena.: *Nonexistence of a ηNN quasi-bound state.* Phys. Rev. C 63 (2001) p. R21001.

[88] H. Calén et al.: *The $pp \to pp\eta$ reaction near the kinematical threshold.* Phys. Lett. B366 (1996) 39

[89] F. Plouin et al.: *Identification and analysis of the $np \to d\eta$ cross section near threshold.* Phys. Rev. Lett. 65 (1990) 690

[90] H. Calén et al.: *Threshold Structure of the Quasifree $p + n \to d + \eta$ Reaction.* Phys. Rev. Lett. 80 (1998) 2069.

[91] B. Mayer et al.: *Reactions $pd \to^3$He η and $pd \to^3$ He $\pi^+\pi^-$ near the η threshold.* Phys. Rev. C53 (1996) 2068

[92] F. Hibou et al.: *Near-threshold η production in the $pd \to pd\eta$ reaction.* Eur. J. Phys. A7 (2000) 537

[93] N. Willis et al.: *Eta-Helium Quasi-Bound States* Phys. Lett. B 406 (1997) 14

[94] J. Weiss et al.: *Exclusive measurement of quasi-free η-photoproduction from deuterium.* Eur. phys. J. A11 (2001) 371 -374

[95] L. R. Suelzle et al.: *Elastic Electron Scattering from ^{6}Li and ^{7}Li .* Phys. Rev. 162, 992 (1967)

[96] B. Krusche, I. Sick, private communication.

[97] M. Pfeiffer et al.: *Photoproduction of η-mesic ^{3}He.* Phys. Rev. Lett. 92 (2004) 252001

[98] B. Krusche, F. Pheron, private communication.

[99] C. Wilkin et al.: *Is there an View the η ^{3}He quasi-bound state?.* Phys. Lett. B654 (2007) 92-96

[100] R. Beck (Spokesperson of A2 collabration): *Coherent photoproduction of η-mesons from light nuclei - Search for η-mesin nuclei.* Proposal for an experiment by the CrystalBall@MAMI collaboration. Ex.p-Nr A2/7-03.

[101] K. Aulenbacher, C. Nachtigall et al.: *The MAMI source of polarized electrons.* Nucl. Inst. and Meth. A 391 498 (1997)

[102] I. Anthony et al.: *Design of a tagged photon spectrometer for use with the Mainz 840 MeV microtron.* Nucl. Inst. and Meth. A **301** 230 (1991)

[103] F.Zehr: *Double pion photoproduction off the proton at threshold and in the second resonance region.* PhD Thesis, Universität Basel (2008)

[104] S. Schumann: PhD Thesis, Universität Mainz (2008)

[105] E. Downie: *Radiative π^0 photoproduction in the region of the Δ(1232) resonance.* PhD Thesis, University of Glasgow (2007)

[106] C. Wilkin and B. Krusche, private communication.

[107] http://pcweb.physik.uni-giessen.de/taps/publications/publi.html

[108] D. Krambrich: *Aufbau des Crystal Ball-Detektorsystems und Untersuchung des Helizitätasymmetrie in $\gamma p \rightarrow n\pi^+\pi^0$.* PhD thesis, Universität Mainz (2007)

[109] P. Drexler: *Entwicklung und Aufbau der neuen TAPS-Elektronik.* PhD Thesis, Universität Gießen (2004)

[110] J. R. M. Annand: *Data Analysis within an AcquRoot Framework.* University of Glasgow (2005)

[111] http://www.nuclear.gla.ac.uk/ jrma/

[112] http://wwwa2.kph.uni-mainz.de/A2/ $\rightarrow$ Experiments $\rightarrow$ Standard Instruments $\rightarrow$ Tagger Calibration

[113] M. Horras: *The walk correction in a nuclear physical experiment.* Semester project, Universität Basel (2006)

[114] S. Lugert: PhD Thesis, Universität Gießen (2007)

[115] M. Kotulla: *Experiment zur Bestimmung des magnetischen Moment der Δ^+(1232) Resonanz.* PhD Thesis, Universität Gießen (2001)

[116] A. Marin et al.: *Detection of charged pions and protons in the segmented electromagnetic calorimeter TAPS* NIM A417 (1998) 137-149

[117] B. Krusche, I. Sick and I. Jaegle, private communication.

[118] M. Tomaselli et al.: *Matter and charge distributions of ^{6}He and ^{5,6,7,9}Li within the dynamic-correlation model* Phys. Rev. C 62, 067305 (2000).

[119] S.S Kamalov and E. Oset et al.: *Coherent two pion photoproduction on ^{12}C* Nuc. Phys A625 (1997) 873-892.

[120] C.M. Tarbert et al.: *Incoherent pion photoproduction on ^{12}C* Phys.Rev.Lett.100:132301 (2008).